Conductance, thermopower and thermal conductance measurements in single-molecule junctions and atomic contacts

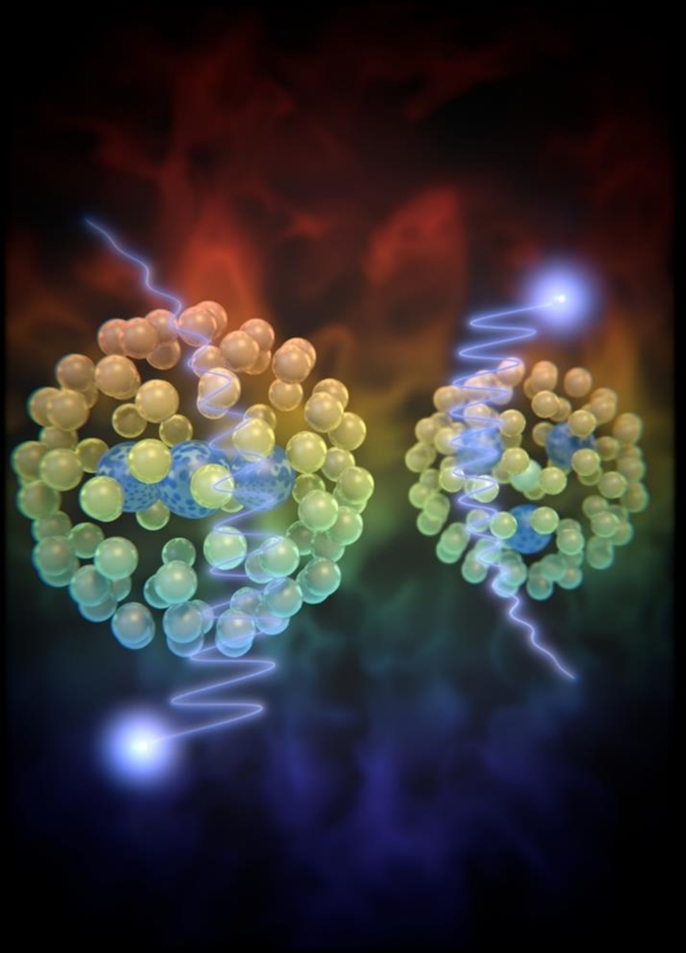

Laura Rincón García

Thesis Supervisor: Prof. Nicolás Agraït de la Puente
Departamento de Física de la Materia Condensada
Universidad Autónoma de Madrid

Cover: $Sc_3N@C_{80}$ molecular junctions in a thermal gradient (red to blue) which generates a thermoelectric response. The direction of the thermoelectric current (depicted in light blue) depends on the orientation of the molecule. Image by E. Sahagún (www.scixel.es)

Conductance, thermopower and thermal conductance measurements in single-molecule junctions and atomic contacts

Thesis presented by

Laura Rincón García

for the degree of Doctor in Physics

by Universidad Autónoma de Madrid

UAM
UNIVERSIDAD AUTONOMA
DE MADRID

FACULTAD DE
CIENCIAS
UNIVERSIDAD AUTÓNOMA DE MADRID

Thesis Supervisor

Prof. Nicolás Agraït de la Puente

Department of Condensed Matter Physics, Faculty of Sciences

Madrid, November 2019

Conductance, thermopower and thermal conductance measurements in single-molecule junctions and atomic contacts

Memoria presentada por

Laura Rincón García

para optar al grado de Doctora en Ciencias Físicas

por la Universidad Autónoma de Madrid

Dirigida por

Prof. Nicolás Agraït de la Puente

Departamento de Física de la Materia Condensada, Facultad de Ciencias

Madrid, Noviembre 2019

A los míos.

"What I want to talk about is the problem of manipulating and controlling things on a small scale. [..] *Now, you might say, "Who should do this and why should they do it?" Well, I pointed out a few of the economic applications, but I know that the reason that you would do it might be just for fun. But have some fun!*"

Richard P. Feynman, "There's Plenty of Room at the Bottom", December 29th 1959.

Acknowledgements

Esta tesis no habría sido posible sin la contribución en mayor o menor medida de todas las personas que han formado parte de mi vida a lo largo de este tiempo. Han sido cinco años de aprendizaje y duro trabajo, llenos de colaboraciones científicas y proyectos formativos, pero también de grandes momentos personales. En caso de olvidar mencionar a alguien en estas páginas, vaya por delante mi más profundo agradecimiento a todas ellas.

Mi más sincera gratitud a mi director de tesis, Nicolás Agraït, por darme la oportunidad de llevar a cabo esta tesis y por compartir conmigo su visión de la física y su pasión por los experimentos y la programación. Mi trabajo en su grupo comenzó como estudiante de grado con la preparación de un vídeo de divulgación científica y no podía sospechar entonces todo lo que aprendería después. La autonomía en el laboratorio, la asistencia a conferencias, las colaboraciones con otros grupos, las publicaciones realizadas... Todo ello ha sido posible gracias a su buen hacer científico y su generosidad, siempre con nuevas ideas, viendo el lado positivo y con Matlab al alcance de la mano. Realmente he disfrutado trabajando contigo.

En lo referente a posibilitar la realización de esta tesis, gracias igualmente al Ministerio de Educación, Cultura y Deporte por la ayuda no. FPU014/03368 con la que ha financiado la mayor parte de este trabajo y al apoyo financiero de la Universidad Autónoma de Madrid en los inicios de mi doctorado a través de una Ayuda para la realización del plan de investigación.

I would also like to thank Prof. Pramod Reddy and all his group at University of Michigan for welcoming me during my six-month stay in Ann Arbor, and in especial Dakotah Thompson for his great explanations about the near field radiative heat transfer setup and his mentoring in the clean room, where Spanish lessons made waiting times shorter. My stay with you was a very enriching experience.

Special thanks go to all the people I have collaborated with along these years in different scientific projects. To Prof. Colin J. Lambert and his group, in particular, for the theoretical calculations performed and the exciting meetings trying to understand the origin of bi-thermoelectricity. To the different groups of chemical synthesis we have worked with for sharing with us their molecules and their patience with the times of experiments. By extension, thank you to all the people involved in MOLESCO and QuIET European projects. I have experienced with you the feeling of a scientific community working together towards a common goal and it is wonderful, in addition to have had the opportunity to travel all around Europe, to visit different facilities and to learn about different working approaches.

Volviendo al lugar en el que he desarrollado la tesis, me gustaría agradecer a los profesores del Departamento de Física de la Materia Condensada su contribución en mi formación científica. Gracias en especial a Gabino Rubio-Bollinger por sus lecciones en el laboratorio, a José Gabriel Rodrigo por su inestimable ayuda en la preparación de las clases de Técnicas Experimentales II, a Miguel Ángel Ramos por su interés por la docencia, a Sebastián Vieira por su confianza y a Hermann Suderow por la oportunidad de organizar las jornadas del INC de 2017 y por llevarlas a cabo cada año; han sido un valioso punto de referencia.

Gracias de manera muy especial a los estudiantes de doctorado que formaban parte del grupo de Nicolás cuando me incorporé: Charalambos (Chara), Siya (coffee time?), Aday y Jorge. Todos ellos son ya doctores y siendo mi referencia más cercana en el laboratorio, su proceso de aprendizaje ha inspirado sin duda el mío. Mi más profunda gratitud a Chara, por todo lo que aprendí con él de STM, moléculas y termoelectricidad y sobre todo por el equipo fantástico que heredé y que me ha permitido desarrollar la mayor parte del trabajo de esta tesis. Gracias igualmente a otros miembros del grupo: a David (que ya es casi doctor también), a Simon, a Alex, y, de manera particular, a Teresa y a Ed, con los que colaboro en los proyectos de oligoinos y porfirinas y cuya ayuda ha sido esencial para llegar a los resultados y conclusiones que presento. A las nuevas incorporaciones al grupo (Juan, Rubén, Juanjo), el relevo, gracias por vuestro espíritu de trabajo y os deseo todo lo mejor en la aventura de la investigación.

Quisiera agradecer también el granito de arena aportado por otros estudiantes de doctorado o investigadores del departamento, del laboratorio de bajas temperaturas en particular (Pepe, Edwin, Antón, Isabel, Víctor, Fran, Roberto, Tomás, y por extensión Isidoro, Juanpe, Antonio), de los técnicos del departamento (Andrés, Chema, Rafa, Sara, José María, Santiago, Nacho) (vuestra aportación a esta tesis es realmente esencial) y al resto de personal del departamento (Elsa, Luisa, Ana, Macarena). A lo largo de estos años he sentido el departamento como mi segunda casa gracias a todos vosotros, a lo que también han contribuido los miembros de la cafetería de Ciencias.

Y hablando de la cafetería de Ciencias, gracias al grupo de comida formado a lo largo de estos años para compartir desayunos, comidas, meriendas y cenas, en la facultad y fuera de ella. María, Laura, Elena, David, Álex, Sergio, Iris, Gus, Juanfran, Aitor, Alicia. Gracias también por los viajes y actividades varias, por las risas y el estrés compartidos. Habéis sido un verdadero punto de apoyo a lo largo de estos años, avanzando juntos en la iniciación al mundo de la investigación.

Otro punto de apoyo esencial han sido mis chiquitas bonitas, Araceli, Estefanía y María. Gracias por tantas y tantas cenas a lo largo de estos años, las vacaciones y los momentos increíbles que hemos compartido. Cualquier plan con vosotras es siempre inmejorable y me recarga las pilas; somos la prueba de que letras y ciencias pueden hacer buenas migas.

A mi círculo más cercano le debo sin duda el haber conseguido llegar hasta aquí. Gracias a mis padres, Vicenta y Juan Carlos, por su apoyo y su fe en mí; han estado ahí desde el principio y sé que siempre puedo contar con ellos. Ah, y todo en orden, papá, creo que no se ha escapado ninguna molécula del experimento. Gracias a mi hermano, Richi, por su cariño incondicional aunque sea en la distancia; hemos crecido y aprendido juntos y siempre estaremos unidos por ello. Y gracias a Mariano por su apoyo y su paciencia, por el tiempo de cálculo en su torre y las promociones locas, por creer en mí y compartir el camino conmigo; soy mejor física y mejor persona desde que te conozco. Por último, y no por ello menos importante, gracias igualmente al resto de mi familia; os llevo siempre conmigo y todos habéis contribuido a lo que soy.

Esta tesis no habría sido posible sin todos vosotros. ¡Muchas gracias!

Table of Contents

Abstract

Molecular electronics is a very active research field whose ultimate goal is the use of single-molecules as functional building blocks in electronic devices [Aviram1974; Bergfield2013; Aradhya2013; Xiang2016]. This technology has been originally proposed as a potential key to solve the unbeatable limit in the miniaturization of the devices down to the atomic scale. In particular, single-molecule thermoelectricity holds the promise to pave the way for the development of more efficient organic-based thermoelectric devices [Malen2010]. The reduced dimensionality, the discreteness of molecular energy levels and the possibility to tune their properties via chemical synthesis, electrostatic gates, or pressure, among others, have potential applications in waste heat recovery or on-chip cooling. Thermoelectric devices based on organic molecules would also be more cost-effective, environmentally friendly, lighter and more flexible than currently available inorganic thermoelectric devices, which are typically brittle and toxic [Zhang2014].

More importantly, besides the potential technological applications, single molecules connected between two metallic electrodes, the so-called single-molecule junctions, are of great fundamental interest and have proved to be exceptional platforms to test quantum transport theories [Cuevas2010]. Measurements of thermopower in molecular junctions, i.e. the charge response to a temperature difference applied between the electrodes, offer complementary information to traditionally performed conductance measurements and are becoming essential for the understanding of transport processes at the nanoscale and at the organic-inorganic interface [Rincón-García2016]. Major advances have been achieved during the last ten years thanks to the development of adequate experimental techniques to measure thermopower at the single-molecule level [Reddy2007; Widawsky2012; Evangeli2013] and a close collaboration between chemical design, theoretical calculations and experimental measurements towards new strategies for its enhancement.

Complementary, a good understanding about heat transfer at the nanoscale results also essential to bring these ideas to fruition and to shed light on the limits of classical theories [Dubi2011; Cui2017a]. This is particularly challenging from the experimental point of view mainly due to the non-equilibrium effects targeted, the scale of the thermal currents to be measured and the intrinsic nature of heat flow, fundamentally different to charge transport. The first thermal conductance measurements in atomic contacts [Cui2017b; Mosso2017] and single-molecule junctions [Cui2019; Mosso2019] have been recently reported, although result for the moment restrictive in the experimental conditions (ultra-high vacuum) and require microfabrication of devices.

This PhD Thesis aims at the experimental characterization of charge and heat transport properties of single-molecule junctions and atomic contacts to get an insight into their fundamental mechanisms and test strategies for thermopower enhancement. The main general aspects of our current theoretical knowledge about transport at the nanoscale and concepts such as thermoelectricity or heat transfer, are discussed first in this manuscript, in Chapter 1, where their particular application to molecular junctions is also introduced.

To achieve the goal of this Thesis of investigating the thermoelectric response of single-molecule junctions, the main experimental technique employed has been a home-built scanning

tunnelling microscope (STM) operating in ambient conditions and at room temperature. A powerful experimental technique initiated in our group during Dr. Charalambos Evangeli PhD Thesis [Evangeli2014] has allowed us to perform simultaneous measurements of conductance and thermopower of single-molecule junctions. A general introduction to the STM and technical details regarding our working setup and experimental technique are presented in Chapter 2 of this manuscript.

In Chapter 3 we present the results obtained for the thermoelectricity of endohedral metallofullerenes formed by planar metallic clusters inside a C_{80} fullerene cage. Namely, $Sc_3N@C_{80}$, $Sc_3C_2@C_{80}$ and $Er_3N@C_{80}$ molecules connected between gold electrodes have been investigated and are demonstrated to show a bi-thermoelectric behaviour, giving positive or negative thermopower depending on the molecule orientation, without chemical modification. The possibility to tune the value and sign of the thermopower by compression of the molecular junctions is also explored, as well as the thermoelectric response of dimer junctions, i.e. two endohedral metallofullerenes connected in series.

Different strategies for thermopower enhancement have been also addressed using the STM-Break Junction technique and are presented in Chapter 4. Conductance and thermopower measurements with three different groups of molecules (fluorene derivatives, oligoyne wires and porphyrin oligomers) have been performed to investigate the tunability of thermopower by chemical substitution of side groups, by increasing molecular length and by different coupling of the units conforming the molecular backbone. Enhancement of the thermopower is found to occur to more or less extent with all these strategies, demonstrating the suitability of molecular junctions as a versatile test bed to explore different approaches to tune charge transport at the nanoscale.

Finally, during this Thesis a new experimental technique to perform thermal conductance measurements in model nanoscale junctions, such as atomic contacts or molecular junctions, has been developed and it is introduced in Chapter 5. It consists of a Pt hot wire used as local heater and thermometer as well as STM tip to form the nanoscale junctions and to perform simultaneous thermal and electrical conductance measurements. The technique has been tested with Au-Au atomic contacts, employing *ac* lock-in detection combined with a numerical theoretical model, and enough thermal resolution of the hot wire sensors even in ambient conditions is demonstrated. The possibility to scan the metallic surface with the hot wire via tunnelling current is also explored.

References

[Aradhya2013] S. V. Aradhya and L. Venkataraman. “Single-molecule junctions beyond electronic transport”. *Nature Nanotechnology* **8**, 399-410 (2013).

[Aviram1974] A. Aviram and M. A. Ratner. “Molecular rectifiers”. *Chemical Physics Letters* **29**(2), 277-283 (1974).

[Bergfield2013] J. P. Bergfield and M. A. Ratner. “Forty years of molecular electronics: Non-equilibrium heat and charge transport at the nanoscale”. *Physica Status Solidi B* **250**(11), 2249-2266 (2013).

[Cuevas2010] J. C. Cuevas and E. Scheer. “Molecular Electronics: An Introduction to Theory and Experiment”. World Scientific Publishers, Singapore (2010).

[Cui2017a] L. Cui, R. Miao, C. Jiang, E. Meyhofer and P. Reddy. “Perspective: Thermal and thermoelectric transport in molecular junctions”. *The Journal of Chemical Physics* **146**, 092201 (2017).

[Cui2017b] L. Cui, W. Jeong, S. Hur, M. Matt, J.C. Klöckner, F. Pauly, P. Nielaba, J.C. Cuevas, E. Meyhofer and P. Reddy. “Quantized thermal transport in single-atom junctions”. *Science* **355**(6330), 1192-119 (2017).

[Cui2019] L. Cui, S. Hur, Z. Alaia Akbar, J. C. Klöckner, W. Jeong, F. Pauly, S.-Y. Jang, P. Reddy and E. Meyhofer. “Thermal conductance of single-molecule junctions”. *Nature* **572**, 628-633 (2019).

[Dubi2011] Y. Dubi and M. Di Ventra. "Colloquium: Heat Flow and Thermoelectricity in Atomic and Molecular Junctions”. *Review of Modern Physics* **83**, 131-155 (2011).

[Evangeli2013] C. Evangeli, K. Gillemot, E. Leary, M. T. González, G. Rubio-Bollinger, C. J. Lambert and N. Agraït. “Engineering the Thermopower of C_{60} Molecular Junctions”. *Nano Letters* **13**(5), 2141-2145 (2013).

[Evangeli2014] C. Evangeli. “Thermopower and Conductance of Single-Molecule Junctions and Atomic Contacts”. PhD Thesis (2014).

[Malen2010] J. A. Malen, S. K. Yee, A. Majumdar and R. A. Segalman. “Fundamentals of energy transport, energy conversion, and thermal properties in organic-inorganic heterojunctions”. *Chemical Physics Letters* **491**(4-6), 109-122 (2010).

[Mosso2017] N. Mosso, U. Drechsler, F. Menges, P. Nirmalraj, S. Karg, H. Riel and B. Gotsmann. “Heat transport through atomic contacts”. *Nature Nanotechnology* **12**, 430-433 (2017).

[Mosso2019] N. Mosso, H. Sadeghi, A. Gemma, S. Sangtarash, U. Drechsler, C. J. Lambert and Bernd Gotsmann. “Thermal Transport through Single-Molecule Junctions”. *Nano Letters*, doi: 10.1021/acs.nanolett.9b02089 (2019).

[Reddy2007] P. Reddy, S.-Y. Jang, R. A. Segalman and A. Majumdar. “Thermoelectricity in Molecular Junctions”. *Science* **315**, 1568-1571 (2007).

[Rincón-García2016] L. Rincón-García, C. Evangeli, G. Rubio-Bollinger and N. Agraït. “Thermopower measurements in molecular junctions”. *Chemical Society Reviews* **45**(15), 4285-4306 (2016).

[Widawsky2012] J. R. Widawsky, P. Darancet, J. B. Neaton and L. Venkataraman. “Simultaneous Determination of Conductance and Thermopower of Single Molecule Junctions”. *Nano Letters* **12**(1), 354-358 (2012).

[Xiang2016] D. Xiang, X. Wang, C. Jia, T. Lee and X. Guo. “Molecular-Scale Electronics: From Concept to Function”. *Chemical Reviews* **116**, 4318-4440 (2016).

[Zhang2014] Q. Zhang, Y. Sun, W. Xu and D. Zhu. “Organic Thermoelectric Materials: Emerging Green Energy Materials Converting Heat to Electricity Directly and Efficiently”. *Advanced Materials* **26**, 6829-6851 (2014).

Resumen

La electrónica molecular es un campo de investigación muy activo cuyo objetivo último es el uso de moléculas individuales como bloques funcionales de dispositivos electrónicos [Aviram1974; Bergfield2013; Aradhya2013; Xiang2016]. Esta tecnología fue originalmente propuesta como una solución potencial al límite invencible en la miniaturización de dispositivos cuando se alcanza la escala atómica. En particular, termoelectricidad basada en moléculas individuales resulta muy prometedora para abrir el camino al desarrollo de dispositivos termoeléctricos orgánicos más eficientes [Malen2010]. Su reducido tamaño, los niveles de energía moleculares discretos y la posibilidad de variar sus propiedades mediante síntesis química, puertas electrostáticas o presión, entre otros, tienen aplicaciones potenciales en la recuperación energética de pérdidas de calor o en refrigeración local de circuitos integrados. Dispositivos termoeléctricos basados en moléculas orgánicas resultarían también más económicos, respetuosos con el medio ambiente, ligeros y flexibles que los dispositivos termoeléctricos inorgánicos actualmente disponibles, los cuales son típicamente frágiles y tóxicos [Zhang2014].

Más importante aún que las potenciales aplicaciones, moléculas individuales conectadas entre dos electrodos metálicos, las denominadas uniones moleculares individuales, resultan de gran interés fundamental y han demostrado ser plataformas excepcionales para poner a prueba teorías de transporte cuántico [Cuevas2010]. Medidas de coeficiente termoeléctrico en uniones moleculares, es decir, de la respuesta de las cargas a la aplicación de una diferencia de temperatura entre los electrodos, ofrecen información complementaria a las medidas de conductancia realizadas tradicionalmente y están convirtiéndose en esenciales para comprender los procesos de transporte en la escala nanométrica y en las fronteras orgánico-inorgánico [Rincón-García2016]. Durante los últimos diez años se han conseguido grandes avances al respecto gracias al desarrollo de técnicas experimentales adecuadas para la medida del coeficiente termoeléctrico a nivel de una única molécula [Reddy2007; Widawsky2012; Evangeli2013] y a una estrecha colaboración entre diseño químico, cálculos teóricos y medidas experimentales hacia nuevas estrategias para su mejora.

De manera complementaria, una buena comprensión de la transferencia de calor en la escala nanométrica resulta también esencial para llevar estas ideas a buen término y arrojar luz sobre los límites de las teorías clásicas [Dubi2011; Cui2017a]. Esto supone un importante reto sobre todo desde el punto de vista experimental debido a los efectos fuera del equilibrio a estudiar, la escala de las corrientes térmicas a medir y la naturaleza intrínseca del flujo de calor, fundamentalmente diferente a la de transporte de carga. Las primeras medidas de conductancia térmica en contactos atómicos [Cui2017b; Mosso2017] y uniones moleculares individuales [Cui2019; Mosso2019] se han publicado recientemente, aunque resultan por el momento restrictivas en las condiciones experimentales (ultra-alto vacío) y requieren microfabricación de dispositivos.

Esta Tesis Doctoral aspira a la caracterización experimental de las propiedades de transporte de carga y calor en uniones moleculares individuales y contactos atómicos para obtener información sobre sus mecanismos fundamentales y poner a prueba estrategias para la mejora de la respuesta termoeléctrica. Los principales aspectos generales de nuestro conocimiento actual sobre transporte en la escala nanométrica y conceptos como termoelectricidad o

transferencia de calor se comentan en primer lugar en este manuscrito, en el Capítulo 1, donde también se introduce su aplicación a uniones moleculares en particular.

Para alcanzar el objetivo de esta Tesis de investigar la respuesta termoeléctrica de uniones moleculares individuales, la principal técnica experimental utilizada ha sido un microscopio de efecto túnel (STM por sus siglas en inglés) de fabricación propia y operado en condiciones y a temperatura ambiente. La poderosa técnica experimental iniciada en nuestro grupo durante la Tesis Doctoral del Dr. Charalambos Evangeli [Evangeli2014] nos ha permitido realizar medidas simultáneas de conductancia y coeficiente termoeléctrico de uniones moleculares individuales. Una introducción general al STM y detalles técnicos de nuestro equipo experimental y la técnica se presentan en el Capítulo 2 de este manuscrito.

En el Capítulo 3 presentamos los resultados obtenidos sobre la termoelectricidad de fullerenos endohédricos metálicos formados por pequeños grupos planos de átomos metálicos dentro de un fullereno C_{80}. Se han investigado en concreto las moléculas $Sc_3N@C_{80}$, $Sc_3C_2@C_{80}$ y $Er_3N@C_{80}$ conectadas entre electrodos de oro y se ha demostrado que presentan un comportamiento bi-termoeléctrico, con coeficiente termoeléctrico positivo o negativo dependiendo de la orientación de la molécula, sin modificación química. La posibilidad de modificar el valor y el signo del coeficiente termoeléctrico mediante compresión de la unión molecular también se ha explorado, así como la respuesta termoeléctrica de uniones de dímeros, es decir, dos fullerenos endohédricos metálicos conectados en serie.

Diferentes estrategias para el aumento del coeficiente termoeléctrico también se han abordado utilizando la técnica de STM-Break Junction (STM-BJ) y se presentan en el Capítulo 4. Se han llevado a cabo medidas de conductancia y coeficiente termoeléctrico con tres grupos diferentes de moléculas (derivados de fluorenos, cables moleculares de oligoinos y oligómeros de porfirinas) para investigar la variación del coeficiente termoeléctrico mediante sustitución química de los grupos laterales, mediante el aumento de la longitud molecular y mediante diferentes acoples entre las unidades que conforman la estructura central de las moléculas. Se ha obtenido aumento del coeficiente termoeléctrico en mayor o menor medida con todas las estrategias, demostrando la idoneidad de las uniones moleculares como sistemas de prueba versátiles para explorar diferentes enfoques en la modificación del transporte de carga en la escala nanométrica.

Finalmente, durante esta Tesis se ha desarrollado una nueva técnica experimental para realizar medidas de conductancia térmica en uniones nanométricas modelo, como contactos atómicos o uniones moleculares, y se introduce en el Capítulo 5. Consiste en un hilo caliente de Pt utilizado como calentador local y termómetro así como punta de STM para formar las uniones nanométricas y llevar a cabo medidas simultáneas de conductancia térmica y eléctrica. La técnica se ha puesto a prueba en contactos metálicos de Au-Au, empleando detección de señales *ac* con un lock-in en combinación con un modelo teórico numérico, y se ha demostrado resolución térmica suficiente de los hilos calientes utilizados incluso en condiciones ambiente. La posibilidad de escanear la superficie metálica con el hilo caliente mediante corriente túnel también se ha explorado.

Referencias

[Aradhya2013] S. V. Aradhya and L. Venkataraman. “Single-molecule junctions beyond electronic transport”. *Nature Nanotechnology* **8**, 399-410 (2013).

[Aviram1974] A. Aviram and M. A. Ratner. “Molecular rectifiers”. *Chemical Physics Letters* **29**(2), 277-283 (1974).

[Bergfield2013] J. P. Bergfield and M. A. Ratner. “Forty years of molecular electronics: Non-equilibrium heat and charge transport at the nanoscale”. *Physica Status Solidi B* **250**(11), 2249-2266 (2013).

[Cuevas2010] J. C. Cuevas and E. Scheer. “Molecular Electronics: An Introduction to Theory and Experiment”. World Scientific Publishers, Singapore (2010).

[Cui2017a] L. Cui, R. Miao, C. Jiang, E. Meyhofer and P. Reddy. “Perspective: Thermal and thermoelectric transport in molecular junctions”. *The Journal of Chemical Physics* **146**, 092201 (2017).

[Cui2017b] L. Cui, W. Jeong, S. Hur, M. Matt, J.C. Klöckner, F. Pauly, P. Nielaba, J.C. Cuevas, E. Meyhofer and P. Reddy. “Quantized thermal transport in single-atom junctions”. *Science* **355**(6330), 1192-119 (2017).

[Cui2019] L. Cui, S. Hur, Z. Alaia Akbar, J. C. Klöckner, W. Jeong, F. Pauly, S.-Y. Jang, P. Reddy and E. Meyhofer. “Thermal conductance of single-molecule junctions”. *Nature* **572**, 628-633 (2019).

[Dubi2011] Y. Dubi and M. Di Ventra. "Colloquium: Heat Flow and Thermoelectricity in Atomic and Molecular Junctions”. *Review of Modern Physics* **83**, 131-155 (2011).

[Evangeli2013] C. Evangeli, K. Gillemot, E. Leary, M. T. González, G. Rubio-Bollinger, C. J. Lambert and N. Agraït. “Engineering the Thermopower of C_{60} Molecular Junctions”. *Nano Letters* **13**(5), 2141-2145 (2013).

[Evangeli2014] C. Evangeli. “Thermopower and Conductance of Single-Molecule Junctions and Atomic Contacts”. PhD Thesis (2014).

[Malen2010] J. A. Malen, S. K. Yee, A. Majumdar and R. A. Segalman. “Fundamentals of energy transport, energy conversion, and thermal properties in organic-inorganic heterojunctions”. *Chemical Physics Letters* **491**(4-6), 109-122 (2010).

[Mosso2017] N. Mosso, U. Drechsler, F. Menges, P. Nirmalraj, S. Karg, H. Riel and B. Gotsmann. “Heat transport through atomic contacts”. *Nature Nanotechnology* **12**, 430-433 (2017).

[Mosso2019] N. Mosso, H. Sadeghi, A. Gemma, S. Sangtarash, U. Drechsler, C. J. Lambert and Bernd Gotsmann. “Thermal Transport through Single-Molecule Junctions”. *Nano Letters*, doi: 10.1021/acs.nanolett.9b02089 (2019).

[Reddy2007] P. Reddy, S.-Y. Jang, R. A. Segalman and A. Majumdar. “Thermoelectricity in Molecular Junctions”. *Science* **315**, 1568-1571 (2007).

[Rincón-García2016] L. Rincón-García, C. Evangeli, G. Rubio-Bollinger and N. Agraït. “Thermopower measurements in molecular junctions”. *Chemical Society Reviews* **45**(15), 4285-4306 (2016).

[Widawsky2012] J. R. Widawsky, P. Darancet, J. B. Neaton and L. Venkataraman. “Simultaneous Determination of Conductance and Thermopower of Single Molecule Junctions”. *Nano Letters* **12**(1), 354-358 (2012).

[Xiang2016] D. Xiang, X. Wang, C. Jia, T. Lee and X. Guo. “Molecular-Scale Electronics: From Concept to Function”. *Chemical Reviews* **116**, 4318-4440 (2016).

[Zhang2014] Q. Zhang, Y. Sun, W. Xu and D. Zhu. “Organic Thermoelectric Materials: Emerging Green Energy Materials Converting Heat to Electricity Directly and Efficiently”. *Advanced Materials* **26**, 6829-6851 (2014).

1. Motivation and theoretical background

Miniaturization of electronic devices has made the understanding of charge transport at the nanoscale an essential necessity, especially in the field of molecular electronics in which individual molecules can be considered electronic devices themselves. In nanoscale systems, that is a system in which at least one dimension is on the order of few nanometers, transport phenomena are not governed by the same rules as in the classical macroscopic limit and properties such as the electrical conductance, the thermopower, or even the thermal conductance of nanosystems, require a quantum mechanical approach in order to understand and describe them.

In this chapter, we present a general introduction to molecular electronics, motivating the study of transport properties in molecular junctions (Section 1.1). The main concepts and theoretical background from the macroscopic limit towards the nanoscale are revised in Section 1.2 and Section 1.3. In the former, we focus on the charge transport, while in the latter, the thermoelectric effect is presented. These concepts are then applied, in Section 1.4, to the particular case of molecular junctions, which present several particularities. This is complemented with some general aspects about thermal conductance in nanoscale systems introduced in Section 1.5. Finally, we discuss on the efficiency of thermoelectric devices and present the so-called figure of merit, and we consider the requirements in the application of molecular junctions in thermoelectric devices (Section 1.6).

1.1 Molecular electronics

The term *molecular electronics* refers nowadays to the field of nanotechnology that pursue the final goal of using individual molecules as independent electronic elements of a more complex circuit, i.e. using a single organic molecule as an electronic device itself. The reasons to work on this exciting research field are plenty and of diverse nature, and are founded on the development of both fundamental knowledge and technological applications.

Historically[1], besides the fundamental understanding that it offers (we would see this a bit later), the original motivation is based on the miniaturization of microelectronic components, a race that speeded up during the 1950's with the development of the semiconductor industry (based on silicon) thanks to the invention of the transistor (1947) and integrated circuits or chips (1960s). Already back in the late 1950's, there was a clear perception that this trend in microelectronics, already following Moore's law at that time (transistors/chip doubling every two years), would finally reach "a technological dead-end". Multiple visions and ideas emerged to find an alternative and one of them was molecular electronics. Several scientists turned towards molecules as the key element for the expected next breakthrough after the transistor.

This approach was first proposed by Arthur von Hippel in 1956. His idea was to "design desired material characteristics from the bottom-up" and set the basis of *molecular engineering*, mainly oriented to new fabrication strategies, and aimed to overcome the limits of miniaturization. Molecular electronics itself was initially based on these ideas when the concept was publicly used for the first time by the Colonel C. H. Lewis (Air Force) in the 1958 Conference on Molecular

---

[1] Historical background mainly based on Ref. [Choi2009] and [Cuevas2010].

Electronics. At that time it meant the use of “crystalline materials characteristics in microelectronics” or to “make devices utilizing topology of material domains”, but the progresses made in this direction failed in the commercial implementation and the initiative was soon abandoned.

In the 1970s the idea gained renewed interest, this time oriented slightly differently, directly towards the single molecule functionalization. There was still the feeling that the trend in miniaturization would reach eventually an insurmountable limit (a “brick wall”), when the size of the microelectronics would reach nanoscale dimensions. Additionally, the convergence of semiconductor technology towards the nanoscale supposed a real (and urgent) need to get a better understanding of physical properties of matter on a nanometer scale and to find an alternative [Wiesendanger1994].

To go beyond the silicon integrated circuits, the alternative proposed and explored by Ari Aviram, Mark Ratner, Forrest Carter, Robert Metzger, James Tour or Mark Reed, among others, was to use individual organic molecules specifically designed to behave as functioning electronic devices, such as diodes or resistors [Aviram1974]. Initially implemented in the existing technology, molecular electronics was considered to be able to replace completely the semiconductor technology, once it would become a smaller, faster and cheaper platform than silicon. This would lead to the ultimate miniaturization of circuits, based on the ability to tune specific properties in molecules just by chemical design and combine and wire them into a larger-scale electronic device.

With this final goal in mind, a lot of work has been done studying the transport properties of single molecules. At the beginning merely a theoretical proposition [Aviram1974; Carter1983], the invention of the scanning tunnelling microscope (STM) in 1982 [Binnig1982] (see Chapter 2) and the vast capabilities of chemical synthesis allowed experimentally testing the diverse ideas proposed [Aviram1988; Tour1991; Reed1997] and they definitely triggered the development of a field where important progresses have been made. Challenges such as electrically connecting a single molecule or modifying the transport properties by chemical functionalization have been accomplished, for instance.

The truth is that we are currently close to the limiting size ($\sim 5\ \mathrm{nm}$) and that the invention of the transistor and integrated circuits were the last clear breakthroughs in microelectronics. Their potential is still being developed nowadays, although the major developments in industry in the last years are more related to interconnection facilities, accessibility, or data storage than to an actual big change in the technology itself. Beyond all that, molecular electronics still holds the promise to be a key element in the next technology breakthrough to come, although now more oriented to be a silicon microelectronics complement than a competitor [Choi2009].

More importantly, during all these years and still nowadays, molecular electronics has offered and keeps offering the opportunity to gain fundamental knowledge essential to think about any kind of “nanodevice”, being an excellent test bed for investigating transport phenomena in the nanoscale [Cuevas2010]. The capabilities developed since that first molecular conference in 1958 have allowed us to obtain important knowledge about electronic transport itself, but also about connection requirements, electrode needs or devices stability, among others. Molecules have proved to be an excellent playground to explore properties such as thermoelectricity at the nanoscale and other essential questions, such as thermal transport through these systems, are barely starting to be addressed, reason why molecules are still intensively studied. There are many answers to be found before considering molecular electronics as a dead-end and the present Thesis aims to try to find some of them. In order to do so, let us present first a brief overview of electrical conductance, thermoelectricity and thermal conductance of molecular junctions, moving afterwards to the experimental techniques employed (Chapter 2) and, finally, to the systems and results investigated during this Thesis (Chapters 3, 4 and 5).

1.2 Electrical transport: from macroscopic to nanoscopic systems[2]

Charge transport in macroscopic systems is described by the well-known Ohm's law that establishes that a potential difference V applied between the extremes of a conductor or semiconductor is proportional to the electrical current I flowing through it, and the constant of proportionality is the electrical resistance R:

$$V = RI. \qquad \text{Eq. (1.1)}$$

Equivalently, the current flowing through the system is proportional to the potential difference applied and, in this formulation, the constant of proportionality is the electrical conductance G:

$$I = GV, \qquad \text{Eq. (1.2)}$$

$$\text{and } G = 1\ /\ R. \qquad \text{Eq. (1.3)}$$

The conductance reflects the facility of charge carriers to move and for a macroscopic wire is given by the following expression:

$$G = \sigma \frac{S}{L}, \qquad \text{Eq. (1.4)}$$

where σ is the conductivity of the material and S and L are the wire cross-sectional area and length, respectively. Scattering of the charge carriers due to impurities and defects of the material and the sample dimensions determine then the conductance of a macroscopic wire.

When the size of the wire is reduced to nanoscopic dimensions, however, the transport regime changes. Considering a junction or constriction between two macroscopic conductors or electrodes, as the one schematized in Figure 1.1, when its dimensions (L or W, the junction length and width, respectively) are reduced to just few nanometer or less, they become of the order of the Fermi wavelength λ_F of charge carriers, its wave nature needs to be considered and we enter in the full quantum regime. In this limit (coherent nanoscale systems), the scattering approach is the most popular formalism to describe charge transport and the electrical properties [Landauer1957]. It was developed by Rolf Landauer and its central idea is that, ignoring inelastic interactions, a transport problem becomes just a scattering problem and the transmission probability of the charge carriers to cross through the system determines the electronic transport properties.

---

[2] The theoretical background presented in this section is based on the excellent book by J. C. Cuevas and E. Scheer (Ref. [Cuevas2010]), where further details and complementary aspects can be found.

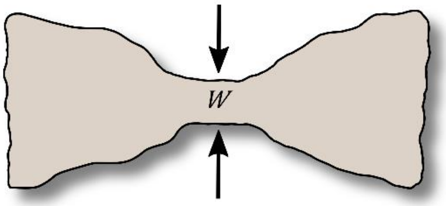

Figure 1.1: Transport regimes and system dimensions. Schematics of a constriction between two macroscopic conductors or electrodes. When the system dimensions L or W (length and width, respectively) become of the same order than the Fermi wavelength λ_F of charge carriers we enter in the full quantum regime.

1.2.1 Landauer formula for coherent transport through a nanojunction

Let us consider a nanoscale junction as the one depicted in Figure 1.2(a), that is, a system with dimensions at the nanoscale electrically connected to two macroscopic electrodes, named 1 and 2. They act as electron reservoirs in thermal equlibrium and have well-defined temperatures T_1 and T_2, respectively, and chemical potentials μ_1 and μ_2, respectively. We consider a one-dimensional situation where the nanosystem is seen by the electrons crossing the junction as a potential barrier of arbitrary shape like the one schematized in Figure 1.2(b), and are elastically scattered by it (ineslastic scatering is restricted to the electron reservoirs). Let us consider first the case of an electron coming from electrode 1 as a plane wave e^{ikz}, where k is the wave vector. The wave is partially reflected by the potential barrier with a probability amplitude r (re^{-ikz}) and partially transmitted with a probability amplitude t (te^{ikz}). The transmission probability of the electron through the nanojunction is given by $\mathcal{T} = |t|^2$.

The electrical current density carried by the electron J_k can be calculated using the following quantum-mechanical expression:

$$J_k = \frac{\hbar}{2im}\left[\psi^*(z)\frac{d\psi}{dz} - \psi(z)\frac{d\psi^*}{dz}\right] = \frac{e}{L}v(k)\mathcal{T}(k), \qquad \text{Eq. (1.5)}$$

where m is the effective mass of the particle, $\hbar$ is Planck's constant h divided by 2π, e is the charge of the electron, L is the length of the nanosystem, and $v(k) = \hbar k/m$ is the group velocity. $\psi(z)$ is the wave function of the incident electron.

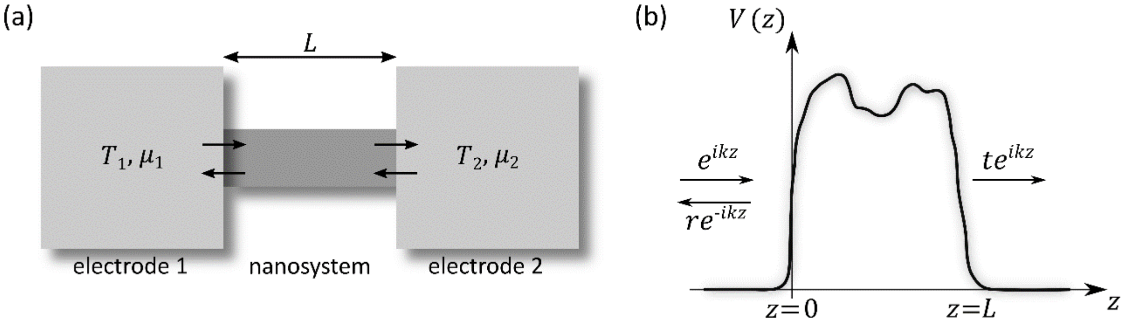

Figure 1.2: Nanoscale junction. (a) Schematic representation of a nanojunction. Two macroscopic electrodes, 1 and 2, in thermal equilibrium with well-defined temperatures and chemical potentials ($T_{1,2}$ and $\mu_{1,2}$, respectively) are connected by a nanoscale system (or nanosystem) of length L (of the order of few nanometer). The electrodes allow to inject current or establish a potential difference through the junction. (b) The nanojunction is seen by the impinging electrons as a one-dimensional potential barrier of arbitrary shape.

When many electrons participate in the transport, as it is the case for a metallic atomic contact or a molecular junction, we need to consider a sum over k and include the factor $f_1(k)[1-f_2(k)]$, where f_1 and f_2 are the Fermi distribution functions of electrodes 1 and 2, respectively. This factor accounts for the Pauli principle and the fact that the chemical potential of the corresponding electrode ($\mu_{1,2}$) can be shifted by an applied voltage V. It also ensures that only those states that are initially occupied in electrode 1 and empty in electrode 2 participate in the current flowing from electrode 1 to electrode 2, given by:

$$J_{1\to 2} = \frac{e}{L}\sum_k v(k)\mathcal{T}(k)f_1(k)[1-f_2(k)]. \qquad \text{Eq. (1.6)}$$

It is possible now to convert the sum into an integral and change from variable k to E, the electron energy, assuming a non-interacting electron gas and using the relation $E = \hbar^2k^2/(2m)$, from where $dk/dE = m/(\hbar^2 k)$. We arrive then to the following expression:

$$J_{1\to 2} = \frac{e}{h}\int \mathcal{T}(E)f_1(E)[1-f_2(E)]dE. \qquad \text{Eq. (1.7)}$$

Equivalently, and considering that the transmission probability is independent of the current direction, the current from electrode 2 to 1 can be written as:

$$J_{2\to 1} = \frac{e}{h}\int \mathcal{T}(E)f_2(E)[1-f_1(E)]dE, \qquad \text{Eq. (1.8)}$$

and the total current, accounting for the spin degeneracy, is simply given by $I(V) = J_{1\to 2} - J_{2\to 1}$, and thus:

$$I(V) = \frac{2e}{h}\int_{-\infty}^{\infty} \mathcal{T}(E)[f_1(E)-f_2(E)]dE. \qquad \text{Eq. (1.9)}$$

This net current arises then from the imbalance between the populations of both electrodes [Agraït2003] fixed by Fermi distribution functions:

$$f_{1,2}(E) = \frac{1}{1+e^{\frac{E-\mu_{1,2}}{k_B T_{1,2}}}}. \qquad \text{Eq. (1.10)}$$

The voltage effect is included in these expressions in the value of $\mu_{1,2}$. Eq. (1.9) is one of the forms of the so-called Landauer formula and it illustrates the close relation between electrical current $I(V)$ and transmission probability $\mathcal{T}(E)$ in nanoscale systems. Assuming low voltages (linear regime) and zero temperature (when $f_{1,2}(E)$ are step functions equal to 0 above $E_F + eV/2$ and $E_F - eV/2$, respectively, and 1 below these energies, E_F being the Fermi energy), this expression simplifies to:

$$I(V) = GV, \qquad \text{Eq. (1.11)}$$

where

$$G = \frac{2e^2}{h}\mathcal{T}(E_F) \qquad \text{Eq. (1.12)}$$

is the electrical conductance of the nanojunction. It is proportional to the transmission evaluated at the Fermi energy and the constant of proportionality is the so-called quantum of conductance G_0:

$$G_0 = \frac{2e^2}{h} = 77.5\ \mu\text{S}. \qquad \text{Eq. (1.13)}$$

From here it is demonstrated that a single-mode conductor, where $\mathcal{T}(E_F) = 1$, has always a finite resistance $1/G_0 \sim 12.9\ \text{k}\Omega$ associated to the resistance at the interfaces between the electrodes and the nanosystem (we will further discuss about the conduction modes in Section 1.2.3). It becomes also clear that in order to calculate the conductance of a given nanojunction, it is required to know its transmission. Before considering a more rigorous derivation of the multi-channel Landauer formula within the scattering formalism, let us introduce a particular example of transmission probability computation, namely, for the case of an electron impinging on a rectangular potential barrier.

1.2.2 Quantum tunnelling

In this section we present the theoretical treatment to compute the transmission probability of a simple situation, namely, the elastic transmission of an electron of energy E and mass m impinging on a one-dimensional rectangular potential barrier of height V_0 and width L (see Figure 1.3). In classical mechanics, the incident electron will be reflected for $E < V_0$, and it will be transmitted for $E > V_0$. However, in quantum mechanics, its wave nature needs to be considered to fully describe its behavior and this translates into a finite probability that the electron passes through the potential barrier, even when its energy is lower than the height of the barrier. This phenomenon is the so-called *quantum tunnelling* or *tunnel effect* and is present in a wide range of nanoscale junctions. Despite the apparent simplicity of the rectangular barrier problem, it offers an essential understanding about tunnelling currents crossing a wide variety of nanojunctions such as scanning tunnelling microscope (STM) junctions or even single-molecule junctions.

To calculate the probability of the particle to pass through the potential barrier, we begin with the one-dimensional time-independent Schrödinger equation:

$$-\frac{\hbar^2}{2m}\frac{d^2\psi_j(z)}{dz^2} + V(z)\psi_j(z) = E\psi_j(z), \qquad \text{Eq. (1.14)}$$

$$\text{where } V(z) = \begin{cases} V_0 & 0 \leq z \leq L \\ 0 & \text{otherwise} \end{cases}$$

and solve it in the three regions shown in Figure 1.3 ($j = 1, 2, 3$). For the case $E < V_0$ the solutions of Eq. (1.14), i.e. the wave function of the particle in each region $\psi_j(z)$, can be written as follows:

$$\begin{aligned} \psi_1 &= a_1 e^{ik_1 z} + b_1 e^{-ik_1 z} \\ \psi_2 &= a_2 e^{k_2 z} + b_2 e^{-k_2 z} \\ \psi_3 &= a_3 e^{ik_3 z} \end{aligned} \qquad \text{Eq. (1.15)}$$

where

$$k_1 = k_3 = \frac{\sqrt{2mE}}{\hbar}, \quad k_2 = \frac{\sqrt{2m(V_0 - E)}}{\hbar} \qquad \text{Eq. (1.16)}$$

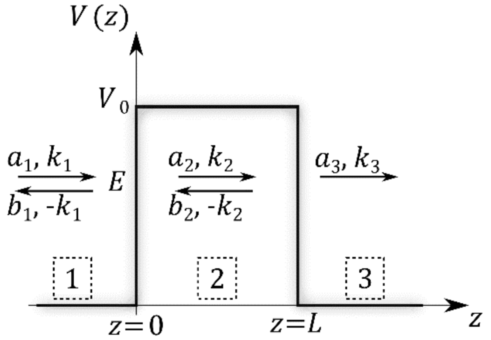

Figure 1.3: One-dimensional rectangular potential barrier. V_0 and L are the barrier height and width, respectively. In quantum mechanics, an incident particle from region 1, of energy E, amplitude $a_1$and wave vector k_1, is partially reflected and transmitted when impinging into the barrier. It is reflected with amplitude b_1 and wave vector $-k_1$ and transmitted into region 2 with amplitude a_2 and wave vector k_2. This wave is itself partially reflected when reaching $z = L$ (with amplitude b_2 and wave vector $-k_2$) and partially transmitted into region 3 with amplitude a_3 and wave vector k_3.

Note that no particle approaching the barrier from region 3 has been considered, only a particle impinging from region 1. A relation for the coefficients $a_{1,2,3}$ and $b_{1,2}$ can be found by means of the 'wave-matching' method (continuity of the wave functions ψ_j and their first derivatives $d\psi_j/dz$ at $z = 0$ and $z = L$, i.e. the discontinuities of the potential $V(z)$). From here we can derive an expression of the barrier energy-dependent transmission coefficient $\mathcal{T}(E)$, which is the ratio of the transmitted and the incident current densities, J_t and J_i respectively. In the example we are considering, where $k_1 = k_3$, the transmission coefficient is directly the ratio between the transmitted and incident coefficients:

$$\mathcal{T}(E) = \left|\frac{a_3}{a_1}\right|^2 = \frac{1}{1+\left(\frac{k_1^2+k_2^2}{2k_1k_2}\right)^2 \sinh^2(k_2L)} = \frac{4E(V_0-E)}{4E(V_0-E)+V_0^2\sinh^2(k_2L)}. \qquad \text{Eq. (1.17)}$$

This is essentially the probability for an electron to pass through the potential barrier and, as it has been advanced, it is different to zero, even in the case that the barrier height is higher than the particle energy ($E < V_0$). In fact, for a strongly attenuating barrier where $k_2L \gg 1$ [Wiesendanger1994], this probability can be simplified to:

$$\mathcal{T}(E) \approx \frac{16k_1^2k_2^2}{(k_1^2+k_2^2)^2} \cdot e^{-2k_2L} \qquad \text{Eq. (1.18)}$$

or, equivalently,

$$\mathcal{T}(E) \propto e^{-2k_2L} = e^{-2L\frac{\sqrt{2m(V_0-E)}}{\hbar}}. \qquad \text{Eq. (1.19)}$$

Then, when $E < V_0$, the transmission through the barrier depends exponentially on the barrier width L and on the square root of the difference between the barrier height and the electron energy, which can be seen as an effective barrier height, $(V_0 - E)^{1/2}$. As stated before, the current through the junction is proportional to the transmission (Eq. (1.9)) and thus, Eq. (1.19) naturally reflects the exponential distance dependence characteristic of tunnelling currents independently of the exact shape of the barrier and it is applicable to nanoscale junctions as the one shown in Figure 1.2(a) (where L is the length of the nanosystem, equivalent to the barrier width).

This quantum tunnelling effect has a major relevance in scanning tunnelling microscopy, the main experimental technique employed during this Thesis (see Chapter 2), and is at the basis of STM experiments, where tunnelling currents are investigated. Given two conducting STM electrodes (1 and 2) of different materials initially far away one from each other, they are electrically isolated and each of them has a certain Fermi energy ($E_{F,1}$ and $E_{F,2}$, respectively) and a work function (Φ_1 and Φ_2, respectively); the vacuum level E_{vac} is common for both of them, as depicted in Figure 1.4(a). The Fermi energy corresponds here to the highest energy of the occupied states in each material and the work function is the energy needed to extract one of those electrons out of the material.

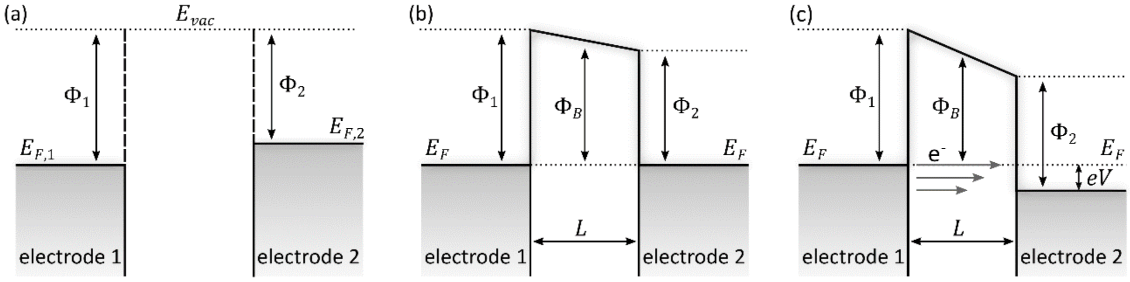

Figure 1.4: STM tunnelling barrier. (a) Conducting electrodes far away from each other, electrically isolated. Each of them has a certain Fermi energy ($E_{F,1}$ and $E_{F,2}$, respectively) and a work function (Φ_1 and Φ_2, respectively). The vacuum level E_{vac} is common for both of them. (b) When the two electrodes are brought into close proximity and the width of the potential barrier L is sufficiently reduced, a small charge transfer takes place at the surface which equilibrates the Fermi levels E_F of both electrodes. Φ_B is the average height of the potential barrier between them. (c) A voltage difference V applied between the electrodes unbalances again both sides of the potential barrier and charges in the energy window $E_F - eV$ can tunnel through it.

When the two electrodes approach each other, before reaching the 'mechanical' point of contact, and when the width of the potential barrier is sufficiently reduced by placing the two systems in close proximity, there is a certain probability for charges to tunnel through the barrier and reach the second electrode. A small (superficial) charge transfer occurs from the electrode with lower work function to the one with higher work function, where they find empty states of lower energy to occupy, until an equilibrium situation is reached with a common Fermi level E_F, as schematized in Figure 1.4(b). Φ_B, the effective barrier height, is determined in this case by the average work function of the electrodes and depends on the material and the conditions of the junction.

When a voltage difference is applied between the electrodes, the so-called bias voltage ($V = V_{bias}$), occupied and empty states at both sides of the potential barrier become again unbalanced as shown in Figure 1.4(c). Electrons in the energy range $E_F - eV$ have enough energy to flow through the barrier generating a tunnelling current proportional to Eq. (1.19), i.e. highly dependent (exponentially) on the barrier width L. In STM experiments, this dependence translates into exceptionally high resolution in the distance determination between electrodes. Considering some numbers as a reference, a barrier width of 5 Å and an effective barrier height of $4\ \mathrm{eV}$ (valid for most metals), would result in $\mathcal{T} \sim 10^{-5}$ and varying the barrier width (the distance between electrodes) by 1 Å typically leads to a change of $\mathcal{T}$ by one order of magnitude [Wiesendanger1994]. Extended to a three-dimensional barrier (as it is the case in real systems), this exponential dependence results into an exceptionally high lateral spatial resolution as well, thanks to the commonly-used tip-sample geometry which reduces the tunnelling area.

Additionally, the tunnelling current expression shows that the transmission is highly influenced by the effective barrier height Φ_B which, in STM experiments, is determined by the work function of the conducting electrodes and the applied bias voltage. The voltage dependence of the transmission probability is thus also required in order to compute the tunnelling current I as a function of V, i.e. the I-V characteristics of a nanojunction. John G. Simmons solved this situation in 1963 using the WKB approximation and he derived an expression for the voltage dependence of the tunnelling current through a potential barrier of arbitrary shape [Simmons1963]. At zero temperature, the net current density is given by:

$$J = J_0\left\{\Phi_B \exp\left(A\sqrt{\Phi_B}\right) - (\Phi_B + eV)\exp\left(-A\sqrt{\Phi_B + eV}\right)\right\}, \qquad \text{Eq. (1.20)}$$

where

$$J_0 = \frac{e}{2\pi h\alpha^2 L^2}, A = \frac{2\alpha L}{\hbar}\sqrt{2m} \qquad \text{Eq. (1.21)}$$

and α is a dimensionless correction factor of order unity. In the case of a small bias voltage $eV\sim 0$, we have $\Phi_B = (\Phi_1 + \Phi_2)/2$ and $\alpha = 1$ (see Figure 1.4(c), considering eV very small). Eq. (1.20) can be then simplified and written as:

$$J = \left[\frac{e^2\sqrt{2m\Phi_B}}{4\pi^2\hbar^2 L}\exp\left(-\frac{2L}{\hbar}\sqrt{2m\Phi_B}\right)\right]V. \qquad \text{Eq. (1.22)}$$

Thus, the current density J varies linearly with the applied voltage V in the low-voltage range, which is known as the Ohmic regime. This formula reflects the linear behaviour of the tunnelling current with V at low bias voltages as well as the exponential dependence with the potential barrier width and the effective barrier height Φ_B. For intermediate voltages $eV < \Phi_B$ an additional term with V^3 enters in the expression.

Note also that in the case of STM tunnelling junctions, image charges in the two electrodes would be induced by the tunnelling current, affecting the potential barrier. The average barrier height would be typically reduced and the transmission increased [Cuevas2010]. A thorough consideration of tunnelling junctions requires therefore the analysis of these effects.

1.2.3 Scattering formalism – multichannel Landauer formula

Let us return here to the nanoscale junction previously introduced (Section 1.2.1) in order to derive the multichannel Landauer formula using the scattering formalism more rigorously [Agraït2003; Cuevas2010].

In Figure 1.2(a) the electrodes 1 and 2 connecting the nanosystem, as already mentioned, are electron reservoirs characterized by a certain temperature ($T_{1,2}$, respectively) and chemical potential ($\mu_{1,2}$, respectively) and electrons inside them follow Fermi distribution functions ($f_{1,2}(E)$, respectively) given by Eq. (1.10). Far from the nanoscale system, electron motion can be separated in longitudinal (along transport direction) and transverse (perpendicular to transport direction) contributions. For the first one, the system is open, i.e. there are no spatial restrictions, and the electron plane waves present continuous wave vectors k_l and longitudinal energies $E_l = \hbar^2 k_l^2/2m$. For the second case, transverse electron motion through the nanosystem is quantized due to lateral confinement. Similarly to a wave-guide problem, the quantization of transverse momentum defines a set of incoming and outgoing modes with respect to each electrode, which can be different for each of them. Thus, we can denote N_α to the discrete number of incoming and outgoing modes for electrode $\alpha = 1{,}2$, with transverse energy E_{N_α}. These N_α modes are generally known as (transverse) quantum channels and, since the total energy of a given electron E can be written as $E = E_l + E_{N_\alpha}$ and E_l is positive, only a finite number of channels is possible.

At this point it is convenient and intuitive to consider creation and annihilation operators for incoming ($\hat{a}_{N_\alpha}^\dagger(E)$ and $\hat{a}_{N_\alpha}(E)$, respectively) and outgoing ($\hat{b}_{N_\alpha}^\dagger(E)$ and $\hat{b}_{N_\alpha}(E)$, respectively) electrons of energy E in the transverse channel N_α for electrode α. All these operators are related through the so-called scattering matrix $\hat{S}$. By definition, this is the $(N_1 + N_2) \times (N_1 + N_2)$ matrix that relates all the incoming and outgoing states in both electrodes. The scattering matrix has the following block structure:

$$\hat{S} = \begin{pmatrix} \hat{r} & \hat{t}' \\ \hat{t} & \hat{r}' \end{pmatrix}, \qquad \text{Eq. (1.23)}$$

where blocks $\hat{r}$ and $\hat{r}'$ describe electron reflection back to the reservoirs 1 and 2, respectively, and have sizes of $N_1 \times N_1$ and $N_2 \times N_2$. Blocks $\hat{t}$ and $\hat{t}'$ in this expression describe the electron transmission through the nanosystem and have sizes of $N_2 \times N_1$ and $N_1 \times N_2$.

The most important consequence for our present discussion that can be extracted from Eq. (1.23) is the possibility to derive an expression for the current through the nanosystem which, accounting for the unitarity of the scattering matrix required for current conservation, can be written as:

$$I(V) = \frac{2e}{h}\int_{-\infty}^{\infty} \mathrm{Tr}\left[\hat{t}^\dagger(E)\hat{t}(E)\right][f_1(E) - f_2(E)]dE. \qquad \text{Eq. (1.24)}$$

Due to the fact that the matrix $\hat{t}^\dagger\hat{t}$ can be diagonalized, it has a set of eigenvalues $\mathcal{T}_n(E)$, where $n = (1, N_1 + N_2)$ indexes the transverse quantum channels, and corresponding eigenfunctions, typically referred to as eigenchannels or conduction channels. It is advantageous to express the current in terms of this natural basis:

$$I(V) = \frac{2e}{h}\sum_n \int_{-\infty}^{\infty} \mathcal{T}_n(E)[f_1(E) - f_2(E)]dE, \qquad \text{Eq. (1.25)}$$

where $\mathcal{T}_n(E)$ are the so-called transmission coefficients ($0 < \mathcal{T}_n(E) < 1$). Hence, at the low bias voltage and zero temperature approximations, the conductance G is given by:

$$G = \frac{2e^2}{h}\sum_n \mathcal{T}_n(E) = G_0 \sum_n \mathcal{T}_n(E), \qquad \text{Eq. (1.26)}$$

which is the multichannel generalization of the Landauer formula.

In the case of metallic systems of reduced size, such as atomic contacts whose transverse dimension approaches the electronic wavelength, the number of channels per atom typically varies between 1 and 3 and can be estimated as $N \sim (k_F R/2)^2$, where R is the atom radius.

Thus, supported by Eq. (1.26), Landauer formalism accounts already for the quantization of the conductance typically observed in metallic atomic contacts [Agraït2003].

Despite its success in describing the main aspects of electronic transport in nanoscale systems, giving a fairly intuitive idea of transport mechanisms and explaining many quantum phenomena, scattering formalism does not give a complete theoretical treatment for quantum transport properties [Cuevas2010]. On the one side, it does not offer any information about the transmission probability through the nanojunctions, so it becomes necessary to derive it by other means, such as density functional theory (DFT) and Green's function techniques (see Section 1.4). Secondly, Landauer formalism is restricted to quantum coherent transport with just elastic interactions, although these conditions would only be valid at exactly zero temperature and for electrons at the Fermi energy. Real systems typically show inelastic scattering processes, such as electron-electron collisions or electron-phonon interactions, which can hardly be neglected in some cases. Therefore, other approaches as the Landauer-Büttiker formalism or methods such as the Green's function techniques are required for a proper theoretical description of quantum electron transport in these situations.

1.3 Thermoelectric effect: from macroscopic to nanoscopic systems

Thermoelectricity arises from the coupling between thermal and charge transport and, similarly to what occurs with electrical conductance, the theoretical framework differs when dealing with macroscopic or nanoscopic systems. Let us begin with the general classical definitions and main concepts of thermoelectric phenomena present in bulk conductors (and semiconductors) (Section 1.3.1) to introduce later the treatment for quantum thermoelectric effects at the nanoscale (Section 1.3.2).

1.3.1 Macroscopic scale

There are three thermoelectric effects:

1) The Seebeck effect: it appears when a temperature gradient $\vec{\nabla}T$ is applied along a macroscopic conductor or semiconductor. Charge carriers (electrons in the case of Figure 1.5) are more energetic, and hence have greater velocities, in the hot side than in the cold one and therefore they drift [Kasap2006]. The net diffusion of electrons towards the cold side of the material leaves the hot side positively charged, thereby creating an electromotive electric field $\vec{E}_{th} = -S\vec{\nabla}T$ across the system, where S is the Seebeck coefficient. The presence of the electric field finally prevents further electron motion and when a steady state is reached (with no current flow), an open-circuit potential difference is therefore generated between the extremes. The thermoelectric response of a given material, the amount of electrical potential difference per unit temperature difference needed, is quantified by the Seebeck coefficient or thermopower S, which is expressed in volts per kelvin, or more often in $\mu\mathrm{V/K}$, and given by:

$$S = -\frac{\Delta V}{\Delta T} = -\frac{V_h - V_c}{T_h - T_c}. \qquad \text{Eq. (1.27)}$$

The negative sign in this expression is established by convention in order to have negative thermopower when charge carriers are electrons ($S < 0$) and positive thermopower when they are holes ($S > 0$). It is important to remark that this magnitude is defined at the equilibrium state under zero current conditions, that is, open-circuit conditions.

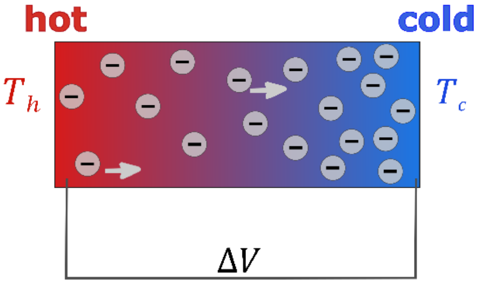

Figure 1.5: Macroscopic Seebeck effect. When the two sides of a single macroscopic conductor or semiconductor are at different temperatures, T_h and $T_c < T_h$ (i.e. a temperature gradient $\Delta T = T_h - T_c$ is established along it), an open-circuit voltage difference $\Delta V = V_h - V_c$, proportional to ΔT, appears between the extremes [Kasap2006]. This is due to the fact that the charge carriers in the material diffuse from the hot side towards the cold one, which generates a net charge imbalance once the system reaches a steady state.

2) The Peltier effect: it consists on the heating or cooling at the interface between two dissimilar conductors or semiconductors (A and B) when a current I flows through it. The Peltier heat absorbed or generated at the junction by unit time can be written as:

$$Q = \Pi_{AB} I = (\Pi_A - \Pi_B) I, \qquad \text{Eq. (1.28)}$$

where Π_A and Π_B are the Peltier coefficients of conductors (or semiconductors) A and B, respectively, and $\Pi_{AB} = \Pi_A - \Pi_B$ is the Peltier coefficient of the junction. The direction of the current flow and the value of the Peltier coefficient of the junction determine whether heat is absorbed or liberated [Rowe1995]. The Peltier effect is a manifestation of the entropy change experienced by the electrical charge carriers as they cross an interface between different materials. Π_{AB} represents how much heat is carried by a unit charge and quantifies the heat exchange at the junction per unit current and per unit time. Since it depends linearly on the electric current, the Peltier coefficient is sensitive to the sign of the charge carriers of the system, as it happens with the Seebeck coefficient. Both serve to determine whether transport is dominated by electrons or holes [Dresselhaus2001]. A relation between the Peltier and Seebeck coefficient was established in 1851 by W. Thomson (Lord Kelvin):

$$\Pi = TS. \qquad \text{Eq. (1.29)}$$

The Peltier coefficient is hence generally expressed in V (typically mV or $\mu\mathrm{V}$). Finally, it should be noticed that other phenomena beside the Peltier effect, such as Joule heating or thermal gradient effects (namely**,** the Thomson effect explained next), can influence the total heat flow through the junction.

3) The Thomson effect: when an electrical current passes through a single homogeneous conductor or semiconductor in the presence of a temperature gradient $\vec{\nabla} T$, the material is heated or cooled, depending on the flow direction of the current with respect to the temperature difference [Rowe1995]. Charge carriers absorb heat when flowing in an opposite direction to a thermal gradient, increasing their potential energy, and they liberate heat, decreasing their potential energy, when flowing in the same direction as a thermal gradient. This

may occur in any non-isothermal portion of a conductor. For a given current density $\vec{J}$ passing through the system, the generated or absorbed heat rate per unit volume and unit time is:

$$q = -\tau \vec{\nabla} T \vec{J}. \qquad \text{Eq. (1.30)}$$

The Thomson coefficient τ is then a measure of the reversible heat flow within a single conductor per unit current and per unit temperature gradient. It is related to the Seebeck coefficient through the following expression:

$$\tau = T\frac{dS}{dT}. \qquad \text{Eq. (1.31)}$$

From here we can see that it is expressed in $\mathrm{V/K}$ or more often in $\mu\mathrm{V/K}$, like the Seebeck coefficient.

Note that Thomson and Peltier effects are present thereby when current flows, contrary to the Seebeck effect which exists as long as the temperature gradient is maintained, regardless of whether current flows or not [Rowe1995]. Finally, it is important to remark that all these three thermoelectric effects are thermodynamically reversible and independent of the dimensions and shape of the conductors or semiconductors (or the junctions) involved. This is different, for example, in the case of the Joule effect (heat generated whenever an electrical current flows through a resistive material), which is irreversible, proportional to the dimensions of the system and does not depend on the sense of the current direction.

For the purpose of this Thesis, we will focus in the following on the Seebeck effect, commonly directly called the thermoelectric effect. As already introduced, it consists on the direct conversion of temperature differences to electric voltages, a process characterized by the Seebeck coefficient S, also known as thermoelectric power or simply thermopower. It is a material specific property and a temperature-dependent coefficient, i.e. $S = S(T)$. When this dependence is known for a material (what is called the absolute thermopower), it is possible to calculate the voltage difference between any two points of the system at temperatures T_0 and $T_0 + \Delta T$:

$$\Delta V = \int_{T_0}^{T_0+\Delta T} S(T)\, dT. \qquad \text{Eq. (1.32)}$$

To obtain a more intuitive idea of thermoelectricity mechanisms in macroscopic systems, let us consider the case of metals. The thermopower of bulk metals at ambient temperature can be described using the Mott's semiclassical formula [Ashcroft1976]:

$$S(T) = -\frac{\pi^2}{3}\frac{k_B^2 T}{e}\frac{\sigma'(E_F)}{\sigma(E_F)}, \qquad \text{Eq. (1.33)}$$

where σ is the material conductivity. The sign and magnitude of the thermopower, determined by $\sigma'(E_F)/\sigma(E_F)$, are subject hence to the energy dependence of the conductivity around the Fermi energy, which in turn depends on the inelastic relaxation time and the effective mass, all of them material properties.

The most direct and extended application of the Seebeck effect is the thermocouple, widely used as temperature probes in thermoelectric thermometry. A thermocouple is made by two dissimilar conducting materials electrically connected at one end forming a junction (see Figure 1.6). When a temperature difference is established between this junction and each of the other extremes of the conductors, the corresponding thermoelectric response generated in each material is different and hence it can be used to know the temperature at the junction [Rowe1995]. Via a thermocouple, measurements of the voltage difference between two materials, A and B, whose thermopower temperature dependence is well-calibrated ($S_A(T)$ and $S_B(T)$ are well-known), allow to experimentally find the temperature at the junction based on the following expression:

$$V_m = \Delta V_A - \Delta V_B = \int_{T_1}^{T_2=T_1+\Delta T} [S_A(T) - S_B(T)]\, dT. \qquad \text{Eq. (1.34)}$$

where V_m is the measured voltage and T_2 is the temperature to be found.

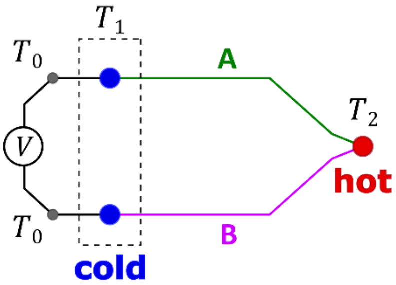

Figure 1.6: Thermocouple working principle. The voltage measured $V = V_m$ between two dissimilar materials A and B whose absolute thermopower $S_A(T)$ and $S_B(T)$ are well-known allows to determine the temperature T_2 at the junction of A and B. T_1 is the known temperature of reference and is the same for both materials. T_0, the temperature of the voltmeter, does not affect the thermovoltage measured, provided that T_1 is the same for A and B and that the connections to the voltmeter are made of a same material.

1.3.2 Nanoscopic scale – Landauer formalism

Thermoelectric properties at the nanoscale are drastically different than in the macroscopic limit (even the transport mechanisms that determine the thermopower are different) and quantum mechanics is required in order to describe the phenomena. The Landauer scattering approach already introduced to describe the electronic transport (conductance) of a nanojunction (Section 1.2) can be also employed to find an expression for its quantum thermopower, which is the goal of this section.

In the case of a macroscopic material as the one represented in Figure 1.7(a), a temperature difference applied between its extremes translates into the generation of a continuous temperature gradient along the material (see Figure 1.7(b)). Considering a nanoscale junction or constriction, as the one previously depicted in Figure 1.1 or Figure 1.2(a), when the electrodes are at different temperatures, charge carriers become more energetic in the hot electrode and they would preferentially move toward the cold one. Carriers of different charge sign would accumulate at opposite sides of the nanoconstriction, thus inducing a thermoelectric voltage (see Figure 1.7(c)). It is important to keep in mind that, in a constriction, any voltage or temperature difference established between the electrodes drop in a distance of the order of the constriction diameter, as schematized in Figure 1.7(d) for the temperature.

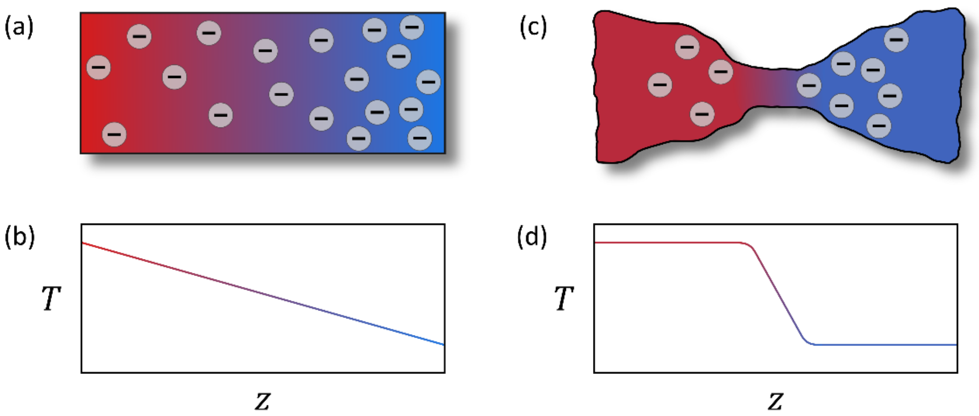

Figure 1.7: Macro- *vs* nanoscale thermopower. (a) Schematic representation of a bulk (macroscopic) conductor or semiconductor whose extremes are at different temperatures (color gradient from red to blue represents the continuous temperature gradient from the hot to the cold side, as shown in (b)). Charge carriers (electrons) move preferentially towards the cold side and give rise to a potential difference. Thermopower is thereby dominated by electron diffusion (phonon drag contribution is considered negligible above the Debye temperature). (b) Approximate temperature T profile as a function of the position z for the system described in (a), showing a continuous temperature gradient in the material. (c) Schematic representation of a nanoscale constriction between two macroscopic electrodes that act as electron reservoirs. Both electrodes are at different well-defined temperatures (color gradient from red to blue represents the sharp drop in temperature taking place at the nanoconstriction, as shown in (d)). Charge carriers (electrons) move preferentially towards the cold electrode and give rise to a potential difference. Thermopower is thereby dominated by quantum transport through the junction (constriction diameter considered to be smaller than the Fermi wavelength of electrons). (d) Approximate temperature profile as a function of the position for the system described in (c), showing a sharp drop of the temperature at the constriction. In a nanoscale constriction, any voltage or temperature difference between the electrodes drop in a distance of the order of the constriction diameter.

Since thermopower of a nanojunction is a quantum transport property, in the case of coherent elastic transport (i.e. non-interacting charge carriers), we can consider the Landauer formula to describe the electrical current through the junction I, given by the already introduced Eq. (1.9):

$$I(V) = \frac{2e}{h}\int_{-\infty}^{\infty} \mathcal{T}(E)[f_1(E) - f_2(E)]dE.$$

The electrical current through a nanoscale system depends thus on the transmission probability $\mathcal{T}$ for an electron to cross the junction, which is a function of the electron energy E and depends generally on the geometry of the nanoconstriction and the local electronic structure, which is itself influenced by the coupling to the electrodes. Note that, for the moment, no electrical voltage is applied to the junction ($V = 0$) and let us remind that f_1 and f_2 are the Fermi distribution functions of electrodes 1 and 2, respectively, given by Eq. (1.10). The difference between both distributions depends on the temperature difference between the electrodes ΔT_{1-2} and the chemical potential difference $\Delta\mu_{1-2}$ and can be expanded with reference to electrode 1 [Malen2010]:

$$f_1(E) - f_2(E) = \left(\frac{\partial f}{\partial \mu}\bigg|_{\mu=\mu_1}\right)_{T_1} \Delta\mu_{1-2} + \left(\frac{\partial f}{\partial T}\bigg|_{T=T_1}\right)_{\mu_1} \Delta T_{1-2}. \qquad \text{Eq. (1.35)}$$

Writing both derivatives in terms of energy E:

$$\frac{\partial f}{\partial \mu} = -\frac{\partial f}{\partial E} \text{ and } \frac{\partial f}{\partial T} = -\left(\frac{E-\mu}{T}\right)\frac{\partial f}{\partial E}, \qquad \text{Eq. (1.36)}$$

the difference between both distributions can thus be expressed as follows:

$$f_1(E) - f_2(E) = -\frac{\partial f_1}{\partial E}\Delta\mu_{1-2} - \left(\frac{E-\mu_1}{T_1}\right)\frac{\partial f_1}{\partial E}\Delta T_{1-2}. \qquad \text{Eq. (1.37)}$$

Since the thermopower of a system is defined at open-circuit conditions (that is, with no current flow), we equal Eq. (1.9) to 0 and replace Eq. (1.37) in it to get:

$$0 = \frac{2e}{h}\int_{-\infty}^{\infty}\mathcal{T}(E)\left[-\frac{\partial f_1}{\partial E}\Delta\mu_{1-2} - \left(\frac{E-\mu_1}{T_1}\right)\frac{\partial f_1}{\partial E}\Delta T_{1-2}\right]dE, \qquad \text{Eq. (1.38)}$$

$$\Delta\mu_{1-2}\int_{-\infty}^{\infty} -\mathcal{T}(E)\frac{\partial f_1}{\partial E}dE = \Delta T_{1-2}\int_{-\infty}^{\infty}\mathcal{T}(E)\left(\frac{E-\mu_1}{T_1}\right)\frac{\partial f_1}{\partial E}dE, \qquad \text{Eq. (1.39)}$$

$$\frac{\Delta\mu_{1-2}}{\Delta T_{1-2}} = -\frac{1}{T_1}\frac{\int_{-\infty}^{\infty}\mathcal{T}(E)(E-\mu_1)\frac{\partial f_1}{\partial E}dE}{\int_{-\infty}^{\infty}\mathcal{T}(E)\frac{\partial f_1}{\partial E}dE}. \qquad \text{Eq. (1.40)}$$

Note that some electron-hole asymmetry of the transmission function is required in order not to cancel the numerator of this relationship [Cuevas2010]. Assuming that there are no transmission resonances close to the equilibrium chemical potential, $\Delta\mu_{1-2} = -e\Delta V_{1-2}$, where ΔV_{1-2} is the voltage difference between the electrodes created by the difference in chemical potential. In addition, at low temperatures, $\partial f/\partial E \approx \delta(E-\mu)$ and the integral in the denominator of Eq. (1.40) simplifies to the transmission evaluated at μ_1:

$$\frac{\Delta V_{1-2}}{\Delta T_{1-2}} \approx -\frac{1}{eT_1}\frac{1}{\mathcal{T}(E)|_{E=\mu_1}}\int_{-\infty}^{\infty}\mathcal{T}(E)(E-\mu_1)\frac{\partial f_1}{\partial E}dE. \qquad \text{Eq. (1.41)}$$

Finally, considering a Taylor expansion (i.e. $\mathcal{T}(E) = \mathcal{T}(E)|_{E=\mu_1} + (E-\mu_1)\left[(\partial\mathcal{T}(E)/\partial E)|_{E=\mu_1}\right]$) and using the Sommerfeld expansion [Ashcroft1976], we get the following expression for the thermopower of the nanojunction (by definition $S = \Delta V_{1-2}/\Delta T_{1-2}$):

$$S = \frac{\Delta V_{1-2}}{\Delta T_{1-2}} = -\frac{\pi^2}{3}\frac{k_B^2 T}{e}\frac{d[ln\mathcal{T}(E)]}{dE}\bigg|_{E=\mu}, \qquad \text{Eq. (1.42)}$$

where T is the mean temperature of the electrodes ($T = (T_1 + T_2)/2$) and μ, the mean chemical potential ($\mu = (\mu_1 + \mu_2)/2$) [Paulsson2003].

Furthermore, at zero temperature, the equilibrium chemical potential is the so-called Fermi energy E_F and Eq. (1.42) can be written as:

$$S = -\frac{\pi^2}{3}\frac{k_B^2 T}{e}\frac{1}{\mathcal{T}(E_F)}\frac{d\mathcal{T}(E)}{dE}\bigg|_{E_F} = -\frac{\pi^2}{3}\frac{k_B^2 T}{e}\frac{\mathcal{T}'(E_F)}{\mathcal{T}(E_F)}. \qquad \text{Eq. (1.43)}$$

Eq. (1.43) shows that the thermopower depends on the variation of the transmission for carriers above and below the Fermi energy: larger transmission above E_F will cause the electrons to go to the cold electrode resulting in negative thermopower and the opposite. It must be remarked that, based on Landauer formalism, these equations are only valid for non-interacting charge carriers. Furthermore, they have been obtained under low-temperature and small voltage approximations (away from transmission resonances) and they also ignore the interaction between phonons and electrons, i.e. phonon drag. A full discussion of their validity can be found in Ref. [Dubi2011].

1.4 Electrical conductance and thermopower of molecular junctions

A molecular junction, a particular case of nanoscale junctions and the principal system of interest of this Thesis, is simply a single molecule connected between two metallic electrodes, like the one schematized in Figure 1.8. As introduced at the beginning of the chapter, the idea of using molecules as electronic components in functional devices or as building blocks of nanoscale circuits has impelled extensive experimental and theoretical research of charge transport through molecular junctions. Typical molecular sizes are small enough to be in the full quantum regime and they offer a large versatility in physical phenomenology not present in atomic contacts, for example, where transport properties are somehow more “rigid” and limited. Some basic electronic functions have been demonstrated [Aradhya2013], but, more importantly, molecular junctions have proved to be exceptional platforms to test quantum transport theories and have greatly contributed to shed light on charge transport mechanisms at the nanoscale [Cuevas2010; Dubi2011].

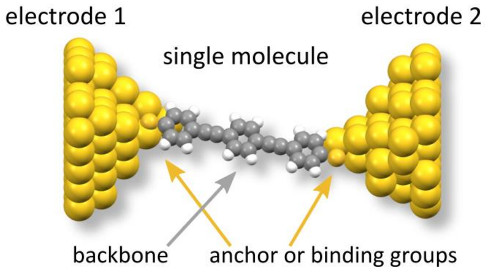

Figure 1.8: Molecular junction schematics. Schematic representation of a molecular junction. A single molecule, typically formed by a backbone and anchor or binding groups at both ends (in its more simple configuration), is connected between two electrodes (1 and 2) that act as electron reservoirs. Electrodes are typically metals.

We focus in this section on the theoretical background needed to understand charge transport and thermoelectricity in molecular junctions. Since they are atomic-scale systems, transport is in most cases coherent (i.e. based on the elastic flow of electrons through the molecule without energy exchange). Thus, many transport properties of molecular junctions can be described and understood within the Landauer scattering approach, already introduced for the more general example of a nanojunction. For the sake of commodity, let us reproduce here the expressions for quantum conductance and thermopower of these nanojunctions (given by Eq. (1.12) and Eq. (1.43)):

$$G = \frac{2e^2}{h}\mathcal{T}(E_F) = G_0\mathcal{T}(E_F),$$

$$S = -\frac{\pi^2}{3}\frac{k_B^2 T}{e}\frac{1}{\mathcal{T}(E_F)}\frac{d\mathcal{T}(E)}{dE}\bigg|_{E_F} = -\frac{\pi^2}{3}\frac{k_B^2 T}{e}\frac{\mathcal{T}'(E_F)}{\mathcal{T}(E_F)}.$$

These expressions are the starting point for the incoming theoretical framework employed to describe transport in molecular junctions, systems where the major particularity is that charge carriers physically flow between metallic electrodes 1 and 2 through the molecule itself, i.e. through a molecular bridge or backbone (see Figure 1.8).

Calculating the conductance and thermopower of a molecular junction within the Landauer scattering approach requires therefore to obtain first its transmission function $\mathcal{T}(E)$. This is normally done by calculating the electronic structure of the junction using density functional theory (DFT) and computing the transmission with the help of Green's function techniques [Pauly2008; Bilan2012]. This is a powerful combination that allows to get an insight into the transport properties of molecular junctions, but that presents also some limitations. In addition to the lack of exact knowledge of the geometry of the junction, which has a strong impact on the transmission, the results obtained from DFT calculations present many theoretical uncertainties, for example, in the relative alignment of molecular energy levels and the Fermi level of the electrodes and in the size of the HOMO-LUMO gap, and hence cannot be considered exact. To this respect, comparison of the theory with the experimental values of both conductance and thermopower, which are given by the transmission and its slope at the Fermi level, respectively, provides an essential feedback to obtain a more accurate description of the molecular junction. For the moment, we present in the next section a simpler model powerful enough to shed light already on many basic aspects of transport through molecular junctions and give useful understanding about its conductance and thermopower.

Before going into the details, let us make one further remark about an essential difference between conductance and thermopower. Thermopower, in contrast to conductance, is an intensive property and is independent of the number of molecules participating in a molecular junction. This can be understood by considering N identical molecules in parallel in a junction. Assuming that (lateral) interference effects are negligible, the total transmission of the junction will be $\mathcal{T}_N = N\mathcal{T}_1$, where $\mathcal{T}_1$ is the transmission of one molecule, and applying Eq. (1.12) and Eq. (1.43) we obtain that the conductance of the junction would be $G_N = NG_1$ (G_1 being the conductance of a single molecule), while for the thermopower we would have $S_N = S_1$, where S_1 is the thermopower of a single molecule.

1.4.1 Transmission function of molecular junctions - Tunnelling in a double potential barrier

We describe in this section a very intuitive theoretical approach to find an expression for the transmission function of a molecular junction $\mathcal{T}(E)$. As we have previously seen, it is all we need for computing its conductance and the thermopower according to Landauer formalism. Thus, the question that arises is how the transmission is affected by the electronic structure of the junction. What is the role played by the molecule?

Briefly, the presence of the molecule between the electrodes typically results in tunnelling of charge carriers through the discrete molecular energy levels. Given its atomic-scale size, an isolated molecule by itself, i.e. the free molecule, shows discrete bound states. This can be understood considering the free molecule as energetically equivalent to a potential well for which energy quantization in confined structures applies. When the molecule becomes embedded in a junction, a chemical bond is established with two metallic electrodes and the molecule becomes connected. Molecular states then broaden and shift in energy due to the interaction with the metals. Transport properties of the whole system are thereby determined by the confined energy levels of the molecule between the electrodes, in particular, by the strength of the coupling and the relative alignment of the molecular levels with respect to the Fermi level of the contacts.

Let us explain all these aspects in more detail, beginning by considering the free molecule and two bulk metallic electrodes, when they are far apart. The energy level scheme of this initial situation is depicted in Figure 1.9(a) in the zero temperature limit and for two electrodes of the same material. While both metals have continuous electronic states filled up to the Fermi energy E_F, the isolated molecule shows a discrete number of energy levels or molecular orbitals. By definition, these energy states are occupied up to the HOMO (Highest Occupied Molecular Orbital), quantified by the ionization potential of the molecule, and unoccupied above the LUMO (Lowest Unoccupied Molecular Orbital), which is given by its electron affinity. HOMO and LUMO are usually known as frontier molecular orbitals.

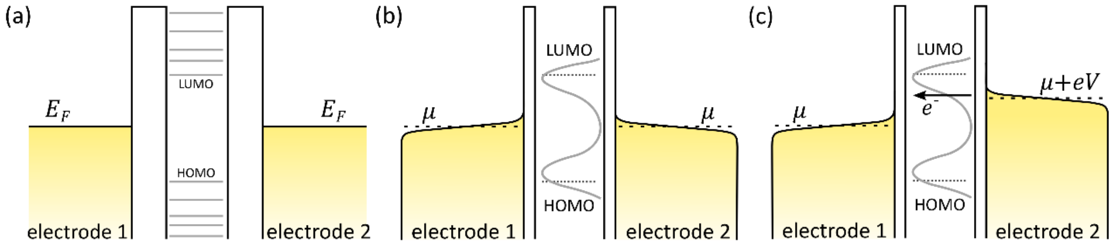

Figure 1.9: Energy level schemes for a molecular junction. (a) Energy diagram at zero temperature for two bulk metallic electrodes, far away from each other, and the free molecule. Metallic electrodes, considered here to be of the same material, have continuous electronic states filled up to the Fermi energy E_F and their Fermi-Dirac electron distributions are given by step functions. The molecule presents discrete bound states and is thus equivalent to a potential well, although it has some energy levels already filled up to the HOMO (Highest Occupied Molecular Orbital) and free above the LUMO (Lowest Unoccupied Molecular Orbital), exhibiting a molecule-characteristic HOMO-LUMO gap. (b) When the molecule is connected between the electrodes, its energy levels may shift in energy and they align with respect to the E_F of the electrodes which lies within the HOMO-LUMO gap. Molecular orbitals also hybridize and become broader due to coupling with the delocalized metallic states. This hybridization results into a continuous transmission probability, depicted in grey for HOMO and LUMO, with higher probability of transmission at energies related to the molecular states. In the presence of temperature (as it is the case in real systems), the continuum of states of the electrodes is filled following Fermi distributions up to the chemical potential μ or Fermi level. Notice that in (a-b) there are no voltage or temperature differences applied between the electrodes. (c) When applying a bias voltage V to one of the contacts, the junction Fermi level is modified and a tunnelling current flowing through it is favored. In all these energy schemes (a-c) a molecule showing favorable transport through the LUMO has been considered. The equivalent case for transport through the HOMO would simply imply a shift upwards of the molecular orbitals depicted here (i.e. a different relative level alignment).

When the molecule is connected between the electrodes, in a first approximation, the delocalized electronic states of the metals connect to the confined molecular orbitals through two potential barriers originated at the molecule-metal (organic-inorganic) interfaces. According to this assumption, a molecular junction can be considered equivalent to a double barrier structure as the one depicted in Figure 1.9(b), where two tunnelling barriers are in series with respect to the transport direction and bound states are found between two scattering interfaces [Malen2010; Kittel1953; Datta2005]. In this diagram we have also considered the effect of temperature in the electrodes function distribution, as it is the case in real systems. The continuum of states is filled in this case following Fermi distributions up to the chemical potential μ or Fermi level.

Some charge transfer from the metals to the molecular orbitals may occur, typically resulting in a shift of the energy levels with respect to their original position. In fact, the HOMO-LUMO gap, i.e. the energy separation between the frontier orbitals, is generally reduced when contacting the molecule. Additionally, mediated by this charge transfer, a relative alignment of the molecular levels with respect to the Fermi level of the electrodes, which is somewhere in between the frontier orbitals, is achieved. The Fermi level lies then within the HOMO-LUMO gap, occupied states below and unoccupied states above. In principle, many molecular orbitals can participate in transport, although typically only the frontier orbitals have a significant contribution.

Furthermore, upon connection, molecular orbitals hybridize with the continuum of states of the metallic electrodes, i.e. a chemical bond is formed between the metallic atoms of the electrodes and the molecule or its anchor groups (see Figure 1.8). As a consequence, molecular orbitals broaden and the width of the levels depends on the strength of the metal-molecule coupling. The local electronic structure of the metals also influences the broadening of the discrete levels. Molecular orbitals hybridization results thereby into a continuous transmission probability with resonances (pronounced peaks with higher probability of transmission) at energies related to the molecular states (schematized in grey in Figure 1.9(b) only for the HOMO and LUMO).

These energy diagrams (Figure 1.9(a-b)) offer already useful understanding about charge transport in a metal|molecule|metal junction. Namely, the energy-dependent probability to tunnel between the electrodes through the confined states of the molecule, that is, the transmission function of the molecular junction, depends on the electronic structure of the molecule (its molecular orbitals) and shows resonances at energies close to the position of the original discrete states. In particular, transmission is determined by the position of the molecular levels (its relative alignment with respect to μ) and their bond with the delocalized metallic states (the coupling to the extended states of the electrodes).

Additionally, in the presence of a small voltage difference V between the electrodes, the energy level diagram of the molecular junction can be represented as shown in Figure 1.9(c). The voltage applied allows to shift the Fermi level or chemical potential μ of the electrode with respect to the molecular orbitals (whose relative position is hence voltage-dependent) and electrons with an energy close to the Fermi level of the junction are free to participate in transport. A tunnelling current is generated which enables to explore the conductance G and the I-V characteristics of the molecular junction (see also Section 1.4.2).

In the limit in which molecular orbitals are energetically well separated, transmission resonances can be approximated by a Lorentzian peak and hence, the transmission probability through the molecular orbital m can be written using the Breit-Wigner formula [Cuevas2010]:

$$\mathcal{T}_m(E,V) = \frac{4\Gamma_{m,1}\Gamma_{m,2}}{[E-\varepsilon_m(V)]^2 + \left[\Gamma_{m,1}+\Gamma_{m,2}\right]^2}. \qquad \text{Eq. (1.44)}$$

In this expression, $\varepsilon_m(V)$ is the difference in energy between the resonance and the Fermi level μ (set at zero energy) and it is voltage-dependent as mentioned above. $\Gamma_{m,1}$ and $\Gamma_{m,2}$ (divided by $\hbar$) are the scattering rates associated to the potential barriers at both molecule-metal interfaces. They are considered to be energy- and voltage-independent, which is a good approximation when the electrodes density of states is rather flat around the Fermi level (valid for noble metals like Au). $\Gamma_m = \Gamma_{m,1} + \Gamma_{m,2}$ is hence the broadening of the discrete molecular level m (the half width at half maximum, HWHM) due to the coupling and it is produced by its finite lifetime as a double barrier bound state.

Considering tunnelling in a double potential barrier model, therefore, the total transmission function of the junction $\mathcal{T}(E,V)$ can be described with resonant Lorentzian peaks at energies determined by the molecular levels [Kittel1953]. Note that this expression is especially accurate for on resonant transport, i.e. for energies around the discrete level [Datta1995]. Summing over all the molecular orbitals participating in transport M, we get that the energy- and voltage-dependent total transmission of the junction is:

$$\mathcal{T}(E,V) = \sum_{m=1}^{M} \frac{4\Gamma_{m,1}\Gamma_{m,2}}{[E-\varepsilon_m(V)]^2 + \left[\Gamma_{m,1}+\Gamma_{m,2}\right]^2}. \qquad \text{Eq. (1.45)}$$

Since mainly HOMO and LUMO contribute to electron transport, the sum in Eq. (1.45) extends usually until $M = 2$, accounting only for the frontier orbitals. This is the so-called two level model and it is depicted in Figure 1.10, showing both the case where the HOMO is closer to the Fermi level (Figure 1.10(a)) and the case where the LUMO is closer (Figure 1.10(b)). The levels position in the energy diagrams are denoted by ε_H and ε_L, respectively, while coupling to the corresponding electrode is $\Gamma_{m,1}$ and $\Gamma_{m,2}$, with $m = H, L$ for HOMO and LUMO respectively. The top panel in Figure 1.10(c) shows the energy dependence of the transmission given by Eq. (1.45), for the two alignments mentioned.

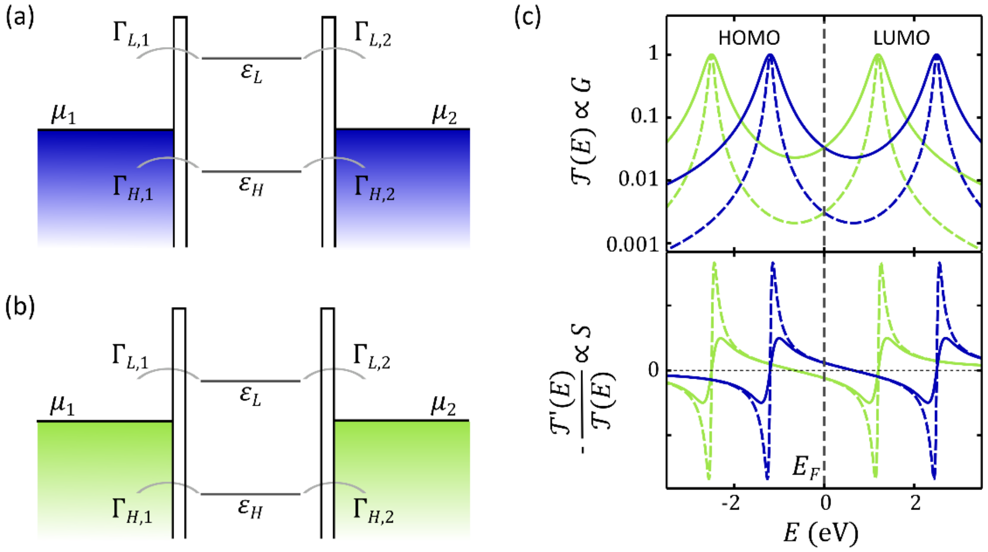

Figure 1.10: Two level model applied to a molecular junction. (a-b) Energy diagrams for a molecular junction in the absence of a bias voltage ($\mu_1 = \mu_2$, where $\mu_{1,2}$ is the chemical potential of electrode 1 and 2, respectively). Two different level alignments are presented: in (a) the Fermi level is closer to the HOMO and in (b) it is closer to the LUMO. (c) $\mathcal{T}(E)$ and $-\mathcal{T}'(E)/\mathcal{T}(E)$ for the two level model described by Eq. (1.45) (with $M = 2$). Blue curves correspond to (a) $\varepsilon_H = -1.2$ eV and $\varepsilon_L = 2.5$ eV, and green ones to (b) $\varepsilon_H = -2.5$ eV and $\varepsilon_L = 1.2$ eV. The conductance G is proportional to $\mathcal{T}(E)$ at the Fermi level E_F and hence it is the same for both alignments (a) and (b). The thermopower S is proportional to $-\mathcal{T}'(E)/\mathcal{T}(E)$ at the Fermi level E_F and hence it is positive for (a) and negative for (b). Two different symmetric couplings of the molecules to the electrodes have been considered: $\Gamma_{m,1} = \Gamma_{m,2} = 0.1$ eV (solid line) and $\Gamma_{m,1} = \Gamma_{m,2} = 0.03$ eV (dashed line; weaker coupling), where $m = H, L$ accounts for HOMO and LUMO. It can be observed that for $E = \mu = E_F$, coupling has a major effect in G while for S it only acquires importance when the Fermi level approaches the resonant level. For further examples, see Ref. [Cuevas2010].

Having obtained then an expression for the transmission, we can reconsider Landauer formula (Eq. (1.12)), for a small applied voltage $V{\sim}0$, and find that the conductance of the junction is then given by:

$$G = G_0\mathcal{T}(E_F, V{\sim}0) = G_0 \sum_{m=1}^{2} \frac{4\Gamma_{m,1}\Gamma_{m,2}}{[E_F - \varepsilon_m(V{\sim}0)]^2 + \left[\Gamma_{m,1} + \Gamma_{m,2}\right]^2}. \qquad \text{Eq. (1.46)}$$

We extract several important conclusions from Eq. (1.46). For example it tells us that, for a given level m whose transmission is expressed by Eq. (1.44), the conductance is maximized when $E_F = \varepsilon_m$, which is known as the resonant condition. It occurs when the molecular orbital aligns exactly at the same energy than the Fermi level of the electrodes (as depicted in Figure 1.10(c), top panel). Additionally, the maximum possible transmission through the resonant level is reached in the symmetric case, i.e. when both potential barriers are equal or, equivalently, when the coupling of the molecular level to both electrodes is the same. In this situation we have that the scattering rates $\Gamma_{m,1}$ and $\Gamma_{m,2}$ are identical and, satisfying also the resonant condition, in the symmetric case we get that $\mathcal{T}_m(E_F) = 1$. The maximum G of each individual level is hence equal to G_0, independently of the coupling. This is illustrated with two different examples of symmetric coupling in Figure 1.10(c) (solid *vs* dashed lines).

Finally, let us consider the case of a temperature difference ΔT applied between the metallic electrodes (as depicted in Figure 1.11)). Note that, similarly to the nanoconstriction schematized in Figure 1.7(c-d), ΔT would sharply drop at the molecular junction since we are considering coherent transport and the electrodes are electron reservoirs at a well-defined temperature. The energy diagram for this case is shown in Figure 1.11. The first consequence of the application of the temperature gradient is on the electron distribution of the hot electrode since, when the temperature is raised, it extends to higher energies.

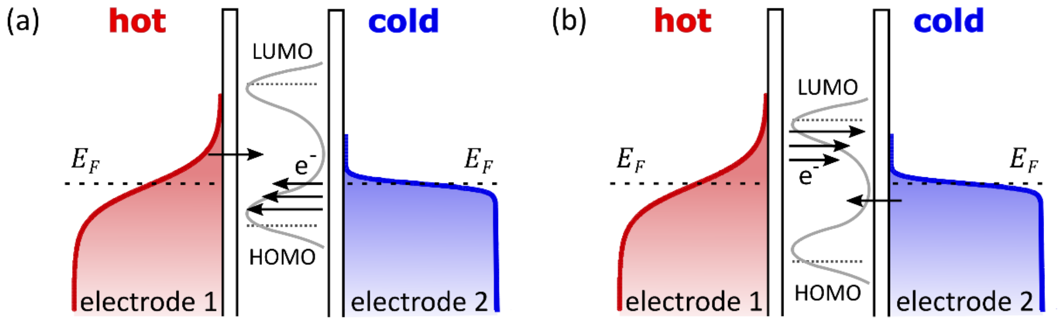

Figure 1.11: Thermoelectricity of molecular junctions and sign of the Seebeck coefficient. Energy diagrams for a molecular junction where a temperature difference is applied between the electrodes; in particular, the temperature of electrode 1 is raised above that of electrode 2 (electron distributions are represented in red and blue for electrodes 1 and 2, respectively). The transmission function of the molecular junction within the two level model (in grey) is schematized between the two potential barriers generated at both molecule-metal interfaces. (a) Electrons below the Fermi level have larger transmission probability than those above: the net flow of electrons will be towards the hot side and $S > 0$. (b) Electrons above the Fermi level have larger transmission probability than those below: the net flow of electrons will be towards the cold side and $S < 0$. Note that in both diagrams, no bias voltage is considered and the tunnelling currents depicted are produced by the temperature difference applied (as far as this is maintained).

Similarly to the conductance, the thermopower of the junction can be obtained within the Landauer formalism (Eq. (1.43)) and the transmission function given by Eq. (1.45). This is plotted in Figure 1.10(c), bottom panel, for the two level model. The most important feature is the change of sign of the thermopower in the two alignments considered (HOMO *vs* LUMO transport). In comparison with the conductance G, which is proportional to the transmission function $\mathcal{T}$ at the Fermi level (or chemical potential) (Figure 1.10(c), top panel), the thermopower S is related to the slope of the transmission $\mathcal{T}'$, also at the Fermi level, which influences its sign: positive for HOMO-dominated transport (in blue) and negative for LUMO-dominated transport (in green). Thus, complementary to the study of the conductance, thermopower offers an additional fundamental insight into the electronic structure of the molecular junction and have become an essential characterization tool of their transport properties [Paulsson2003].

Diagrams in Figure 1.11 also reflect the dependence of the sign of the Seebeck coefficient on the main molecular orbital involved in transport. For instance, without changing the temperature difference with respect to the electrodes, more electrons would flow towards the hot electrode if the Fermi level is closer to the HOMO (Figure 1.11(a)) while if it is closer to the LUMO, electrons would tunnel preferentially towards the cold side (Figure 1.11(b)). This is somehow equivalent to the dependence of the sign of S on the sign of the charge carriers valid for macroscopic systems. In the case of HOMO-dominated transport, since $S > 0$, we may speak of hole-like carriers, whereas for LUMO-dominated transport, $S < 0$ and the carriers are considered electron-like. In reality, as reflected by the expression of the thermopower at the nanoscale (Eq. (1.43)), it is important to keep in mind that thermopower at the nanoscale depends on the variation of the transmission for carriers above and below the Fermi level: larger transmission above the Fermi level will cause the electrons to go to the cold electrode resulting in negative thermopower and the opposite.

Summarizing, conductance G and thermopower S of a molecular junction depend on the value of the transmission function $\mathcal{T}(E)$ and its derivative at the Fermi level $E = E_F = \mu$ (Eq. (1.12) and (1.43)). Consequently, the position of the HOMO and the LUMO with respect to the Fermi level of the electrodes, the so-called level alignment, and their broadening, the so-called coupling, are crucial in determining the transport properties of the junction. In particular, the coupling to the electrodes largely influences the value of the conductance while the sign of the thermopower is a signature of the dominant molecular orbital in transport.

More importantly, Figure 1.10(c) offers some clues on how to optimize the conductance and thermopower of molecular junctions, a question of huge interest for the development of thermoelectric devices as we will discuss in Section 1.6. Interestingly, we can observe that near a transmission peak, both G and S are maximum since both the transmission value and its slope are concurrently increased in the proximity of a resonant level. Tuning the level alignment with the goal of maximizing conductance and thermopower is then one of the key strategies in the experimental research on the transport properties of molecular junctions [Yee2011; Kim2014].

Additionally, another important conclusion can be drawn from Figure 1.10(c) observing how the transmission resonances vary with the coupling of the molecule to the electrodes. Clearly, a smaller coupling results in steeper HOMO and LUMO resonances and hence, in a larger thermopower, although conductance is in this case lower except when transport is precisely on resonance.

Finally, another potentially important effect on the conductance and thermopower of molecular junctions is quantum interference, which would result in more complex features in the transmission function, reflecting in the form of Fano resonances [Finch2009] or transmission nodes [Bergfield2010]. In the case of the Fano resonance, the interference effect originates when a molecule has a side group in the backbone not directly connected to the electrodes. In this situation, the transmission close to one of the molecular resonances will not be just a standard Breit-Wigner resonance as shown until now [Papadopoulos2006], but will be given by:

$$\mathcal{T}(E) = \frac{4\Gamma_{0,1}\Gamma_{0,2}}{\left[E - \varepsilon_0(V) - \frac{\gamma^2}{E - \varepsilon_{00}(V)}\right]^2 + \left[\Gamma_{0,1} + \Gamma_{0,2}\right]^2}. \qquad \text{Eq. (1.47)}$$

where $\Gamma_{0,1}$ and $\Gamma_{0,2}$ represent the coupling to the electrodes; $\varepsilon_0(V)$ and $\varepsilon_{00}(V)$ are the position of the molecular level and the side level, respectively; and γ is the coupling between the molecular level and the side level (see Figure 1.12). When the side group is weakly coupled to the backbone, i.e. $\gamma \ll |\varepsilon_0 - \varepsilon_{00}|$, the transmission has a Breit–Wigner resonance at $E = \varepsilon_0$ and an antiresonance at $E = \varepsilon_{00}$, where $\mathcal{T}(E)$ vanishes. In addition, it has a Fano peak at $E \cong \varepsilon_{00} - \gamma^2/|\varepsilon_0 - \varepsilon_{00}|$. If the Fano peak is at the Fermi level, it will have a large impact on the G and S, as can be seen in Figure 1.12(b). An in-depth tutorial review on quantum interference effects can be found in Ref. [Lambert2015].

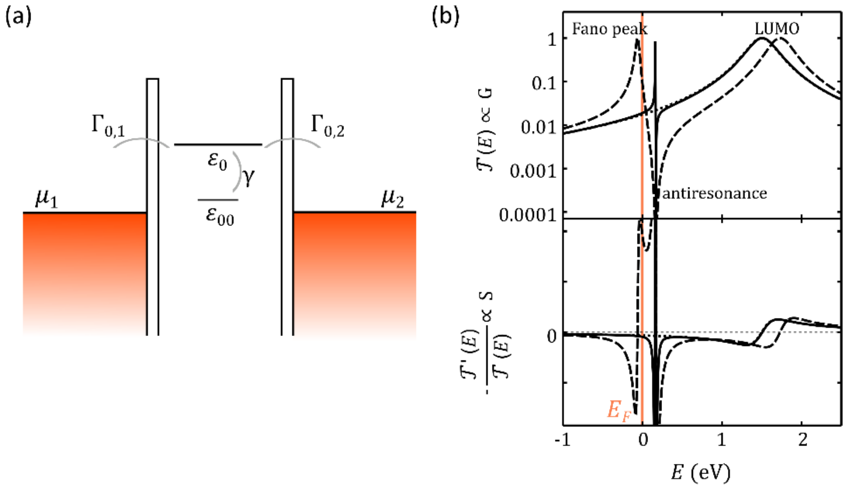

Figure 1.12: Fano resonance in the transmission function of a molecular junction. (a-b) Energy diagram (a) and $\mathcal{T}(E)$ and $-\mathcal{T}'(E)/\mathcal{T}(E)$ (b) for a molecular junction in the case of a Fano resonance close to the LUMO and in the absence of bias voltage ($\mu_1 = \mu_2$, where $\mu_{1,2}$ is the chemical potential of electrode 1 and 2, respectively). $\mathcal{T}(E)$ and $-\mathcal{T}'(E)/\mathcal{T}(E)$ are calculated from the model described by Eq. (1.47), using $\varepsilon_0 = 1.5$ eV, $\varepsilon_{00} = 0.17$ eV (resonance close to the LUMO) and $\Gamma_{0,1} = \Gamma_{0,2} = 0.1$ eV, and considering three different resonant couplings: $\gamma = 0$ eV (dotted line), $\gamma = 0.1$ eV (solid line) and $\gamma = 0.6$ eV (dashed line). If the Fano peak is at the Fermi level, it will have a large impact on both G and S. For further examples, see Ref. [Cuevas2010].

1.4.2 I-V characteristics of molecular junctions

Considering again the molecular junction depicted in Figure 1.9(c), where a molecule is connected between two metallic electrodes and a voltage difference is applied between them, the voltage dependence of the tunnelling current trough the junction, that is, the I-V characteristics of the junction, can be addressed.

Within the Landauer approach, let us recall that the current through a nanojunction can be written using Eq. (1.9):

$$I(V) = \frac{2e}{h}\int_{-\infty}^{\infty}\mathcal{T}(E)[f_1(E) - f_2(E)]dE.$$

Explicitly including the chemical potential and the voltage, applied to electrode 2:

$$I(V) = \frac{2e}{h}\int_{-\infty}^{\infty}\mathcal{T}(E,V)[f_1(E,\mu_1) - f_2(E,\mu_2 + eV)]dE, \qquad \text{Eq. (1.48)}$$

or, considering it applied to both electrodes:

$$I(V) = \frac{2e}{h}\int_{-\infty}^{\infty}\mathcal{T}(E,V)[f_1(E,\mu_1 - eV/2) - f_2(E,\mu_2 + eV/2)]dE. \qquad \text{Eq. (1.49)}$$

For the molecular junction we are considering, $\mathcal{T}(E,V)$ is the energy- and voltage-dependent transmission function introduced in the previous section and, for the case of off-resonant transport, it is given by the Breit-Wigner formula (Eq. 1.44).

$$\mathcal{T}_m(E,V) = \frac{4\Gamma_{m,1}\Gamma_{m,2}}{[E - \varepsilon_m(V)]^2 + \Gamma_m^2}.$$

where $\Gamma_m = \Gamma_{m,1} + \Gamma_{m,2}$. Assuming a symmetric voltage drop at both interfaces, equivalent to assume that the coupling to the electrodes is symmetric ($\Gamma_{m,1} = \Gamma_{m,2}$), an analytical expression for the current can be derived, in the zero-temperature limit [Cuevas2010]:

$$I(V) = \frac{2e}{h}\frac{4\Gamma_{m,1}\Gamma_{m,2}}{\Gamma}\left[\arctan\left(\frac{eV/2 - \varepsilon_m}{\Gamma}\right) + \arctan\left(\frac{eV/2 + \varepsilon_m}{\Gamma}\right)\right]. \qquad \text{Eq. (1.50)}$$

In the low-voltage regime, i.e. before reaching the resonant level, this can be seen as a linear and cubic terms with V as the main contributions to the shape of the I-V characteristics ($I(V) = AV + BV^3$), equivalently to the solution proposed by Simmons for tunnelling currents generated with intermediate voltages.

An important aspect of Eq. (1.50) is that, within this tunnelling model through a double potential barrier, I-V curves of molecular junctions are symmetric with respect to voltage polarity inversion as long as the molecule is equally connected to both electrodes. However, this is based on the assumption that the voltage drop across the junction is symmetric, which is not always the case. This can be modified within the model considering an asymmetric situation through different coupling $\Gamma_{m,1}$ and $\Gamma_{m,2}$ to each electrode. Being the scattering rates different, we can assume that the voltage drop at each organic-inorganic interface will be different and include it in the model as $\varepsilon_m(V) = \varepsilon_m + (eV/2)(\Gamma_{m,1} - \Gamma_{m,2})/\Gamma$. This expression implies that the molecular level ε_m will be more influenced by the shift in the Fermi level ($E_F = \mu$) of the electrode to which it is more coupled. In other words, the molecular level will follow the chemical potential, shifted when the voltage is applied, of the electrode to which it is better coupled. In the extreme, when the ratio between the couplings is very different to one, the I-V characteristics become very asymmetric, showing a rectifying behaviour.

Asymmetry in molecular junctions can be easily introduced in several ways. For example, directly in the molecular structure, which can show an asymmetric geometry. This was the original proposal by Aviram and Ratner for the use of single asymmetric molecules as strongly rectifying diodes [Aviram1974]. Interestingly, asymmetry in the I-V characteristics can be also introduced by establishing a different coupling between the electrode and the molecule directly from an asymmetric junction configuration. For example, when one of the electrodes is kept at a certain distance of the molecule (something feasible in STM experiments as we are going to show in this manuscript), the gap between the molecule and that electrode will effectively largely reduce its coupling to that electrode, while tunnelling current would still be allowed and I-V characteristics can be explored as long as the distance between the electrode and the molecule is small enough. This is the so-called tunnelling spectroscopy because these I-V curves and the asymmetry with different bias polarity would give us information about the electronic states contributing to the tunnelling current [Wisendanger1994] and whether they are mainly occupied or unoccupied states.

1.5 Thermal conductance in nanoscopic systems

In the nanoscopic systems considered until now, and in particular in molecular junctions, applying a temperature difference ΔT between the electrodes not only translates into a thermoelectric response of the system, which is mainly a charge effect as it has been shown, but it also results into heat transfer (energy flow) through the junction from the hot electrode towards the cold one.

Briefly, in macroscopic systems this phenomenon has been traditionally described based on Fourier's law [Dubi2011]. This law, valid for the linear regime, states that a temperature gradient ∇T applied across a bulk material induces a thermal current density j_{th} which is linearly proportional to ∇T and the constant of proportionality is the thermal conductivity of the material κ (or σ_{th} in analogy to commonly-used electrical variables). Fourier's law is then:

$$j_{th} = -\kappa \nabla T. \qquad \text{Eq. (1.51)}$$

The thermal current density contains in this expression electron and phonons (lattice vibrations) contributions, both participating in the heat transfer.

Heat transport through nanoscopic systems can be also described to some extent within the Landauer scattering formalism presented in this chapter [Wang2019]. Equivalently to bulk materials, energy is carried through nanoscale systems by electrons and phonons and thus the thermal conductance G_{th} can be considered as the sum of both contributions: $G_{th} = G_{th,el} + G_{th,ph}$. Considering typical dimensions of nanojunctions (and molecular junctions in particular) and the inelastic mean free path (distance between inelastic scattering processes) of electrons and phonons (tens of nanometers in the case of electrons and between a few and tens of nanometers for phonons), Landauer formalism can be used to describe heat transport in these junctions [Klöckner2017a], resulting in the following expressions for electron and phonon thermal currents:

$$J_{th,el} = \frac{2}{h}\int_{-\infty}^{\infty} (E - E_F)\mathcal{T}(E,V)[f_1(E,\mu_1) - f_2(E,\mu_2)]dE \qquad \text{Eq. (1.52)}$$

and

$$J_{th,ph} = \int_{0}^{\infty} (h\nu)\mathcal{T}_{ph}(\nu)[g_1(\nu) - g_2(\nu)]dE, \qquad \text{Eq. (1.53)}$$

where ν is the frequency of the phonon, $\mathcal{T}_{ph}(\nu)$ is its transmission function and $g_1(\nu)$ and $g_2(\nu)$ are the Bose-Einstein distributions of the corresponding electrode (acting as thermal reservoirs), which also depend on their temperature. Note that the voltage influence in the Fermi-Dirac distribution functions has been included in Eq. (1.52) in the chemical potential of the electrodes ($\mu_1 - \mu_2 = eV$).

Additionally, in macroscopic systems at low temperatures a further contribution to thermal currents from photons (electromagnetic waves) might need to be also considered [Dubi2011]. In the case of molecular junctions this has been recently theoretically proposed, since thermal radiation or photon tunnelling may occur between the electrodes forming a molecular junction [Klöckner2017b].

Finally, electrical and thermal properties of nanojunctions can be also combined within the scattering approach starting with the measurable thermoelectric coefficients, namely, the conductance $G = 1/R$, the thermopower S, the Peltier coefficient Π and the thermal conductance G_{th} [Finch2009]. They relate the charge and heat currents, I and Q respectively, to the voltage and temperature differences applied, ΔV and ΔT respectively, by the equations:

$$\begin{pmatrix} \Delta V \\ Q \end{pmatrix} = \begin{pmatrix} R & S \\ \Pi & G_{th} \end{pmatrix} \begin{pmatrix} I \\ \Delta T \end{pmatrix}. \qquad \text{Eq. (1.54)}$$

Note that only electron contribution to heat current is being considered in these expressions. In the linear voltage and temperature regimes, an expression for the coefficients G, S and G_{th} as a function of the moments L_n of the transmission function can be derived:

$$G = \frac{2e^2}{h} L_0, \qquad \text{Eq. (1.55)}$$

$$S = -\frac{1}{eT} \frac{L_1}{L_0} \qquad \text{Eq. (1.56)}$$

and

$$G_{th} = -\frac{2}{h} \frac{1}{T} \left(L_2 - \frac{{L_1}^2}{L_0} \right), \qquad \text{Eq. (1.57)}$$

where

$$L_n = \int_{-\infty}^{\infty} (E - E_F)^n \mathcal{T}(E) \frac{\partial f(E)}{\partial E} dE. \qquad \text{Eq. (1.58)}$$

1.6 Thermoelectric devices: efficiency and figure of merit

Besides experimentally exploring the validity and limits of the theoretical framework discussed until now, the ultimate technological goal of the present Thesis is the development of more efficient thermoelectric devices based on organic molecules, serving our work of these years for the acquisition of strategies in this direction. The study of molecular junctions might pave the way to the development of new environmentally friendly organic-based thermoelectric devices with a lower cost than present inorganic semiconducting thermoelectrics [Zhang2014]. Devices with a high thermoelectric efficiency would enable direct conversion of heat into electricity in energy harvesting applications or on-chip cooling in nanoscale electronic devices. Molecular junctions are promising candidates to achieve these high efficiencies due to the already discussed discreteness of the energy levels responsible for transport and the tunability of their properties via chemical synthesis, electrostatic gates, or pressure [Rincón-García2016; Cui2017].

First things first, a thermoelectric device consists, basically, of alternating branches (or ingots) of *p*-type and *n*-type materials, i.e. with positive and negative charge carriers, respectively. These branches are connected electrically in series (i.e. current flows through all of them, one after the other) and thermally in parallel, since they are typically sandwiched between two ceramic plates (electrically insulating, but thermally conducting, thus keeping a uniform temperature at each side of all the branches). This design is depicted in Figure 1.13 for simple thermoelectric devices formed by two branches and operated for their basic straightforward applications: power generation and refrigeration.

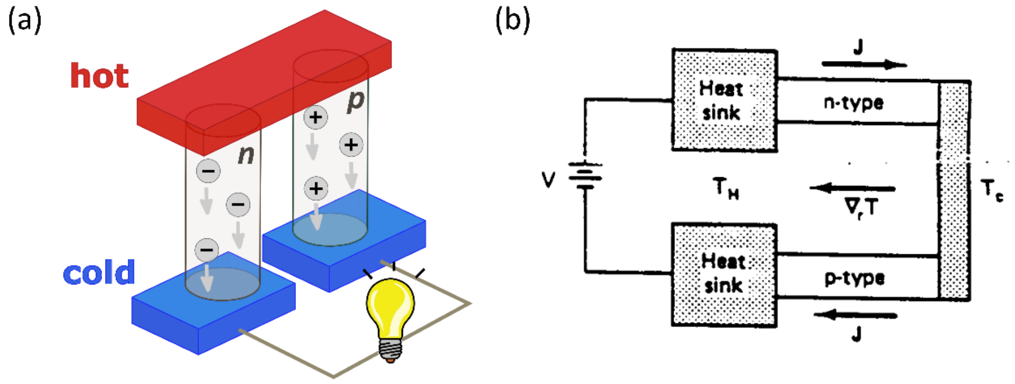

Figure 1.13: Thermoelectric devices for power generation (a) and refrigeration (b). (a) Schematic representation of a thermoelectric device operating as power generator. An electrical current is established thanks to the *n*-type and *p*-type thermoelectric materials and the temperature difference established. (b) Schematic diagram for a thermoelectric refrigerator. The heat sinks (at $\mathrm{T_H}$) and cold side (at $\mathrm{T_C}$) are metals that form ohmic contacts to the active thermoelectric *n*-type and *p*-type semiconductors. Establishing a current J through the device, a net flow of heat towards the hot side takes place in this configuration, thus refrigerating the cold side. From Ref. [Dresselhaus2001].

In the case of thermoelectric generators (see Figure 1.13(a)), when a temperature difference is established across each of the branches (between the ceramic plates), the thermovoltage generated in the alternating positively and negatively charged materials translates into a current able to deliver electrical power to an external load connected to the device.

Inversely, in the case of thermoelectric refrigerators (see Figure 1.13(b)), an electric current passing through the branches produces the appearance of a temperature gradient across each of them due to heat transfer from one face to the other: it is absorbed at one side of the device and rejected at the other.

Applications of thermoelectric generators, despite the simplicity of their working principle, can become much fancier than a modest light bulb power supply and they include energy harvesting systems, waste heat recovery or space exploration applications, since they offer autonomous sources of electrical power [Rowe1995]. In comparison with thermomechanical conversion systems, these unique devices for conversion of thermal to electrical energy result especially advantageous in terms of reliability, absence of moving parts and silent operation. With respect to standard thermoelectric devices, surmounting their relatively high cost and low efficiency (typically less than 5%), they are ideally suited for many kind of applications in medical physics, space exploration or exploitation of Earth's resources in inaccessible locations. Complementary, thermoelectric cooling has been successfully applied in domestic food refrigerators or air conditioning [Rowe1995]. The possibility to apply thermoelectric refrigeration directly for on-chip cooling is especially appealing. Finally, it is also possible to use thermoelectric devices as temperature controllers or for thermoelectric thermometry (with a thermocouple, for example, as introduced in section 1.3.1).

1.6.1 Figure of merit

In a thermoelectric generator the efficiency of conversion of heat into electricity depends mainly on the temperature difference $\Delta T = T_h - T_c$ over which the device operates (where T_h and T_c are the temperature at the hot and cold side of the device, respectively), on its average temperature of operation $T = (T_h + T_c)/2$ and on the performance of the thermoelectric material, which is given by its figure of merit Z [Rowe1995]. More generally, we can consider that the efficiency of a material for converting thermal to electrical energy depends on the dimensionless figure of merit ZT, for a specific temperature T.

In the case of a bulk material ZT is given by:

$$ZT = \frac{\sigma S^2 T}{\kappa}, \qquad \text{Eq. (1.59)}$$

where σ and κ are the electrical and thermal conductivity, respectively. As mentioned in the previous section, heat is transported by electrons and phonons and, consequently, $\kappa = \kappa_{el} + \kappa_{ph}$. Eq. (1.59) implies that ZT of bulk materials does not depend on the geometry of the material, but only on its physical properties. In contrast, for nanoscale (molecular) junctions, the figure of merit is:

$$ZT = \frac{GS^2 T}{G_{th}}, \qquad \text{Eq. (1.60)}$$

where the thermal conductance can again be decomposed into electron and phonon contributions ($G_{th} = G_{th,el} + G_{th,ph}$). Writing explicitly the electron and phonon contributions to the thermal conductance, we have:

$$ZT = \frac{GS^2T}{G_{th,el} + G_{th,ph}} = \frac{GS^2T}{G_{th,el}(1 + G_{th,ph}/G_{th,el})} = \frac{S^2}{L_0(1 + G_{th,ph}/G_{th,el})}, \qquad \text{Eq. (1.61)}$$

where we have taken into account Wiedemann-Franz law, i.e. that the ratio of thermal conductance due to electrons to the electrical conductance is proportional to the temperature $G_{th,el} = L_0 T G$, where L_0 is the Lorenz number ($L_0 = (k_B/e)^2 \pi^2/3 = 2.44 \times 10^{-8}\ \mathrm{W\Omega K^{-2}}$).

Based on these expressions of ZT for molecular junctions, determining their thermoelectric efficiency (i.e. experimentally measuring the figure of merit) requires the measurement of the electrical conductance, the thermopower and the thermal conductance, goals of the present Thesis. Using a STM setup introduced in Chapter 2, conductance and thermopower measurements of different molecular junctions are presented in Chapters 3 and 4, while for the third magnitude, a very demanding task due to the small thermal flows involved, thermal conductance measurements are experimentally addressed in Chapter 5 for atomic contacts as a proof-of-concept for a novel technique developed.

References

[Agraït2003] N. Agraït, A. Levy Yeyati and J. M. van Ruitenbeek. “Quantum properties of atomic-sized conductors”. *Physics Reports* **377**, 81-279 (2003).

[Aradhya2013] S. V. Aradhya and L. Venkataraman. “Single-molecule junctions beyond electronic transport”. *Nature Nanotechnology* **8**, 399-410 (2013).

[Ashcroft1976] N. W. Ashcroft and N. D. Mermin. “Solid State Physics”. Saunders, Philadelphia, USA (1976).

[Aviram1974] A. Aviram and M. A. Ratner. “Molecular rectifiers”. *Chemical Physics Letters* **29**(2), 277-283 (1974).

[Aviram1988] A. Aviram. “Molecules for memory, logic, and amplification”. *Journal of the American Chemical Society* **110**(17), 5687-5692 (1988).

[Bergfield2010] J. Bergfield, M. Solis and C. Stafford. “Giant Thermoelectric Effect from Transmission Supernodes”. *ACS Nano* **4**, 5314-5320 (2010).

[Bilan2012] S. Bilan, L. A. Zotti, F. Pauly and J. C. Cuevas. “Theoretical study of the charge transport through C60-based single-molecule junctions”. *Physical Review B* **85**, 205403 (2012).

[Binnig1982] G. Binnig, H. Rohrer, Ch. Gerber and E. Weibel. “Surface Studies by Scanning Tunneling Microscopy”. *Physical Review Letters* **49**(1), 57-61 (1982).

[Carter1983] F. Carter. “Molecular Level Fabrication Techniques and Molecular Electronics Devices”. *Journal of Vacuum Science and Technology B* **1**, 959-968 (1983).

[Choi2009] H. Choi and C. C. M. Mody. “The Long History of Molecular Electronics: Microelectronics Origins of Nanotechnology”. *Social Studies of Science* **39**(1), 11-50 (2009).

[Cuevas2010] J. C. Cuevas and E. Scheer. “Molecular Electronics: An Introduction to Theory and Experiment”. World Scientific Publishers, Singapore (2010).

[Cui2017] L. Cui, R. Miao, C. Jiang, E. Meyhofer and P. Reddy. “Perspective: Thermal and thermoelectric transport in molecular junctions”. *The Journal of Chemical Physics* **146**, 092201 (2017).

[Datta1995] S. Datta. “Electronic Transport in Mesoscopic Systems”. Cambridge University Press, Cambridge, UK (1995).

[Datta2005] S. Datta. “Quantum Transport: Atom to Transistor”. Cambridge University Press, Cambridge, UK (2005).

[Dresselhaus2001] M. S. Dresselhaus. “Transport properties of solids”. Solid State Physics course (2001).

[Dubi2011] Y. Dubi and M. Di Ventra. “Colloquium: Heat flow and thermoelectricity in atomic and molecular junctions”. *Review of Modern Physics* **83**, 131-155 (2011).

[Finch2009] C. M. Finch, V. M. García-Suárez and C. J. Lambert. “Giant thermopower and figure of merit in single-molecule devices”. *Physical Review B* **79**, 033405 (2009).

[Kasap2006] S. O. Kasap. “Principles of Electronic Materials and Devices”. McGraw-Hill Education (2006).

[Kim2014] Y. Kim, W. Jeong, K. Kim, W. Lee and P. Reddy. “Electrostatic control of thermoelectricity in molecular junctions”. *Nature Nanotechnology* **9**, 881-885 (2014).

[Kittel1953] C. Kittel. “Introduction to Solid State Physics”. John Wiley & Sons (1953).

[Klöckner2017a] J. C. Klöckner, M. Matt, P. Nielaba, F. Pauly and J. C. Cuevas. "Thermal conductance of metallic atomic-size contacts: Phonon transport and Wiedemann-Franz law". *Physical Review B* **96**, 205405 (2017).

[Klöckner2017b] J. C. Klöckner, R. Siebler, J. C. Cuevas and F. Pauly. "Thermal conductance and thermoelectric figure of merit of C60-based single-molecule junctions: Electrons, phonons, and photons". *Physical Review B* **95**, 245404 (2017).

[Lambert2015] C. J. Lambert. "Basic concepts of quantum interference and electron transport in single-molecule electronics". *Chemical Society Reviews* **44**, 875-888 (2015).

[Landauer1957] R. Landauer. "Spatial variation of currents and fields due to localized scatterers in metallic conduction". *IBM Journal of Research and Development* **1**(3), 223-231 (1957).

[Malen2010] J. A. Malen, S. K. Yee, A. Majumdar and Rachel A. Segalman. "Fundamentals of energy transport, energy conversion, and thermal properties in organic–inorganic heterojunctions". *Chemical Physics Letters* **491**, 109-122 (2010).

[Papadopoulos2006] T. A. Papadopoulos, I. M. Grace and C. J. Lambert. "Control of electron transport through Fano resonances in molecular wires". *Physical Review B* **74**, 193306 (2006).

[Paulsson2003] M. Paulsson and S. Datta. "Thermoelectric effect in molecular electronics". *Physical Review B* **67**, 241403(R) (2003).

[Pauly2008] F. Pauly, J. K. Viljas and J. C. Cuevas. "Length-dependent conductance and thermopower in single-molecule junctions of dithiolated oligophenylene derivatives: A density functional study". *Physical Review B* **78**, 035315 (2008).

[Reed1997] M. A. Reed, C. Zhou, C. J. Muller, T. P. Burgin and J. M. Tour. "Conductance of a molecular junction". *Science* **278**, 252-254 (1997).

[Rincón-García2016] L. Rincón-García, C. Evangeli, G. Rubio-Bollinger and N. Agraït. "Thermopower measurements in molecular junctions". *Chemical Society Reviews* **45**(15), 4285-4306 (2016).

[Rowe1995] D. M. Rowe (editor). "CRC Handbook of Thermoelectrics". Taylor & Francis (1995).

[Simmons1963] J. G. Simmons. "Generalized formula for the electric tunnel effect between similar electrodes separated by a thin insulating film". *Journal of Applied Physics* **34**, 1793 (1963).

[Tour1991] J. M. Tour, R. L. Wu and J. S. Schumm. "Extended Orthogonally Fused Conducting Oligomers for Molecular Electronic Devices". *Journal of the American Chemical Society* **113**, 7064-7066 (1991).

[Wang2019] K. Wang, E. Meyhofer and P. Reddy. "Thermal and Thermoelectric Properties of Molecular Junctions". *Advanced Functional Materials* (online version), 1904534 (2019).

[Wiesendanger1994] R. Wiesendanger. "Scanning Probe Microscopy and Spectroscopy: Methods and Applications". Cambridge University Press (1994).

[Yee2011] S. K. Yee, J. A. Malen, A. Majumdar and R. A. Segalman. "Thermoelectricity in Fullerene-Metal Heterojunctions". *Nano Letters* **11**(10), 4089-4094 (2011).

[Zhang2014] Q. Zhang, Y. Sun, W. Xu and D. Zhu. "Organic Thermoelectric Materials: Emerging Green Energy Materials Converting Heat to Electricity Directly and Efficiently". *Advanced Materials* **26**, 6829-6851 (2014).

PART 1:

CONDUCTANCE AND THERMOPOWER MEASUREMENTS IN MOLECULAR JUNCTIONS

2. Experimental technique: scanning tunnelling microscope (STM)

In this chapter we will introduce the principal aspects of the experimental technique used during the Thesis: the scanning tunnelling microscope (STM). As it is going to be shown, STM results a highly suitable tool to experimentally investigate the quantum transport properties of molecular junctions and atomic contacts, due to its capacity to measure tunnelling currents and perform subnanometer scale displacements.

After beginning with a general overview (Section 2.1), we will describe the STM working principle and its main elements (Section 2.2) and we will present the home-built STM experimental setup utilized during the present Thesis (Section 2.3). After this, the experimental measurement techniques that have been employed will be introduced (Section 2.4). We have used two different approaches for simultaneous conductance and thermopower characterization, namely, the STM-Imaging technique and the STM-Break Junction (STM-BJ) technique. The choice of one or other technique depends on the particular nanoscale system under investigation. In addition, Section 2.4 includes valuable information regarding the offsets calibration procedure, essential to obtain accurate data. Finally, and getting ahead slightly into Part 2 (Chapter 5), it should be noticed that even the new technique developed to measure thermal conductance at the nanoscale and fully introduced in that chapter is somehow based on the STM configuration and working principle, despite being adapted to measure with a different probe and electronics. In summary, the STM has been the working cornerstone of this Thesis, the key tool to shed light on the nanoscale transport properties targeted.

2.1 Introduction

The scanning tunnelling microscope (STM) was developed by Gerd Binnig, Heinrich Rohrer, Christoph Gerber and Edmund Weibel in 1982 to perform surface microscopy using vacuum tunnelling currents [Binnig1982]. In particular, Au(110) surfaces were examined obtaining topographic images of monoatomic steps and evidencing the great potential of the setup to inspect surfaces at the nanometer scale. A year later, the (7x7) reconstruction of Si(111) was probed achieving for the first time lateral atomic resolution [Binnig1983]. This instrumental achievement was undoubtedly a major breakthrough in the history of science. It was so recognized in 1986 when Binnig and Rohrer were awarded the Nobel Prize in Physics “for their design of the scanning tunnelling microscope”, an exceptional instrument that made it possible to acquire surface information on the atomic scale directly in real space thanks to a feedback loop on the vacuum tunnelling current measured between a metal tip and a sample and to the capacity of controlling subnanometer scale displacements, based on the use of piezoelectric materials.

Since then, the STM has become an indispensable tool to investigate surface phenomena and processes (surface reconstructions, catalysis, surface reactions) at the atomic scale. It has been adapted and combined with other techniques to examine multiple and diverse properties (electronic, magnetic, optic, thermal, spectroscopy, electrochemistry, spintronic, etc.), it has been employed in the characterization of a wide variety of systems (metallic surfaces, single-molecule junctions, semiconductors, polymers, superconductors, 2D materials, etc.) and it has been operated in various environmental conditions (at room, low, or high temperatures; in vacuum, air, or liquids, etc.).

STM was also the inspirational trigger for the development of a whole new research field based on scanning probe microscopies (SPMs). As local probe techniques, they give access to properties of materials at the nanoscale, otherwise inaccessible, using almost every kind of possible interaction between a tip and a sample (such as mechanical forces) as the feedback control signal. All in all, many different scientific disciplines have experienced great advances in the last forty years thanks to the STM, especially fields such as condensed matter physics, chemistry, biology, optics or materials science [Cuevas2010]. It has also greatly stimulated interdisciplinary research because of its broad applications and its ability to probe matter locally down to the atomic level.

For a more complete vision and explanation of STM history, theory, experiments, applications and prospects, we would suggest Ref. [Wiesendanger1994] or [Cuevas2010].

2.2 STM working principle

The STM working principle is based on the quantum tunnelling effect introduced in Section 1.2.2. The model developed for a one-dimensional rectangular potential barrier can be directly extrapolated to a STM tunnelling barrier between two conducting electrodes (typically metals) facing each other in close proximity, namely a tip (electrode 1) and a sample (electrode 2). This tip-shaped electrode, typically a metallic wire, is one of the main features of the STM since it acts as a powerful local probe that allows measuring physical properties on the atomic scale.

The main elements of a STM are depicted in Figure 2.1. A bias voltage V_{bias} is applied with a voltage source between the tip and the sample whose properties are to be investigated. Using a coarse movement system (not shown in Figure 2.1), both electrodes can be approached, thus reducing the dimension of the potential barrier between them. When a nanometric separation is achieved, electronic evanescent waves can go through the barrier and a tunnelling current flows between the electrodes before reaching the 'mechanical point contact' (see Section 1.2.2). Let us remind that this current depends exponentially on the distance between tip and sample and thus is very sensitive to small variations. For most metals, changes of 1 Å typically lead to a change of the tunnelling current of one order of magnitude [Wiesendanger1994].

By monitoring the current it is possible to preserve the tip-sample separation by establishing a desired setpoint for a feedback loop that keeps the current constant. An increase (decrease) of the tunnelling current is translated into a withdraw (approach) of the tip to maintain the current setpoint value, thus avoiding mechanical contact between the electrodes.

In practice, this fine gap maintenance is performed by means of piezoelements, whose working principle is based on the piezoelectric effect discovered by Pierre Curie in 1880. This effect is only present in certain materials such as quartz, barium titanate or lead zirconium titanate (also known as PZT and commonly used in STM setups) and it consists on the generation of a voltage difference across the system as a response to mechanical deformations (when squeezing it, for example). The opposite effect, the one actually employed in STM, is also possible and compression or elongation of the piezoelectric material can be achieved by applying a voltage.

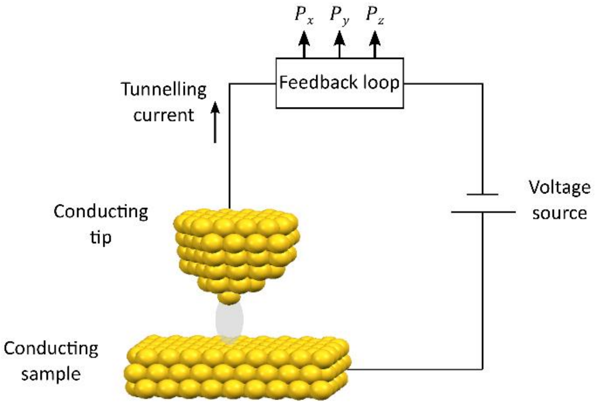

Figure 2.1: STM working principle. Basic elements of a STM: two conducting electrodes (a tip and a sample), a voltage source to apply a voltage difference (the bias voltage V_{bias}) between the electrodes so that there is tunnelling current (tunnelling of electrons represented in light grey) and feedback loop to control the total current or the tip position, depending on the scanning mode; the feedback loop is typically connected to piezoelectric elements P_z to control the vertical tip position with subnanometer scale precision (thanks to the exponential dependence of the tunnelling current with distance) and to piezoelectric elements P_x, P_y to scan the surface.

Voltages applied from the feedback loop to the piezoelements can be translated hence into variations of the tip position, which can be vertically, i.e. perpendicularly to the surface, moved as required to keep a constant current. We consider this to be the z-direction. In some STM setups the fine positioning of the electrodes is performed moving the sample instead of the tip, but we consider here the case where the tip vertical movement is coupled to the piezodrive P_z.

Besides controlling the z position of the tip, it is common to have additional piezoelements (P_x and P_y) to also move the tip in the x- and y-directions, i.e. in the sample surface plane. In this way, surface topography can be probed by scanning the surface with the tip. This is laterally displaced over the sample while the feedback loop controls its vertical position (z) in order to maintain the current equal to the setpoint value. Recording the vertical displacements performed as function of the lateral tip position gives rise to $z(x, y)$ images. This scanning approach, schematized in Figure 2.2(a), is known as constant current mode and it is the scanning mode used to obtain all the STM images shown in this Thesis.

For very flat surfaces, another scanning mode called constant height mode becomes of interest. In this case, the feedback loop is turned off so that the tip vertical movement is blocked, as depicted in Figure 2.2(b). In these images only the current is displayed as function of the (x, y) position, which allows to generate images faster than the constant current mode although tip and surface may touch, thus losing the information from the tunnelling current, if the surface is not flat enough or the tip movement does not correctly follow the sample surface plane.

In summary, a STM is based on a conducting tip that probes locally the sample via electron tunnelling thanks to the presence of a bias voltage between the electrodes and a feedback loop that prevents mechanical contact. Additionally, piezoelectric elements allow to scan the sample surface with the tip and generate three-dimensional $z(x, y)$ images (in the constant current mode).

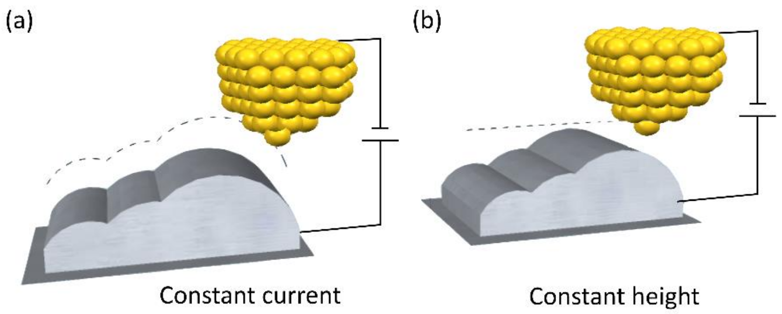

Figure 2.2: STM scanning modes. (a) Constant current mode. The current between the tip and the substrate (plotted in yellow and grey, respectively) is kept constant while scanning and the tip vertical position varies (following the dashed line). (b) Constant height mode. The tip vertical position is fixed while scanning (indicated by the dashed line) and the tunnelling current is allowed to vary. After Ref. [Evangeli2014].

Although powerful, the STM working principle implies two fundamental constraints of STM measurements. Firstly, the presence of electrons free to move at a given energy is essential, which in a certain way establishes a limit to the potential systems that can be studied using a STM (insulating surfaces result therefore excluded since they would not present tunnel effect). Secondly, the distance between the electrodes, or the dimensions of any system connected between them, must be in the nanometer scale, in order to allow the evanescent electron wave to go through the potential barrier. This scale can be though increased to some extent if the potential barrier is reduced by other means, such as intermediate states or higher bias voltage, or the energy of the moving electrons is increased (with temperature, for example).

Related to the STM imaging capability, one of its most remarkable features is that this system works directly in real space and provides local information. This is a significant difference with traditional diffraction techniques where properties are averaged over macroscopic sample volumes or surface areas, providing thus insights, for example, about crystal lattices parameters. STM real-space local information, however, enables to investigate disorder degree on a surface or defect structures, for instance. It essentially allows to detect and study non-periodic features on a sample surface, such as the absence of one atom in the most external crystal layer or even the presence of a single molecule deposited on it, a feature of fundamental importance for this Thesis.

Furthermore, STM enables to experimentally form nanoscale junctions, such as atomic contacts or molecular junctions (as we are going to detail a bit later), and it has proven to be a versatile tool to explore their charge transport [Agraït1993; Pascual1993; Agraït2003; Xu2003] and thermoelectric properties [Reddy2007; Widawsky2012; Evangeli2013; Evangeli2015], which depend on the transmission characteristics of the nanojunctions, as introduced in Chapter 1.

We describe next the main features of the STM setup (Section 2.3) and the technique (Section 2.4) developed in our group prior to this Thesis to simultaneously characterize the conductance and thermopower of nanoscale junctions [Evangeli2014], as well comment on some adaptations incorporated.

2.3 STM experimental setup

During this Thesis, electric and thermoelectric characterization of atomic contacts and molecular junctions has been performed using a home-built STM working in ambient conditions and at room temperature. The setup was mounted in the group prior to the work described in this manuscript [Evangeli2014] and it facilitates these combined experiments [Evangeli2013].

The STM setup is principally formed by three brass blocks (see Figure 2.3):

- the head, where the piezotube and the tip support are mounted;
- the body, which is a massive brass block used to keep the head mechanically stable over the sample;
- the table, where the sample and the bias voltage electrode are placed. Two screws with micromanipulators and an electrical motor also located in the table serve as support of the body. They are used for the coarse vertical movement of the head over the table, i.e. the tip over the sample.

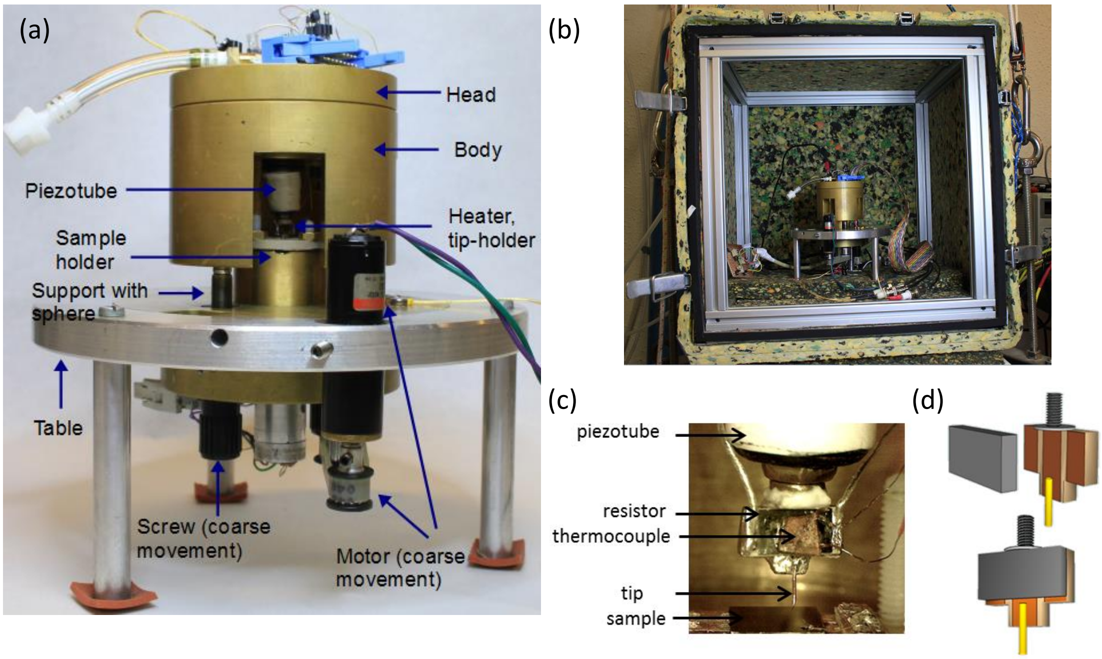

Figure 2.3: STM setup employed in our experiments, operated under ambient conditions and at room temperature. (a) Image of the three brass blocks conforming the STM and its main elements. (b) Image of the metallic box where the STM is placed, with isolation sponge inside and outside. (c) Image of the tip support screwed to the piezotube. The resistive element acting as heater and the thermocouple to monitor its temperature are also visible. (d) Schematic representation of the tip support and heater. After Ref. [Evangeli2014].

This configuration has been employed to obtain atomically resolved STM images as well as to form stable single-molecule junctions [Evangeli2013], thanks to its mechanical stability and low thermal drift (normal drift of few Angstroms per minute) [Evangeli2014]. The whole STM is placed inside a box that acts as a Faraday cage since its metallic structure is grounded in order to isolate the STM from external electromagnetic signals (see Figure 2.3(b)). The box is also covered inside and outside with a noise-isolating sponge and is hanged from the ceiling using a pulley system and elastic ropes to isolate the STM from mechanical vibrations of the building.

Our STM electronics are schematized in Figure 2.4(a). Data acquisition and communication with the setup is achieved using a computer with a multifunctional card, NI PCI-7833R. Briefly describing the whole STM circuit, the card allows us to apply the bias voltage to the sample, while the tip is grounded and connected to a current-to-voltage amplifier. The tunnelling current through the sample-tip junction is thus amplified after flowing to the tip and, already converted to a voltage, it is registered by the FPGA. This one, through the feedback loop, controls the z-piezoelement elongation and corrects the tip position over the sample to maintain the tunnelling current. x- and y-piezoelements are also controlled by the FPGA to acquire STM images in constant current mode. Let us describe further all these stages.

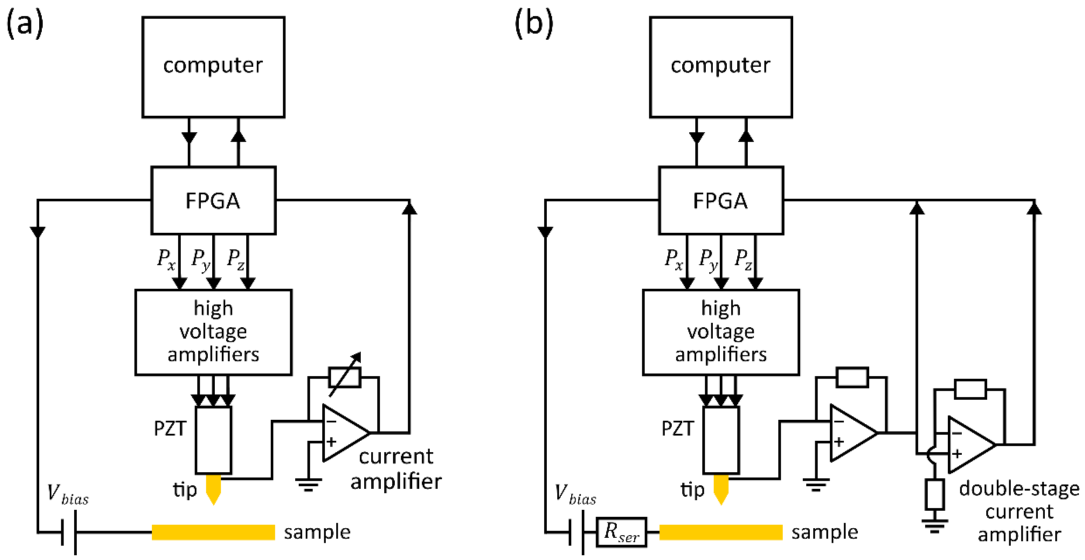

Figure 2.4: Scheme of the home-built STM used during this Thesis. (a) Scheme of the standard configuration of the STM. Using a FPGA a bias voltage V_{bias} is applied to the sample to establish a tunnelling current with the tip which is then amplified in a commercial current-to-voltage amplifier with a variable gain and recorded with the FPGA; a feedback loop to the piezotube controls the tip vertical and lateral position. This configuration is used to perform G and S measurements with the STM-Imaging technique (see Section 2.4.2 for more details on the technique). (b) Scheme of the second configuration of the STM with two main modifications: a series resistor is connected before the voltage is applied to the substrate and a double-stage home-built I-V amplifier is used. This configuration is employed to perform G and S measurements with the STM-Break Junction technique (see Section 2.4.3 for more details on the technique).

In our system the bias voltage V_{bias} required to establish the tunnelling current is applied to the sample by a macroscopic copper electrode electrically coupled to it. The voltage is given by the digital-to-analogue converter (DAC) of the card, which has a total output range of $\pm\, 10\ \mathrm{V}$. We generally divide this output by a factor 10 to reduce the voltage output noise, using in experiments an actual range of $\pm\, 1\ \mathrm{V}$ for V_{bias}. This is essential to perform thermopower measurements where very small voltages are involved, as we are going to detail a bit later. For some experiments, such as tunnelling spectroscopy (see results in Chapter 3), a smaller voltage divider is used in order to be able to apply slightly larger V_{bias}.

Tunnelling current is measured after flowing to the tip, which is grounded. Tips employed in our experiments are mechanically cut gold wires ($0.25\ \mathrm{mm}$ diameter, 99.99% purity, Goodfellow). We commonly use a commercial programmable current amplifier Keithley 428, with variable gain (10^7 V/A or 10^8 V/A is selected depending on the experiment). The current-to-voltage amplifier circuit is schematized in Figure 2.5(a)). The voltage signal is afterwards received by the FPGA where the analogue-to-digital converter (ADC) transforms it to a digital signal recorded by the computer.

Tip position over the sample is then adjusted using the feedback loop, which in our setup is based on a digital proportional-integral-differential (PID) controller. When measuring in constant current mode, the signal received by the card is compared with a predefined setpoint and the comparison yields a certain error. The PID controller tries to minimize it over time and adjust the tip position to maintain the pre-established current value. The feedback signal generated is sent from the computer DACs (with a $\pm$ 10 V range) to high voltage amplifiers, in particular, Nanonis electronics (a high voltage amplifier HVA4 and its corresponding high voltage power supply HVS4). The output signal, with a total range of $\pm$ 150 V, is then sent to the piezotube to control its elongation in the z-direction.

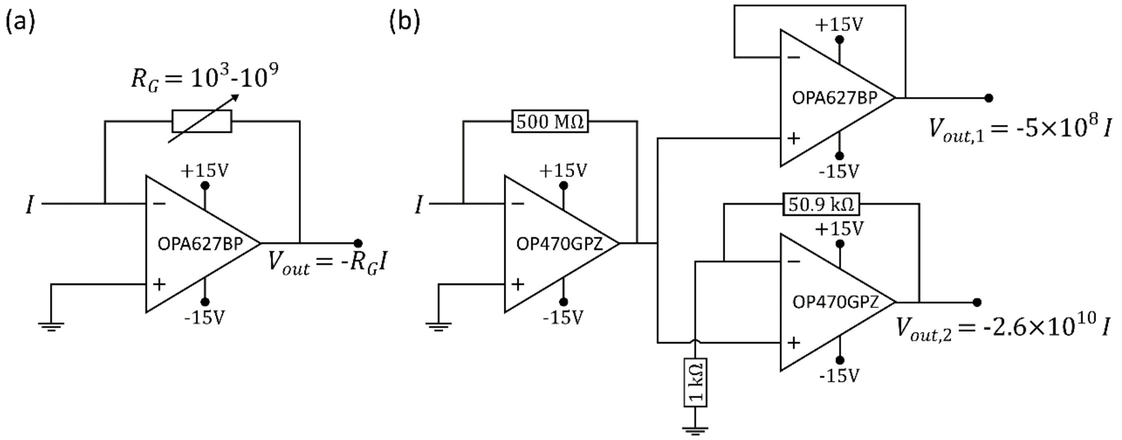

Figure 2.5: Schematic diagrams of the current-to-voltage (I-V) amplifiers employed. (a) Commercial programmable current amplifier Keithley 428. The I-V amplifier converts the current into a voltage via an OPA627BP amplifier with a variable gain. The output voltage is proportional to the input current and is given by $V_{out} = -R_G \cdot I_{in}$. (b) Double-stage home-made current-to-voltage amplifier. Tunnelling current is amplified in the first stage and it is then directed to a second amplifier and a buffer, thus generating two signals V_{out_1} and V_{out_2}.

The piezotube in our STM is directly glued to the brass head (see pictures and scheme in Figure 2.3(a,c-d)). A washer glued on the free extreme of the piezotube makes it possible to mount the tip support on it, using a screw. The tip support is just a piece of circuit board where the tip is welded, and washer and screw are completely electrically isolated from the piezotube. This is formed by five independent piezoelectric blocks, ordered on an empty cylinder in such a way that two control the movements on the x-direction; two, on the y-direction and one, the inner face of the cylinder, controls the movements on the z-direction (vertical movements) (see Figure 2.6). Lateral displacements of the tip for surface scanning are controlled with $\pm X$ and $\pm Y$ voltage ramps in such a way that the cylindrical piezotube “bends” laterally toward the desired direction, without any feedback control. The piezotube has been calibrated prior to this Thesis [Evangeli2014] and has a total scanning range of 1×1 μm^2 and a total vertical displacement of 660 nm (conversion factor of 2.2 nm/V).

Additionally to the STM configuration described until now, a second configuration with some changes has been also used during the Thesis. This has been motivated by the low conductance of some of the molecules investigated, which sometimes made it challenging to measure the transport properties of the junction. To be able to characterize both conductance and thermopower of these systems, with the so-called STM-Break Junction (STM-BJ) technique fully described in Section 2.4.3, two main modifications are introduced in the STM electronics, as schematized in Figure 2.4(b). One of them consists on the connection of a resistor in series to the sample (R_{ser} in Figure 2.4(b)). It increases the saturation limit of the current and enables to measure a wider range of conductance values, from below the low conductance molecular signal (around $10^{-5}G_0$ or even $10^{-6}G_0$ in some cases) up to the tip-sample metallic contact which serves as a reference (Au-Au one-atom contact shows a well-known conductance $G = G_0 = 2e^2/h = 77.5 \times 10^{-6}$ S, the quantum of conductance [Agraït2003]). The second major setup modification is in the current amplification stage. In this configuration we use a home-made double-stage current-to-voltage amplifier with a total gain of 2.6×10^{10} V/A (see circuit diagram in Figure 2.5(b)).

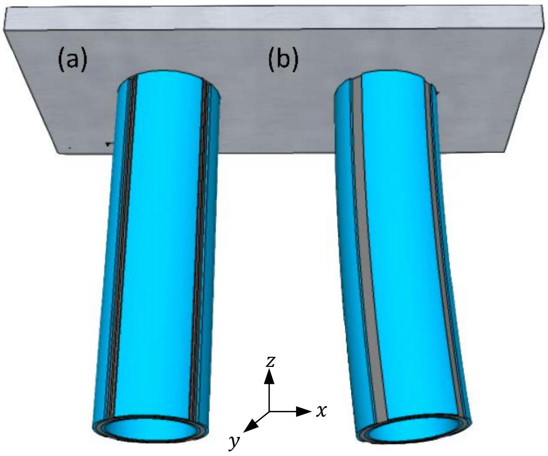

Figure 2.6: Schematics of the cylindrical piezotube. (a) Piezotube at rest position (no voltage applied). (b) Piezotube laterally bent in the x-direction. After Ref. [Evangeli2014].

2.4 Simultaneous conductance G and thermopower S measurement techniques

Thanks to the STM capacity to measure quantum tunnelling currents, this setup can be also applied to the measurement of thermoelectric properties of nanoscale systems [Evangeli2014]. In the particular case of molecular junctions, the possibility to perform conductance and thermopower experimental measurements can be schematized as depicted in Figure 2.7. As shown in Figure 2.7(a)), metallic STM electrodes allow to apply a voltage difference V_{bias} between the extremes of the targeted molecule. In this way, a tunnelling current $I(V_{bias})$ is established and the molecular junction conductance $G = I/V_{bias}$ can be measured.

Complementary, Figure 2.7(b) shows the basic requirements for thermopower measurements. Let us recall that the thermopower or Seebeck coefficient S is defined, in open-circuit conditions ($I = 0$), by Eq. (1.27):

$$S = -\frac{\Delta V}{\Delta T} = -\frac{V_h - V_c}{T_h - T_c}. \qquad \text{Eq. (2.1)}$$

Thus, considering Figure 2.7(b), a temperature difference $\Delta T = T_1 - T_2$ applied between the electrodes would generate a thermoelectric voltage difference across the junction $\Delta V = V_1 - V_2$. Measuring ΔV and knowing ΔT, the calculation of the thermopower is straightforward.

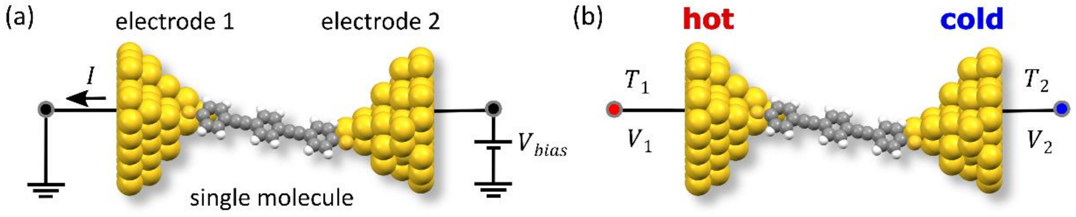

Figure 2.7: Conductance and thermopower measurements in a molecular junction. (a-b) Schematic representation of a molecular junction. A single molecule is electrically and thermally connected between two electrodes (1 and 2) that act as electron reservoirs (a). The electrodes allow to apply an electrical bias voltage V_{bias} across the junction and inject through it a proportional current $I = GV_{bias}$, where G is the conductance of the molecular junction. Complementary, when the two sides of the molecular junction are at different temperatures, T_1 and T_2, as depicted in (b), a thermoelectric voltage difference $V_1 - V_2 = -S(T_1 - T_2)$ (where S is the Seebeck coefficient of the molecular junction) appears between the electrodes in open-circuit conditions.

Both aspects, temperature difference application and thermovoltage measurements, imply some technical challenges that will be introduced in Section 2.4.1 and Section 2.4.4. The experimental technique employed for simultaneous G ans S measurements is also described below. In practice, there are two versions of the technique, depending on the molecules under study: the so-called STM-Imaging technique (presented in Section 2.4.2) and the STM-Break Junction technique (introduced in Section 2.4.3). Both have been used during this Thesis.

2.4.1 Equivalent thermal circuit

The major modification introduced in the standard STM setup to perform thermopower measurements is the addition of a surface mount $1\ \mathrm{k\Omega}$ resistor on the tip support which acts as a heater (see Figure 2.3(c-d)) [Evangeli2013]. A current flowing through the resistor heats it up by Joule effect and allows us to control to some extent its temperature rise above room temperature. The tip is in good thermal contact with the back of the resistor and the temperature drop through the tip has been calibrated to be less than 1% [Evangeli2014]. The substrate, thermally coupled to the macroscopic copper electrode, is maintained at room temperature T_c (approximately at $300\ \mathrm{K}$) and hence a temperature difference $\Delta T = T_h - T_c$ between tip and sample is established, where T_h is the temperature of the tip (and $T_h > T_c$). We monitor the resulting ΔT with two thermocouples placed on the heating resistor and on the sample. The temperature drop in the tip is taken into account when determining the actual ΔT. Depending on the experiment, the temperature difference ranges from $15\ \mathrm{K}$ to $40\ \mathrm{K}$, approximately.

In practice, when applying a ΔT and despite the fact that the STM setup is allowed to stabilize for around 15-30 minutes before measurements are initiated, the temperature rise generally affects the thermal drift of the setup, which is considerably increased when measuring with a heated tip. This translates into some practical requirements depending on the particular experiment carried out. For example, in the case of the STM-Imaging technique (introduced in more detail in Section 2.4.2), the increased thermal drift makes it necessary to use especially fast imaging to locate isolated molecules deposited on the substrate and to track them. For measurements performed with the STM-Break Junction (STM-BJ) technique (introduced in more detail in Section 2.4.3), the molecular junctions formed are typically more unstable than in normal conditions so their length becomes usually shorter and it is necessary to find a compromise between the frequency of thermopower measurements and the speed of the junction breaking.

When heating the tip a temperature difference is not only established between tip and sample but also a temperature gradient across the tip-connecting lead appears, which gives rise to an additional thermoelectric voltage that needs to be considered. The total thermovoltage experimentally measured V_{th} contains initially both contributions, from the junction and from the lead. The equivalent thermal circuit for measuring the Seebeck coefficient is depicted in Figure 2.8. Considering this circuit, the current through the STM junction can be written as:

$$\begin{aligned} I &= G[V_{bias} - S(T_h - T_c) - S_{lead}(T_c - T_h)] = \\ &= G[V_{bias} - S\Delta T + S_{lead}\Delta T] = G[V_{bias} - V_{th}], \end{aligned} \qquad \text{Eq. (2.2)}$$

where

$$V_{th} = S\Delta T - S_{lead}\Delta T = (S - S_{lead})\Delta T, \qquad \text{Eq. (2.3)}$$

V_{bias} is the applied bias voltage; G and S are the conductance and Seebeck coefficient of the junction, respectively, and S_{lead} is the Seebeck coefficient of the tip-connecting lead, which in our system is a copper wire, so $S_{lead} = S_{Cu} = 1.83\ \mu\mathrm{V/K}$ [Cusak1958]. The practical application of this expression allows us to measure simultaneously both conductance G and thermopower S as we are going to explain in the next sections.

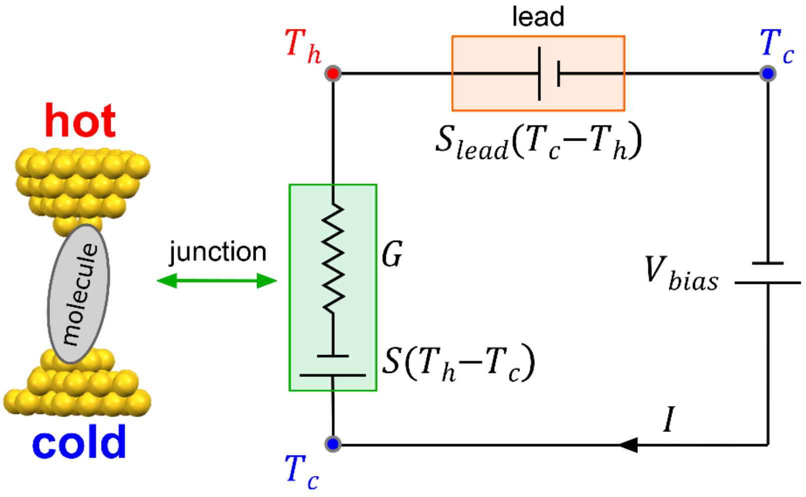

Figure 2.8: Schematic representation of the equivalent thermal circuit. The tip is heated to a temperature T_h above ambient temperature (in red), while the substrate and body of the STM are maintained at ambient temperature T_c (in blue), establishing a temperature difference $\Delta T = T_h - T_c$ that generates a thermoelectric response both in the junction (in green) and in the tip-connecting lead (in orange). S and S_{lead} are their corresponding Seebeck coefficients. The purely electrical circuit consists on the bias voltage applied to the substrate (V_{bias}) and the current I flowing through the STM junction of electrical resistance $1/G$.

Before doing so, let us make some further comments regarding the ΔT actual value during junction formation, while tip and sample are separated just by a molecule or even an atom. In this kind of experiments, precise application and detection of the temperature difference plays a key role. According to our experiments, ΔT remains constant in the timescale of the experiments as we see a clear thermoelectric response, independently of the total time of the experiment. The tip and the sample are huge thermal reservoirs where the temperature is well-defined and the atom(s) or the molecule act in the junction as a nanoconstriction where the drop of temperature takes place since there is coherent transport of electrons through it.

2.4.2 STM-Imaging technique for simultaneous G and S measurements

The STM-Imaging technique is essentially the technique introduced in Ref. [Evangeli2013] for the study of C_{60} molecules and was developed in our group prior to this Thesis, period when it has been applied to the investigation of the transport properties of endohedral metallofullerene junctions (see Chapter 3). Its most important characteristic is the use of STM images prior to junction formation in order to contact individual fullerenes adsorbed on the Au surface. Once a single molecule is targeted, both conductance G and thermopower S can be simultaneously measured doing small voltage ramps during the approach and retraction of the STM tip with respect to the molecule as described in Figure 2.9.

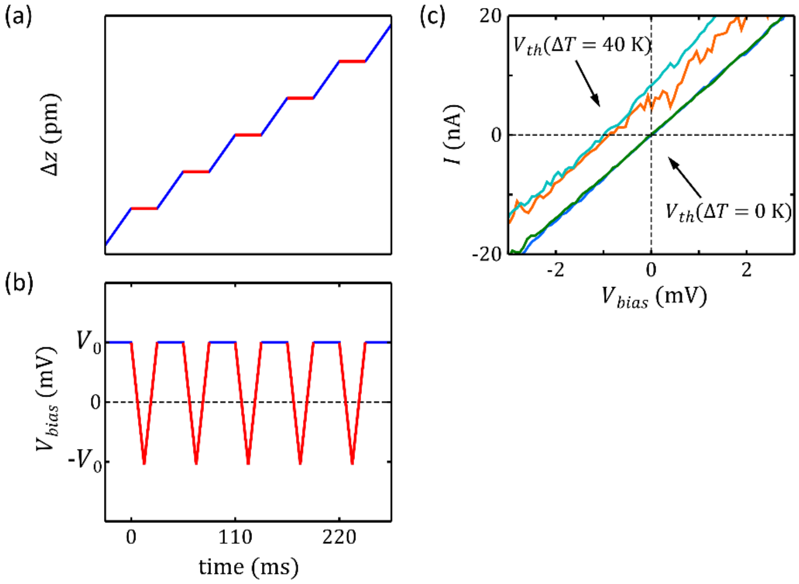

Figure 2.9: Technique for simultaneous conductance G and thermopower S measurements within the STM-Imaging technique. (a-b) Tip displacement Δz and applied bias voltage V_{bias} at the molecular junction, respectively, as a function of time. The bias voltage is maintained at a fixed value V_0 during the tip motion (in blue) and every few picometers it is swept between $\pm V_0$ while the tip is stationary (in red). (c) Experimental I-V traces zooming for voltage values close to zero. In the presence of a temperature difference $\Delta T \neq 0$ K, a voltage offset V_{th} appears.

The bias voltage V_{bias} applied to the sample is kept constant at a given value V_0 (typically around 10 mV) during the tip motion towards the molecule and backward. The tip motion is stopped every few picometers ($15 - 25$ pm) and the bias voltage is ramped between $\pm V_0$ while the tip is stationary (typically between ± 10 mV). These low-voltage I-V traces show linear ohmic behaviour, proving good coupling of the molecule to the electrodes and a HOMO-LUMO gap larger than the bias voltage [Joachim1995]. When no temperature difference is applied between both STM electrodes, i.e. $\Delta T = 0\ \mathrm{K}$ in Eq. (2.2), we have:

$$I = GV_{bias} \qquad \text{Eq. (2.4)}$$

and $I = 0\ \mathrm{A}$ takes place at zero bias voltage in the experimental I-V curves (see Figure 2.9(c)). When a non-zero temperature difference is established between tip and sample, the I-V curves show a ΔT-dependent voltage offset at zero current. Replacing $I = 0\ \mathrm{A}$ in Eq. (2.2):

$$0 = G[V_{bias} - V_{th}] \Rightarrow V_{bias} = V_{th} \qquad \text{Eq. (2.5)}$$

and therefore, the ΔT-dependent voltage offset of the I-V trace at zero current corresponds to the thermovoltage response of the system V_{th}, given by Eq. (2.3): $V_{th} = (S - S_{lead})\Delta T$. In this way, measuring ΔT and V_{th} and knowing S_{lead} (once the setup electrical offsets are taken into account (see Section 2.4.4)), the calculation of the thermopower of the junction S is straightforward. In addition and simultaneously, the slope of the I-V curve corresponds to the conductance G of the junction.

Experimentally, when this technique is employed (see results in Chapter 3), the current I is measured using the commercial current-voltage amplifier Keithley 428 with a digitally controlled variable gain that is set to $10^7\ \mathrm{V/A}$ for these experiments (see Figure 2.5(a)).

Finally, the STM-Imaging technique offers also the possibility to scan the area around the molecule under study after the junction formation in order to monitor possible modifications of the molecule position. If it remains stable after junction formation, the technique enables to perform further transport measurements in the very same molecule by successive approach-retraction cycles of the tip. In each approach-retraction cycle, approximately 50-100 I-V curves are typically shot, giving as many values of Seebeck coefficient.

2.4.3 STM-Break Junction technique for simultaneous G and S measurements

Conductance and thermopower measurements using the STM-Break Junction technique are very similar to those performed with the STM-Imaging technique introduced in the previous section. The main difference lies in the molecular junction formation, which determines also the kind of molecules targeted with each technique. While in the previous case high-conductance molecules such as fullerenes offer the possibility to localize them on the surface [Evangeli2013], molecules studied with the STM-BJ technique have typically a much smaller conductance (around two orders of magnitude smaller, at least), so junctions are “blindly” formed without prior STM images of the molecules on the surface [Xu2003; González2006; Leary2015]. This is also the reason behind the general chemical structure of most organic molecules characterized by means of BJ techniques (see Figures 2.10 or 1.8). Molecules under investigation, defined mainly by the so-called backbone (since molecules have usually a linear structure), are functionalized at both ends with binding groups, or anchor groups, which favour bond formation of the molecule with the metal atoms. Binding groups are typically “small” chemical groups with dangling bonds and good affinity for the electrode material, so they are willing to form chemical bonds with the metallic delocalized states.

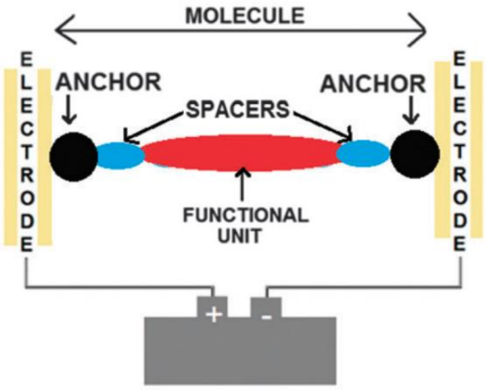

Figure 2.10: Schematics of a commonly investigated organic molecule. The molecule is typically formed by a functional unit, spacers (in the case of oligomers in particular) and anchor or binding groups to favor bonding with the electrodes. From Ref. [Leary2015].

Regarding junction formation in the STM-BJ technique, the tip is repeatedly indented into the surface, forming a metallic contact with the Au substrate, and then withdrawn. Upon breakage of the Au-Au contact, a small gap on the order of $0.2-0.5$ nm opens up between the electrodes (due to elastic deformation of the tip apex while breaking the metallic contact) [Leary2015]. When molecules are present in the vicinity of the electrodes, one may bind between the Au contacts and bridge momentarily the gap, thus allowing for the characterization of the transport properties of the junction, in our case, conductance G and thermopower S. This junction formation process is repeated hundreds of times for each compound and for each temperature difference established in order to be able to do a statistical analysis and get the most probable values of G and S of the investigated molecular junctions.

The main results of the experiments performed during this Thesis with the STM-BJ technique are presented in Chapter 4. Some of the systems explored show quite a low conductance which sometimes make it challenging to measure the transport properties of the junction. In this respect, several modifications have been added to the experimental setup and optimization of the experimental technique parameters has been accomplished in order to be able to characterize both conductance and thermopower. Experimentally, current is amplified using the home-made double-stage current-to-voltage amplifier described in Figure 2.5(b), with an overall gain of 2.6×10^{10} V/A. This large amplification is required to measure molecules with low conductance. For this same reason, the bias voltage V_{bias} applied to the sample is in this case generally set at 100-200 mV. Furthermore, a 12 MΩ resistor is connected in series with the STM junction to monitor the Au-Au one-atom contact. These implementations allow us to measure a wide range of conductance values from picosiemens (noise level in $G \sim 10^{-7} G_0 \sim 8 \times 10^{-12}$ S) to tens of microsiemens (Au-Au one-atom contact shows a conductance equal to $G_0 = 77.5 \times 10^{-6}$ S). Further details are given for each particular experiment in Chapter 4.

To simultaneously characterize conductance and thermopower of the molecular junctions formed, the experimental technique employed is equivalent to the procedure introduced in the previous section. Small I-V curves are recorded in the presence of a temperature difference ΔT between tip and sample during the breaking of the junctions (i.e. during the retraction of the Au tip), as described in Figure 2.11. The tip motion is typically stopped every $25-80$ pm, depending on molecular length and junction stability. The bias voltage, typically set at $V_{bias} =$ 100-200 mV during tip motion, is then swept typically twice between $\pm\Delta V_0 = \pm 10 - \pm 40$ mV while the tip is stationary. This range of ΔV_0 values is caused by the large range of conductance of the molecules investigated. Molecules with a very low conductance require to reach slightly larger voltages in the I-V ramps in order to be able to discern the transport properties from the instrumental noise (see Section 2.4.4). Doing so, the low-voltage I-V traces show a linear ohmic behaviour, proving good coupling of the molecule to the electrodes and a HOMO-LUMO gap larger than the bias voltage [Joachim1995]. When no temperature difference is applied between both STM electrodes, i.e. $\Delta T = 0$ K in Eq. (2.2), we have:

$$I = GV_{bias} \qquad \text{Eq. (2.6)}$$

and $I = 0$ A takes place at zero bias voltage in the experimental I-V curves (see Figure 2.11(c)). When a non-zero temperature difference is established between tip and sample, the I-V curves show a ΔT-dependent voltage offset at zero current. Replacing $I = 0$ A in Eq. (2.2):

$$0 = G[V_{bias} - V_{th}] \Rightarrow V_{bias} = V_{th} \qquad \text{Eq. (2.7)}$$

and therefore, the ΔT-dependent voltage offset of the I-V trace at zero current corresponds to the thermovoltage response of the system V_{th}, given by Eq. (2.3): $V_{th} = (S - S_{lead})\Delta T$. In this way, measuring ΔT and V_{th} and knowing S_{lead} (once the electrical offsets of the setup are taken into account (see Section 2.4.4)), the calculation of the thermopower of the junction thermopower is straightforward. In addition and simultaneously, the slope of the I-V curve corresponds to the conductance G of the junction. In fact, the conductance is measured both from the current values recorded while moving the tip (with $V_{bias} = 100\text{-}200$ mV) and from the slope of the I-V traces. The values obtained are found to be equivalent, as it is shown in Chapter 4.

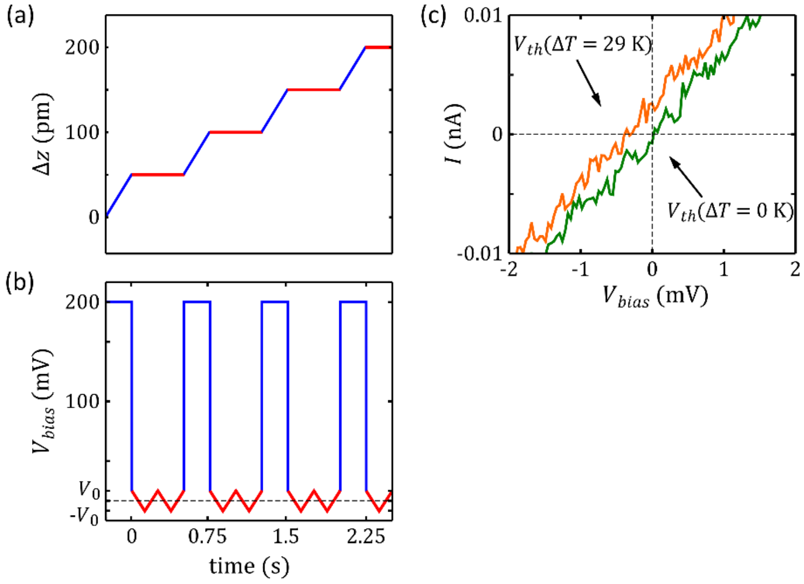

Figure 2.11: Technique for simultaneous conductance G and thermopower S measurements within the STM-Break Junction technique. (a-b) Tip displacement Δz and applied bias voltage V_{bias} at the molecular junction, respectively, as a function of time. The bias voltage is maintained at a fixed value, typically $V_{bias} = 200$ mV, during the tip motion (in blue) and every few picometers it is swept twice between $\pm\Delta V_0$ while the tip is stationary (in red). (c) Experimental I-V traces zooming for voltage values close to zero. In the presence of a temperature difference $\Delta T \neq 0$ K, a voltage offset V_{th} appears.

Thermoelectric properties of each molecule are typically measured for three different ΔTs, ranging between $\Delta T = T_h - T_c = 15\ \mathrm{K}$ and $\sim 30\ \mathrm{K} - 40\ \mathrm{K}$, monitored with thermocouples positioned on the resistor and on the substrate. Control "thermoelectric" measurements with $\Delta T = 0\ \mathrm{K}$, i.e. without heating the tip, are also performed. Experiments at several ΔT ensure a good linear fit of V_{th} *vs* ΔT values, whose slope gives the average Seebeck coefficient (Eq. (2.1)). Further details about the data analysis are provided in Chapter 4.

2.4.4 Electrical offsets calibration

One important aspect of the aforementioned techniques is the offsets calibration. Thermopower characterization of molecular junctions involves very small thermovoltage values measured at zero-current conditions and this implies that the zero needs to be well-characterized, i.e. the electronic offsets of the setup need to be precisely known. Additionally, some of these offsets drift over time, so periodic offset calibration is required.

There are three electrical offsets to be considered when measuring with the STM-Imaging technique, shown in the electronic circuit diagram depicted in Figure 2.12:

- Bias voltage offset V_a. This offset is associated to the error of the DAC that applies the bias voltage. Its output has a small offset, V_a.

- Output current offset I_{off}. When there is no current in the input of the I-V amplifier, the output is not exactly zero, it is I_{off}. This is caused by the output offset voltage $V_{off} = -R_G I_{off}$, where R_G is the gain of the amplifier [Terrell1996].

- I-V amplifier input voltage offset V_e. This offset is created because the virtual ground of the current-to-voltage amplifier is not exactly zero. This translates into an effective voltage source at the positive entry of the op-amp whose contribution has to be subtracted to the current signal coming from the junction.

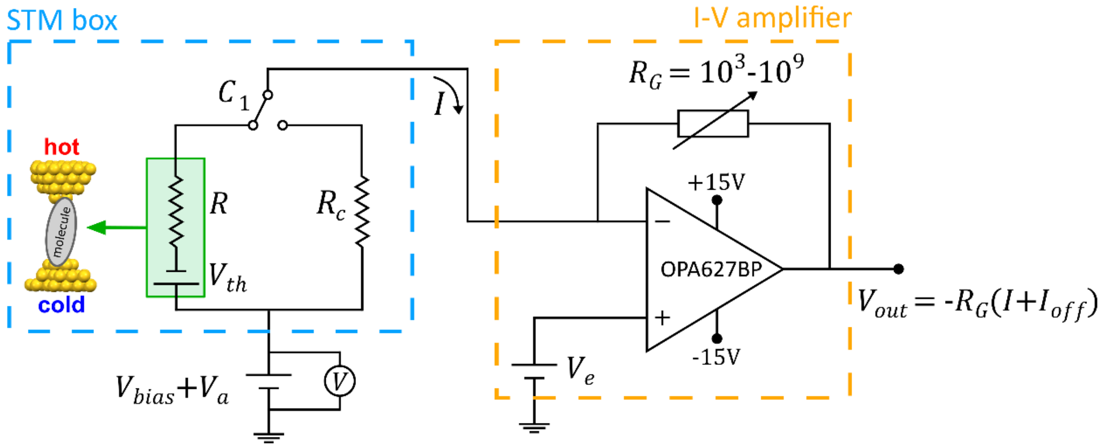

Figure 2.12: Electrical offsets in the STM circuit. With switch C_1 (inside the STM box, schematized within the blue dashed line) it is possible to switch the input of the current amplifier (within the brown dashed line) between the STM junction formed between the tip and the substrate and a known resistor R_c that acts as an equivalent junction. After Ref. [Evangeli2014].

Considering the equivalent electrical circuit schematized in Figure 2.12, we can write the following expression:

$$V_{bias} + V_a - V_{th} - V_e = \frac{I}{G}, \qquad \text{Eq. (2.8)}$$

where V_{th} is the thermovoltage of the STM junction, given by Eq. (2.3) ($V_{th} = (S - S_{lead})\Delta T$). G is the STM junction conductance ($G = 1/R$) and I is the current flowing through it. In open-circuit conditions ($I = 0$),

$$V_{th} = V_{bias} + V_a - V_e. \qquad \text{Eq. (2.9)}$$

This is the correction we apply to each thermovoltage value measured and the reason why electrical offset calibration is so important in thermopower measurements.

Depending on the particular offset, calibration is performed after each junction formation (as it is the case for V_a or I_{off}) or every few minutes (V_e, for instance).

V_a is directly measured with a Keithley 2000 voltmeter, also represented in Figure 2.12. At the end of each junction formation, the bias voltage is "set" to zero and the output of the DAC channel is automatically registered using the voltmeter, thus V_a is obtained. The value of this offset is typically around 5 ± 1 μV.

Complementary, I_{off} is also measured at the end of each junction, when the tip is retracted far away from the surface and hence the STM circuit is open ($I = 0$). The tip in this position allows to measure the current noise level I_{off}, that is, the output of the I-V amplifier when there is no input (V_{off}) divided by R_G [Terrel1996]. The value of this offset depends hence on the amplification gain.

Finally, V_e is a bit more complicated to determine because it is not directly accessible and needs some computation. To avoid the presence of the thermovoltage, magnitude that we want to find, we use a switch (C_1 in Figure 2.12) and change from the STM junction to an "equivalent" junction formed only by a known resistor R_c. In this equivalent junction circuit we can write:

$$V_{bias} + V_a - V_e = IR_c. \qquad \text{Eq. (2.10)}$$

Setting $V_{bias} = 0$ we get:

$$V_e = V_a - IR_c. \qquad \text{Eq. (2.11)}$$

To calculate V_e we need also to know I, the current flowing through the junction. The expression for the output at the I-V amplifier, what we actually measure, is given by:

$$V_{out} = -R_G\left(I + I_{off}\right) \qquad \text{Eq. (2.12)}$$

and hence the current flowing through the junction I can be written as:

$$I = -\frac{V_{out}}{R_G} - I_{off} = -\frac{V_{out} - V_{off}}{R_G}, \qquad \text{Eq. (2.13)}$$

where, let us remind, V_{off} is the voltage output of the I-V amplifier when there is no input signal. The offset V_e is then given by:

$$V_e = V_a + \frac{R_c}{R_G}\left(V_{out} - V_{off}\right). \qquad \text{Eq. (2.14)}$$

As we have introduced, V_{off} depends on the gain of the voltage amplifier and hence it is convenient that R_c is chosen similar to the actual resistance of the STM junction, in order to correctly calibrate the offset. “Thermovoltage” measurements and offsets calibration without temperature difference between the electrodes ($\Delta T = 0\ \mathrm{K}$) are also performed in order to ensure an adequate calibration.

Conductance measurements also require this offsets calibration. Considering again the equivalent electrical circuit of Figure 2.12, and replacing Eq. (2.13) into Eq. (2.8), the offset-corrected conductance of the junction $G = 1/R$ is thus given by:

$$G = \frac{I}{V_{bias} + V_a - V_{th} - V_e} = \frac{-\left(\dfrac{V_{out} - V_{off}}{R_G}\right)}{V_{bias} + V_a - V_{th} - V_e}. \qquad \text{Eq. (2.15)}$$

Finally, when measuring with the double-stage current-to-voltage amplifiers (with the STM-BJ technique), there are two output current offsets I_{off} to be considered, one for each amplifier output $V_{out,1}$ and $V_{out,2}$, but the equations presented in this section can be directly extrapolated and applied to each of the current signals generated by the double-stage amplifier.

References

[Agraït1993] N. Agraït, J. G. Rodrigo and S. Vieira. “Conductance steps and quantization in atomic-size contacts”. *Physical Review B* **47**, 12345-12348 (1993).

[Agraït2003] N. Agraït, A. Levy Yeyati and J. M. van Ruitenbeek. “Quantum properties of atomic-sized conductors”. *Physics Reports* **377**, 81-279 (2003).

[Binnig1982] G. Binnig, H. Rohrer, Ch. Gerber and E. Weibel. “Surface Studies by Scanning Tunneling Microscopy”. *Physical Review Letters* **49**(1), 57-61 (1982).

[Binnig1983] G. Binnig, H. Rohrer, Ch. Gerber and E. Weibel. “7x7 Reconstruction on Si(111) Resolved in Real Space”. *Physical Review Letters* **50**(2), 120-123 (1983).

[Cuevas2010] J. C. Cuevas and E. Scheer. “Molecular Electronics: An Introduction to Theory and Experiment”. World Scientific Publishers, Singapore (2010).

[Cusak1958] N. Cusak and P. Kendall. “The absolute scale of thermoelectric power at high temperature”. *Proceedings of the Physical Society* **72**(5), 898-901 (1958).

[Evangeli2013] C. Evangeli, K. Gillemot, E. Leary, M. T. González, G. Rubio-Bollinger, C. J. Lambert and N. Agraït. “Engineering the Thermopower of C_{60} Molecular Junctions”. *Nano Letters* **13**(5), 2141-2145 (2013).

[Evangeli2014] C. Evangeli. “Thermopower and Conductance of Single-Molecule Junctions and Atomic Contacts”. PhD Thesis (2014).

[Evangeli2015] C. Evangeli, M. Matt, L. Rincón-García, F. Pauly, P. Nielaba, G. Rubio-Bollinger, J. Carlos Cuevas and N. Agraït. “Quantum Thermopower of Metallic Atomic-Size Contacts at Room Temperature”. *Nano Letters* **15**(2), 1006-1011 (2015).

[González2006] M. T. González, S. Wu, R. Huber, S. J. van der Molen, C. Schönenberger and M. Calame. “Electrical Conductance of Molecular Junctions by a Robust Statistical Analysis”. *Nano Letters* **6**(10), 2238-2242 (2006).

[Joachim1995] C. Joachim and J. K. Gimzewski. “Analysis of Low-Voltage *I*(*V*) Characteristics of a Single C_{60} Molecule”. *Europhysics Letters* **30**(7), 409-414 (1995).

[Leary2015] E. Leary, A. La Rosa, M. T. González, G. Rubio-Bollinger, N. Agraït and N. Martín. “Incorporating single molecules into electrical circuits. The role of the chemical anchoring group”. *Chemical Society Reviews* **44**, 920-942 (2015).

[Pascual1993] J. I. Pascual, J. Méndez, J. Gómez-Herrero, A. M. Baró, N. García and Vu Thien Binh. “Quantum contact in gold nanostructures by scanning tunneling microscopy”. *Physical Review Letters* **71**, 1852-1855 (1993).

[Reddy2007] P. Reddy, S.-Y. Jang, R. A. Segalman and A. Majumdar. “Thermoelectricity in Molecular Junctions”. *Science* **315**, 1568-1571 (2007).

[Terrell1996] D. Terrell. “Op Amps: Design, Application, and Troubleshooting”. Elsevier Science (1996).

[Widawsky2012] J. R. Widawsky, P. Darancet, J. B. Neaton and L. Venkataraman. “Simultaneous Determination of Conductance and Thermopower of Single Molecule Junctions”. *Nano Letters* **12**(1), 354-358 (2012).

[Wiesendanger1994] R. Wiesendanger. “Scanning Probe Microscopy and Spectroscopy: Methods and Applications”. Cambridge University Press (1994).

[Xu2003] B. Xu and N. J. Tao. “Measurement of Single-Molecule Resistance by Repeated Formation of Molecular Junctions”. *Science* **301**(5637), 1221-1223 (2003).

3. Bi-thermoelectricity in endohedral metallofullerene (EMF) junctions

Fullerenes are molecules formed by carbon atoms typically arranged in fused-rings of five and six atoms until forming a closed cage (although some fullerenes can also show a partially open cage) [Kroto1991]. Its most common, naturally-occurring and famous member is the *pristine fullerene* or C_{60}, formed by sixty carbon atoms. This allotrope of carbon has proved to be a very appealing system to study conductance and thermoelectricity, as shown in Section 3.1 for its previous characterization in our group [Evangeli2013] and other groups [Yee2011; Lee2014; Kim2014]. Its stability in ambient conditions (and even at high pressures), its high conductance values in comparison to other organic molecules and its relatively high negative thermopower are promising features for applications in molecular electronics. However, intrinsic transport properties of pristine fullerene junctions may sometimes result too robust to offer versatility in the applications. For example, C_{60} junctions show a relative alignment of the HOMO-LUMO gap such that the closest resonance (the LUMO) is quite far away from the Fermi level E_F of common noble metal electrodes, which makes it difficult to improve the transport conditions. In this sense, a derivative of the pristine fullerene known as *endohedral metallofullerenes* becomes of great interest.

Endohedral metallofullerenes (EMFs) consist of a hollow fullerene cage with one or more metal atoms encapsulated inside and possess unique properties unexpected for empty fullerenes. They are commonly named indicating first the metal atom or molecule and then the fullerene, with the symbol '@' in the middle [Chai1991]. For example, the most abundant member of the family is $Sc_3N@C_{80}$ [Stevenson1999; Popov2012]. The main special feature of these molecules is the strong ionic bond between the metal atoms in the central cavity and the carbon cage, which largely affects the chemical and physical properties of the empty fullerenes [Akasaka2002].

Consequently, EMFs hold the promise to offer variability of transport properties with respect to its original predecessor, the pristine C_{60}. From a chemical point of view, the presence of the inner atoms incorporate new discrete energy levels (new electronic states) allowing, for instance, to modify the relative alignment of the molecular levels and even adding new features near the E_F (in the best scenario, new narrow transport resonances), depending on the inner cluster energy diagram. Regarding the transport performance of EMF junctions, and according to theoretical calculations [Finch2009; Bergfield2010], the presence of transport resonances close to the Fermi level has in fact the potential to improve both conductance and thermopower values in comparison to C_{60}.

In this Thesis, three endohedral metallofullerenes have been investigated: $Sc_3N@C_{80}$, $Sc_3C_2@C_{80}$ and $Er_3N@C_{80}$, all of them sharing the icosahedral fullerene cage I_h-C_{80}. In particular, we have studied the conductance G and thermopower S of Au|EMF|Au junctions using the home-built scanning tunnelling microscope (STM) and the STM-Imaging technique introduced in Chapter 2. $Er_3N@C_{80}$ was synthesized and the three molecules were purified by the group of Prof. Kyriakos Porfyrakis, in Oxford University (United Kingdom). As already mentioned, $Sc_3N@C_{80}$ is the most abundant EMF and, in addition, it is particularly stable at room temperature and above, quality that also applies to the rare-earth-based $Er_3N@C_{80}$ [Nörenberg2008]. In the case of the paramagnetic $Sc_3C_2@C_{80}$, it has been chosen as an excellent third-party to discern between the effect of the chemical nature of the metal atoms or the influence of the inner cluster symmetry on the transport properties of the junctions. Section 3.2.1 contains a more detailed motivation of the choice of these molecules.

To offer an appropriate background for our experiments, this chapter starts with a section about the pristine fullerene C_{60} and its thermoelectric properties reported by our group and others prior to this Thesis (Section 3.1). After this, the three aforementioned EMFs and the different experiments performed are presented, together with a discussion of the results obtained when experimentally investigating the transport properties of Au|single-EMF|Au junctions and a comparison with pristine C_{60} measurements (Section 3.2). This is followed by theoretical calculations for some of the systems investigated performed by the group of Prof. Colin J. Lambert, at Lancaster University (United Kingdom) (Section 3.3). We present then our experiments to study the transport properties of EMF dimers (i.e. two molecules connected in series between the electrodes) (Section 3.4) and, finally, we close the chapter with some general conclusions (Section 3.5).

3.1 Background: Pristine fullerene C_{60}

3.1.1 Introduction to C_{60}

The pristine fullerene C_{60} is a quite simple molecule in its shape and composition: sixty carbon atoms arranged in the vertices of twenty hexagons and twelve pentagons whose edges (the covalent bonds between atoms) form a truncated icosahedron that resembles a soccer ball (symmetry I_h-C_{60}) (see Figure 3.1(a,b)). As a curiosity, the pentagons of the structure are completely surrounded by hexagons and do not share an edge nor a vertex. Despite its structure, electron delocalization in the molecule is quite poor due to the tendency of the pentagonal rings to avoid having double bonds, so the fullerene has quite a high electronic affinity (2.6-2.8 eV) and is an excellent electron acceptor [Yang1987; Kroto1991].

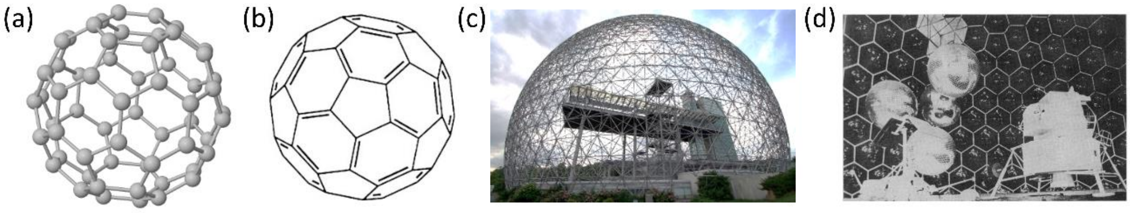

Figure 3.1: Buckminsterfullerene C_{60}. (a) Ball-and-stick representation of the chemical structure of the pristine fullerene C_{60}, formed by sixty carbon atoms organized in twenty hexagons and twelve pentagons. (b) Chemical structure of the pristine fullerene C_{60}. (c) Geodesic dome; image from Ref. http://www.spatialagency.net/database/buckminster.fuller. (d) "View inside the U.S. pavilion at Expo 67 in Montreal. One pentagon is evident and hexagons are distorted". From Ref. [Kroto1988].

Although the existence of such a molecule was already theoretically predicted in the late 1960s [Katz2006], it was not synthesized until 1984 when Eric Rohlfing, Donald Cox and Andrew Kaldor used a laser to vaporize carbon in a supersonic helium beam and formed several clusters that included C_{60} molecules, among others such as C_{70}, although they did not fully realized about the impact of their experiment at that moment [Rohlfing1984; Smalley1996]. A year later, in September 1985, Harold Kroto, James R. Heath, Sean O'Brien, Robert Curl and Richard Smalley repeated the experiment and recognized the most common structure in the mass spectrum as a C_{60} [Kroto1985]. This new molecule, the first one of the family to be discovered and the most abundant, was deduced to have a cage-like icosahedral structure and was named *buckminsterfullerene*, or informally *buckyball*, after Buckminster Fuller, an American architect. This was due to the C_{60} structural resemblance to the geodesic spheres popularized by Fuller in the 1940s and 1950s, although this can be misleading since in a geodesic sphere the hexagons are generally distorted and the domes are usually divided into triangles (see Figures 3.1(c,d)). Kroto, Curl and Smalley were awarded the 1996 Nobel Prize in Chemistry “for their discovery of fullerenes” [Smalley1996]. After their ‘accidental’ synthesis, these molecules were detected in nature, in soot for example [Kroto1988; Buseck1992], and in deep space [Kroto1988; Cami2010], making of C_{60} the most-common naturally occurring fullerene. Very recently, in April 2019, ionized C_{60} molecules in the interstellar medium between some stars have been detected using the Hubble Space Telescope [Cordiner2019].

The technique for the fullerene synthesis is quite straightforward and one of its strengths is the production of macroscopic quantities of the material per day (even several grams of C_{60} powder), allowing its commercial production. Thanks to this, research interest in buckminsterfullerene rapidly expanded. It has been extensively studied both for its chemical and physical properties as well as its potential technological applications and fields such as materials science, optics, electronics or nanotechnology have shown great interest on this molecule. Due to its electron-acceptor nature, C_{60} has become commonly used in donor-acceptor based solar cells [Katz2006]. In addition, its optical absorption properties adjust especially well to the solar spectrum, a property that makes of C_{60}-based films suitable candidates for photovoltaic applications [Katz2006]. Pristine fullerenes have also proved useful in biomedical applications such as in drug delivery or in the design of contrast agents for high-performance MRI or X-ray imaging, among others [Lalwani2013].

3.1.2 Thermoelectric measurements in C_{60} junctions

The first time a C_{60} molecule was connected with metallic electrodes using a scanning tunnelling microscope (STM) was in 1995 [Joachim1995a] and during the last twenty-four years, C_{60} transport properties have been extensively studied in different conditions. Current-voltage I-V characteristics of fullerenes adsorbed on diverse noble metal surfaces (Au, Ag, Cu) have been widely explored as well [Joachim1995b; Rogero2002; Lu2003; Néel2008; Schull2008], showing, for example, linear behaviour of the current at low voltages due to overlapping of the tails of the HOMO and LUMO resonances at the Fermi level despite being placed far away from E_F. Different characterization techniques confirmed a large HOMO-LUMO gap of the free molecule when compared to other fullerenes [Yang1987], and a HOMO-LUMO gap of around 1.5-2.5 eV when adsorbed on gold [Gimzewski1994] (equal to 2.3 eV on Au(111) surface [Rogero2002]). This is not a very wide gap in comparison to other organic systems such as alkane or phenyl molecules whose HOMO-LUMO gap is on the order of 5-10 eV [Yee2011]. Thus, C_{60} electronic structure facilitates, upon molecule connection, a fairly good alignment of the molecular orbitals with respect to the Fermi level of typical metallic electrodes, resulting in a relatively high conductance [Joachim1995a].

Thermoelectricity of fullerene junctions was not measured until 2011 when Yee *et al.* applied their recently developed technique to measure conductance G and thermopower S of single-molecule junctions [Reddy2007] to diverse fullerene molecules (C_{60}, C_{70} and PCBM) connected with different metallic tips (Au, Pt, Ag) (see Figure 3.2) [Yee2011]. The substrate, which was the electrode heated to establish the temperature difference required to measure thermopower, was in all cases Au. Regarding the pristine fullerene and Au contacts (the system of interest for this Thesis), they reported a thermopower $S = -14.5 \pm 1.2\,\mu\mathrm{V/K}$, the highest value measured to that moment and the confirmation of transport through the LUMO of the molecule, which behaves as an electron acceptor.

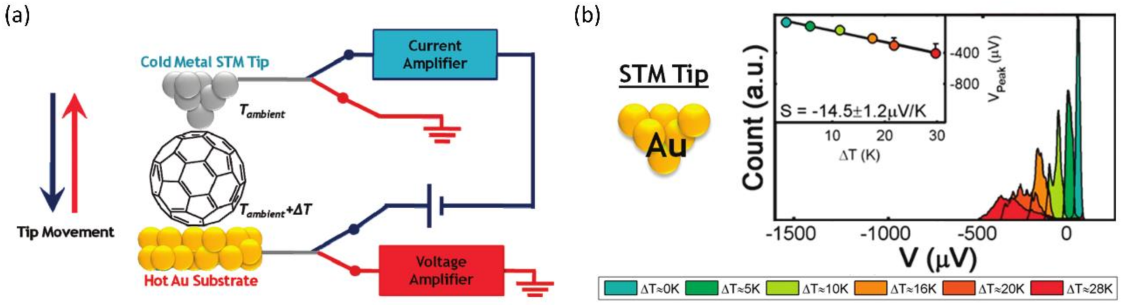

Figure 3.2: First thermopower measurements of Au|C$_{60}$|Au junctions. (a) Schematics of the experimental setup employed by Yee *et al*. A switches system allows to alternate between current (in blue) and voltage (in red) measurements, giving information about the conductance and thermopower of the molecular junctions. (b) Thermovoltage histograms for six temperature differences and linear regression (inset) to find the thermopower value S of C$_{60}$ molecules connected between gold electrodes. They reported $S = -14.5 \pm 1.2\,\mu\mathrm{V/K}$. Figures after Ref. [Yee2011].

Transport properties of Au|C$_{60}$|Au junctions were also investigated by our group. In Ref. [Evangeli2013] simultaneous conductance G and thermopower S measurements in ambient conditions and at room temperature were performed using for the first time the STM-Imaging technique (introduced in Section 2.4.2). Figure 3.3 shows that isolated molecules were deposited and localized on Au substrates offering the possibility to form single-fullerene junctions, with the number of molecules in the junction precisely determined, and explore a wide range of configurations via contact formation with many different molecules. Most probable conductance value at first contact was found to be $\bar{G} = 0.10 \pm 0.08\ G_0$. Note that this conductance is different to the one obtained when considering the whole G histogram instead of just the values measured right after electrical contact between the tip and the C$_{60}$.

In addition, the novel experimental technique based on small I-V ramps facilitated a more complete characterization of the junctions, achieved thanks to continuous and simultaneous G and S measurements while forming and breaking the junctions. In Figure 3.4 an individual example of these simultaneous measurements is shown, as well as the histogram built with all the values found. The reported most probable Seebeck coefficient was $\bar{S} = -18 \pm 7\,\mu\mathrm{V/K}$. In Ref. [Evangeli2013] the transport properties of C$_{60}$ dimers (two fullerenes connected in series) were also investigated. As expected, these junctions showed a smaller conductance ($\bar{G} = 0.0018 \pm 0.0022\ G_0$) but thermopower was considerably enhanced ($\bar{S} = -33 \pm 12\,\mu\mathrm{V/K}$) (see Figure 3.3(f,g) and Figure 3.4(d-f)).

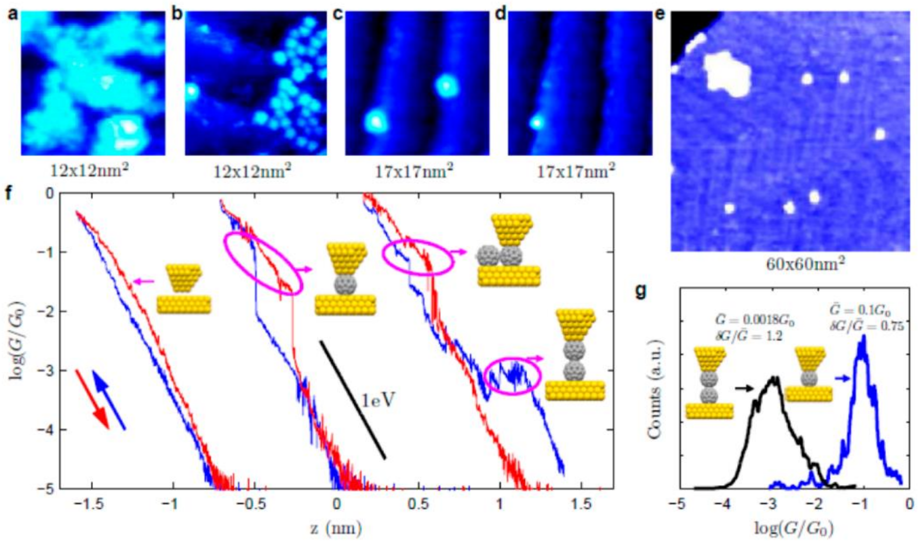

Figure 3.3: STM images of C$_{60}$ deposited on Au(111) and conductance G characterization of Au|C$_{60}$|Au and Au|C$_{60}$|C$_{60}$|Au junctions using the STM-Imaging technique. (a–e) STM images of C$_{60}$ molecules on Au(111). (f) Approach (blue) and retraction (red) G curves for a tunnelling gold-gold junction (leftmost traces); gold tip on an isolated C$_{60}$ molecule (central traces); and C$_{60}$ tip on an isolated C$_{60}$ molecule (rightmost traces). (g) Histograms of the conductance of a gold tip on an isolated C$_{60}$ molecule (blue curve) and of a C$_{60}$ tip on an isolated C$_{60}$ molecule (black curve) at the points where contact is established. From Ref. [Evangeli2013].

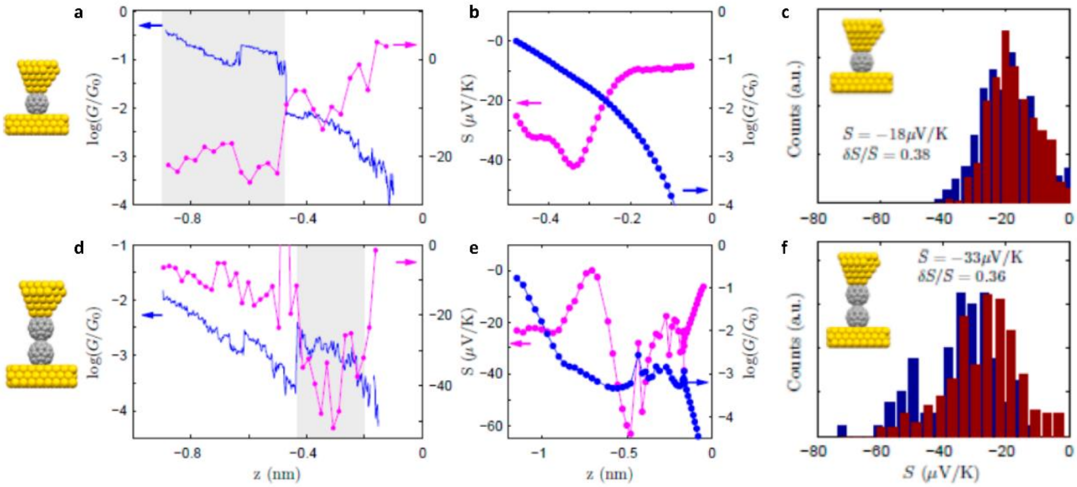

Figure 3.4: Simultaneous conductance G and thermopower S measurements of Au|C$_{60}$|Au and Au|C$_{60}$|C$_{60}$|Au junctions using the STM-Imaging technique. (a) "Conductance at $100\ \mathrm{mV}$ (blue) and thermopower (magenta), simultaneously acquired, for approach on a single C$_{60}$ molecule. In this measurement the temperature difference was $\Delta T = 25\ \mathrm{K}$. The shaded area indicates the range of z for which the Au|C$_{60}$|Au junction is already formed. (b) Theoretical G (blue) and S versus distance for a single C$_{60}$. (c) Histogram of experimental S values at contact for a single C$_{60}$ molecule, measured at $\Delta T = 12\ \mathrm{K}$ (blue) and $25\ \mathrm{K}$ (red). (d) Conductance at $100\ \mathrm{mV}$ (blue) and thermopower (magenta), simultaneously acquired, during the formation of the C$_{60}$ dimer. In this measurement, $\Delta T = 12\ \mathrm{K}$. The shaded area indicates the range in which the C$_{60}$ dimer is in the junction. (e) Theoretical G (blue) and S versus distance for the C$_{60}$ dimer. (f) Histogram of experimental S values at contact for a C$_{60}$ dimer, measured at $\Delta T = 12\ \mathrm{K}$ (blue) and $25\ \mathrm{K}$ (red)". From Ref. [Evangeli2013].

Further studies of thermoelectricity of the pristine fullerene include Ref. [Lee2014] and Ref. [Kim2014]. In the former, the effect of ferromagnetic electrodes (Ni) on the transport properties is explored with a STM, finding that in the case of C_{60} junctions they have little influence with no significant spin-splitting due to the spin-degeneracy of the LUMO. The latter, Ref. [Kim2014], reports G and S characterization while tuning the Fermi level position using a gate electrode in an electromigrated break junction setup with an integrated heater. Within a gate voltage range of $\pm 8\ \mathrm{V}$, a large thermopower tuning of around 300% was observed. Proof of on-resonance charge transport was also obtained from the shape of the S dependence on the gate voltage applied.

In summary, pristine molecule C_{60} has a relatively small HOMO-LUMO gap (1.5-$2.5\ \mathrm{eV}$) that facilitates chemical potential alignment close to a resonance. When connected with Au electrodes in ambient conditions and at room temperature, transport takes place predominantly through the broadened LUMO, placed near the Fermi level. In terms of conductance and thermopower, properties of interest of this Thesis, Au|C_{60}|Au junctions show quite a high conductance, on the order of $0.1\ G_0$, and a negative Seebeck coefficient of approximately $-20\ \mu\mathrm{V/K}$. Their conductance seems to be quite sensitive to molecular junction conformation details, but not so much the thermopower. C_{60} is thereby a robust thermoelectric material with a consistently-negative thermopower.

However, what happens if we add a small molecule or a cluster of atoms inside the fullerene cage? How do these new atoms affect the transmission of the electrons through the whole molecule? Let us present next the answers we obtain in the case of the endohedral metallofullerenes investigated.

3.2 G and S measurements in single-EMF junctions using the STM-Imaging technique

The STM-Imaging technique used to investigate the transport properties of endohedral metallofullerenes is essentially the same introduced in Ref. [Evangeli2013] for the study of C_{60} molecules and was developed in our group prior to this Thesis. Its most important characteristic is the use of STM images prior to junction formation in order to contact individual fullerenes adsorbed on the Au surface. Once a single molecule is targeted, both conductance and thermopower can be simultaneously measured in the presence of a temperature difference between tip and sample by means of small voltage ramps shot while forming and breaking the molecular junctions, as it has been introduced in Chapter 2 (Section 2.4.2). The STM-Imaging technique offers also the possibility to scan the area around the molecule investigated right after junction formation in order to monitor possible modifications of the molecule position.

In this section, we will briefly introduce some further information about EMFs, the particular molecules investigated and the sample preparation technique and we will then present the main results of the experiments we perform to explore the electric and thermoelectric properties of Au|single-EMF|Au junctions. This includes STM images, conductance *vs* tip displacement characteristics, simultaneous conductance and thermopower measurements, tunnelling spectroscopy and, in the case of $Sc_3N@C_{80}$ junctions, compression cycles.

Most of the study of Au|$Sc_3N@C_{80}$|Au junctions has been published in Ref. [Rincón-García2016].

3.2.1 Motivation: EMFs and introduction to the molecules investigated

Endohedral fullerenes or endofullerenes consist of a fullerene with an atom or molecule inside. Fullerenes are empty cages perfectly capable of housing, in principle, any atom or small molecule inside the cavity. In fact, in the original experiments of the pristine fullerene discovery, a La atom encapsulated in a C_{60} cage was already detected and named $C_{60}La$ [Heath1985]. Several carbon-carbon bonds would have to break in order to free the La atom, so the molecule is chemically stable. A bit later, in 1991, La@C_{82} was reported to be the first isolated endofullerene and the first stabilized member of a new sub-family: endohedral metallofullerenes [Chai1991].

Endohedral metallofullerenes (EMFs) are endofullerenes with metallic species trapped inside and represent a fascinating class of nanomaterials, whose optical [Ito2007], electrochemical [Dunsch2007] or magnetic [Chen2017] properties are determined by the type of metal atom(s) encapsulated in the fullerene shell. This is due to the generally strong ionic bond between the inner metal atom(s) and the fullerene, with charge transfer from the metal to the carbon cage. It is the reason why EMFs show completely different chemical and physical properties than the corresponding empty fullerenes and why EMFs have attracted particular interest [Akasaka2002]. Metallic clusters are typically divided in several groups: (i) mono-, di- and trimetals; (ii) metal nitrides; (iii) metal carbides; (iv) metal oxides and (v) metal sulfides, where metals can be alkaline metals, group 3 elements and rare-earth metals (mainly Sc, Y and La, but also Ti and most lanthanides such as Ce, Nd, Gd, Tb, Dy, Ho, Er, Tm, Yb, Lu) [RodríguezFortea2011a].

These molecules are usually synthesized in an arc reactor using metal-doped graphite, in contrast to endofullerenes with non-metal atoms, which are generally formed introducing the cluster into a previously existing carbon cage. Synthesis of EMFs using the classic Krätschmer-Huffman electric-arc generator [Krätschmer1990] produces typically low yields ($< 0.5\%$) and samples with multiple isomers, which makes it difficult to study their properties.

A major step in the consolidation of EMFs as systems of research interest was taken in 1999, when Stevenson and co-workers developed a process to synthesize, isolate and purify some EMFs in macroscopic quantities, in particular, those encapsulating trimetallic nitride clusters (M_3N@C_{2n} or $M'M_2N$@C_{2n} with mixed metals). The method was named 'trimetallic nitride template' process and nowadays EMFs formed using this technique are commonly referred to as TNT molecules. The most abundant TNT (and the third most abundant fullerene after I_h-C_{60} and D_{5h}-C_{70}) is Sc_3N@C_{80}, one of the molecules investigated in this Thesis [Akasaka2002; Popov2012]. It is known to have a relatively high electron affinity [Campanera2002] and a relatively small energy band-gap (estimated to be of only $0.8\,\mathrm{eV}$ [Stevenson1999]) and it is particularly stable at room temperature and above [Nörenberg2008]. Complementary, I_h-C_{80} is the fullerene shell where the largest diversity of clusters are trapped.

With respect to the EMFs family, the large variety of interesting and unique properties shown results especially appealing. Indeed, their combined fullerene and metallic properties have made of them a new class of technologically relevant materials, especially promising for applications in optoelectronic devices [Guha2005]. For example, erbium containing EMFs possess a characteristic $1520\,\mathrm{nm}$ emission associated with the Er ion [Macfarlane2001], which is of fundamental importance for telecommunication applications. Er_3N@C_{80} in particular is magneto-optically active in the near-infrared range and it has potential applications as a readout pathway in quantum information processing [Nörenberg2008]. There is also a broad spectrum of scandium containing metallofullerenes, including the paramagnetic $Sc@C_{82}$ and $Sc_3C_2@C_{80}$ [Popov2012], which can find promising applications as spin probes and quantum information processing components. The latter, $Sc_3C_2@C_{80}$, exhibits a unique diamond shaped EPR with respect to the three equivalent Sc atoms [Roukala2017].

Considering all these aspects, we have selected three EMFs to investigate in this Thesis: $Sc_3N@C_{80}$, $Sc_3C_2@C_{80}$ and $Er_3N@C_{80}$. Their chemical structures are shown in Figure 3.5 and in this manuscript, we will called them EMF-1, EMF-2 and EMF-3, respectively. All of them have I_h-C_{80} fullerene cages to facilitate its direct comparison and comparison with control measurements performed with the I_h-C_{60} molecule, which shares the same symmetry. Another common point between these EMFs is the symmetry of the inner clusters, which are in all cases planar units [Nörenberg2008]. For EMF-2 an isomer with a pyramidal structure of the inner atoms is also possible [RodríguezFortea2011b], but it is not the case in our system.

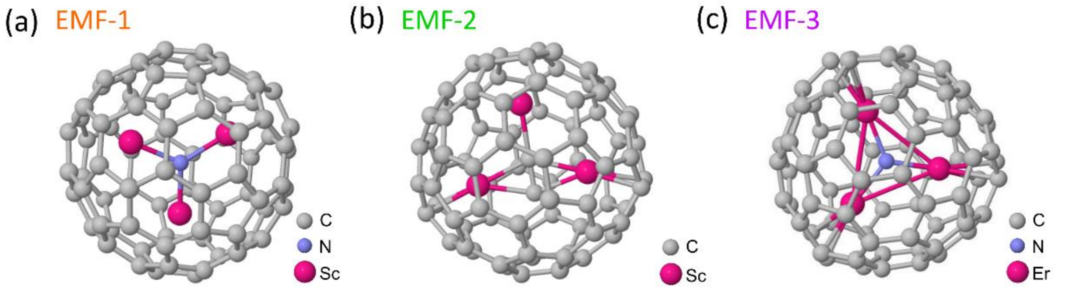

Figure 3.5: Endohedral metallofullerenes (EMF) studied. (a) Schematic of the EMF-1 ($Sc_3N@C_{80}$); note the Sc_3N inner moiety in the fullerene cage. (b) Schematic of the EMF-2 ($Sc_3C_2@C_{80}$); note the Sc_3C_2 cluster inside the C_{80} cage. (c) Schematic of the EMF-3 ($Er_3N@C_{80}$); note the Er_3N internal moiety in the centre of the fullerene cage.

There are further points of similarity and contrast between the molecules chosen:

(i) Regarding the metallic atoms and valence band electrons, EMF-1 and EMF-2 have both three Sc atoms in the inner moiety (with *d*-electrons in the valence band), while EMF-3 is a rare-earth based fullerene whose Er atoms have *f*-electrons in its valence band.

(ii) Regarding the non-metallic atoms and inner cluster dynamics, EMF-1 and EMF-3 are both TNT molecules with a N in the centre of the encapsulated cluster, while EMF-2 is a trimetallic carbide EMF with two C atoms. This greatly affects the mobility of the inner moieties. In general, M_3N clusters present free rotation inside the fullerene cavity, without any preferential orientation according to DFT calculations, although the lowest energy configurations (by a small difference) are those where the metal ions are oriented towards the [6:5] ring junctions [Campanera2002]. The dynamic rotation is expected to be slightly reduced for larger inner molecules, so Er being larger than Sc, Er_3N cluster is expected to have larger difficulties to freely rotate inside the fullerene. In the case of the carbide EMF, Sc_3C_2 moiety exhibits fast rotational motion between orientations along the equatorial six-membered ring belt of the C_{80} buckyball [Jin2014]. This free rotation is in fact what produces the symmetrical EPR spectrum.

In contrast to these previous connections, EMF-2 and EMF-3 have in principle nothing in common besides the fullerene cage. It is important to remark that the I_h-C_{80} cage is in all cases stabilized upon charge transfer from the inner moieties to the external carbon atoms, since the shell is not stable in its empty form. Curiously, trimetallic nitride clusters are neither stable by themselves as single molecules. Considering an ionic model of interaction between the moities and the cage, we can describe the TNT molecules as $(M_3N)^{6+}@(C_{80})^{6-}$ and the EMF-2 valence state as $(Sc^{3+})_3(C_2)^{3-}@(C_{80})^{6-} = (Sc_3C_2)^{6+}@(C_{80})^{6-}$ (an unpaired electron remains in the metallic moiety, conferring the paramagnetic nature to the molecule) [Langa2011]. Thus, stabilization of the I_h-C_{80} cages, and hence of these EMF molecules, is due to an equivalent charge transfer of six electrons from the inner atomic clusters, enough to avoid the carbon shell disintegration.

Finally, deposition and adsorption of some of these EMFs onto metallic surfaces have been previously reported. Leigh and co-workers investigated self-assembly of $Sc_3N@C_{80}$ and $Er_3N@C_{80}$ (that is, EMF-1 and EMF-3) on different surfaces (Ag/Si(111), Au(111)/mica, Si(111) and Si(001)) using a variable temperature STM [Leigh2007]. Regarding the deposition of EMF-3 on Au(111) surfaces, bonding with the substrate was proposed to be mainly van-der-Waals and, more interestingly, bias dependent contrast changes were observed in some fullerenes and were initially suggested to be due to surface defects in the underlying Au substrate, responsible for a Fermi level shift. Further investigation of these bias-dependent contrast anomalies concluded that they were possibly caused by different electron density of states on the molecules depending on the molecule orientation and the associated charge transfer from the substrate [Nörenberg2008].

3.2.2 Sample preparation

Samples prepared consist of the endohedral metallofullerene of interest deposited on a polycrystalline gold surface.

The 250-nm-thick Au films on glass substrates ($11 \times 11\ \mathrm{mm}^2$, Arrandee, Germany) are flame annealed with a butane gas torch prior to the molecule deposition in order to have clean gold reorganized in a polycrystalline (111) surface. The surface of the Au samples is estimated to reach a temperature above $900\ \mathrm{K}$ (emission in the visible range, in a bright orange colour) for less than one minute, enough for the top layers of material to locally melt and reorganize in a crystalline order. The sample is afterwards allowed to cool down to room temperature in ambient conditions. STM characterization of the Au samples shows that the whole surface is not homogeneously crystalline (i.e. it is not a monocrystal) but large Au(111) atomically flat areas, generally separated by monoatomic steps, can be easily found (see next Section 3.2.3). Occasionally the Au(111)-22x√3 reconstruction (the so-called 'herringbone' reconstruction) can be also observed.

Endohedral fullerenes are afterwards deposited using the drop-casting technique. EMFs are initially in solid state forming a dark powder and, since we aim to address the transport properties of individual molecules, they need to be diluted in order to be deposited with low coverages of the Au surface. Proceeding in several steps, we begin with an initial EMF solution in 1,2,4-trichlorobenzene (TCB) ($> 99\%$, Sigma-Aldrich) of around $10^{-3}\ \mathrm{M}$ and, adding adequate quantities of solvent, get a very dilute EMF solution (10^{-7}-$10^{-8}\ \mathrm{M}$). This is kept as much as possible in darkness in order to avoid damaging of the molecules. To deposit them, a drop of the low concentration solution is placed on the pre-annealed Au surface for about three minutes and it is then blown off with streaming nitrogen and allowed to dry overnight in ambient conditions, in a recipient closed with Parafilm and covered with Al-foil to avoid interaction with light.

Before starting the experiments and after mounting the sample on the STM, it is allowed to stabilize for another hour in order to reach thermal equilibrium with the setup and minimize the thermal drift. Since the sample is then kept continuously inside the STM in ambient conditions, they get usually deteriorated after a week of measurements, approximately, moment when a new sample needs to be prepared. Complementary, we use mechanically cut Au tips as STM probes (Goodfellow, 0.25-nm-diameter, 99.99% purity). The gold wire is gently soldered on the tip support and afterwards cut with a shear movement in order to favour the presence of a single Au atom in the apex of the tip.

3.2.3 Surface and molecule imaging

STM images of the Au surface and the EMFs adsorbed on it are acquired at room temperature (RT) and in constant-current mode with the bias voltage V_{bias} applied to the sample. As introduced in Chapter 2, the current is measured using the commercial current-to-voltage amplifier Keithley 428 with a gain of $10^8\ \mathrm{V/A}$ in this case (see electrical circuit in Figure 2.4 or 2.5). For EMF STM imaging we typically use a V_{bias} of several hundreds of mV (between 300 and $500\ \mathrm{mV}$ in most of the cases, but also up to $800\ \mathrm{mV}$ sometimes) and set a tunnelling current of around $1\ \mathrm{nA}$ (typically between 0.5 and $1.2\ \mathrm{nA}$) to control the vertical piezo position and scan the surface.

Figure 3.6 show representative examples of STM images of the three EMFs deposited on Au(111). The fact that we are able to image these EMFs on the gold surface tells us already that, despite their thickness, conductance through their molecular orbitals is not negligible with respect to the metallic electrodes direct tunnelling.

Scan areas presented in Figure 3.6 vary from more than $100 \times 100\ \mathrm{nm}^2$ to less than $10 \times 10\ \mathrm{nm}^2$. Thanks to the low EMF concentration of the TCB solutions prepared, we easily localize areas on the Au surface where isolated EMFs have adsorbed, preferentially at monoatomic steps (Figures 3.6(a,b,d-i)) but also on flat terraces (Figures 3.6(a-c,g)). Preferred bonding at step edges is to be expected since the Au atoms in these positions have more dangling bonds that the rest, favouring the adsorption of the electron acceptor molecules. In fact, covalent bonding of the EMFs is taking place, which implies hybridization of molecular orbitals and extended electronic states of the metal surface (as discussed in Chapter 1) and a net charge transfer from the electron-rich substrate towards the molecule is occurring. This bonding is stronger than the attachment produced by van der Waals interactions and is enhanced at more reactive sites such as step edges. Thus, most of the EMFs contacted in our experiments are sitting at these positions.

No clear difference between the three EMFs is observed in the STM images, which might not be surprising since the fullerene cage (I_h-C_{80}), which constitutes the external electronic states of the molecules, is the same in all cases.

Van der Waals diameter of I_h-C_{80} cage is expected to be around $1.1\ \mathrm{nm}$, but EMFs in our STM images typically present an apparent height of 0.5-$0.8\ \pm\ 0.1\ \mathrm{nm}$ and lateral dimensions larger than $2\ \mathrm{nm}$. This enlarged lateral dimensions are possibly due to several factors: electronic modifications of the molecule upon adsorption (substrate-molecule interactions), overlap of wave functions in the vicinity of the tip apex or tunnelling contributions from the inhomogeneous background that enlarge the molecule size, among others [Chen1992]. Concerning the low apparent height of the adsorbed molecules, as if they were “embedded” in the Au surface, it is typically caused by the wave functions of the delocalized metallic electrons extending further into the tunnelling gap region than those of the EMFs [Chen1992].

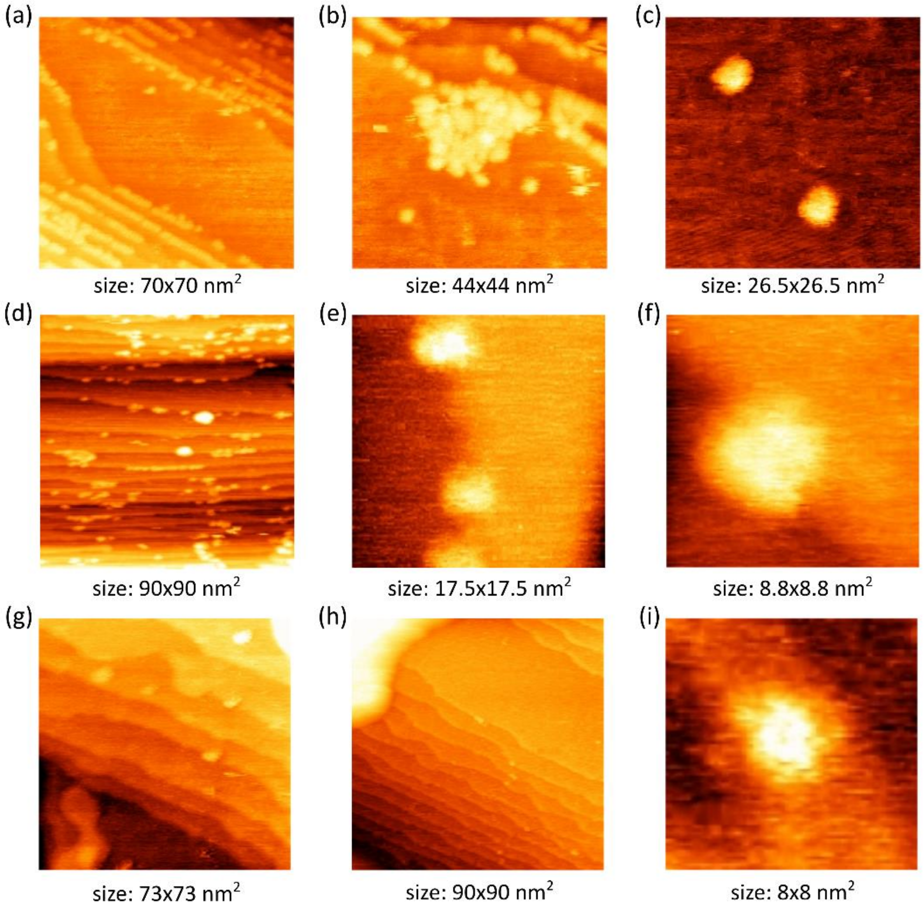

Figure 3.6: Scanning tunnelling microscope images. (a-c) STM images of EMF-1 molecules on atomically flat Au(111) surfaces showing preferential adsorption at step edges (a), islands (b) and isolated molecules (c). (d-f) STM images of EMF-2 molecules on atomically flat Au(111) surfaces showing preferential attachment at step edges (d-f) and islands (d). (g-i) STM images of EMF-3 molecules on atomically flat Au(111) surfaces showing preferential adsorption on terraces (g) and at step edges (g-i). Images have been treated with the Gwyddion software [Nečas2012]. No thermal drift or piezo creep corrections have been applied to these images.

In general, we do not observe internal molecular structure, probably because of blurring of the atomic detail by thermal averaging. Exceptionally, when the thermal drift is greatly reduced compared to usual conditions, some internal structure suggestive of the fullerene orbitals has been observed (see Figure 3.6(f,i)). Due to this lack of intramolecular resolution, when contacting the molecules we cannot distinguish molecular orientations, which strongly influence transport properties of single-EMF junctions as it will be exposed a bit later. UHV experiments performed by other groups at low temperatures have indeed shown intramolecular details when the rotation of the molecules is frozen [Nörenberg2008].

As already observed for C_{60} [Evangeli2013], the imaging capability is possible not only thanks to the relatively high conductance of these carbon-based molecules, but also because of the experiments being performed under ambient conditions, a situation in which an ambient layer is known to be present on top on the Au surface, mainly formed of water and nitrogen. C_{60} and also EMFs have been reported to diffuse in UHV experiments on the Au(111) surface without adsorbing on it [Fujita1996; Rogero2002]. Hence, the passive action of the ambient water layer results a great advantage and allows the controlled single-molecule junction formation.

With respect to the mobility of molecules, those which are adsorbed on terraces are usually more easily displaced by the tip than those bonded to step edges, which are generally more stable under scanning and contact formation, as can be seen in Figures 3.6(b,g). Diffusion of molecules, mainly induced by interactions with the tip while scanning, reflects in sudden, short and discontinuous jumps in the contrast of the STM images. Typically, a higher setpoint of the tunnelling current or a smaller bias voltage favour this mobility of EMF molecules, as well as higher temperatures (thermal-induced motion), larger concentrations of molecules or adsorption of the molecules on flat terraces as mentioned.

Additionally, molecules are found to occasionally form small islands or clusters nucleating from a step edge into a terrace (see Figure 3.6(b,d)). EMFs are usually not very stable in these aggregates, especially on the edges of the cluster where molecules move easily when scanning. Interaction between molecules in an island is expected to be through van der Waals' forces.

In conclusion, RT-STM imaging of EMFs deposited on polycrystalline Au substrates shows stable adsorption of the three EMF molecules with submonolayer coverages. Despite not being able to obtain intramolecular resolution, molecules seem to do not suffer any bonding-induced structural damage, they are generally well anchored to the metallic surface although certain tip-induced mobility is sometimes observed and they show a clear preference to attach to monoatomic step edges.

Besides the aforementioned characterization based on the STM images, our final goal is to connect an individual EMF molecule between the Au electrodes. To this extent, STM images result a powerful tool because they allow us to find a single molecule and track it and, additionally, scan the area around the molecule right before and after junction formation. Initially, large areas of the Au sample with a lot of points (namely, 256×256 or 512×512) are "slowly" scanned ($0.5\text{-}1\ \mathrm{lines/sec}$) in order to localize flat terraces or monoatomic steps with adsorbed molecules (Figure 3.7(a)). A desired zone is then selected and we "zoom in" progressively, imaging intermediate-size areas in the process to ascertain the tip's lateral position (see Figure 3.7(b-e)). Smaller scale images with less points are gradually reached in order to focus on a single EMF and the area is reduced down to a scale at which the molecule occupies most of the image. These small areas are usually scanned at a much higher speed, approximately at $2.5\ \mathrm{lines/sec}$ or even $10\text{-}20\ \mathrm{lines/sec}$, in order to track the fullerene on the surface (Figure 3.7(e)). Repeatedly imaging above a certain EMF we counteract the effect of thermal drift and piezoelectric creep. The tip positioning precision is increased until we are finally able to place it directly above the molecule and connect it, forming a single-molecule junction (Figure 3.7(f)) (more details about junction formation will be given below, in Section 3.2.4).

This scanning zooming process, although essential to image the targeted molecule right before and after contact formation (Figure 3.7(e,g)), can sometimes result quite challenging, depending on the thermal drift (typically $0.01\text{-}0.1\ \mathrm{nm/min}$) [Evangeli2014] and the piezoelectric creep following lateral translations of the tip. Due to these effects, the relative (x,y) position of the tip over the surface is constantly varying, when the tip is just "stationary" over the surface and also while taking a STM image. In this case, without modifying the (x,y) piezoelements, the sample might appear displaced in a second image. In order to focus on a single EMF, we need hence to actively track the molecule relative movement.

Occasionally another problem may appear when a molecule is transferred to the tip while scanning or during a junction formation. However, this transfer modifies the images resolution and thus, STM imaging proves also useful in these cases and serves to monitor to some extent the cleanliness of the tip. We discuss further about this in Section 3.4.

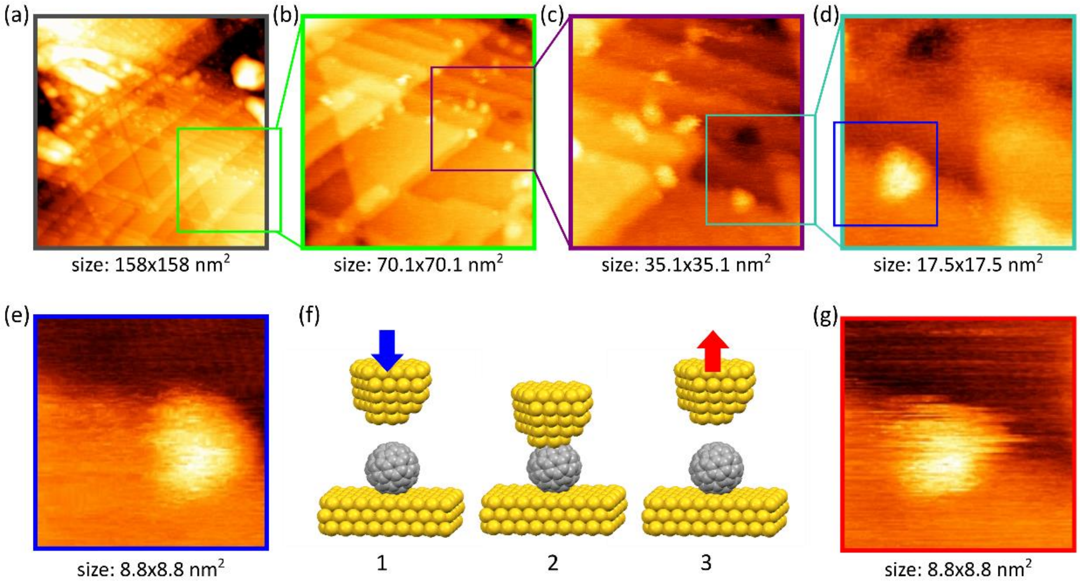

Figure 3.7: Scanning zooming process. (a-e) Scanning zoom to localize and focus on a single EMF (an EMF-1) on the Au surface. We start with large area images, where molecules on flat terraces and at step edges can be identified, and progressively reduce the scan size until centring an individual molecule of our choice. (f) Schematic representation of junction formation once a single molecule is targeted and the tip is positioned over it. It consists of three steps: 1) the feedback loop is opened and the tip is approached toward the molecule; 2) the junction is formed and the EMF becomes electrically connected between the electrodes, and 3) the tip is retracted back to tunnelling and the feedback loop is again activated. Section 3.2.4 contains further details. (g) STM image after junction formation which allows to confirm that the molecule is still in place, although in this case it seems to be slightly more mobile or the tip more unstable than prior to the contact since there are more jumps in the scanning signal. Images in this figure have been treated using the Gwyddion software [Nečas2012].

3.2.4 Conductance G *vs* tip displacement Δz measurements

Once a suitable single-molecule is targeted, as already introduced in previous Section 3.2.3, and in order to measure its conductance G, we carefully position the tip directly above the centre of the molecule and proceed to contact it as depicted in Figure 3.7(f). First, we open the feedback loop and move the tip forward toward the molecule (approaching it) at a given bias voltage V_{bias} while simultaneously recording the current I. In this way, we are able to characterize the evolution of the junction conductance while it is being formed and, when lastly brought into contact, electrically connect a single EMF between two Au electrodes (step 2 in Figure 3.7(f)). Finally, after junction formation, the tip is retracted back into the tunnel gap, completing what we call a “conductance trace” or “approach-retraction cycle”. The conductance $G = I/V_{bias}$ *vs* tip displacement Δz is monitored during the whole movement of the tip.

In these experiments, V_{bias} is reduced to just $10\ \mathrm{mV}$ and the current-to-voltage gain is switched to $10^7\ \mathrm{V/A}$ to avoid saturation of the ADC input before one Au atom contact is reached (that is, $G_0 \sim 77.5\ \mu\mathrm{S} \sim 1/12.9\ \mathrm{k\Omega}$, i.e. $I \sim 775\ \mathrm{nA}$, where $G_0 = 2e^2/h$ is the quantum of conductance, e is the electron's charge and h is Planck's constant). We control the maximum vertical movement of the tip by predefining a top threshold of conductance, i.e. an upper limit of current. When the feedback loop is open and the approach-retraction cycle begins, the tip is approached towards the molecule in steps of approximately $0.01\ \mathrm{nm}$ ($10\ \mathrm{pm}$). To avoid metallic contact between the electrodes, the motion of the tip is reversed when the conductance reaches the top threshold, $G_{top} < G_0$. G_{top} is generally chosen to be above the conductance value of the molecule, once this is known, in order to be sure to form the contact in each tip indentation. Once the top threshold is reached, the tip is retracted until a bottom threshold of conductance is registered and the approach-retraction cycle is complete.

Figure 3.8 shows examples of conductance traces (approach-retraction cycles) of the three molecules investigated, where approach of the tip is plotted in blue and retraction, in red. Leftmost curves in the figure correspond to Au-Au tunnelling junction plotted for comparison (Au tip approaching bare Au surface). Conductance traces behave similarly for the three EMFs and share characteristics with Au|C_{60}|Au junctions previously reported [Evangeli2013]. Initially, when the approach begins, the tip is far away from the surface and the conductance value is below the instrumental noise level, that is, around $10^{-4}\ G_0$ at $V_{bias} = 10\ \mathrm{mV}$ and the aforementioned gain. Then, conductance starts increasing exponentially (linearly in the semilogarithmic plots) [González2006] from $10^{-4}\ G_0$ to $10^{-3}\ G_0$, revealing electron tunnelling from the tip to the sample without noticing the presence of the EMF [Néel2007]. This is shown by a similar apparent energy barrier of about $1\ \mathrm{eV}$, extracted from the slope of the curves, as in the case of Au-Au junctions (Figure 3.8a). These junctions show featureless conductance traces with a linear dependence of $G(\Delta z)$ when represented in a semilogarithmic scale, which reflects tip motion in tunnelling regime. The apparent energy barrier found is approximately five times smaller than the Au work function ($\varphi_{\mathrm{Au}} = 5.1\ \mathrm{eV}$) in UHV conditions [Ohno1991]. This reduction is typically observed when measuring in ambient conditions and it is mainly caused by the ambient water layer reported to be present on both electrodes [Hahn1998; Evangeli2013].

Traces become usually more unstable between $10^{-3}\ G_0$ and $10^{-2}\ G_0$ and a change in the slope of the conductance (a gentle bump) can be observed in most of the curves recorded (see, for example, the approach of traces c or f in Figure 3.8). This feature has been reported to be a signature of the already mentioned adsorbate layer, trapped between the molecule and the approaching tip right before it slips away and the tip finally connects the molecule.

The electrical contact point is usually reached at 10^{-1}-$10^{-1.5}\ G_0 = 0.01$-$0.03\ G_0$, depending on the EMF as it will be shown below. It typically takes place after a sudden and sharp rise of G, i.e. a jump-to-contact of around half an order of magnitude that can be appreciated, for example, in traces b, c, d or f in Figure 3.8. This rapid increase is never observed in the case of Au-Au tunnelling junctions and is a clear evidence of molecular junction formation. At this point, a chemical bond is established between the fullerene orbitals and the tip metal states without deformation of neither the EMF nor the tip [Joachim1995a].

In the contact regime, further approaching of the tip towards the substrate results in the EMF being pressed by the tip and conductance keeps increasing with a strong reduction in the slope. In this situation, both tip and molecule undergo compression and may be eventually deformed, especially the tip apex, structurally softer than the rigid fullerene cages. Elastic deformations followed by nanoscale rearrangements of the Au atoms may take place and have been reported to be the reason behind more sudden jumps (normally smaller than the rapid rise of contact formation) sometimes observed in the conductance signal in the contact regime [Agraït1995; Agraït1996; Rubio1996]. Another possible reason for these jumps in conductance after junction formation is local rotation of the molecule being compressed by the tip.

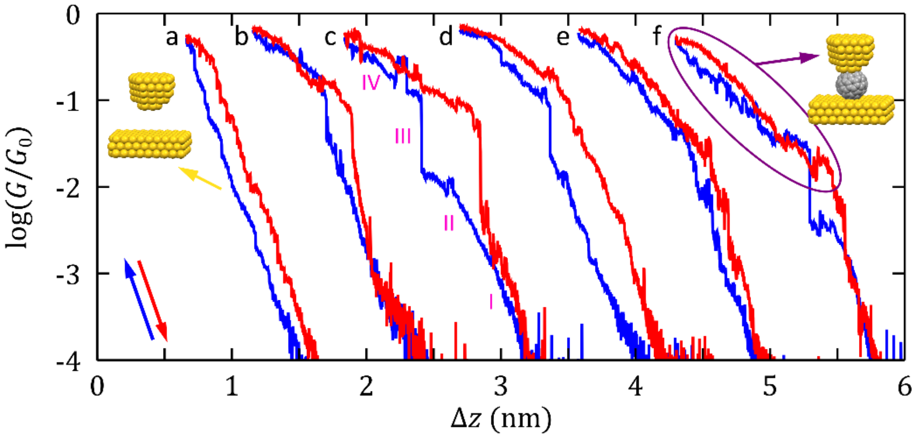

Figure 3.8: Conductance G *vs* tip displacement Δz of single-EMF molecular junctions. Examples of approach-retraction conductance traces (in blue and red, respectively) for a Au-Au tunnelling junction as the one depicted on the left (pair of traces a) and five EMF junctions: pairs b-c correspond to EMF-1 junctions; d, to EMF-2, and e-f, to EMF-3. The different features identifiable during the tip approach have been marked in the blue curve of c: tunnelling regime (I); mechanical contact and water layers repulsion (II); jump-to-contact and electrical contact point (III), and contact regime (IV). This regime, schematized by the junction on the right, is also highlighted with the purple curve for the traces f. Δz of the different pairs of traces has been displaced for the sake of clarity. $G_0 = 2e^2/h$ is the conductance quantum (e is the electron's charge and h is Planck's constant).

Retraction traces (red curves in Figure 3.8) show generally similar features as described for the approaches, although some hysteresis is typically observed and they are usually slightly shifted in Δz, possibly due to elastic deformations of the Au tip apex or the Au atoms below the molecule. The tip is typically retracted back into the noise level.

After each approach-retraction cycle, a small area of the surface is rescanned to confirm that the fullerene is still in the same position and hence, that the single-EMF junction has correctly formed (see Figure 3.7(g)). This inspection allows us also to confirm that the molecule has not transferred to the tip, as it sometimes happens. If the molecule transfers to the tip, it disappears from the next image and, at the same time, resolution of the tip improves because of tunnelling of electrons between the surface and the fullerene instead of directly with the tip [Schull2009; Nishino2005; Repp2005] (as we have introduced in Chapter 2, the tunnelling current depends on the density of states of both electrodes; a fullerene acting as the apex of the tip gives a different resolution than a gold atom). When this transfer takes place, the molecule usually drops by itself from the tip while scanning the next image or after a new approach-retraction cycle into the gold surface, but it is sometimes required to consciously clean the tip in a section apart, by deep indentation of the tip into the gold, in order to be able to form again single-molecule junctions in a controlled way. On the other hand, the presence of a fullerene on the tip can also be advantageous, as we consider in Section 3.4.

Regarding the reproducibility of the approach-retraction cycles, the exact configuration of the molecular junction highly influences its details which depend, for example, on molecular orientation or contact geometry. In order to explore a wide variety of junction configurations, we measure several conductance traces for each EMF and plot G *vs* Δz 2D histograms of the approach curves, which are shown in Figure 3.9(a-c)). The 2D histogram built with 50 approaching curves of bare Au-Au tunnelling junctions is also included for comparison (see Figure 3.9(d)). To build these histograms, the individual traces are aligned using a conductance value $G_{align} \sim 10^{-3.5} G_0$ that is initially placed in $\Delta z = 0\,\mathrm{nm}$. To avoid creating a false discontinuity in the 2D histogram, the slope around this G_{align} is obtained and the individual curves are finally aligned using this tunnel slope as a reference. Features introduced with the individual examples of approach-retraction cycles in Figure 3.8 are also identifiable in the 2D histograms, showing good reproducibility of these measurements. Nevertheless, some spread is observed possibly due to the variety of configurations sampled or thermally induced fluctuations affecting the charge transport through the junctions [Yee2011]. In fact, EMF-1 histogram, the one with more curves and, thus, more configurations explored, shows a slightly larger dispersion than the other histograms.

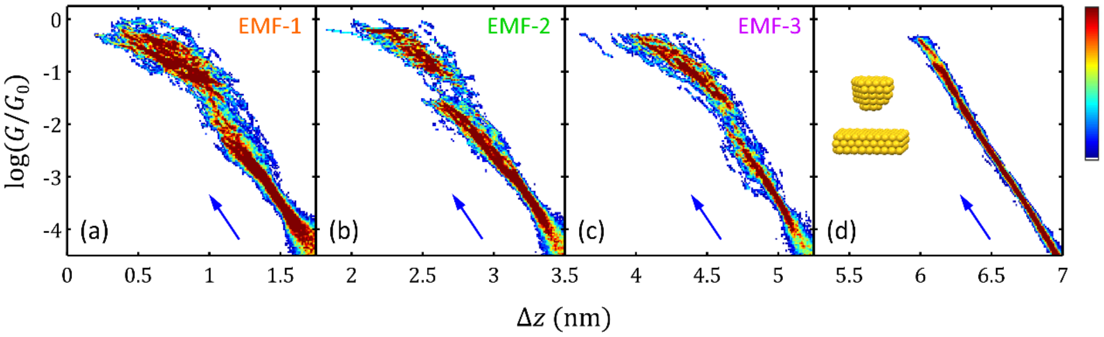

Figure 3.9: Conductance G *vs* tip displacement Δz 2D histograms of Au|EMF|Au and Au-Au junctions. (a-d) G *vs* Δz 2D histograms of 60 approach curves on single $Sc_3N@C_{80}$ (EMF-1) molecules (a), 46 approach traces on isolated $Sc_3C_2@C_{80}$ (EMF-2) molecules (b), 36 approach curves on individual $Er_3N@C_{80}$ (EMF-3) molecules (c) and 50 approach traces on bare Au (d). Complete traces, from tunnelling to tip-compression of the molecules, are shown. The colour scale accounts for the number of points in each histogram.

For direct comparison between the EMFs, conductance 1D histograms for the whole approach traces of each molecule, corresponding to the 2D histograms in Figure 3.9(a-c), are presented in Figure 3.10(a)). They evidence the different regimes already introduced. A peak corresponding to the noise level can be observed below $10^{-4}\,G_0$. Between $10^{-3}\,G_0$ and $10^{-2}\,G_0$, a broad peak is created by the elastic deformation of the adsorbate layer trapped in the forming junction. Finally, due to the compression of the EMFs in the contact regime, a further broad peak is created at high conductance values ($G > 10^{-2}\,G_0$). A sharp final peak in the EMF-2 histogram, at $G > 10^{-0.5}\,G_0$, is an artefact of the measurements in these junctions, caused by extended contact with the tip in some traces, not performed with the other molecules. This histogram also shows a broader peak for the case of the ambient layer being pressed between tip and molecule, which reaches higher G values than the other EMFs. This is possibly due to its paramagnetic nature.

Conductance 1D histograms are also plotted in order to find the most probable conductance value $\bar{G}$ of each EMF at first contact, that is, the molecular junction without compression.

Focusing only on the first contact of the molecule with the tip, we select the data points corresponding to $0.1\ \mathrm{nm}$ of tip displacement right after the jump-to-contact in the conductance traces (or after a large change in the slope). With these points (highlighted in cyan in Figure 3.10(b) for three individual examples), we build additional 1D histograms, plotted in Figure 3.10(c). The mean conductance value of each histogram $\bar{G}$ and the corresponding standard deviation are collected in Table 3.1. Note that 1D histograms of the complete curves (Figure 3.10(a)) do not show peaks exactly at these values, being the first-contact hidden inside the broader peak caused by the whole contact regime (highlighted in yellow in the individual traces of Figure 3.10(b)). We find that the first-contact conductance value is $0.05\ G_0$ for EMF-1 junctions, $0.10\ G_0$ for EMF-2 and $0.03\ G_0$ in the case of EMF-3 single-molecule junctions. Thus, considering the three molecules investigated, EMF-2 shows the largest $\bar{G}$ and EMF-3, the smallest, being around 30% smaller than the carbide-EMF $\bar{G}$. Comparing to the pristine fullerene, let us remind that for Au|C_{60}|Au junctions in ambient conditions the reported conductance value at first contact is $0.1\ G_0$ [Evangeli2013], very similar to the value shown by single EMF-2 junctions while typical first-contact G values of trinitrate EMFs are generally smaller by a factor of two (EMF-1) or three (EMF-3).

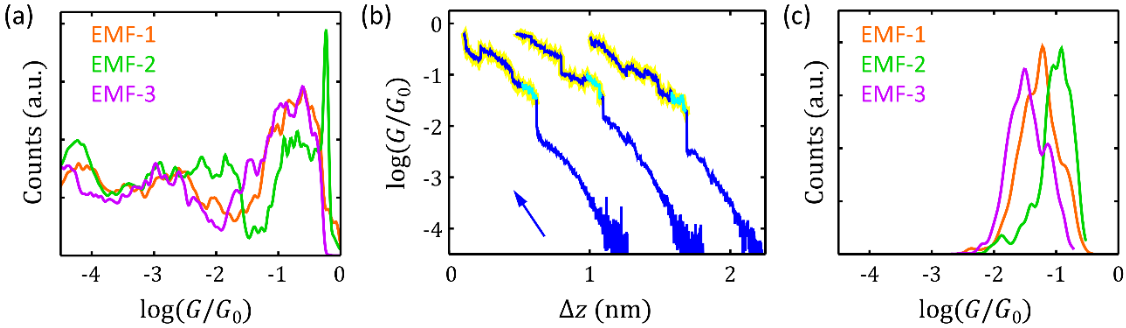

Figure 3.10: Conductance G 1D histograms. (a) G 1D histograms for the three EMFs investigated built with the complete approach traces included in the corresponding 2D histogram of Figure 3.9. (b) Examples of approach curves on each of the three EMFs, from left to right: EMF-1, EMF-2 and EMF-3 single-molecule junctions. The contact regime is highlighted in yellow and selected first-contact points ($0.1\ \mathrm{nm}$ after junction formation) are coloured in cyan. (c) G 1D histograms built with the first-contact points of all the approach curves of each molecule EMF. Mean values $\bar{G}$ and standard deviations σ_G of these 1D histograms can be found in Table 3.1.

Table 3.1: Mean first-contact conductance value $\bar{G}$ for each EMF investigated and standard deviation σ_G. Values obtained for the histograms in Figure 3.10(c).

	$\bar{G}\ (G_0)$	$\sigma_G\ (G_0)$
EMF-1 ($Sc_3N@C_{80}$)	$10^{-1.27}$	$10^{0.30}$
EMF-2 ($Sc_3C_2@C_{80}$)	$10^{-1.00}$	$10^{0.27}$
EMF-3 ($Er_3N@C_{80}$)	$10^{-1.46}$	$10^{0.29}$

3.2.5 Simultaneous conductance G and thermopower S *vs* tip displacement Δz measurements

After presenting our study of the conductance of single-EMF junctions, we aim at the characterization of their thermoelectric properties. We have already introduced in Chapter 2 (Section 2.4.2) the technique developed in our group prior to this Thesis, namely, the STM-Imaging technique, for the simultaneous measurement of conductance G and thermopower S of single-fullerene junctions [Evangeli2013]. For completeness we summarize here the main technical aspects of the experiments performed with EMFs.

In order to measure the thermopower S, a temperature difference ΔT between tip and sample is stablished by means of a resistive element acting as a heater on the tip support. A thermocouple placed on top of it serves to monitor the tip temperature. The substrate, meanwhile, is maintained at room temperature (approximately at $295\ \mathrm{K}$), monitored with a second thermocouple.

After heating up the tip, temperatures are allowed to stabilize for 15-30 minutes before a new thermal equilibrium of the setup is reached and we start measuring. In these experiments we typically establish a temperature difference ΔT of around $42\ \mathrm{K}$ for EMF-1, $34\ \mathrm{K}$ for EMF-2 and $37\ \mathrm{K}$ for EMF-3, monitored every few minutes. It is important to remind that the thermal drift increases considerably when heating up the tip, so all the process to find and track a given isolated molecule in a “stable” position with respect to the tip becomes more challenging than when no ΔT is applied and it makes it necessary to use fast imaging, even decreasing the number of lines per image, in order to be able to follow the isolated molecule.

Once an individual endohedral metallofullerene is targeted, we proceed as in Section 3.2.4 to measure the conductance G, with the difference that the tip motion is stopped every 10-20 steps (every 10-20 pm), both while approaching to and retracting from the molecule, and the Seebeck coefficient S is measured. As described in Figure 2.9 (Section 2.4.2), while the z-piezoelectric movement is stopped, small I-V ramps, typically of $\pm 10\ \mathrm{mV}$, are shot and recorded. These I-V curves show a voltage offset at zero current which is proportional to the temperature difference ΔT applied (see Figure 2.9) and the factor of proportionality, once the electronic offsets of the setup are considered (see Section 2.4.4), is the Seebeck coefficient: $V_{th} = -S\Delta T$. Simultaneously, the slope of the I-V trace corresponds to the conductance G of the junction, which is typically the same as the conductance measured with V_{bias} right before the I-V ramp is acquired, as long as the junction is stable enough. In each conductance G *vs* tip displacement Δz curve (one approach-retraction cycle), approximately 50-100 I-V ramps are shot, giving as many values of the Seebeck coefficient.

It is important to notice at this point that I-V characteristics of EMFs junctions are linear at small voltages even when the junction is formed and the molecule is being pressed. This means that, even beyond the electrical contact point and physical compression of the molecule, there is a linear $I(V)$ dependence proving good coupling of the molecule to the electrodes and a HOMO-LUMO gap larger than the voltage applied [Joachim1995b].

Figures 3.11, 3.12 and 3.13 show examples of simultaneous G and S traces measured on different single-EMF junctions (EMF-1 junctions in Figure 3.11; EMF-2 junctions in Figure 3.12; EMF-3 junctions in Figure 3.13). Surprisingly, and before going into the detail, the major feature of these junctions is that, for all the compounds, thermopower can be positive or negative, depending on the particular molecule connected.

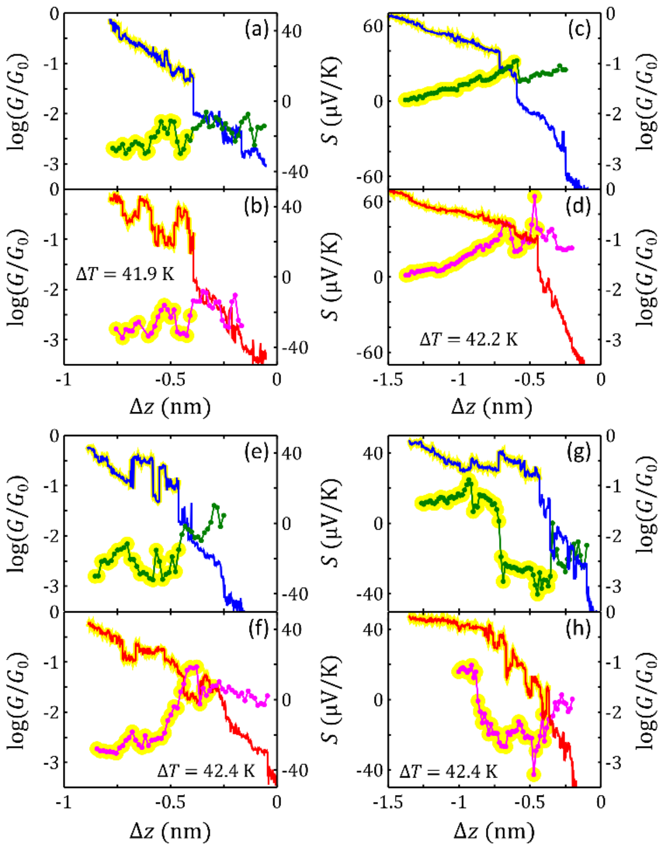

Figure 3.11: Conductance G and thermopower S simultaneous measurements in EMF-1 junctions. Four examples of approach (a,c,e,g) and retraction (b,d,f,h) cycles on single-molecule Au|$Sc_3N@C_{80}$|Au junctions, where the conductance G (in blue and red for approach and retraction of the tip, respectively) and thermopower S (in green and magenta for approach and retraction of the tip, respectively) are simultaneously acquired. For the molecule in (a-b), S is always negative, while for that one in (c-d), it is always positive. The EMF-1 in (e-f) has a mainly negative Seebeck coefficient and clearly shows correlation between small jumps in G and S, possibly due to structural rearrangements in the configuration of the junction. For the molecule in (g-h) an abrupt change in the sign of S during junction formation is observed. At the electrical contact point ($\Delta z \simeq -0.5$ nm), the molecule shows negative Seebeck coefficient $S = -30\ \mu\mathrm{V/K}$. After moving the tip closer to the surface by $\Delta z \simeq 0.25$ nm (compressing the molecule), a sudden modification of the junction takes place and we observe a drop in G and an inversion of the sign of S, flipping from negative to positive ($S = +15\ \mu\mathrm{V/K}$). In all these measurements the temperature difference is $\Delta T \sim 42$ K. The portion of G and S corresponding to contact regime is highlighted in yellow.

Conductance traces presented in Figures 3.11-3.13 (in blue and red for approach and retraction of the tip, respectively) are pretty much equivalent to those already discussed in the previous section. Typically, an abrupt jump in the G approach curve indicates contact formation which, in these experiments, can be also identified in the thermopower traces, plotted in green and magenta for approach and retraction of the tip, respectively. When the electrical contact point is reached, a jump is typically observed in the thermopower curve as well. In the contact regime (highlighted in yellow in the three figures), subsequent jumps observed in G, possibly due to atomic rearrangements, are also reflected in jumps in S, proving the sensitivity of both signals to atomic details. Retraction curves are almost the same indicating that junctions remain mostly unaltered, although typically with some hysteresis with respect to the approach possibly due to elastic deformations in the tip.

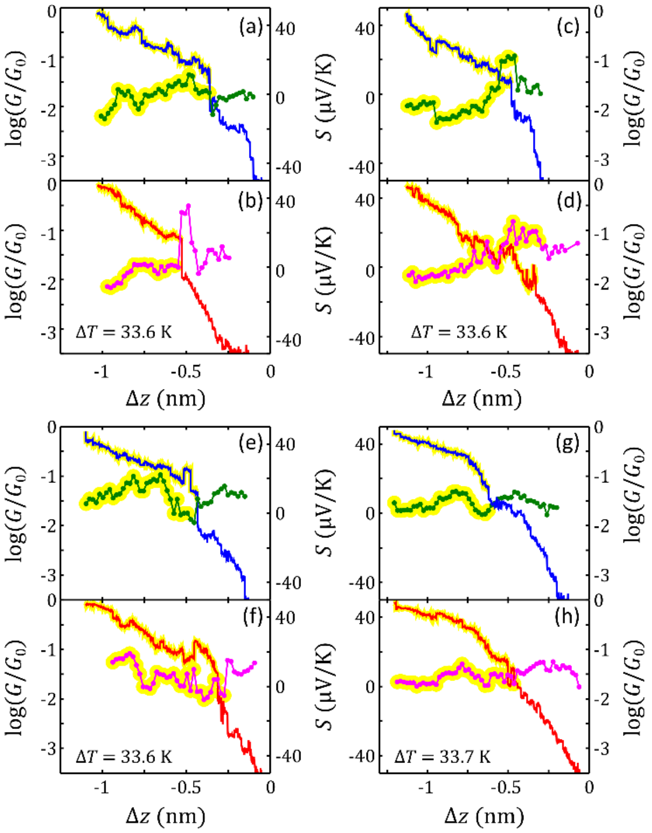

Figure 3.12: Conductance G and thermopower S simultaneous measurements in EMF-2 junctions. Four examples of approach (a,c,e,g) and retraction (b,d,f,h) cycles on single-molecule Au|$Sc_3C_2@C_{80}$|Au junctions, where the conductance G (in blue and red for approach and retraction of the tip, respectively) and thermopower S (in green and magenta for approach and retraction of the tip, respectively) are simultaneously acquired. Molecules in the first two junctions, (a-b) and (c-d), show initially a positive Seebeck coefficient that undergoes a change of sign as the tip keeps approaching towards the surface and compresses the molecule. The molecule in the third junction, (e-f), has an almost zero S that changes abruptly to a larger positive value in the contact regime of the approach. The reversed change is also observed, with some hysteresis, in the retraction curve. Finally, the EMF-2 in (g-h) presents a small positive thermopower and shows correlation between G and S changes. The temperature difference is $\Delta T \sim 34$ K in all these measurements. The portion of G and S corresponding to contact regime is highlighted in yellow.

As mentioned, the most remarkable aspect of the thermoelectric characterization of the EMF junctions investigated is the possibility to find molecules with both signs of the Seebeck coefficient. For example, junctions in Figure 3.11(a-b,e-f) for EMF-1 and Figure 3.13(c-d) for EMF-3 show all negative thermopower, while junctions in Figure 3.11(c-d) for EMF-1, Figure 3.12(e-f,g-h) for EMF-2 and Figure 3.13(e-f,g-h) for EMF-3 present positive thermopower. This is an outstanding behavior since, as we introduced in Section 1.1, the pristine fullerene is a robust thermoelectric material with a consistently negative Seebeck coefficient and because, to the best of our knowledge, this is the first time that bi-thermoelectricity, i.e. showing either positive of negative S, is observed in a single material, without requiring chemical modification.

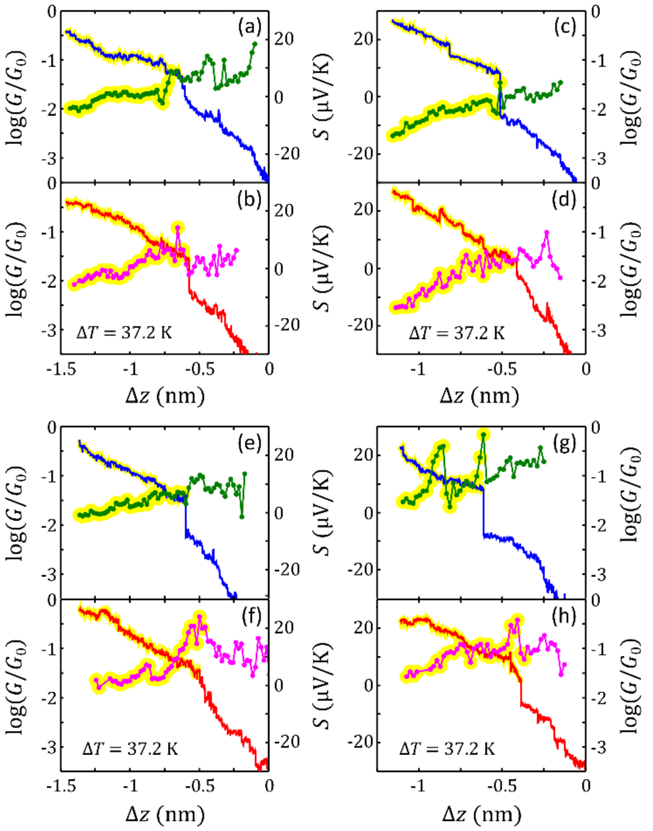

Figure 3.13: Conductance G and thermopower S simultaneous measurements in EMF-3 junctions. Four examples of approach (a,c,e,g) and retraction (b,d,f,h) cycles on single-molecule Au|$Er_3N@C_{80}$|Au junctions, where the conductance G (in blue and red for approach and retraction of the tip, respectively) and thermopower S (in green and magenta for approach and retraction of the tip, respectively) are simultaneously acquired. Molecular junction in (a-b) experiments a gradual change from positive to negative Seebeck coefficient as the molecule is compressed. The EMF-3 junction in (c-d) exhibits a mainly negative thermopower, while junctions shown in (e-f) and (g-h) present positive Seebeck coefficients. Two large abrupt jumps in S are observed in the approach trace of the fourth junction, (g-h), correlated with changes in G: the first jump in S is correlated with the contact-formation G rapid increase and the second one is correlated with a small jump down in G and a subtle change in the slope. In these measurements the temperature difference is $\Delta T \sim 37$ K. The portion of G and S corresponding to contact regime is highlighted in yellow.

In addition, some junctions whose S is initially positive but of small magnitude show a gradual change towards negative Seebeck coefficients when the contact regime is maintained and the molecule is further compressed. This is the case, for instance, in Figure 3.12(a-b,c-d) for EMF-2 junctions and in Figure 3.13(a-b) for EMF-3 junctions. Based on these observations, we have accomplished a complementary experiment with EMF-1 junctions that consists on performing “compression cycles” with the tip while the contact regime is maintained. For a given junction, we do a total of three compression cycles and acquire G and S *vs* Δz traces without breaking the contact with the EMF. The results obtained are shown and discussed later in this chapter (see Section 3.2.7).

Finally, it is also possible to find some individual junctions with abrupt changes in the sign of S, simultaneously with jumps in G (see Figure 3.11(g-h)), suggesting a major change in the junction configuration, such as rotation of the whole endohedral metallofullerene triggered by compression or thermal induced fluctuations. A similar situation is possibly occurring in the EMF-3 junction shown in Figure 3.13(g-h) where no change of sign of the thermopower is observed, but the junction shows large abrupt jumps in the Seebeck coefficient correlated with changes in the conductance: the first jump observed in S is correlated with the contact-formation rapid increase of the conductance, while the second one is correlated with a small jump down in G and a subtle change in the slope.

For comparison, we present in Figure 3.14 examples of simultaneous G and S measurements in Au-Au tunnelling junctions and pristine fullerene C_{60} junctions, with an applied temperature difference of around $42\ \mathrm{K}$. The first ones show a small negative thermopower ($S \sim -1\ \mu\mathrm{V/K}$), in good agreement with previously reported results [Evangeli2015]. The Seebeck coefficient remains relatively constant as the tip approaches the surface and the conductance increases exponentially (linearly in the semilogarithmic plot). With respect to the C_{60} junctions shown, they exhibit negative thermopower and a jump in the S traces is typically observed when reaching the electrical contact point. In contrast to the results obtained for the EMF junctions, large compression of the pristine fullerene sometimes result in a gradual reduction towards zero of the thermopower values, as can be seen in the example of Figure 3.14(b).

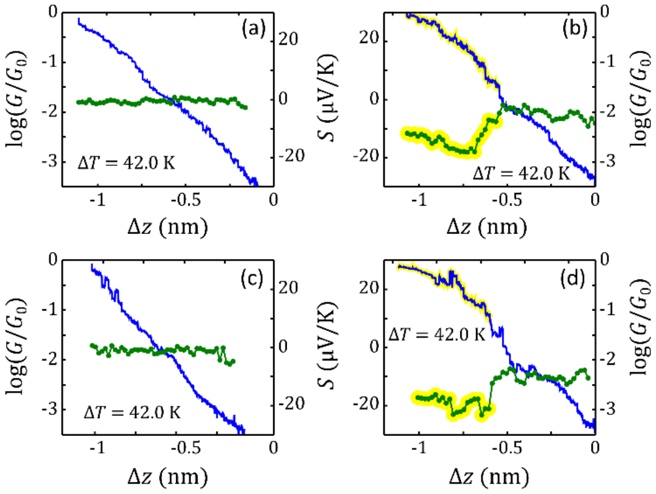

Figure 3.14: Conductance G and thermopower S simultaneous measurements in Au-Au tunnelling junctions and Au|C_{60}|Au junctions. Examples of individual approach traces in Au-Au tunnelling junctions (a,c) and Au|C_{60}|Au junctions (b,d) where conductance G (blue) and thermopower S (green) are simultaneously acquired during the approaching of the tip towards the surface or the molecule. In all these measurements the temperature difference is $\Delta T \sim 42\ \mathrm{K}$.

In order to directly compare the results obtained for the three EMFs and to explore the variability introduced by different junction configurations, we perform several measurements with each of the endohedral metallofullerenes and collect multiple G and S *vs* Δz traces of Au|single-molecule|Au junctions. G and S *vs* Δz 2D histograms are presented in Figure 3.15, together with 2D histograms for pristine C_{60} junctions, measured for comparison.

As in the case of the pure conductance characterization introduced in Section 3.2.4, G *vs* Δz 2D histograms in Figure 3.15(a-d) reflect the different features observed in the individual traces. These histograms are built with the complete approach of the G traces, i.e. from tunnelling to molecule-compression with the tip, measured at V_{bias}, and are equivalent to those plotted in Figure 3.9. On the other hand, it is more difficult to identify individual-junction behaviours in the

S *vs* Δz 2D histograms shown in Figure 3.15(i-l), although contact formation is roughly identifiable in the histograms either by an increase in the dispersion of the values (see, for example, Figure 3.15(i,j)) or a more or less abrupt step in the general shape of the histogram (see, for instance, Figure 3.15(k-l)). In Figure 3.15(e-h), we plot the 2D histograms of the corresponding G obtained from the slope of the I-V ramps shot to measure the thermopower. As it can be seen, these histograms are pretty much the same to those built with the whole approach G traces, indicating that junction configuration is stable during the acquisition of the voltage ramps.

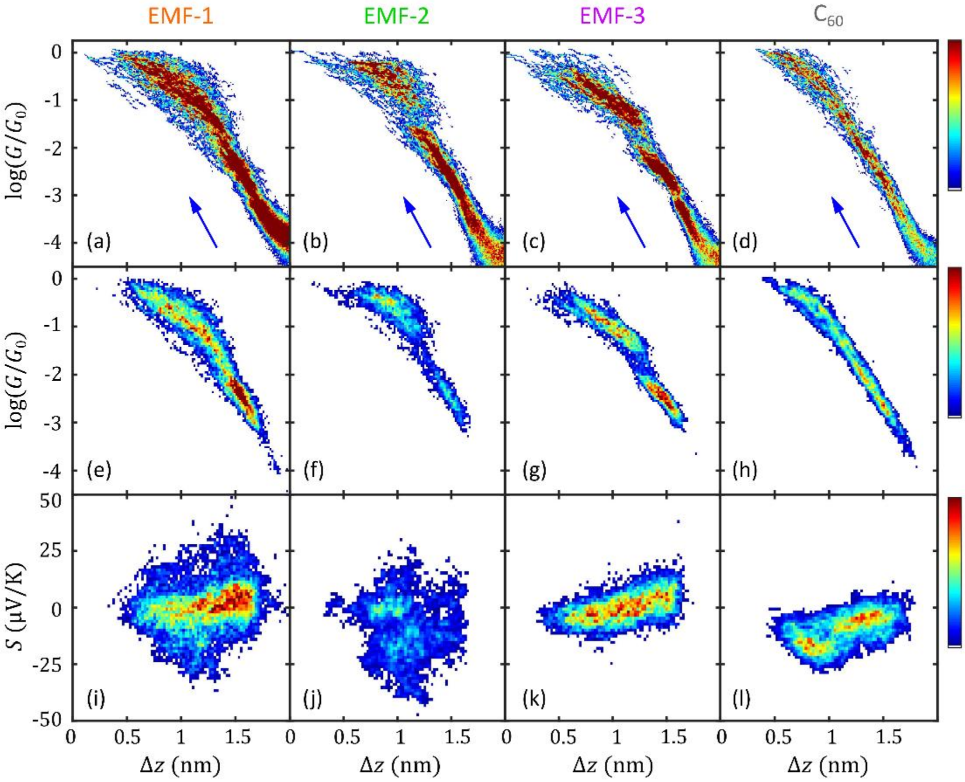

Figure 3.15: Conductance G and thermopower S *vs* tip displacement Δz 2D histograms of Au-EMF-Au and Au-C_{60}-Au junctions. (a-d) G *vs* Δz 2D histograms of 131 approach curves on single EMF-1 ($Sc_3N@C_{80}$) molecules (a), 99 approach traces on isolated EMF-2 ($Sc_3C_2@C_{80}$) molecules (b), 83 approach curves on individual EMF-3 ($Er_3N@C_{80}$) molecules (c) and 50 approach traces on single C_{60} molecules (d). Complete G *vs* Δz individual traces, from tunnelling to molecule-compression by the tip, are plotted. (e-h) G *vs* Δz 2D histograms of the same junctions as (a-d), but where conductance values are obtained from the slope of the I-V ramps shot every 10-20 pm to measure thermopower (see Section 2.4.2). (i-l) S *vs* Δz 2D histograms of the same junctions as (a-d) and the same I-V ramps as (e-h). Approximate temperature differences for each compound (EMF-1, EMF-2, EMF-3 and C_{60}) are $\Delta T \sim 42$ K, 34 K, 37 K and 42 K, respectively. The colour scale accounts for the number of points in each histogram.

Further discussing the thermopower 2D histograms (Figure 3.15(i-l)), those of EMF junctions evidence the bi-thermoelectricity of these systems, in marked contrast to the pristine fullerene. This translates into the possibility to have both positive and negative Seebeck coefficients, although each endohedral metallofullerene presents a particular characteristic behaviour. In terms of dispersion, EMF-1 and EMF-2 junctions (both scandium-based molecules) show larger variability of S values than EMF-3, whose thermopower dispersion is notably smaller and similar to that of the pristine fullerene C_{60}.

Additionally, since the different conductance regimes that constitute the complete approach of the tip to form the molecular junctions may show different thermoelectric behaviours, it is interesting to separate the contact regime from the rest of the curve and, in a second step, the first-contact values from the complete contact regime. In this sense, thermopower S *vs* conductance G 2D histograms are especially useful to discern the different regimes and result a representation of great interest to find trends or possible correlations between these magnitudes. They are plotted in Figure 3.16 for the three EMFs investigated and the pristine fullerene. It should be noticed that G values in these histograms (and for now on in this section) are those obtained from the slope of the small I-V ramps. Figure 3.16(a-d) histograms are formed with the complete G and S traces, including the whole tip movement from the tunnelling until close to the metallic contact. Figure 3.16(e-h) gather G and S experimental data measured in the contact regime, while the tip is in contact with the fullerene cage. Finally, in Figure 3.16(i-l) only G and S values at first-contact, i.e. within 0.1 nm after junction formation, are collected.

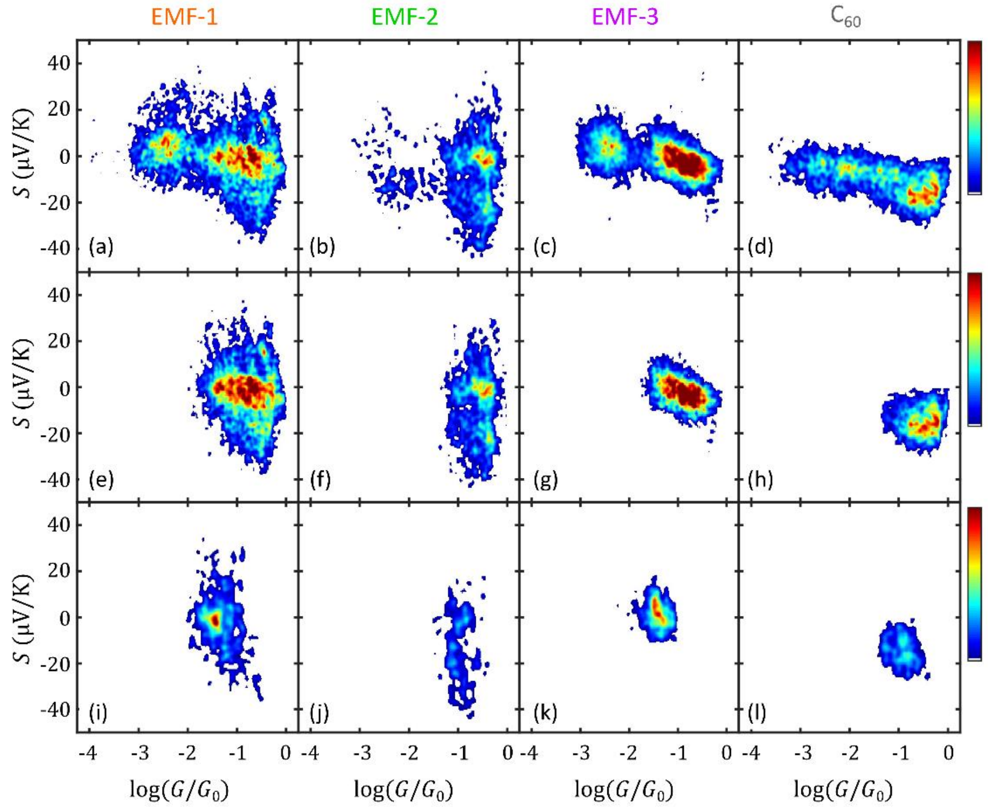

Figure 3.16: Thermopower S *vs* conductance G 2D histograms for the three EMFs and the pristine fullerene C_{60}. (a-d) S *vs* G 2D histograms built with the data from the I-V ramps shot during the complete traces, from the noise level until close to the metallic contact. Each column corresponds to one molecule, as indicated on top. From left to right: $Sc_3N@C_{80}$ (EMF-1), $Sc_3C_2@C_{80}$ (EMF-2), $Er_3N@C_{80}$ (EMF-3) and C_{60}. (e-h) S *vs* G 2D histograms of the contact regime. Only the experimental data measured after junction formation, while the tip is in contact with the fullerene, is gathered in these histograms. (i-l) S *vs* G 2D histograms built with first-contact values, i.e. within 0.1 nm after junction formation. These data correspond to the junction without compression. All the data in this figure come from the same molecular junctions of Figure 3.15.

We can observe in these histograms, especially in those of first-contact values (Figure 3.16(i-l)), that EMF-1 and EMF-3 junctions present slightly smaller conductance values than EMF-2 and C_{60} systems, as already obtained in the pure conductance characterization summarized in Table 3.1.

With respect to the thermopower, these two trinitrate molecules (EMF-1 and EMF-3) present both positive and negative Seebeck coefficients mostly centred at zero. Thermopower of EMF-2 junctions, in contrast, despite also showing both signs and a considerable dispersion, seems to be preferentially displaced toward negative values. C_{60} junctions, in good agreement with previously reported experiments [Evangeli2013], presents only negative S.

In order to quantify and better compare the different systems, we build 1D histograms as shown in Figure 3.17. The three different regimes analysed in Figure 3.16 (that is, complete traces, complete contact regime and first-contact values) are also considered and plotted separately in this figure. Finally, for the first-contact G and S 1D histograms, the mean conductance $\bar{G}$ and thermopower $\bar{S}$ values and their corresponding standard deviations, σ_G and σ_S respectively, are gathered in Table 3.2. For the molecular junctions presented in Figure 3.15, 3.16 and 3.17, we find that the first-contact $\bar{G}$ is $0.05\ G_0$ in the case of EMF-1 single-molecule junctions, $0.11\ G_0$ for EMF-2 and $0.04\ G_0$ for EMF-3 junctions, while the first-contact mean Seebeck coefficients are $\bar{S} = -2.3 \pm 17.4\ \mu\mathrm{V/K}$ for EMF-1, $\bar{S} = -12.23 \pm 18.7\ \mu\mathrm{V/K}$ for EMF-2 and $\bar{S} = 1.2 \pm 7.6\ \mu\mathrm{V/K}$ for EMF-3. For the pristine fullerene C_{60} we obtain $\bar{G} = 0.11\ G_0$ and $\bar{S} = -16.3 \pm 6.6\ \mu\mathrm{V/K}$, in good agreement with previously reported measurements [Evangeli2013]. In the case of EMF-2 first-contact thermopower (green curve in Figure 3.17(f)), two peaks appear in the 1D histogram, approximately centered at $-25\ \mu\mathrm{V/K}$ and $0\ \mu\mathrm{V/K}$.

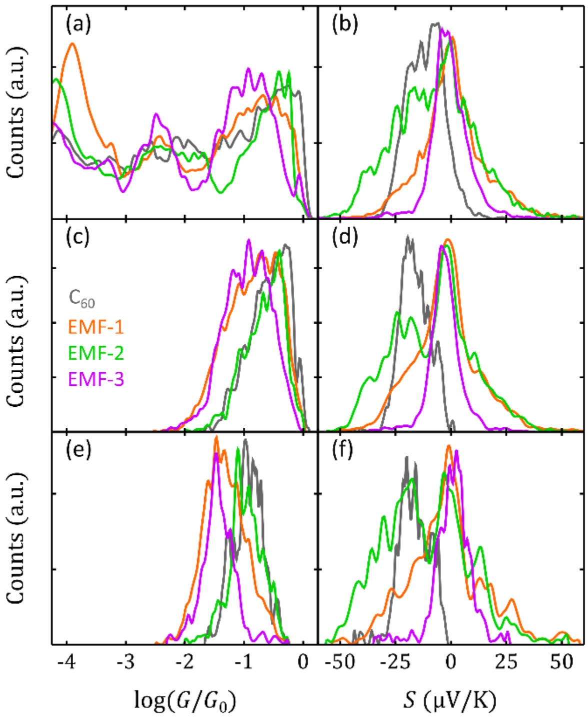

Figure 3.17: Conductance G and thermopower S 1D histograms. (a,b) G and S 1D histograms for complete traces (from tunnelling to molecule-compression) measured for the three EMFs investigated (EMF-1 in orange, EMF-2 in green and EMF-3 in purple) and for C_{60} junctions (in grey) for comparison. (c,d) G and S 1D histograms for the complete contact regime of each molecular junction. (e,f) G and S at first-contact 1D histograms whose mean values $\bar{G}$ and $\bar{S}$, and standard deviations σ_G and σ_S, can be found in Table 3.2. Data in this figure correspond to the molecular junctions presented in Figures 3.15 and 3.16.

Table 3.2: Mean conductance $\overline{G}$ and thermopower $\overline{S}$ values at first-contact for the EMFs investigated and the fullerene C_{60}, and corresponding standard deviations, σ_G and σ_S, respectively. Statistical analysis has been performed with the data plotted in Figure 3.17(e,f).

	$\overline{G}\ (G_0)$	$\sigma_G\ (G_0)$	$\bar{S}\ (\mu V/K)$	$\sigma_S\ (\mu V/K)$
EMF-1 ($Sc_3N@C_{80}$)	$10^{-1.33}$	$10^{0.35}$	-2.3	17.4
EMF-2 ($Sc_3C_2@C_{80}$)	$10^{-0.96}$	$10^{0.28}$	-12.2	18.7
EMF-3 ($Er_3N@C_{80}$)	$10^{-1.44}$	$10^{0.27}$	1.2	7.6
Fullerene C_{60}	$10^{-0.94}$	$10^{0.26}$	-16.3	6.6

As already observed in the previous section, the contact conductance of EMF-1 and EMF-3 junctions is in fact smaller than that of C_{60} by a factor of two-three, approximately, while EMF-2 presents very similar conductance values to C_{60}. Considering only the endohedral metallofullerenes, EMF-3 is the one showing the smallest conductance at first contact, although is still quite large compared to other organic molecular junctions.

Regarding the thermopower, conclusions from the mean value of Seebeck coefficient should be extracted with care. EMF-1 junctions show a very small mean thermopower, but they can also present very large values at first-contact, up to $\pm 40\ \mu V/K$ (as shown by the orange curve in Figure 3.17(f)). In the case of EMF-2 junctions, the two peaks in the histograms mean that it is equally likely to connect a molecule with a small value of S close to zero or with a negative thermopower with a value similar to that of C_{60} (see green curve in Figure 3.17(f)). Finally, according to the EMF-3 histogram in Figure 3.17(f) (purple curve), this Er-based molecule typically shows a small Seebeck coefficient at first contact, with the peak slightly positive but close to zero and with a dispersion of values notably smaller than the Sc-based EMFs.

The bi-thermoelectric response characterized so far in these EMFs junctions, whose thermopower can be positive or negative without requiring chemical modification and depending just on the particular molecule connected, is clearly concluded from our experimental observations and confirms our initial intuition that EMFs could offer a larger variability in the transport properties investigated than the robust properties shown by the pristine C_{60}. This interesting behaviour is not observed in Ref. [Lee2015], the only other reported study of thermoelectricity of endohedral metallofullerenes, to the best of our knowledge. In this reference, $Gd@C_{82}$ and $Ce@C_{82}$ and the empty C_{82} were reported to present negative Seebeck coefficients, enhanced in the endohedral fullerenes with respect to the C_{82} from $S_{C_{82}} = -22.7 \pm 0.9\ \mu V/K$ to $S_{Gd@C_{82}} = -31.6 \pm 1.2\ \mu V/K$ and $S_{Ce@C_{82}} = -30.0 \pm 1.0\ \mu V/K$. Self-energy corrected first-principles transport calculations were performed and showed that transport in these molecules is mainly through the LUMO localized in the C_{82} cage, without a direct contribution from the lanthanide inner atoms which nevertheless produce changes in the electronic- and geometrical structure enough to explain the enhancement in the thermopower. Compared to our investigated EMFs, the main difference with the systems studied in Ref. [Lee2015] is the total number of metal atoms inside the fullerene cage, which in the case of Ref. [Lee2015] is only one atom placed out of centre.

In the following, we aim at further investigating the peculiar conduct we observe in our compounds with complementary experiments presented in Sections 3.2.6 and 3.2.7. Tunnelling spectroscopy characteristics are first characterized to get an insight into the behaviour of the current through the junctions when larger bias voltage values are applied, which give us some hints about the transmission function of these systems. In Section 3.2.7 we present our results when performing compression cycles in EMF-1 and C_{60} junctions to explore the reproducibility of changes in the thermopower values.

3.2.6 Tunnelling spectroscopy

Considering the coherent charge transport Landauer formalism introduced in Chapter 1, the sign of the Seebeck coefficient is a consequence, and hence a signature, of the slope of the transmission function of the molecular junction at the Fermi level position. Within this formalism, the peculiar bi-thermoelectric behaviour observed in the EMF junctions investigated suggests then different sign of the slope of the transmission function at the Fermi level from molecule to molecule.

Tunnelling spectroscopy characteristics of EMF junctions are performed to explore the variation of the tunnelling current with positive and negative bias voltage. In a simple way, this spectroscopy allows us to gain some insight into the sign of the slope of the transmission function at the Fermi level, i.e. towards which energies, positive or negative with respect to the Fermi level, the current increases more rapidly [Wiesendanger1994].

The STM-Imaging technique results also very advantageous to perform these experiments since it allows us to localize individual molecules on the surface. Once the tip is precisely placed on top of a single EMF, maintaining the tunnelling current, we perform tunnelling spectroscopy at constant height blocking the z-piezo position and ramping the bias voltage to obtain the current-voltage (I-V) characteristics of the molecule. We typically ramp the V_{bias} between $\pm$ 1 V, since higher values of the bias voltage may result in field emission effects in the apex of the Au tip, due to working in ambient conditions.

It is important to notice that these large I-V curves are measured while the tip is not in contact with the molecule and hence the junction coupling is asymmetric and transport is through tunnelling (see inset in Figure 3.18). Molecules are strongly coupled to one of the electrodes (the substrate) and weakly coupled to the other one (the tip). This is in fact what we use to extract information about the slope of the transmission function at the Fermi level.

Tunnelling spectroscopy is also a useful tool to confirm that the tip is clean and we do not have any fullerene on it (since, as mentioned, it is possible that an EMF is transferred into the tip when a junction is formed). I-V curves on top of a crystalline gold surface without fullerenes help to determine whether the tip is free of molecules (or at least, the part of the tip interacting with the surface). Tunnelling I-V curves of Au electrodes are symmetric and follow the Simmons model, while the presence of an EMF on one electrode or the other introduces an asymmetry in the current increase with positive or negative bias voltage. Special care is taken to this respect in our experiments because I-V curves obtained with the same molecule placed on the substrate or on the tip would present inversed asymmetry [Evangeli2014].

Figure 3.18 shows representative examples of the I-V characteristics of single EMF-1 junctions. Tunnelling spectroscopy on different isolated molecules reveals linear I-V curves at low voltages (up to $\pm 200 - 300\ \mathrm{mV}$), showing that the HOMO-LUMO gap of the junctions exceeds in all cases the voltage applied in this region and that the transmission varies softly around the Fermi level, suggesting off-resonant transport [Joachim1995b].

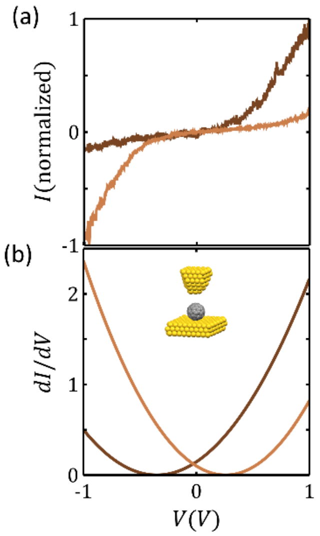

Figure 3.18: Tunnelling spectroscopy of EMF-1 junctions. I-V characteristics (a) and differential conductance (b) in tunnelling regime on two different $Sc_3N@C_{80}$ molecules, presenting opposite rectifying behaviour. The differential conductance has been calculated from a fit of the experimental I-V curve.

For higher voltages (above $\pm 200-300\ \mathrm{mV}$), Au|EMF|tunnel|Au junctions show asymmetric I-V characteristics, that is, rectifying behaviour. We find that some molecules exhibit higher current for positive bias voltage (dark brown curves in Figure 3.18), similar to what is observed in C_{60} junctions, while others have higher current for negative voltage (light brown curves in Figure 3.18). The rectifying behaviour shown by these curves reflects the aforementioned asymmetry of the junction structure and it is mainly caused by the asymmetric coupling of the molecule to both electrodes. However, the polarity of the bias at which the current increases faster is a consequence of a nearby resonance, placed on one side or the other of the Fermi level, depending on the particular molecule measured, something which is more directly shown by the differential conductance presented in Figures 3.18(b). Molecule-dependent rectifying behaviour is also observed in the other two endohedral metallofullerenes investigated. In the case of EMF-1 and EMF-3, this variation in the electronic behaviour of particular molecules has been also reported in UHV experiments [Nörenberg2008] and has been attributed to different orientations of the molecules on the surface and hence, different charge transfer from the substrate to the molecules.

More interestingly, we find a correlation between the asymmetry of the I-V curves and the sign of the thermopower of a given EMF molecule, connected right after the tunnelling spectroscopy characterization. We observe that molecules for which the current is higher at positive bias voltage present negative thermopower at first-contact, while molecules for which the current is higher at negative voltage show positive thermopower. This is consistent with the Landauer formalism and with the dependence of thermoelectric properties of molecular junctions on the magnitude and derivative of the transmission at the Fermi level of the electrodes [Paulsson2003], given by Eq. (1.44) and reproduced here for the sake of commodity:

$$S = -\frac{\pi^2 k_B^2 T}{3e} \frac{d \ln \mathcal{T}(E)}{dE}\bigg|_{E=E_F}.$$

In this expression, $\mathcal{T}(E)$ is the junction transmission function dependent on electron energy E, k_B is the Boltzmann constant and T is the average temperature of the junction.

EMFs I-V characteristics are then in good agreement with the bi-thermoelectric behaviour of these molecular junctions when they are contacted with both electrodes and, according to Ref. [Nörenberg2008], indicate that different orientations of the molecules targeted, which affects the charge transfer from the substrate, may be the reason behind different sign of the Seebeck coefficient from molecule to molecule.

3.2.7 Compression cycles for $Sc_3N@C_{80}$ and C_{60} junctions

Considering again the contact regime, thermopower after junction formation in individual traces presents typically an unusual trend towards more negative values, as already introduced in Section 3.2.5. The Seebeck coefficient becomes normally more negative as the molecule starts being compressed by the tip, behaviour which is observed for the three endohedral metallofullerenes investigated.

In order to explore the reproducibility of this conduct we perform an extended experiment, with EMF-1 junctions in particular, consisting on "compression cycles" with the tip while maintaining contact with a given molecule. For this, small amplitude ($< 0.5\,\mathrm{nm}$) fix-size (200 points) compression (approach-retraction) cycles, without breaking contact with the EMF. In these cycles, as the tip advances after the first contact and retracts without breaking it, a variable pressure is exerted on the junction.

Simultaneous variations of G and S measured as a function of tip displacement Δz during three consecutive cycles for three different molecules are shown in Figure 3.19. The power factor GS^2 is also calculated and plotted (see Chapter 1, Section 1.6). Compression of the molecules with the tip corresponds to an increase of tip displacement (towards negative values), as well as an increase in conductance. These three molecules have been chosen as representative examples of different behaviours of S: molecule 1 shows a large positive thermopower at first contact (in red); molecule 2 has initially a small positive thermopower (in blue); and molecule 3 has almost zero thermopower right after contact formation (in green).

To get a further insight into the variations induced by the tip cyclic compression, we plot G, S and GS^2 as a function of time, in arbitrary units, as presented in Figure 3.20(a-c) for the same cycles of Figure 3.19. In this representation, the three different compression cycles performed on each molecule are clearly identifiable. We observe that for all molecules both the conductance and thermopower vary monotonically with pressure: the conductance increases and the thermopower decreases, becoming more negative, as the tip presses the molecule. This behaviour of the conductance is to be expected, since pressing will result in an increased coupling and consequently in a larger conductance. However, the behaviour of the thermopower is most unusual: very large variations are observed and even a change in sign for molecule 2. This extreme sensitivity of thermopower of molecular junctions to pressure has never been reported before, to the best of our knowledge, and has a marked effect on the power factor GS^2 as shown in Figure 3.20(c). For molecule 1, the power factor decreases with compression, while for molecule 2, it increases reaching values of around $5\ \mathrm{fW/K^2}$. In contrast, for molecule 3, GS^2 remains small during the whole cycle.

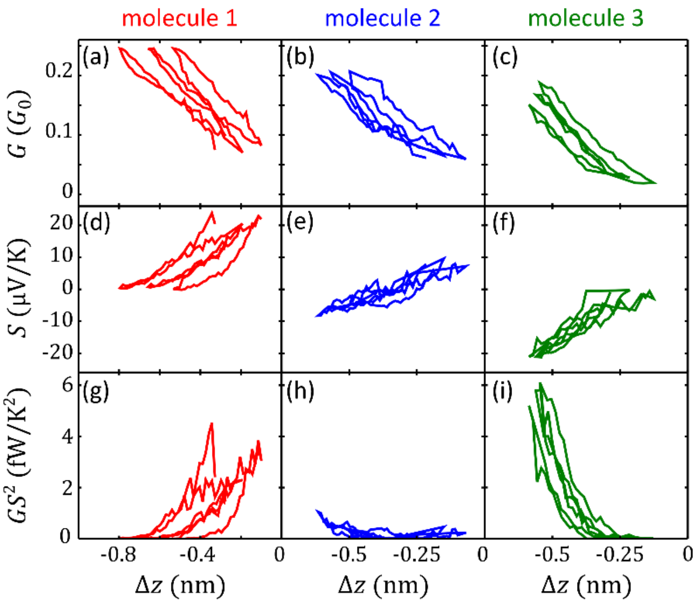

Figure 3.19: Compression cycles on EMF-1 ($Sc_3N@C_{80}$) junctions as a function of tip displacement. (a-i) Reproducible variations of the conductance G (a-c), the thermopower S (d-f) and power factor GS^2 (g-i) as a function of the tip displacement Δz. For molecule 1 (red), compressing the molecule results in S varying from $+20\ \mu V/K$ to almost $0\ \mu V/K$; for molecule 2 (blue), S varies from $+10\ \mu V/K$ to $-5\ \mu V/K$; and for molecule 3 (green), S varies from approximately $0\ \mu V/K$ to $-20\ \mu V/K$. Each half cycle corresponds to less than 0.5 nm.

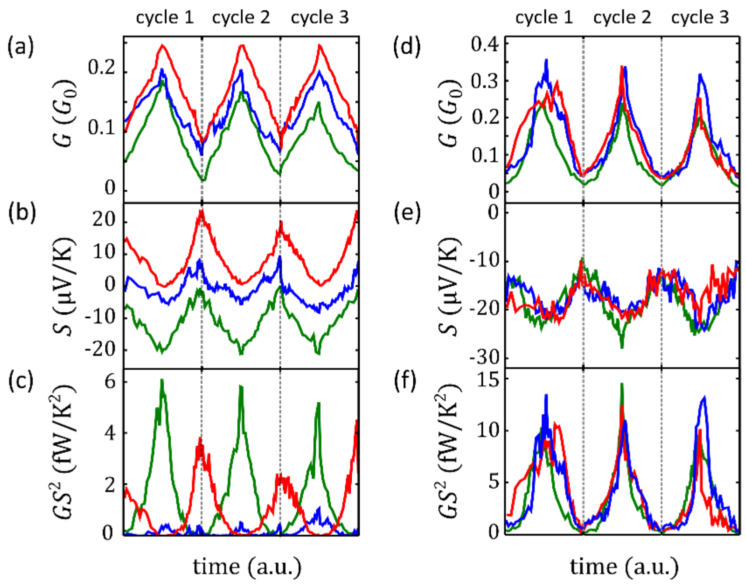

Figure 3.20: Effect of compression on $Sc_3N@C_{80}$ single-molecule junctions and comparison with C_{60} junctions. (a-c) Periodical variations of the conductance G, thermopower S and power factor GS^2, respectively, of EMF-1 junctions, as the STM tip advances and retracts during three consecutive compression cycles. This is the same data as in Figure 3.19 and the colours correspond to same three molecules. (d-f) Periodical variations of the conductance G, thermopower S and power factor GS^2, respectively, of C_{60} junctions, as the STM tip advances and retracts during three consecutive compression cycles. Each colour corresponds to a different molecule. As in the case of EMF-1 junctions, each half cycle corresponds to less than 0.5 nm.

The periodic nature of these curves indicates that the junction, i.e. the molecule and the gold electrodes, deforms elastically in response to the pressure. Larger amplitude (> 0.5 nm) cycles destroy this periodicity indicating the onset of plastic deformation (atomic rearrangements) in the gold electrodes [Agraït1995]. Taking into account previous results for gold contacts [Rubio-Bollinger2001] and the fact that fullerene molecules are much stiffer than gold [Ruoff1991], we can safely assume that most of the elastic deformation corresponds to the electrodes and that the maximum pressure at the junction during our measurements is about 4 GPa [Agraït1995].

The peculiarity of this conduct of EMF junctions can be better understood when compared with C_{60}. To do so, we perform the same experiments with the pristine fullerene, i.e. rounds of three compression cycles over a given molecule maintaining the contact with the tip. The results obtained for three different C_{60} junctions are presented in Figure 3.20(d-f). We find that the Seebeck coefficient is in this case always negative during the three consecutive cycles, as expected. Interestingly, the relatively high conductance and thermopower of C_{60}, together with the fact that the Seebeck coefficient is consistently negative and its value increases as the molecule is gently compressed, result in a power factor increase upon compression to values of around $10\ \mathrm{fW/K^2}$. This means that it is in fact easier to reach high power factor values with C_{60} based junctions than with EMFs equivalent systems. However, the variability in the Seebeck coefficient offered by Au|EMF|Au junctions could never be accomplished with the pristine fullerene.

3.3 Theoretical calculations of the transport properties of $Sc_3N@C_{80}$ and C_{60} junctions

Theoretical calculations performed by the group of Prof. Colin J. Lambert for $Sc_3N@C_{80}$ (EMF-1) and C_{60} junctions have greatly contributed to shed light on the origin of the bi-thermoelectric response of the endohedral metallofullerenes. A detailed description of the theoretical calculations they performed can be found in Ref. [Rincón-García2016]. We reproduce here the main aspects and conclusions of these theoretical calculations.

To elucidate the origin of the bi-thermoelectric effect of $Sc_3N@C_{80}$ junctions and the behaviour shown by the compression cycles, they used density functional theory (DFT) to simulate the contact and pressing of the molecule. Employing a combination of the quantum transport code Gollum [Ferrer2014] and the DFT code SIESTA [Soler2002], both the conductance and thermoelectric properties of the molecule contacted between gold electrodes were calculated.

To calculate the electronic structure using the DFT code SIESTA, they obtained the optimum geometry of the C_{80} cage and encapsulated Sc_3N molecule by searching through atomic configurations until the lowest energy was found. In each case the molecule was relaxed until all the forces on the atoms were less than 0.05 V/Ang. SIESTA employs pseudo-atomic orbitals and the relaxation was carried out using a double-zeta plus polarization orbital basis set. Norm-conserving pseudopotentials were used and an energy cutoff of 200 Rydergs defined the real space grid. The exchange correlation functional was LDA. To calculate electron transport, the molecule was attached to gold leads and, due to the large contact area of the C_{80} cage, a 5 by 6 atom layer of Au(111) was taken to be the surface of the lead. The optimum binding location, approximately 2.3 Å, was found by calculating the binding energy as a function of the separation distance z taking into account basis set error corrections. The extended molecule included 6

layers of Au(111) and the Hamiltonian describing this structure was produced using SIESTA. The transmission coefficient $\mathcal{T}(E)$ and thermopower S were then calculated using the Gollum code.

Three major inputs enter into the simulations to reproduce the compression cycles experiments. The first is the position of the molecule with respect to the electrodes z. The effect of pressure on the transport properties was explored by varying z around the equilibrium distance, 2.3 Å. The orientation of the whole molecule was kept fixed while z is varied. A second input to the simulations is the orientation of the molecule with respect to the gold surface. The electronic structure of the isolated molecule shows a LUMO resonance located primarily on the Sc_3N molecule and therefore transport properties are expected to depend on the orientation of the Sc_3N, locked in position within the fullerene cage, with respect to the gold surface. $\theta = 0°$ was defined to be the orientation when the plane of the Sc_3N molecule is normal to the gold surface, such that at $\theta = 90°$ the Sc_3N is parallel to the surface. To explore a range of orientations, they rotated through 180°, at intervals of 3°, and at each angle compute the zero bias transmission coefficient $\mathcal{T}(E)$. A third important input to the simulations is the energetic location of the molecular energy levels relative to the Fermi energy of the electrodes, since G and S are related to the value of the transmission and its derivative at the Fermi level. Since the DFT-predicted value E_F^0 is not reliable, to find the *true* Fermi level, they computed the transmission as a function of the energy for different orientations and pressures and a single Fermi energy was identified that reproduced the experimentally observed behaviour, i.e. S is either positive or negative and it always decreases shifting to more negative values as the molecule is pressed, in some cases passing through zero. They found that the *true* Fermi level is located between the LUMO resonance and the LUMO of the fullerene cage and takes a value $E_F = E_F^0 + 0.23$ eV.

With this choice of E_F, Figure 3.21(a-c) show G, S and GS^2 as a function of z, for three different orientations of the endohedral molecule ($\theta = 150°$ in red, $\theta = 57°$ in blue and $\theta = 63°$ in green), which match the experimental behaviour of molecules 1, 2 and 3 in Figure 3.20(a-c). These results illustrate that the diverse experimental behaviours can be attributed to different orientations of the endohedral metallofullerene and reflect the shift towards negative values of the thermopower with pressure. The origin of this effect lies in the extreme sensitivity to pressure and orientation of the transmission function $\mathcal{T}(E)$, due to the presence of the resonance close to the Femi level (see Figure 3.21(d-f)). For all the orientations, as the tip advances, the resonance becomes broadened and shifts to lower energies, as a consequence of changes in the imaginary and real parts, respectively, of the self-energy [Lambert2015], that is, in the coupling of the molecule to the electrodes. This results in an increase of the value of the conductance while the value of the thermopower becomes more negative as the molecule is pressed. For certain orientations, the junction shows a small positive thermopower and pressing the molecule produces an S that varies from positive to negative values Figure 3.21(e), in good agreement with experimental results. The calculations reveal the essential role played by the coupling of the molecule to the electrodes in the observed changes in the thermopower, while the deformation of the molecule plays only a minor role, in contrast with the mechanism proposed in Ref. [Vacek2015], which relied in intramolecular deformation.

To further illustrate formation of the LUMO resonance due to the Sc_3N, the same theoretical calculations were performed for C_{60} junctions, showing that in this case the Fermi level is always located in the smooth, increasing slope of the LUMO peak (Figure 3.21(g)). Figure 3.21(h-i) show the transmission functions of $Sc_3N@C_{80}$ and C_{60} junctions, respectively, clearly showing that the main difference between these two systems is the LUMO resonance in the case of the endohedral metallofullerene. With respect to the compression cycles in C_{60} junctions, theoretical calculations were also performed similarly to those of the $Sc_3N@C_{80}$ molecule and the obtained G, S and GS^2 as a function of z are plotted in black in Figure 3.21(a-c) and match the behaviour observed in the experimental measurements (Figure 20(d-f)).

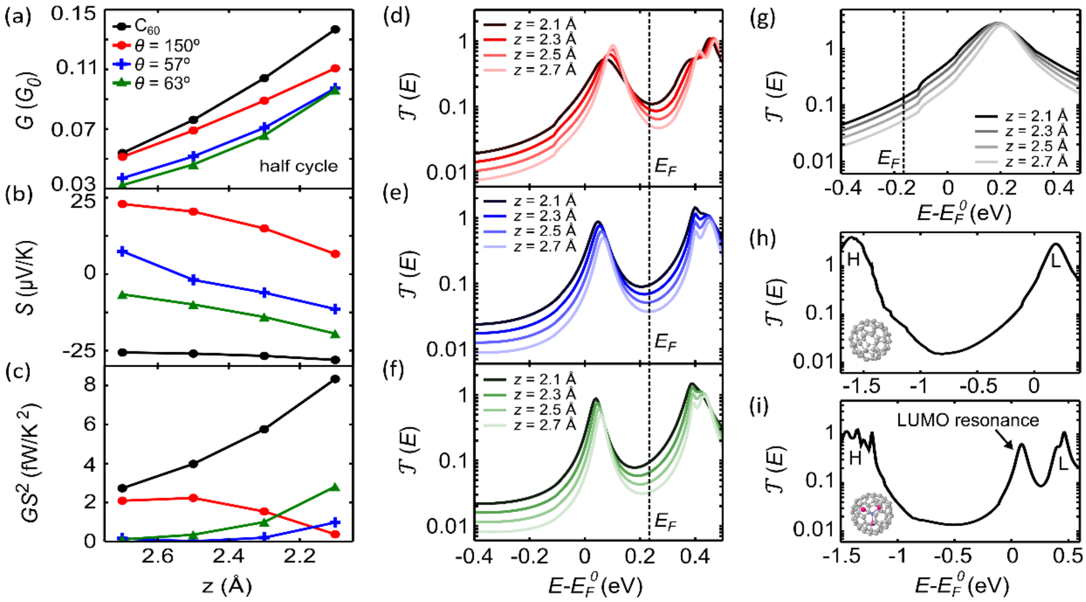

Figure 3.21: Theoretical calculations for $Sc_3N@C_{80}$ molecular junctions and comparison with C_{60} junctions. (a-c) Calculated G, S and GS^2, respectively, for three different orientations θ of EMF-1 as the tip-molecule separation z decreases from 2.7 Å to 2.1 Å, which corresponds to increasing pressure in the first half of experimental cycles. The orientations have been chosen such as to present similar amplitude variations as the experimental curves. Calculated G, S and GS^2 are shown for C_{60} junctions (in black). (d-f) Transmission curves $\mathcal{T}(E)$ of EMF-1 junctions for the same three different molecular orientations ($\theta = 150°$ in red, $\theta = 57°$ in blue and $\theta = 63°$ in green, respectively) and for different z. The Fermi level is shifted from the position given by DFT and the black dotted line indicates the *true* Fermi level as explained in the text. (g) Transmission curves $\mathcal{T}(E)$ of C_{60} junctions for different z. The Fermi level is shifted from the position given by DFT and the black dotted line indicates the true Fermi level as explained in the text. In this case, $E_F = E_F^0 - 0.165$ eV, chosen such as to present similar amplitude variations as the experimental curves. (h-i) Transmission curves $\mathcal{T}(E)$ for C_{60} and $Sc_3N@C_{80}$ junctions, respectively, showing the calculated HOMO-LUMO gap. Letters H and L indicate the HOMO and LUMO peaks of the fullerene cages. The main difference between both systems is the resonance present in the case of the endohedral metallofullerene. After figures from Ref. [Rincón-García2016].

3.4 Conductance G and thermopower S measurements in EMF-dimer junctions using the STM-Imaging technique

As it has been already mentioned, it was common to find that, after an indentation of the tip to connect a single EMF, the fullerene had moved from the surface to the tip, resulting sometimes in a very interesting fullerene-tip if the EMF is well placed on the apex of the Au tip or close to it.

These EMF-tip sallow us, for example, to obtain an improved resolution in the surface scanning tip [Schull2009; Nishino2005; Repp2005]. The STM-Imaging technique results indeed very useful to discern when a molecule has been transferred to the tip and it serves to monitor to some extent the cleanliness of the tip. It is typically possible to detect the transfer of an EMF to the tip because of a change in the resolution of the STM images. If the EMF on the tip is "well" placed on the apex (forming a C_{80}-tip), improved resolution of the surface features and smaller diameters for the EMFs are observed, as can be seen in Figure 3.22. On the contrary, if the EMF is laterally placed on the tip, some small spherical features on the side of the scanned EMFs are typically found, being simply a consequence of the lateral interaction between the EMFs on the substrate and on the tip. This is for instance the case in the STM image shown in Figure 3.22(e), where a small, round "molecule" is observed next to the fullerene on the substrate.

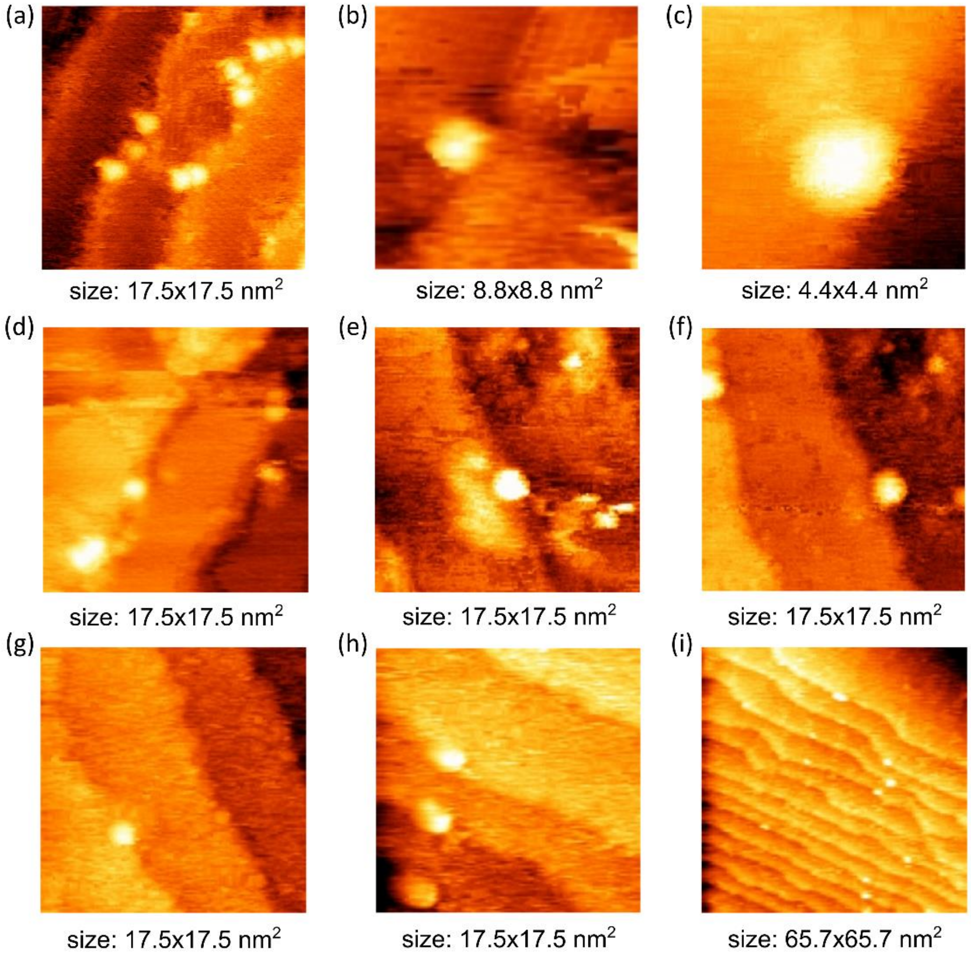

Figure 3.22: STM images with an EMF-tip. (a-c) EMF-1 molecules ($Sc_3N@C_{80}$) on a gold surface imaged with an EMF-1 molecule on the Au tip. (d-f) EMF-2 molecules ($Sc_3C_2@C_{80}$) on a gold surface imaged with an EMF-2 molecule attached to the Au tip. (g-i) EMF-3 molecules ($Er_3N@C_{80}$) on a gold surface imaged with an EMF-3 molecule on the Au tip. All of them are the result of having an EMF in the tip apex, except (e) that clearly reflects an EMF molecule laterally placed on the tip. Images have been treated using Gwyddion software [Nečas2012]. No thermal drift or piezo creep corrections have been applied to these images.

These EMF-tips, besides an improved resolution in the surface scanning, allow us also to form dimer junctions, that is, connect two fullerenes in series between the electrodes. If the EMF on the tip is stable enough, it is sometimes possible to scan the surface to find a second EMF on the surface, place the fullerene-tip on top of it and connect both molecules at the same time, as it was also previously done in our group for the pristine fullerene [Evangeli2013].

Conductance G and thermopower S characterization of EMF dimer junctions has been performed. Individual examples of approach traces of G and S showing dimer formation features are presented in Figure 3.23. The main signature of dimer formation is a shoulder in the conductance signal, highlighted in yellow in the figure. The conductance starts increasing as the tip with the EMF on it approaches the EMF molecule on the substrate and, after $0.5-0.75\ \mathrm{nm}$ of tip displacement, one or several drops in the conductance are typically observed before it starts increasing again. This behaviour in the conductance traces, previously reported for C_{60} dimers [Evangeli2013], indicates the formation of a Au|EMF|EMF|Au junction while the characteristic shoulder is observed, at a conductance value $G\sim 10^{-3}G_0$. The subsequent drop(s) in conductance are possibly due to atomic rearrangements caused by the increasing pressure and to finally squeezing out of the junction one of the EMF molecules. Conductance keeps increasing with further tip displacement toward the surface and a single-molecule junction is sometimes observed in the signal.

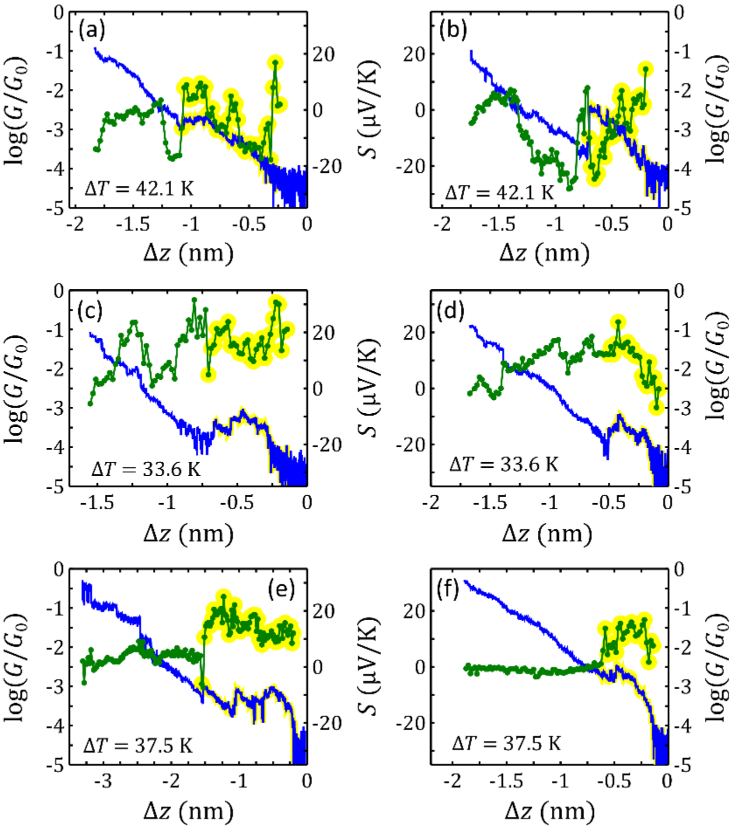

Figure 3.23: Conductance G and thermopower S individual measurements in EMF dimer junctions. (a-b) EMF-1 (Sc_3NC_{80}) dimer junctions showing the characteristic shoulder in the approach G trace and both positive and negative Seebeck coefficients during the dimer formation. (c-d) EMF-2 ($Sc_3C_2@C_{80}$) dimer junctions showing the characteristic shoulder in the approach G trace and positive Seebeck coefficients during the dimer formation. (e-f) EMF-3 (Er_3NC_{80}) dimer junctions showing the characteristic shoulder in the approach G trace and positive thermopower during the dimer formation.

Thermopower values of the dimer junctions are measured with the same procedure introduced for the monomers (single-molecule junctions), stopping the tip movement every few steps and shooting small I-V ramps in the presence of a temperature difference ΔT between tip and sample. Diverse thermoelectric responses are observed for the EMF dimer junctions, which yield both positive and negative Seebeck coefficients as the monomer counterparts.

To better account for junction-to-junction variability, several approach-retraction curves are acquired for each of the EMF dimers. 2D histograms of thermopower S *vs* conductance G are plotted in Figure 3.24. In Figure 3.24(a-c) 2D histograms built with the complete approach traces, from tunnelling to almost metallic contact formation, are shown, although only the low conductance values correspond to dimer junctions. In order to analyse the dimer behaviour, data obtained from the I-V ramps shot during the characteristic shoulder in each individual G curve are selected and 2D histograms of Figure 3.24(d-f) are built. They are the result of thermopower and conductance simultaneous measurements while forming and squeezing dimer junctions and they collect data from above the instrumental noise to the drop in the conductance when the dimer junction breaks. We observe that these histograms present peculiar shapes and a distribution of values less uniform than in the case of the monomers (Figure 3.16).

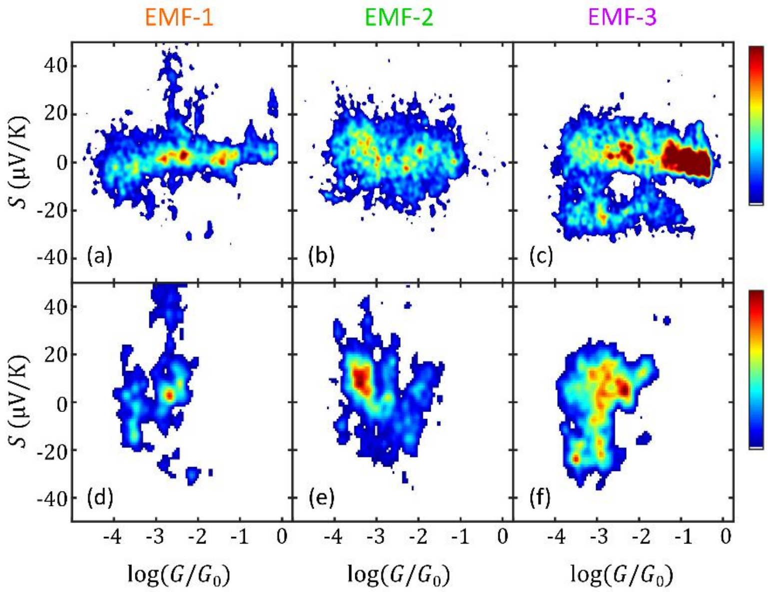

Figure 3.24: Thermopower S *vs* conductance G 2D histograms for EMF dimers. (a-c) S *vs* G 2D histograms built with the complete traces, from the noise level until close to the metallic contact. Each column corresponds to one molecule, as indicated on top. The number of dimer junctions used for each histogram is, from left to right: 35 $Sc_3N@C_{80}$ (EMF-1) dimer junctions, 48 $Sc_3C_2@C_{80}$ (EMF-2) dimer junctions and 52 $Er_3N@C_{80}$ (EMF-3) dimer junctions. (d-f) S *vs* G 2D histograms of the dimer formation, from the noise level to the drop in conductance, is gathered in these histograms.

This can be further analysed in the corresponding conductance and thermopower 1D histograms, presented in Figure 3.25. Dimer formation is difficult to identify in the conductance histogram of the whole approach traces (Figure 3.25(a)) and the histogram built just with the data for the shoulder (Figure 3.25(c)) gives a better idea of the dimers behaviour, which also applies to the thermopower histograms (Figure 3.25(b,d)). Mean conductance $\overline{G_{dim}}$ and thermopower $\overline{S_{dim}}$ values obtained from the data of the shoulder (i.e. dimer formation) are gathered in Table 3.3, as well as the standard deviations, $\sigma_{G,dim}$ and $\sigma_{S,dim}$, respectively. Conductance of the EMF dimers is found to be around one and a half orders of magnitude smaller than the conductance of single-molecule junctions (see Table 3.2). We obtain $\overline{G_{dim}} =$

$0.0012\ G_0$ for EMF-1, $\overline{G_{dim}} = 0.0011\ G_0$ for EMF-2 and $\overline{G_{dim}} = 0.0012\ G_0$ for EMF-3 dimer junctions, respectively, all of them slightly smaller than the previously reported value for the conductance of C_{60} dimers, $\overline{G_{dim}} = 0.0018\ G_0$ [Evangeli2013]. Additionally, the double peak that appears in the EMF-1 histogram results quite peculiar for conductance measurements.

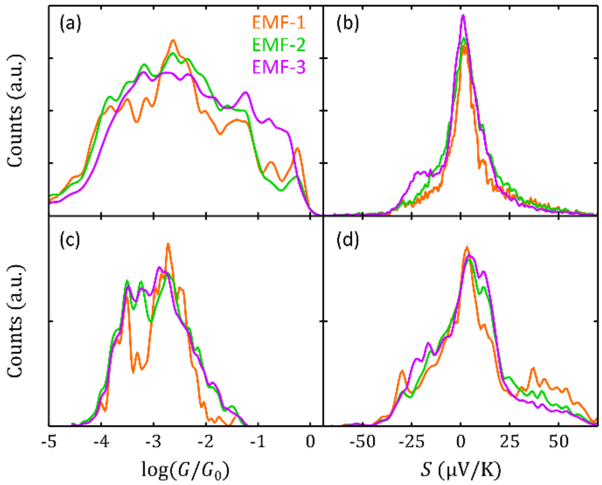

Figure 3.25: Conductance G and thermopower S 1D histograms for EMF dimers. (a,b) Conductance G and thermopower S 1D histograms for complete traces measured for dimer junctions formed with the three EMFs investigated: EMF-1 in orange, EMF-2 in green and EMF-3 in purple. (c,d) G and S 1D histograms for the complete dimer-characteristic shoulder of each molecular junction. Mean values $\overline{G_{dim}}$ and $\overline{S_{dim}}$, and standard deviations $\sigma_{G,dim}$ and $\sigma_{S,dim}$, can be found in Table 3.3. The data plotted in this figure correspond to the molecular junctions shown in Figure 3.24.

Table 3.3: Mean conductance $\overline{G}$ and thermopower $\overline{S}$ values for EMF-dimers, and corresponding standard deviations, σ_G and σ_S, respectively. This statistical analysis has been performed with the data plotted in Figure 3.25(c,d).

	$\overline{G_{dim}}$ (G_0)	$\sigma_{G,dim}$ (G_0)	$\overline{S_{dim}}$ (μV/K)	$\sigma_{S,dim}$ (μV/K)
EMF-1 ($Sc_3N@C_{80}$) dimers	$10^{-2.93}$	$10^{0.35}$	8.1	27.0
EMF-2 ($Sc_3C_2@C_{80}$) dimers	$10^{-2.94}$	$10^{0.28}$	5.3	21.7
EMF-3 ($Er_3N@C_{80}$) dimers	$10^{-2.93}$	$10^{0.27}$	2.7	20.6

Regarding the thermopower, histograms shown in Figure 3.25(d) are more or less centred on zero but they are not symmetric for positive and negative values. This asymmetry of the histograms is possibly an indication of some kind of interaction between the molecules forming the dimers. Considering the transmission functions shown in Figure 3.21(d-f) for EMF-1 single-molecule junctions and assuming that a similar mechanism (a LUMO resonance) originates the bi-thermoelectric response of the other endohedral metallofullerenes investigated, a simple picture for the thermopower of dimer junctions would be to consider the addition of the thermopower of each individual molecule participating in the junction, based on Landauer formalism introduced in Chapter 1. EMF-1 and EMF-3 single-molecule junctions at first-contact show positive and negative Seebeck coefficients mainly centred on zero, with different dispersion of values for each of them, while EMF-2 shows values centred on zero but also around $-25\ \mu\mathrm{V/K}$. It can be expected, thus, that the addition of the thermopower of two EMFs in series results also in a histogram centred at zero and with twice the dispersion of the single-molecule histograms. Comparison of the values shown in Table 3.2 and 3.3 evidences that this is the situation for EMF-3 junctions, the Er-based metallofullerene. Interestingly, the mean thermopower of EMF-3 dimers is approximately double than the mean thermopower of single-molecule junctions, while the dispersion also increases by a factor 2.7. The histograms of the other two molecules show a slightly larger dispersion in the case of dimer junctions but not a clear relation between the mean S values of dimers and monomers are observed. The tendency, though, does change and EMF-1 and EMF-2 dimer junctions show a larger probability of having a positive thermopower than the monomers.

From these observations we deduce that there is possibly interaction between the EMFs molecules forming the dimers and that some configurations are more favourable than others. In particular, dimer junctions exhibit a certain tendency to present positive thermopower values, in marked contrast with C_{60} dimer junctions previously reported to have a mean thermopower $\overline{S_{d\imath m}} = -33\ \mu\mathrm{V/K}$ [Evangeli2013].

3.5 Conclusions

In this chapter we have presented our experimental investigation of the conductance and thermopower of endohedral metallofullerenes (EMFs) single- and double-molecule junctions, namely, $Sc_3N@C_{80}$, $Sc_3C_2@C_{80}$ and $Er_3N@C_{80}$. The last one was synthesized and the three EMFs were purified by the group of Prof. Kyriakos Porfyrakis, in Oxford University (United Kingdom).

The STM-Imaging technique has been exploited to investigate the transport properties of these molecules connected with Au electrodes, in ambient conditions and at room temperature. STM images of individual EMFs on the surface have been used to confirm formation of single-molecule junctions whose conductance and thermopower have been simultaneously acquired, thus offering information about the evolution of the junction. For the three EMF investigated, first-contact conductance is found to be slightly smaller than that of the pristine C_{60} but still quite high for organic molecular junctions. Regarding thermoelectricity, all the compounds present positive or negative Seebeck coefficient depending on the particular molecule connected and without modifying the chemical composition, an effect that we have named bi-thermoelectricity.

Interestingly, tunnelling spectroscopy performed on different isolated molecules have shown a correlation between the asymmetry of the I-V curves and the sign of the thermopower obtained when contacting the molecule, further indicating a change in the slope of the transmission function from molecule to molecule.

Tunability of the sign of the thermopower by mechanical compression of the junctions have been demonstrated by performing consecutive compression cycles with the tip without breaking contact with the molecules.

Finally, DFT theoretical calculations performed by the group of Prof. Colin J. Lambert for $Sc_3N@C_{80}$ junctions have demonstrated that bi-thermoelectricity is produced by the presence of a LUMO resonance close to the Fermi level of the electrodes. This resonance is associated to the presence of the metallic cluster inside the fullerene cage and its exact energy and shape are molecular orientation- and compression-dependent, in good agreement with the tunnelling spectroscopy and the compression cycles observations.

Additionally, dimer EMF junctions (two molecules connected in series) have shown similar bi-thermoelectricity with a shift towards positive thermopower and an even larger dispersion of values, especially for $Er_3N@C_{80}$ junctions, possibly due to the combined effect of the individual molecules.

References

[Agraït1995] N. Agraït, G. Rubio and S. Vieira. “Plastic Deformation of Nanometer-Scale Gold Connective Necks”. *Physical Review Letters* **74**(20), 3995 (1995).

[Agraït1996] N. Agraït, G. Rubio and S. Vieira. “Plastic Deformation in Nanometer Scale Contacts”. *Langmuir* **12**(19), 4505-4509 (1996).

[Akasaka2002] T. Akasaka and Sh. Nagase (editors). “Endofullerenes: A New Family of Carbon Clusters”. Springer (2002).

[Bergfield2010] J. P. Bergfield, M. A. Solis and C. A. Stafford. “Giant thermoelectric effect from transmission supernodes”. *ACS Nano* **4,** 5314–5320 (2010).

[Buseck1992] P. R. Buseck, S. J. Tsipursky and R. Hettich. "Fullerenes from the Geological Environment". *Science* **257**(5067), 215-217 (1992).

[Cami2010] J. Cami, J. Bernard-Salas, E. Peeters, S. E. Malek. "Detection of C_{60} and C_{70} in a Young Planetary Nebula". *Science* **329**(5996), 1180-1182 (2010).

[Campanera2002] J. M. Campanera, C. Bo, M. M. Olmstead, A. L. Balch and J. M. Poblet “Bonding within the Endohedral Fullerenes $Sc_3N@C_{78}$ and $Sc_3N@C_{80}$ as Determined by Density Functional Calculations and Reexamination of the Crystal Structure of $\{Sc_3N@C_{78}\}\cdot Co(OEP)\}\cdot 1.5(C_6H_6)\cdot 0.3(CHCl_3)$”. *The Journal of Physical Chemistry A* **106**(51), 12356-12364 (2002).

[Chai1991] Y. Chai, T. Guo, C. Jin, R. E. Haufler, L. P. F. Chibante, J. Fure, L. Wang, J. M. Alford and R. E. Smalley. “Fullerenes with metals inside”. *The Journal of Physical Chemistry* **95**(20), 7564-7568 (1991).

[Chen1992] T. Chen, S. Howells, M. Gallagher, D. Sarid, L. D. Lamb, D. R. HuAman and R. K. Workman. “Scanning-tunneling-microscopy and spectroscopy studies of C_{70} thin films on gold substrates”. *Physical Review B* **45**(24), 14411-14414 (1992).

[Chen2017] C.-H. Chen, D. S. Krylov, S. M. Avdoshenko, F. Liu, L. Spree, R. Yadav, A. Alvertis, L. Hozoi, K. Nenkov, A. Kostanyan, T. Greber, A. U. B. Wolter and A. A. Popov. “Selective arc-discharge synthesis of Dy_2S-clusterfullerenes and their isomer-dependent single molecule magnetism”. *Chemical Science* **8**, 6451-6465 (2017).

[Cordiner2019] M. A. Cordiner, H. Linnartz, N. L. J. Cox, J. Cami, F. Najarro, C. R. Proffitt, R. Lallement, P. Ehrenfreund, B. H. Foing and T. R. Gull. “Confirming Interstellar C_{60}^+ Using the Hubble Space Telescope”. *The Astrophysical Journal Letters* **875**(2) (2019).

[Dunsch2007] L. Dunsch and S. Yang. “Metal Nitride Cluster Fullerenes: Their Current State and Future Prospects”. *Small* **3**(8), 1298-1320 (2007).

[Evangeli2013] C. Evangeli, K. Gillemot, E. Leary, M. T. González, G. Rubio-Bollinger, C. J. Lambert and N. Agraït. “Engineering the Thermopower of C_{60} Molecular Junctions”. *Nano Letters* **13**(5), 2141-2145 (2013).

[Evangeli2014] C. Evangeli. “Thermopower and Conductance of Single-Molecule Junctions and Atomic Contacts”. PhD Thesis (2014).

[Evangeli2015] C. Evangeli, M. Matt, L. Rincón-García, F. Pauly, P. Nielaba, G. Rubio-Bollinger, J. Carlos Cuevas and N. Agraït. “Quantum Thermopower of Metallic Atomic-Size Contacts at Room Temperature”. *Nano Letters* **15**(2), 1006-1011 (2015).

[Ferrer2014] J. Ferrer, C. J. Lambert, V. M. García-Suárez, D. Zs Manrique, D. Visontai, L. Oroszlany, R. Rodríguez-Ferradás, I. Grace, S. W. D. Bailey, K. Gillemot, H. Sadeghi and L. A. Algharagholy. “GOLLUM: a next-generation simulation tool for electron, thermal and spin transport”. *New Journal of Physics* **16,** 093029 (2014).

[Finch2009] C. M. Finch, V. M. García-Suárez and C. J. Lambert. “Giant thermopower and figure of merit in single-molecule devices”. *Physical Review B* **79,** 033405 (2009).

[Fujita1996] D. Fujita, T. Yakabe, H. Nejoh, T. Sato and M. Iwatsuki. “Scanning tunneling microscopy study on the initial adsorption behavior of C_{60} molecules on a reconstructed Au(111)-(23 x √3) surface at various temperatures”. *Surface Science* **366**, 93-98 (1996).

[Gimzewski1994] J. K. Gimzewski, S. Modesti and R. R. Schlittler. “Cooperative Self-Assembly of Au Atoms and C_{60} on Au(110) Surfaces”. *Physical Review Letters* **72**(7), 1036 (1994).

[González2006] M. T. González, S. Wu, R. Huber, S. J. van der Molen, C. Schönenberger and M. Calame. “Electrical Conductance of Molecular Junctions by a Robust Statistical Analysis”. *Nano Letters* **6**(10), 2238-2242 (2006).

[Guha2005] S. Guha and K. Nakamoto. “Electronic structures and spectral properties of endohedral fullerenes”. *Coordination Chemistry Reviews* **249**, 1111-1132 (2005).

[Hahn1998] J. R. Hahn, Y. A. Hong and H. Kang. “Electron tunneling across an interfacial water layer inside an STM junction: tunneling distance, barrier height and water polarization effect”. *Applied Physics A* **66**(1), S467-S472 (1998).

[Heath1985] J. R. Heath, S. C. O'Brien, Q. Zhang, Y. Liu, R. F. Curl, F. K. Tittel and R. E. Smalley. “Lanthanum complexes of spheroidal carbon shells”. *Journal of the American Chemical Society* **107** (25), 7779-7780 (1985).

[Ito2007] Y. Ito, T. Okazaki, S. Okubo, M. Akachi, Y. Ohno, T. Mizutani, T. Nakamura, R. Kitaura, T. Sugai and H. Shinohara. “Enhanced 1520 nm Photoluminescence from Er^{3+} Ions in Di-erbium-carbide Metallofullerenes $(Er_2C_2)@C_{82}$ (Isomers I, II, and III)”. *ACS Nano* **1**(5), 456-462 (2007).

[Jin2014] P. Jin, C. Tang, Z. Chen. “Carbon atoms trapped in cages: Metal carbide clusterfullerenes”. *Coordination Chemistry Reviews* **270-271**, 89-111 (2014).

[Joachim1995a] C. Joachim, J. K. Gimzewski, R. R. Schlittler and C. Chavy, “Electronic Transparence of a Single C60 Molecule”, *Physical Review Letters* **74** (11), 2102-2105 (1995).

[Joachim1995b] C. Joachim and J. K. Gimzewski. “Analysis of Low-Voltage *I*(*V*) Characteristics of a Single C_{60} Molecule”. *Europhysics Letters* **30**(7), 409-414 (1995).

[Katz2006] E. A. Katz. "Fullerene Thin Films as Photovoltaic Material". Chapter 13 in “Nanostructured materials for solar energy conversion”; T. Sōga (editor). Elsevier (2006).

[Kim2014] S. Kim, W. Jeong, K. Kim, W. Lee and P. Reddy. “Electrostatic control of thermoelectricity in molecular junctions”. *Nature Nanotechnology* **9,** 881-885 (2014).

[Krätschmer1990] W. Krätschmer, L. D. Lamb, K. Fostiropoulos and D. R. Huffman, “Solid C_{60}: a new form of carbon”, *Nature* **347**, 354-358 (1990).

[Kroto1985] H. W. Kroto, J. R. Heath, S. C. O’Brien, R. F. Curl and R. E. Smalley, “C_{60}: Buckminsterfullerene", *Nature* **318**, 162-163 (1985).

[Kroto1988] H. Kroto. “Space, Stars, C_{60}, and Soot”. *Science* **242**(4882), 1139-1145 (1988).

[Kroto1991] H. W. Kroto; A. W. Allaf and S. P. Balm. “C_{60}: Buckminsterfullerene”. *Chemical Reviews* **91**(6), 1213-1235 (1991).

[Lalwani2013] G. Lalwani and B. Sitharaman. “Multifunctional fullerene and metallofullerene based nanobiomaterials”. *Nano LIFE* **03**(03), 1342003 (2013).

[Lambert2015] C. J. Lambert. “Basic concepts of quantum interference and electron transport in single-molecule electronics”. *Chemical Society Reviews* **44,** 875-888 (2015).

[Langa2011] F. Langa De La Puente and J.-F. Nierengarten (editors). “Fullerenes: Principles and Applications”. RSC Publishing (2011).

[Lee2014] S. K. Lee, T. Ohto, R. Yamada and H. Tada. “Thermopower of Benzenedithiol and C_{60} Molecular Junctions with Ni and Au Electrodes”. *Nano Letters* **14,** 5276-5280 (2014).

[Lee2015] S. K. Lee, M. Buerkle, R. Yamada, Y. Asai and H. Tada “Thermoelectricity at the molecular scale: a large Seebeck effect in endohedral metallofullerenes”. *Nanoscale* **7**, 20497 (2015).

[Leigh2007] D. F. Leigh, C. Nörenberg, D. Cattaneo, J. H. G. Owen, K. Porfyrakis, A. Li Bassi, A. Ardavan, G. A. D. Briggs. “Self-assembly of trimetallic nitride template fullerenes on surfaces studied by STM”. *Surface Science* **601**, 2750-2755 (2007).

[Lu2003] X. Lu, M. Grobis, K. H. Khoo, S. G. Louie and M. F. Crommie. “Spatially Mapping the Spectral Density of a Single C_{60} Molecule”. *Physical Review Letters* **90**(9), 096802 (2003).

[Macfarlane2001] R. M. Macfarlane, D. S. Bethune, S. Stevenson, and H. C. Dorn. “Fluorescence spectroscopy and emission lifetimes of Er^{3+} in $Er_xSc_{3-x}N@C_{80}$ (x=1–3)”. *Chemical Physics Letters* **343**, 229-234 (2001).

[Nečas2012] D. Nečas and P. Klapetek. “Gwyddion: an open-source software for SPM data analysis”. *Central European Journal of Physics* **10**, 181-188 (2012).

[Néel2007] N. Néel, J. Kröger, L. Limot, T. Frederiksen, M. Brandbyge and R. Berndt. “Controlled Contact to a C_{60} Molecule”. *Physical Review Letters* **98**, 065502 (2007).

[Néel2008] N. Néel, J. Kröger, L. Limot and R. Berndt. “Conductance of Oriented C_{60} Molecules”. *Nano Letters* **8**(5), 1291-1295 (2008).

[Nishino2005] T. Nishino, T. Ito and Y. Umezawa. “A fullerene molecular tip can detect localized and rectified electron tunneling within a single fullerene-porphyrin pair”. *Proceedings of the National Academy of Sciences of the United States of America* **102**(16), 5659-5662 (2005).

[Nörenberg2008] C. Nörenberg, D.F. Leigh, D. Cattaneo, K. Porfyrakis, A. Li Bassi, C.S. Casari, M. Passoni, J. H. G. Owen and G. A. D. Briggs. “Self-assembly and electronic effects of $Er_3N@C_{80}$ and $Sc_3N@C_{80}$ on Au(111) and Ag/Si(111) surfaces”. *Journal of Physics: Conference Series* **100,** 052080 (2008).

[Ohno1991] T. R. Ohno, Y. Chen, S. E. Harvey, G. H. Kroll, J. H. Weaver, R. E. Hauler and R. E. Smalley. “C_{60} bonding and energy-level alignment on metal and semiconductor surfaces”. *Physical Review B* **44**(24), 13747-13755 (1991).

[Paulsson2003] M. Paulsson and S. Datta. “Thermoelectric effect in molecular electronics”. *Physical Review B* **67**, 241403(R) (2003).

[Popov2012] A. A. Popov, S. Yang and Lothar Dunsch. “Endohedral Fullerenes”. *Chemical Reviews* **113**, 5989-6113 (2013).

[Reddy2007] P. Reddy, S.-Y. Jang, R. A. Segalman and A. Majumdar. “Thermoelectricity in Molecular Junctions”. *Science* **315**, 1568-1571 (2007).

[Repp2005] J. Repp, G. Meyer, S. M. Stojković, A. Gourdon and C. Joachim. “Molecules on Insulating Films: Scanning-Tunneling Microscopy Imaging of Individual Molecular Orbitals”. *Physical Review Letters* **94**(2), 026803 (2005).

[Rincón-García2016] L. Rincón-García, Ali K. Ismael, C. Evangeli, I. Grace, G. Rubio-Bollinger, K. Porfyrakis, N. Agraït and C. J. Lambert. “Molecular design and control of fullerene-based bi-thermoelectric materials”. *Nature Materials* **15**, 289-294 (2016).

[Rodríguez-Fortea2011a] A. Rodríguez-Fortea, A. L. Balch and J. M. Poblet. “Endohedral metallofullerenes: a unique host-guest association”. *Chemical Society Reviews* **40**, 3551-3563 (2011).

[Rodríguez-Fortea2011b] A. Rodríguez-Fortea, S. Irle and J. M. Poblet. “Fullerenes: formation, stability, and reactivity”. *WIREs Computational Molecular Science* **1**(3), 350-367 (2011).

[Rogero2002] C. Rogero, J. I. Pascual, J. Gómez-Herrero and A. M. Baró. “Resolution of site-specific bonding properties of C_{60} adsorbed on Au(111)”. *Journal of Chemical Physics* **116**(2), 832-836 (2002).

[Rohlfing1984] E. A. Rohlfing, D. M. Cox and A. Kaldor. "Production and characterization of supersonic carbon cluster beams". *Journal of Chemical Physics* **81**(7), 3322 (1984).

[Roukala2017] J. Roukala, M. Straka, S. Taubert, J. Vaara and P. Lantto. “Ratcheting rotation or speedy spinning: EPR and dynamics of $Sc_3C_2@C_{80}$”. *Chemical Communications* **53**, 8992-8995 (2017).

[Rubio1996] G. Rubio, N. Agraït and S. Vieira. “Atomic-Size Metallic Contacts: Mechanical Properties and Electronic Transport”. *Physical Review Letters* **76**(13), 2302-2305 (1996).

[Rubio-Bollinger2001] G. Rubio-Bollinger, S. R. Bahn, N. Agraït, N., K. W. Jacobsen and S. Vieira. “Mechanical properties and formation mechanisms of a wire of single gold atoms”. *Physical Review Letters* **87,** 026101 (2001).

[Ruoff1991] R. S. Ruoff and A. L. Ruoff. “The bulk modulus of C_{60} molecules and crystals: A molecular mechanics approach”. *Applied Physics Letters* **59,** 1553 (1991).

[Schull2008] G. Schull, N. Néel, M. Becker, J. Kröger and R. Berndt. “Spatially resolved conductance of oriented C_{60}”. *New Journal of Physics* **10**, 065012 (2008).

[Schull2009] G. Schull, T. Frederiksen, M. Brandbyge and R. Berndt. “Passing Current through Touching Molecules”. *Physical Review Letters* **103**(20), 206803 (2009).

[Smalley1996] R. Smalley, “Discovering the Fullerenes”, Nobel Lecture, p. 97 (07-12-1996); nobelprize.org

[Soler2002] J. M. Soler, E. Artacho, J. D. Gale, A. García, J. Junquera, P. Ordejón and D. Sánchez-Portal. “The SIESTA method for ab initio order-N materials simulation”. *Journal of Physics: Condensed Matter* **14,** 2745 (2002).

[Stevenson1999] S. Stevenson, G. Rice, T. Glass, K. Harich, F. Cromer, M. R. Jordan, J. Craft, E. Hadju, R. Bible, M. M. Olmstead, K. Maitra, A. J. Fisher, A. L. Balch and H. C. Dorn. “Small-bandgap endohedral metallofullerenes in high yield and purity”. *Nature* **401,** 55-57 (1999).

[Vacek2015] J. Vacek, J. Vacek Chocholoušová, I. G. Stará, I. Starýa and Y. Dubi. “Mechanical tuning of conductance and thermopower in helicene molecular junctions”. *Nanoscale* **7,** 8793-8802 (2015).

[Wiesendanger1994] R. Wiesendanger. “Scanning Probe Microscopy and Spectroscopy: Methods and Applications”. Cambridge University Press (1994).

[Yang1987] S. H. Yang, C. L. Pettiette, J. Conceicao, O. Cheshnovsky and R. E. Smalley. “Ups of buckminsterfullerene and other large clusters of carbon”. *Chemical Physics Letters* **139**(3,4), 233-238 (1987).

[Yee2011] S. K. Yee, J. A. Malen, A. Majumdar and R. Segalman. “Thermoelectricity in Fullerene Metal Heterojunctions”. *Nano Letters* **11**(10), 4089-4094 (2011).

4. Conductance and thermopower measurements with the STM-Break Junction technique: fluorenes, oligoynes and porphyrins

Single-molecule junctions are a key system to address and answer many open questions about charge transport at the nanoscale [Malen2010]. One of their major strengths is the possibility to advantageously tune their transport characteristics by means of an appropriate chemical design of the molecules. Combined experimental and theoretical studies have demonstrated that both the conductance and thermopower of single-molecule junctions are dependent upon chemical composition and the position of the molecular energy levels with respect to the Fermi level of the metal electrodes [Baheti2008].

In a single-molecule junction (see Figure 2.10), several structural elements or factors can be modified to influence on the transport properties in a more or less controlled way. Examples of reported strategies include varying the chemical composition playing with substituents in the core [Baheti2008] or with conjugated *vs* non-conjugated bridging units [Chang 2014], modifying chemical connections in the backbone (para- *vs* meta-) [Maio2018], varying the anchor groups within a family of molecules [Chang2014; Malen2009a; Tan2011; Balachandran2012, Widawsky2013; Baheti2008], tuning the position of intramolecular energy levels relative to the work function of metallic electrodes [Yee2011; Lee2014; Guo2013], varying the molecular length [Malen2009a; Tan2011; Widawsky2013; Chang2014], tuning the interaction between two neighbouring molecules [Evangeli2013], or controlling the transport properties with an electrostatic gate [Kim2014a] or electrochemically [García-Suárez2014]. Examples of organic molecules used in these investigations include fullerenes [Yee2011; Lee2014; Evangeli2013; Rincón-García2016a], benzenedithiol [Yee2011; Lee2014; Reddy2007], oligothiophenes with thiolate end-groups [Chang2014] and molecules with amine or pyridyl anchors, namely 1,4-diaminobenzene and π-extended analogs, and 4,4'bipyridine [Kim2014b]. All these single-molecule experiments yielded room-temperature values of S ranging in magnitude from about 1 to $50\ \mu\mathrm{V/K}$.

Within this general background, we present in this chapter our investigation about the electric and thermoelectric properties of three different groups of molecules: fluorene-based compounds, oligoyne wires and Zn-porphyrin oligomers. In these experimental studies, Au|single-molecule|Au junctions are formed with each compound and their conductance and thermopower are simultaneously measured in ambient conditions and at room temperature using the so-called STM-Break Junction (STM-BJ) technique introduced in Chapter 2 of this manuscript (Section 2.4.3).

Our already published study about a group of five fluorene derivatives, where transport properties tunability is partially achieved by chemical substitution of the side-group on a fix backbone, is gathered in Section 4.1 [Yzambart2018]. Next, we focus our attention on the length dependence of thermopower of single-molecule junctions and present the experimental results obtained when investigating a family of four oligoyne systems (Section 4.2) and a series of three oligo-porphyrins (Section 4.3). We analyse in these two sections the influence on the charge transport of the molecular length, varied by increasing the number of constituent elements of the backbone (single-triple carbon bonds or porphyrin units, respectively). Finally, conclusions about the results obtained for the three series of molecules investigated are gathered in Section 4.4.

4.1 Fluorene derivatives

To study the influence on transport properties of different side-groups on the same backbone, one of the families of molecules investigated during this Thesis is a series of five 2,7-dipyridylfluorene derivatives with different substituents at the C(9) position [Yzambart2018].

The molecules, whose chemical structures are shown in Figure 4.1, have been synthesized by the group of Prof. Martin R. Bryce at Durham University (United Kingdom). The fluorene (Fl)-based molecules have terminal pyridyl anchor units at both ends to favour bonding with the Au electrodes atoms and they differ only in the substituents at C(9), namely 2H, 2Me, 2OMe, $2CF_3$ and O (named Fl-H, Fl-Me, Fl-OMe, Fl-CF_3 and Fl-O, respectively).

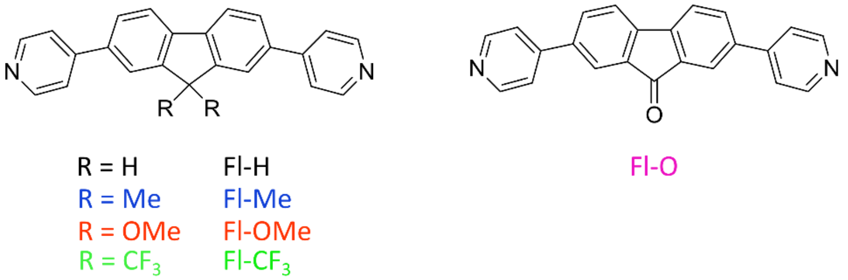

Figure 4.1: Chemical structure of the five fluorene (Fl)-based molecules explored. The series consists of 2,7-dipyridylfluorene derivatives with different substituents (2H, 2Me, 2OMe, $2CF_3$ and O) at the C(9) position. Molecules are named Fl-H, Fl-Me, Fl-OMe, Fl-CF_3 and Fl-O, respectively. All the fluorene derivatives bind to the Au electrodes through pyridine anchor groups at both ends.

Fluorene is a polycyclic aromatic hydrocarbon formed by two phenyl rings linked by an extra carbon atom in position 9 (Fl-H in Figure 4.1). This planarized biphenyl molecule has proved to perform well as molecular-wire [Atienza-Castellanos2007] and has been chosen as the backbone of this family for three reasons:

(i) it is a well-established system whose conductance has been extensively studied in recent years with break-junction techniques [Haiss2008; Vonlanthen2009; Klausen2014; Gantenbein2017] although its thermoelectric performance has not, to our knowledge, been investigated so far;

(ii) based on chemical substitution, it is possible to attempt a systematic variation of the substituents at C(9) position to attach electron-donating (Me or OMe) or electron-withdrawing (CF_3) side-groups;

(iii) the C(9) carbon is sp^3 hybridized in most of the molecules under study (except in Fl-O), so the pendant substituents are not directly conjugated to the π-system of the backbone. This allows us to investigate the effects of non-conjugated side-groups on the junction's thermoelectric properties. In the case of the fluorenone Fl-O, the pendant oxygen atom is conjugated to the backbone through the sp^2-hybridized C(9) carbon, making this compound, in principle, electronically different to the other four.

Samples are prepared by drop-casting the compounds onto gold substrates. As in Chapter 3, we use 250-nm-thick Au films on glass substrates (Arrandee^{TM}, Germany), that are flame annealed to form a polycrystalline Au(111) surface (see more details in Section 3.3.2). After cooling down and retrieving room temperature, the Au substrates are immersed in a 10^{-3} M dichloromethane

(DCM) solution ($> 99.9\%$, Sigma-Aldrich) of the corresponding molecule for 30 minutes in darkness and are finally blown dry under nitrogen to prevent that excess material deposits on the surface during solvent evaporation. Samples are afterwards transferred to the STM chamber and the whole setup is allowed to stabilize for at least 15 minutes in order to equilibrate thermally and mechanically. Freshly mechanically cut Au wire ($0.25\ \mathrm{mm}$ diameter, 99.99% purity, Goodfellow) is used as tips.

4.1.1 Conductance G characterization

Conductance G characterization of the Fl-based compounds is accomplished using the so-called STM-Break Junction technique introduced in detail in Chapter 2 (Section 2.4.3), in which molecules are connected between the electrodes after the Au-Au metallic contact is broken.

For all the experiments with fluorene-based molecules, a bias voltage $V_{bias} = 100 - 200\ \mathrm{mV}$ applied to the substrate is employed, as well as a $12\ \mathrm{M\Omega}$ resistor connected in series to the sample in order to extend the total range of conductance monitored. We use a double-step current-to-voltage amplifier with a total gain of $2.5 \times 10^{10}\ \mathrm{V/A}$, which allows for an experimental total range of conductance ($G = I/V_{bias}$) from $10^{-6.5}G_0$ up to $10^{0.5}G_0$, expanding seven orders of magnitude. $G_0 = 2e^2/h$ is the quantum of conductance, e is the electron's charge and h is Planck's constant.

Au|single-molecule|Au junctions are randomly formed when doing approach-retraction cycles with the tip, reaching each time the metallic contact, identified by conductance values larger than G_0 (the G value of one Au atom contact). After indenting the substrate with the STM tip and breaking the Au-Au contact, a molecule may be connected between both electrodes, as detailed in Section 2.4.3. The low concentration of molecules deposited facilitates the binding of a single molecule to the gold electrodes as the tip retracts from the surface, although this also implies that it is possible to find areas without molecules where junction formation is not observed. This is for instance the case for the conductance G *vs* tip displacement Δz retraction curve shown in Figure 4.2(a). Metallic contact breaking is clearly identifiable in this curve by a sudden jump down in the conductance of several orders of magnitude. Since no molecule is present in the junction, the signal recovers the tunnelling regime while the tip is still retracting (linear dependence with Δz when plotted in semilogarithmic scale) until the noise level is finally reached at the end of the approach-retraction cycle.

Examples of individual G *vs* Δz curves measured during tip retraction and showing junction formation are presented in Figure 4.2(b-f), one for each compound investigated. When a molecule binds between the electrodes, the signal in the G *vs* Δz traces abruptly drops from the one Au atom contact ($G = G_0$) to a conductance value several orders of magnitude smaller and then stabilizes giving rise to a conductance plateau, i.e. as the tip separates further from the surface the conductance remains almost constant, instead of decreasing exponentially as occurs with Au-Au tunnelling junctions (Figure 4.2(a)). The observation of such plateaus in the retraction curves is commonly considered as a signature of the formation of a molecular junction [Xu2003; Venkataraman2006a; González2006]. It also finally breaks as the tip keeps retracting and the conductance drops to the noise level typically with a sudden jump or with direct tunnelling current between the electrodes. Typical length of the observed plateaus generally matches the expected molecular length, suggesting single-molecule junction formation. Experiments show good junction formation probability, between 50% and 80% for all the molecules, as shown in Table 4.1. It is important to notice that, in each of these approach-retraction cycles, the gold tip is crashed into the gold surface ensuring tip cleanliness and some local reorganization of the atoms at the apex.

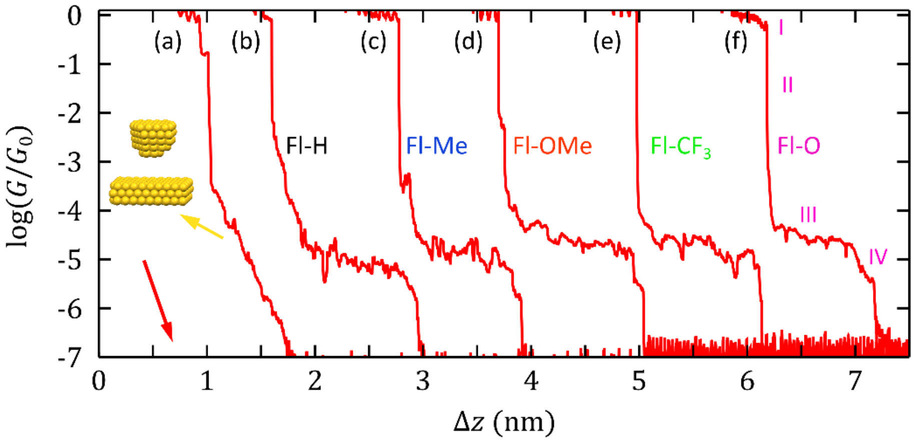

Figure 4.2: Individual conductance G *vs* tip displacement Δz retraction curves. Examples of retraction conductance traces for a Au-Au tunnelling junction as the one depicted on the left (a) and the five Fl-based compounds investigated (b-f). The relevant features identifiable during tip retraction have been marked in (f): one Au atom contact ($G = G_0$) (I); metallic contact breaking (II); conductance plateau signalling molecular junction formation (III), and molecular junction breaking (IV). $G_0 = 2e^2/h$ is the conductance quantum (e is the electron's charge and h is Planck's constant). Δz of the different traces has been displaced for the sake of clarity. The red arrow indicates the direction of increasing Δz and subsequent G decrease.

Table 4.1: Percentage of retraction G *vs* Δz curves showing a plateau values.

Molecule	Ratio
Fl-H	48%
Fl-Me	54%
Fl-OMe	77%
Fl-CF$_3$	71%
Fl-O	55%

Conductance G *vs* tip displacement Δz 2D histograms for each of the fluorene derivatives studied are plotted in Figures 4.3(a-e). These histograms are formed with hundreds of retract traces recorded in several experimental runs for each molecule. In order to plot them together and directly compare all the individual G *vs* Δz curves, the relative tip displacement of each trace is shifted to place the conductance value $G = 0.1\ G_0$ at the zero displacement position ($\Delta z = 0\ \mathrm{nm}$). All the aforementioned features present in an individual retraction curve are perfectly identifiable in these histograms, which also indicates a most probable plateau length of around 1.0-$1.5\ \mathrm{nm}$ for all the molecules. The equivalent G *vs* Δz 2D histogram of Au-Au tunnelling junctions is also shown in Figure 4.3(f), where it is evident the characteristic exponential distance dependence of conductance.

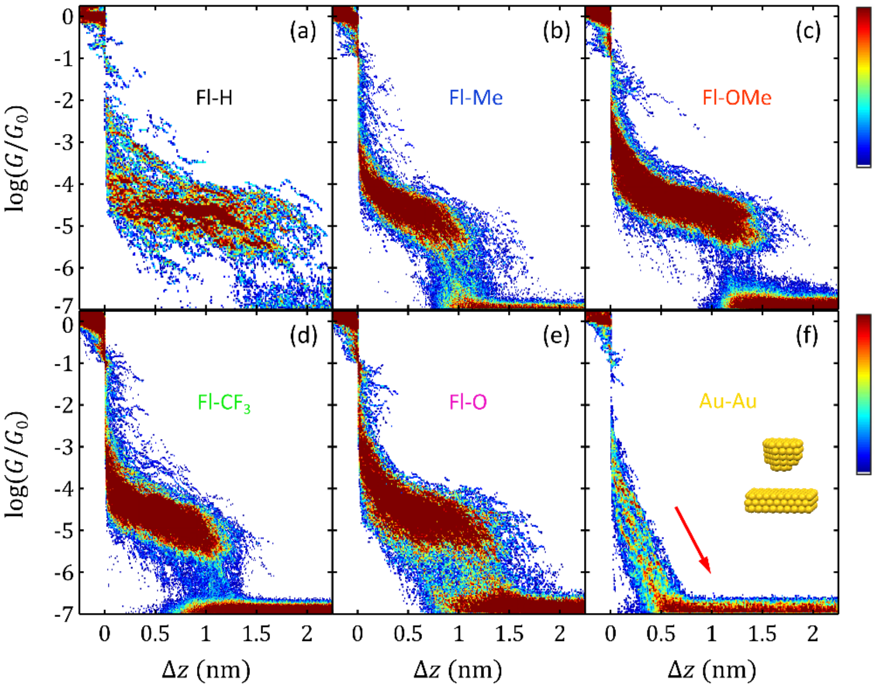

Figure 4.3: Conductance G *vs* tip displacement Δz 2D histograms. (a-e) G *vs* Δz 2D histograms for each of the fluorene derivatives explored. Histograms are formed with 74 Fl-H junctions (a), 350 Fl-Me junctions (b), 526 Fl-OMe junctions (c), 548 Fl-CF$_3$ junctions (d) and 374 Fl-O junctions (e). (f) G *vs* Δz 2D histogram of 96 Au-Au tunnelling junctions where no molecule is connected between the electrodes. In all the cases, the zero displacement ($\Delta z = 0$ nm) is chosen to be the position where $G = 0.1\, G_0$. The colour scale accounts for the number of points in each histogram.

The most probable value of the conductance of each compound $\bar{G}$ is found from the G 1D histograms built from all the conductance values measured and collected in Figure 4.3. The 1D histograms for the five molecules investigated are presented in Figure 4.4. In the histograms, a peak at $G = G_0$ can be identified corresponding to the Au-Au contact. The values on the left side of the histograms correspond to the noise level of the system, below $10^{-6.5} G_0$. An extra peak is observed that is not present when measuring only Au-Au contacts (in yellow in Figure 4.4(f)) and that corresponds to the molecular junction formation. It comes from the plateaus in the G *vs* Δz 2D histograms of Figure 4.3 which generates a junction-characteristic peak in the G 1D histograms. Using a Gaussian fit for each compound peak, $\bar{G}$ (the expected most probable value) and σ_G, the standard deviation, can be obtained. The Gaussian fits are plotted in the corresponding histogram in a lighter color and the values obtained from the fits are shown in the corresponding figure and summarized in Table 4.2 to facilitate comparison. We measure a very similar $\bar{G}$ value for all the molecules, possibly as a consequence of the similar transport pathways in each of them, which are predominantly located on the π-conjugated backbone. The values we obtain are similar to those previously reported using different BJ techniques for other fluorene derivatives (with thiol anchor groups) [Haiss2008; Vonlanthen2009].

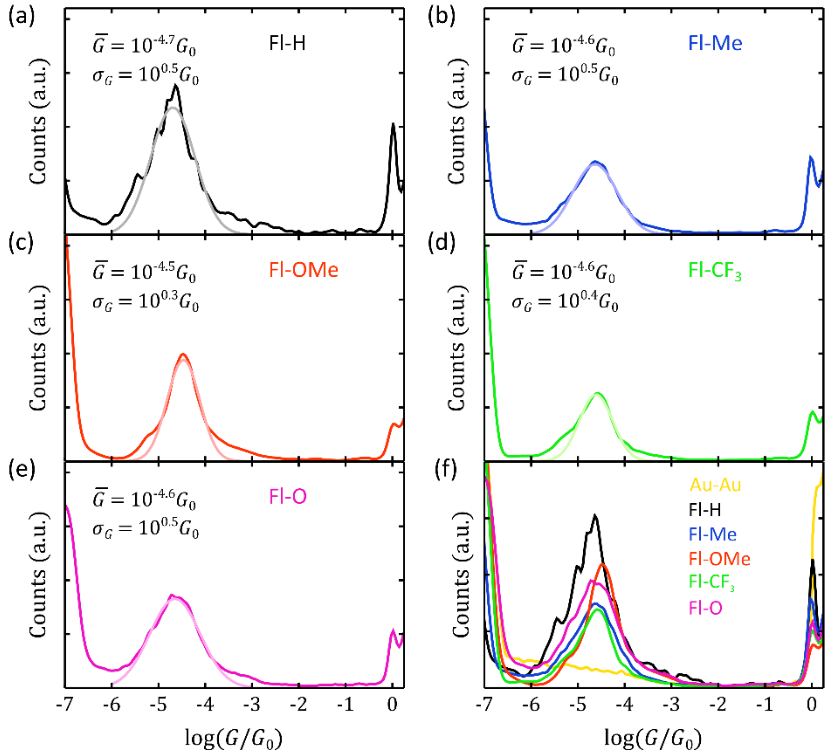

Figure 4.4: Conductance G 1D histograms. (a-e) G 1D histogram of each fluorene derivative and Gaussian fit of the junction-characteristic peak corresponding to the junction values, plotted in a lighter color superimposed to the histograms. $\bar{G}$ and σ_G in each panel are the expected (most probable) value of the conductance and the standard deviation of the fit, respectively. (f) Conductance G 1D histograms of all the molecules and Au-Au tunnelling junctions (in yellow) for comparison. Each histogram is normalized with its total number of measured values.

Table 4.2: Conductance experimental values. Measured expected conductance value $\bar{G}$ (most probable value according to the Gaussian fit applied) and conductance histogram widths σ_G (standard deviation from the same Gaussian fit) for all the fluorene derivatives investigated. The second column shows the bias voltage applied between the electrodes for the measurements of each compound.

Molecule	V_{bias} (V)	$\bar{G}$ (G_0)	σ_G (G_0)
Fl-H	0.20	$10^{-4.7}$	$10^{0.5}$
Fl-Me	0.20	$10^{-4.6}$	$10^{0.5}$
Fl-OMe	0.15	$10^{-4.5}$	$10^{0.3}$
Fl-CF$_3$	0.15	$10^{-4.6}$	$10^{0.4}$
Fl-O	0.10	$10^{-4.6}$	$10^{0.5}$

4.1.2 Thermopower S characterization

Thermopower S of Au|single-molecule|Au junctions is measured in this case using the STM-Break Junction (STM-BJ) technique introduced in detail in Chapter 2 (Section 2.4.3). During the tip motion the bias voltage is set at $V_{bias} = 200\ \mathrm{mV}$ ($V_{bias} = 100\ \mathrm{mV}$ in the case of Fl-O) and we stop it every 40-60 pm during retraction and sweep the voltage twice between $\pm\Delta V_0 = \pm 10\ \mathrm{mV}$. We measure the thermovoltage V_{th} of each fluorene derivative for four ΔTs (four temperature differences between tip and sample), namely, $\Delta T = 0\ \mathrm{K}$, $\sim 15\ \mathrm{K}$, $\sim 22\ \mathrm{K}$ and $\sim 30\ \mathrm{K}$. For each ΔT, the STM setup is allowed to stabilize for around 20 min before starting the measurements.

Examples of simultaneous G and V_{th} measurements for individual Fl-Me junctions are shown in Figure 4.5. In the case of the conductance (Figure 4.5(a)), complete retraction traces obtained at V_{bias} are presented (solid red line) as well as the G values measured from the slope of the I-V small ramps shot to characterize the thermovoltage, plotted as red empty circles. The good agreement between these two measurements of conductance indicates a correct I-V ramps acquisition process. Each of the individual curves shown Figure 4.5 is formed in the presence of a different ΔT applied between tip and sample. This is reflected in the thermovoltage signal, which increases in magnitude when increasing the temperature difference, as can be seen in Figure 4.5(b). Leaving aside the zero-ΔT junction, acquired in order to correct the offsets of the setup and confirm a right acquisition procedure, we obtain a negative value of the thermovoltage in the other three junctions, which indicates a negative thermopower. It is important to notice that conductance and thermovoltage are obtained simultaneously for any junction formed, at a given ΔT, which results a very powerful aspect of the experimental technique [Evangeli2014]. Equivalent curves for the other four compounds can be found in Appendix 4.A (at the end of this chapter).

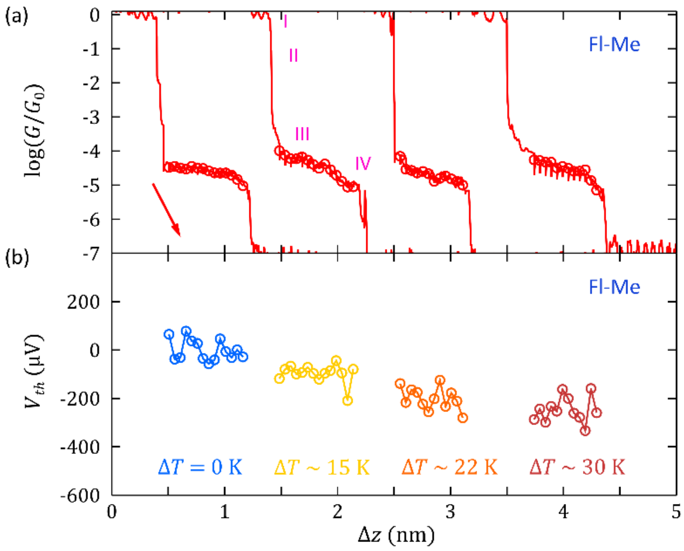

Figure 4.5: Individual conductance G and thermovoltage V_{th} *vs* tip displacement Δz retraction curves. Examples of simultaneous G (a) and V_{th} (b) measurements for single-molecule Fl-Me junctions. Each junction is formed in the presence of a given temperature difference ΔT between tip and sample. The different features identifiable in the G signal have been marked in the second junction: one Au atom contact ($G = G_0$) (I); metallic contact breaking (II); conductance plateau signalling molecular junction formation (III), and molecular junction breaking (IV). Thermovoltage is only acquired in the plateau and the G values obtained from the slope of the corresponding I-V ramps are plotted in (a) as red empty circles, showing good agreement with the complete retraction curve where conductance is measured with $V_{bias} = 200\ \mathrm{mV}$. Δz of the different traces has been displaced for the sake of clarity. The red arrow indicates the direction of tip displacement during the acquisition (retraction or increasing Δz).

In order to account for different junction configurations, we do a statistical analysis of the results and perform several experimental runs for each ΔT and each molecule, collecting hundreds of retraction traces as those shown in Figure 4.5. Figure 4.6 shows thermovoltage V_{th} 1D histograms built with the values of all the runs at each temperature difference. Histogram values are adequately shifted to place the corresponding 0-ΔT histogram correctly centered at zero. As advanced in the case of Fl-Me junctions, thermovoltage values increase in magnitude as the ΔT applied between tip and sample is enhanced and are confirmed to be typically negative for all the compounds. Additionally, histograms seem to become broader with increasing ΔT, which is to be expected because the current through the junction is proportional to the temperature of the tip . Fits to a Gaussian distribution for each histogram are also shown in Figure 4.6, plotted in a lighter color.

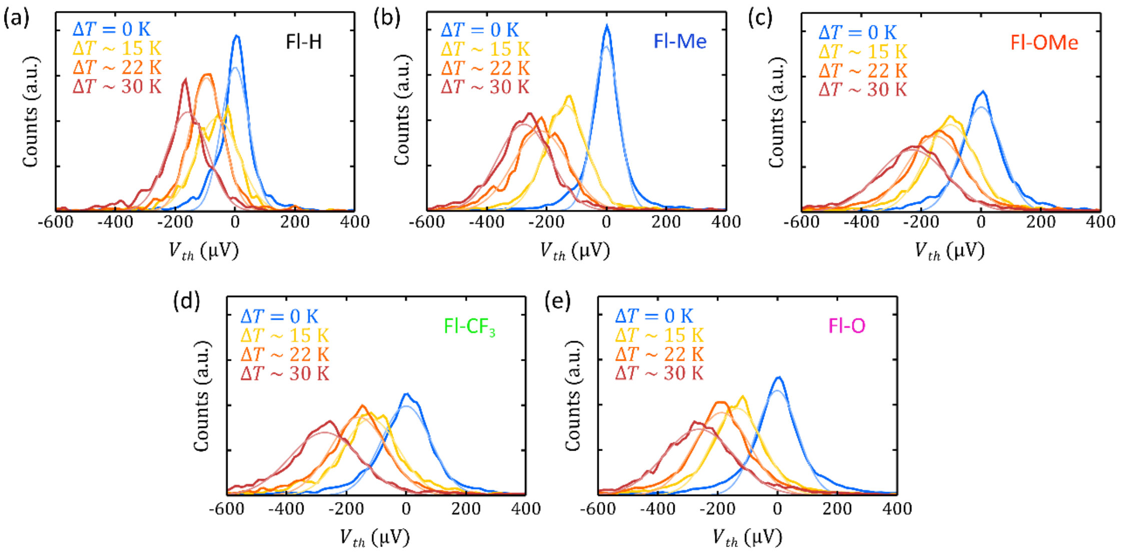

Figure 4.6: Thermovoltage V_{th} 1D histograms. (a-e) V_{th} 1D histograms of the five Fl-based molecules and Gaussian fits, plotted in a lighter color superimposed on the histograms. ΔT is the temperature difference applied between tip and sample. The total number of junctions in each panel is the following: 279 in (a), 800 in (b), 1476 in (c), 1347 in (d) and 1931 in (e).

Figure 4.7 shows the mean value $\overline{V_{th}}$ of each experimental run as a function of ΔT (empty circles). The error bars of $\overline{V_{th}}$ are the standard deviations $\sigma_{V_{th}}$ obtained from the Gaussian fit of each set of measurements. The linear fit shown in Figure 4.7 is is not the linear fit of the mean values of the experimental runs, but rather the linear fit of all the individual V_{th} values independently, giving to all of them the same weight. The slope of this fit corresponds to the average thermopower S of the corresponding molecule and the values are shown as an inset in each plot. The relative error of S obtained with this fit is smaller than 2% in all cases.

The Seebeck coefficient S of the different molecules is summarized in Table 4.3, with a variation from -5.5 μV/K, in the lowest case (compound Fl-H), to -9.0 μV/K, in the highest case (compound Fl-O). The experimental results show that the variation of the C(9) substituents has little effect on the conductance, while having a more significant effect in the thermopower, increasing the Seebeck coefficient by a factor of 1.65. The data show that all the substituents at C(9) slightly increase the thermopower (compared to the unsubstituted molecule Fl-H) and the values for the rest of the molecules do not follow a trend in the electron-donating or electron-withdrawing nature of the substituent. The sign of S for all the compounds is negative, showing that the Fermi level is closer to the lowest unoccupied molecular orbital (LUMO) than to the highest occupied molecular orbital (HOMO) [Rincón-García2016b], consistent with previously reported results for molecules with pyridyl anchor groups using other thermopower characterization techniques.

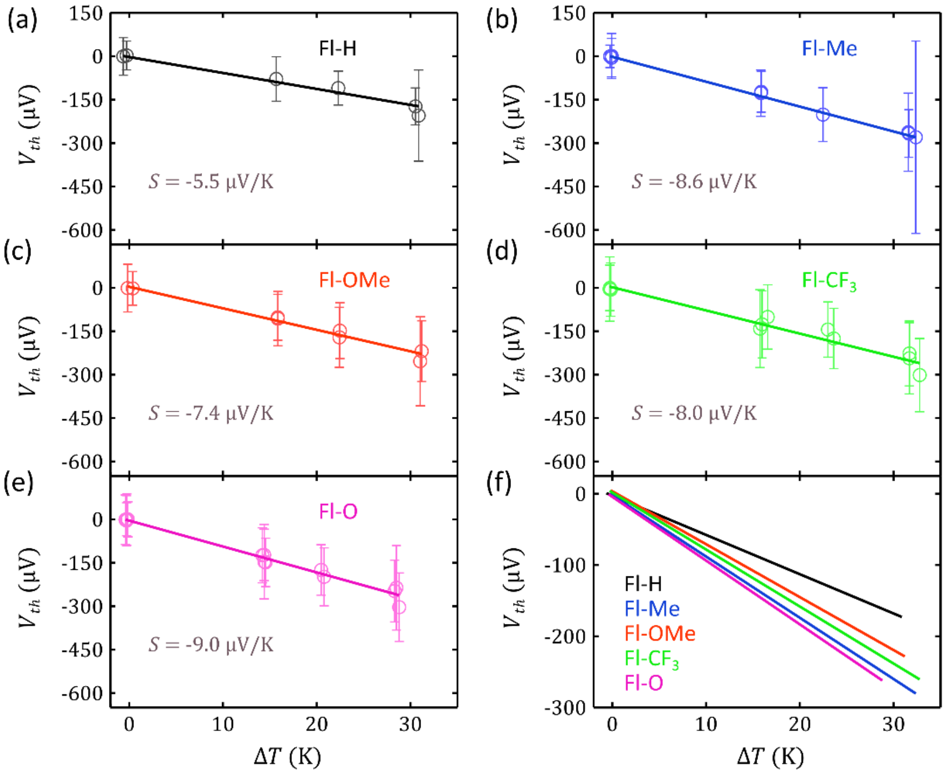

Figure 4.7: Average thermopower S of the five fluorene-derivatives investigated. (a-e) Linear fit to all the V_{th} values of each molecule to obtain its thermopower S, which is the slope of this fit (values are shown in each plot). The empty circles correspond to the mean thermovoltage value $\overline{V_{th}}$ obtained from the Gaussian fit of each set of measurements. The error bars of $\overline{V_{th}}$ are the standard deviations $\sigma_{V_{th}}$. (f) Linear fit of all the V_{th} values shown in panels (a-e), combined to facilitate comparison.

Table 4.3: Average thermopower S of all the fluorene derivatives investigated. Thermopower values are obtained from the slope of the linear fits plotted in Figure 4.7.

Molecule	S (μV/K)
Fl-H	−5.5
Fl-Me	−8.6
Fl-OMe	−7.4
Fl-CF$_3$	−8.0
Fl-O	−9.0

4.1.3 Theoretical calculations and comparison with experimental results

Theoretical calculations about the transport properties of the fluorene derivatives investigated have been performed by the group of Prof. Colin J. Lambert in Lancaster University (United

Kingdom). We reproduce below the main computational details and results published in our joint publication Ref. [Yzambart2018].

Electronic structure calculations are performed using the DFT code SIESTA [Soler2002]. The optimum geometries of the isolated molecules are obtained by relaxing the molecules until all forces on the atoms are less than $0.05\ \mathrm{eV/Å}$. The SIESTA calculations employ a double-zeta plus polarization orbital basis set and norm-conserving pseudopotentials; an energy cutoff of 250 Rydbergs defines the real space grid and the exchange correlation functional is LDA. To calculate their electrical conductance, the molecules are attached to gold leads via the pyridyl anchor groups. The leads are constructed of 6 layers of Au(111) each containing 30 gold atoms and the optimum binding distance is calculated to be 2.4 Å between the terminal nitrogen atoms and a 'top' gold atom (see Figure 4.8(a)). A Hamiltonian describing this structure is produced using SIESTA and the zero-bias transmission coefficient $\mathcal{T}(E)$ is calculated using the Gollum code [Ferrer2014]. Further details are provided in the Supporting Information of Ref. [Yzambart2018].

It is well known that DFT frequently underestimates the HOMO-LUMO gap [Lof1992; Hung2009] and the calculated gaps are indeed smaller than the optically-measured gaps. To overcome this deficiency, a scissor correction is performed by diagonalizing the molecular sub-matrix of the full Hamiltonian, then shifting the eigenvalues below and above the Fermi energy such that the new HOMO-LUMO gap matches the experimental value of the isolated molecule. Finally, the diagonalized matrix is transformed back to the original basis to obtain the corrected full Hamiltonian.

Figure 4.8(b) shows the DFT predicted transmission coefficients $\mathcal{T}(E)$ for the five molecules as a function of $E - E_M$, where E_M is the energy of the middle of the HOMO-LUMO gap. Note that the slope of $\mathcal{T}(E)$ near the mid-gap is not zero, because $\mathcal{T}(E)$ is rather asymmetric within the gap. This asymmetry arises because the HOMOs of these molecules are degenerate. Indeed, as described by the Breit-Wigner formula [Claugthon1995] when on-resonance the transmission coefficient of a symmetric molecule should be unity, unless the resonant level is degenerate. This is why the HOMO transmission resonances in Figure 4.8(b) are much less than unity, whereas the non-degenerate LUMO resonances are close to unity. There is no frontier orbital distribution on the pendant group at C(9) for most of the molecules whereas for molecule Fl-O there is a contribution of the HOMO, LUMO and LUMO+1 on the fluorenone oxygen atom.

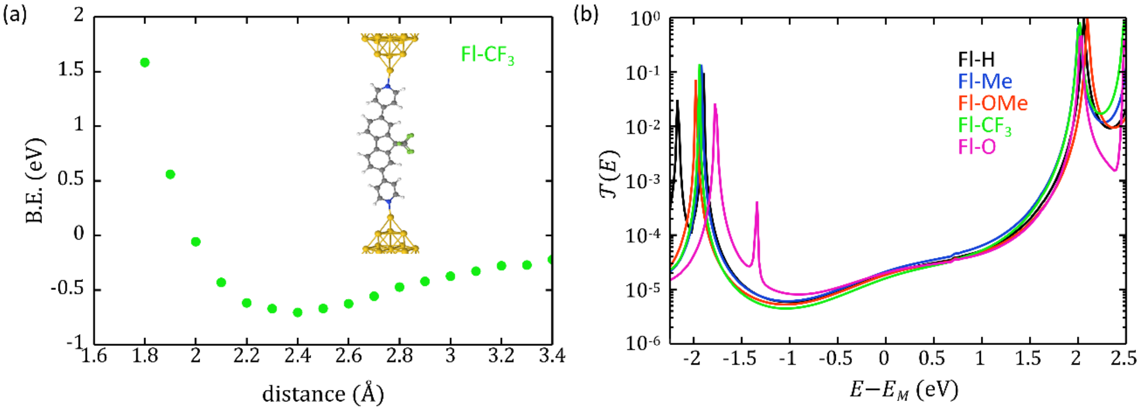

Figure 4.8: Theoretical calculations results. (a) Binding energy $B.E.$ as a function of molecule-contact distance for compound Fl-CF$_3$ attached to Au electrodes as shown in the inset. The equilibrium distance (i.e. the minimum of $B.E.$) is approximately 2.4 Å for this fluorene. (b) Transmission coefficients $\mathcal{T}(E)$ for the five molecules explored after scissor corrections. After Ref. [Yzambart2018].

Obtaining theoretical values of conductance and Seebeck coefficient from the transmission curves shown in Figure 4.8, Figure 4.9 shows a comparison between theoretical and experimental G and S values. In agreement with experiment, the theoretical Seebeck coefficient is found to be negative, due to the presence of the pyridyl anchor groups, which tend to move the LUMO towards the Fermi energy. Since the Fermi energy is determined in part by environmental factors, theoretical results are shown for two values of the Fermi energy, namely $E_F = E_M$ and $E_F = E_M - 0.3$ eV. This window captures both conductance and thermopower experimental values. The differences between experiment and theory most likely arise from the fact that the Fermi energy (relative to frontier orbital energies) varies from molecule to molecule. Table 4.4 shows that almost exact agreement between theory and experiment can be obtained if small variations in E_F occur between the molecules.

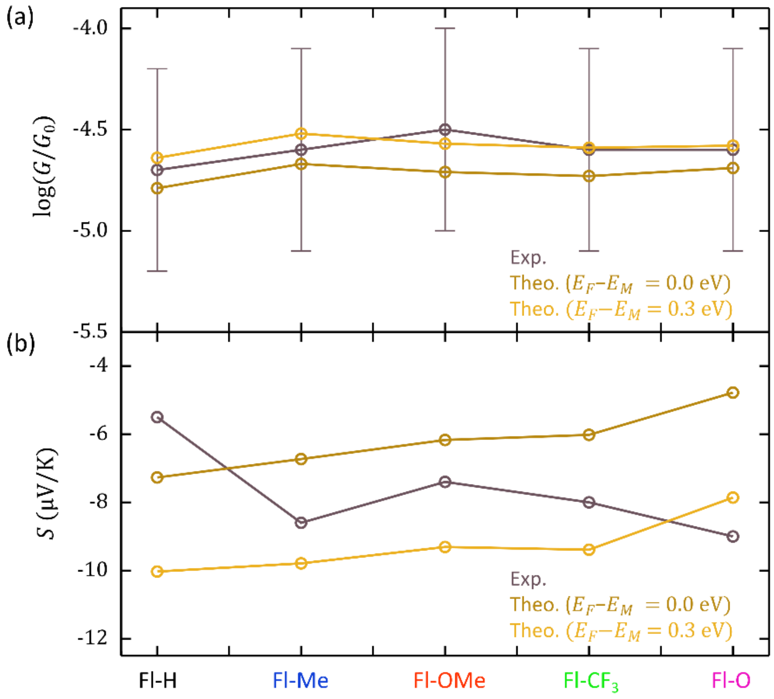

Figure 4.9: Comparison of conductance G and thermopower S theoretical and experimental results. (a) Comparison between measurements and calculations of conductance. The experimental values and error bars correspond to the data shown in Table 4.2. (b) Comparison between measurements and calculations of Seebeck coefficients. The experimental values correspond to the data shown in Table 4.3.

Table 4.4: Comparison of theoretical and experimental results. Theoretical results obtained for G (column 3) and S (column 5) of the fluorene derivative junctions using the Fermi energies shown in column 2 and comparison with the experimental values (columns 4 and 6, respectively).

Molecule	$E_F - E_M$ (eV)	Theo. $\log_{10}(\bar{G}/G_0)$	Exp. $\log_{10}(\bar{G}/G_0)$	Theo. S (μV/K)	Exp. S (μV/K)
Fl-H	0.40	$10^{-4.6}$	$10^{-4.7}$	-6.8	-5.5
Fl-Me	0.10	$10^{-4.6}$	$10^{-4.6}$	-8.6	-8.6
Fl-OMe	0.16	$10^{-4.6}$	$10^{-4.5}$	-7.4	-7.4
Fl-CF$_3$	0.10	$10^{-4.6}$	$10^{-4.6}$	-8.1	-8.0
Fl-O	-0.15	$10^{-4.7}$	$10^{-4.6}$	-9.1	-9.0

4.1.4 Conclusions on fluorene derivatives characterization

Conductance and thermopower characteristics of a group of fluorene derivatives with different pendant substituents in C(9) position have been measured in Au|single-molecule|Au junctions using our modified scanning tunnelling microscope-break junction (STM-BJ) technique. Measurements have been performed in ambient conditions and at room temperature, for four different ΔT between tip and sample, and show good junction formation probability (larger than 20%) for all the compounds.

The results show that the different substituents affect the thermopower, but have a negligible influence on the conductance of the molecular junctions. By systematically varying the pendant group, the average Seebeck coefficient can be varied from $-5.5\ \mu\mathrm{V/K}$ for molecule Fl-H to $-9.0\ \mu\mathrm{V/K}$ for molecule Fl-O, which is an increase of almost 80%, whereas the electrical conductance remains essentially unchanged across the series of molecules, with a most probable value $\bar{G} \approx 10^{-4.6} G_0$.

This combined experimental and computational study demonstrates that fluorene is a suitable backbone unit for measurements of conductance and thermopower and that non-conjugated pendant substituents can influence the thermopower of a molecular system – a topic that has not been studied previously. Future strategies could be to attach substituents at different positions on the fluorene ring for thermopower enhancement in single-molecule junctions and for studying quantum interference effects through a fluorene backbone.

4.2 Oligoyne wires

The second group of molecules investigated with the STM-BJ technique (see details in Chapter 2, Section 2.4.3), chosen to explore the effect of molecular length in the transport properties of single-molecule junctions, is a family of oligoyne wires synthesized by the group of Prof. Rik R. Tykwinski at Friedrich-Alexander-Universität in Erlangen-Nürnberg (Germany) (currently at University of Alberta, in Canada). We perform a combined conductance and thermopower characterization of four oligoynes with up to eight triple bonds in the backbone, namely, di-, tetra-, hexa- and octaynes (number of triple bonds $2n = 2, 4, 6, 8$, respectively) [Krempe2016] [Chalifoux2010]. The molecules are ended by a modified pyridine with two lateral phenyl rings and are named 2-yne, 4-yne, 6-yne and 8-yne. Figure 4.10 shows their chemical structure and the theoretical length l_{mol} of each compound is presented in Table 4.5. This ranges from 1.2 nm for the 2-yne up to 2.8 nm for the longest molecule explored, the 8-yne.

Oligoyne molecular wires are of great fundamental interest because of their structural simplicity, based on alternating single and triple carbon-carbon bonds. They can be seen as rigid rods with a one-dimensional backbone where approximately cylindrical charge delocalization along *sp*-hybridized carbon atoms takes place [Szafert2003; Szafert2006]. Oligoyne wires result, therefore, very appealing systems where charge transport through the linear backbone is independent of rotation around the single bonds, a feature which clearly differentiate these molecular wires from other conjugated oligomers where conforming units can rotate around the backbone axis [Wang2009]. This is the case, for instance, of OPEs [oligo(phenyleneethynylene)] and OPVs [oligo(phenylenevinylene)] derivatives [Taylor2003; James2006]. Oligoynes are also particularly attractive because they offer the possibility to investigate the effect of increasing length on the transport properties, an essential point when considering molecular wiring in electronic circuits. Previous works about the conductance of oligoyne wires, with compounds as long as four triple bonds [Moreno-García2013] [Wang2009], have only reached half of the current length explored. Ref. [Moreno-García2013] also considers the effect of different anchor groups on the oligoynes conductance. Oligoyne thermoelectricity has not been, to the best of our knowledge, previously examined experimentally. Some theoretical studies have been reported [Sadeghi2015; Hüser2015], although considering oligoynes with anchor groups slightly different to those of our compounds.

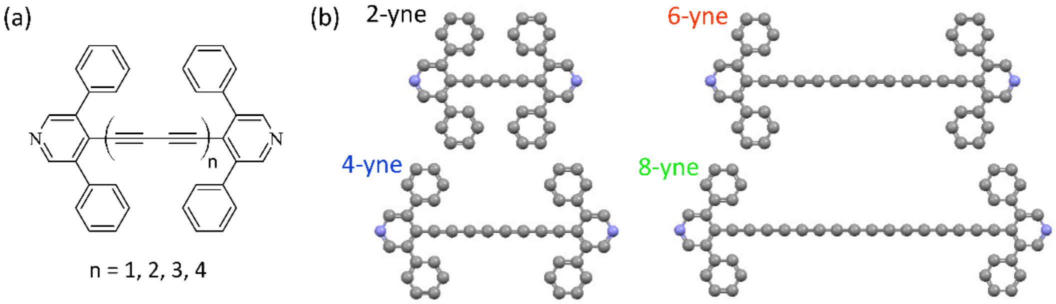

Figure 4.10: Chemical structure of the oligoyne family explored. (a) Schematized 2D chemical structure of the whole family, formed by di-, tetra-, hexa- and octaynes (number of triple bonds 2n = 2, 4, 6, 8, respectively). (b) Ball-and-stick chemical structure of the four molecules. Atom colouring: C, dark grey; N, blue. Hydrogen atoms are not shown.

Table 4.5: Theoretical length of the oligoyne wires investigated.

Molecule	Molecular length l_{mol} (nm)
2-yne	1.23
4-yne	1.72
6-yne	2.28
8-yne	2.78

In our experiments, commercial gold substrates (Arrandee$^{\mathrm{TM}}$, Germany) are used for sample preparation. As in Chapter 3 and previous Section 4.1, we use flame-annealed 250-nm-thick Au films with a polycrystalline Au(111) surface (see more details in Section 3.3.2). After cooling down to room temperature, samples are prepared by immersing the Au substrates in a 10^{-3} M solution of the corresponding molecule in dichloromethane (DCM) for 30 minutes in darkness. Finally the samples are dried with streaming nitrogen and mounted in the STM setup, which is allowed to stabilize for at least 15 minutes. Freshly cut $250\ \mu\mathrm{m}$ Au wire (99.99% purity, Goodfellow) is used as tips. Conductance G and thermopower S measurements are then performed in ambient conditions and at room temperature.

4.2.1 Conductance G characterization

Oligoynes conductance characterization is performed using a bias voltage $V_{bias} = 100\text{-}200\ \mathrm{mV}$ applied to the substrate, as well as a $12\ \mathrm{M\Omega}$ resistor connected in series to the sample in order to increase the total range of conductance monitored. A double-step current-to-voltage amplifier is used with a total gain of $2.5 \times 10^{10}\ \mathrm{V/A}$, which translates into an overall conductance range ($G = I/V_{bias}$) from $10^{-6.5}\ G_0$ up to $10^{0.5}\ G_0$ (seven orders of magnitude). $G_0 = 2e^2/h$ is the quantum of conductance, e is the electron's charge and h is Planck's constant.

Molecular junctions are formed following the same procedure introduced in Section 4.1.1, which consists on indenting the substrate with the tip and then retracting it upwards. This retraction movement results in the metallic tip-substrate contact breaking and, in the presence of molecules on the surface, eventually leads to the connection of one of them between the electrodes. Each time conductance G *vs* tip displacement Δz retraction traces are recorded, thus producing curves as the ones presented in Figure 4.11(a-d). In these examples, molecular junction formation is confirmed by the appearance of a conductance plateau, that is, the stabilization of the conductance around a given value instead of exponentially decreasing with increasing tip displacement as it happens in Au-Au tunnelling junctions (see Figure 4.2(a) for an example). The increasing length of the plateaus in Figure 4.11(a-d) reflects the increasing length of the molecules connected, from the shortest 2-yne to the longest 8-yne. Additionally, the average value of the conductance plateau is also molecule-characteristic and decreases with increasing molecular length, i.e. the longer the molecule is, the lower conductance value it shows. In these plots, the relative tip displacement of each trace is shifted as required to place the conductance value $G = 0.1\ G_0$ at the zero displacement position ($\Delta z = 0\ \mathrm{nm}$).

To better quantify the differences between the four molecules and to account for junction conformation variability, hundreds of individual retraction traces for each compound are recorded and plotted together in 2D histograms, shown in Figure 4.11(e-h). The trends already observed in the individual curves, in terms of plateau length and G value, are confirmed by these plots. Regarding the length of the plateaus, it ranges from typically less than $1\ \mathrm{nm}$ in the case of the 2-yne to $\sim 2.3\ \mathrm{nm}$ for the 8-yne. For all the molecules, plateau lengths get typically shorter than the theoretical molecular length. As molecules become longer, direct tunnelling between the electrodes for small Δz ($< 0.5\ \mathrm{nm}$) becomes more significant. This suggests that molecules are possibly initially bonding further away from the apex of the electrodes and Au-Au tunnelling is the main contribution to the current in this first state. Regarding the G value of the plateau, it can be observed in the 2D histograms that it decreases as the molecules become longer.

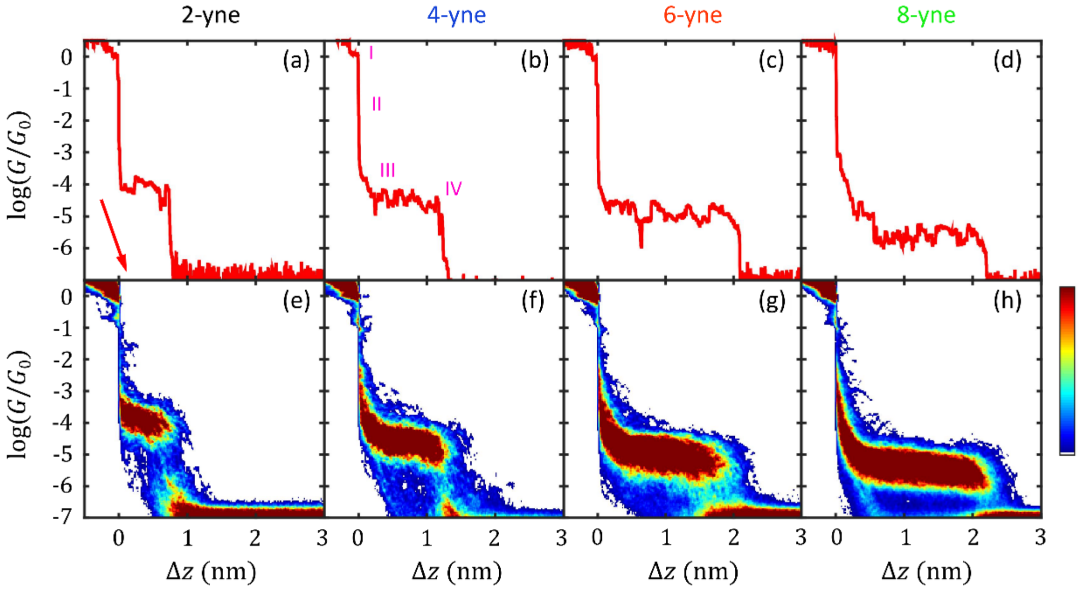

Figure 4.11: Individual traces and 2D histograms of conductance G *vs* tip displacement Δz. (a-d) Individual examples of G *vs* Δz retraction curves. The length and value of the plateaus reflect the molecular increasing length and decreasing G from 2-yne to 8-yne. The different features identifiable during tip retraction have been marked in (b): one Au atom contact ($G = G_0$) (I); metallic contact breaking (II); conductance plateau signalling molecular junction formation (III), and molecular junction breaking (IV). Red arrow indicates the direction of increasing tip displacement and consequent conductance decrease. (e-h) G *vs* Δz 2D histograms the oligoynes investigated, built with 189 2-yne junctions (e), 296 4-yne junctions (f), 573 6-yne junctions (c) and 727 8-yne junctions (h). Measurements have been performed with $V_{bias} = 100\text{-}200$ mV applied to the sample and, for all the panels in this figure, the zero displacement ($\Delta z = 0$ nm) is chosen to be the position where $G = 0.1\ G_0$. $G_0 = 2e^2/h$ is the conductance quantum (e is the electron's charge and h is Planck's constant).

Figure 4.12(a) shows conductance 1D histograms of the four compounds where all the experimental runs are plotted together. To find the most probable conductance $\bar{G}$, we fit the junction-characteristic peaks in the histograms with Gaussian distributions. The mean value of these fits corresponds to the expected $\bar{G}$, while the standard deviation σ_G accounts for the dispersion of the histograms. These parameters are shown in Table 4.6.

To better quantify the decrease of $\bar{G}$ with the molecular length, we present a semilogarithmic plot of these values in Figure 4.12(b). A linear decrease of the most probable conductance value as the molecules become longer is obtained, which suggests coherent tunnelling of electrons through the compounds (see Section 1.2.2). Up to the investigated length (8 triple bonds in the backbone), we do not observe any change of slope that would indicate a change in the electron transmission mechanism. A least square linear fit to the data in Figure 4.12(b) allows us to extract the decay factor or β value of the oligoyne family, that is, the factor that describes the degree to which $\bar{G}$ attenuates as the length of the molecular wire is increased, given by:

$$\bar{G} \propto \exp(-\beta l_{mol}). \qquad \text{Eq. (4.1)}$$

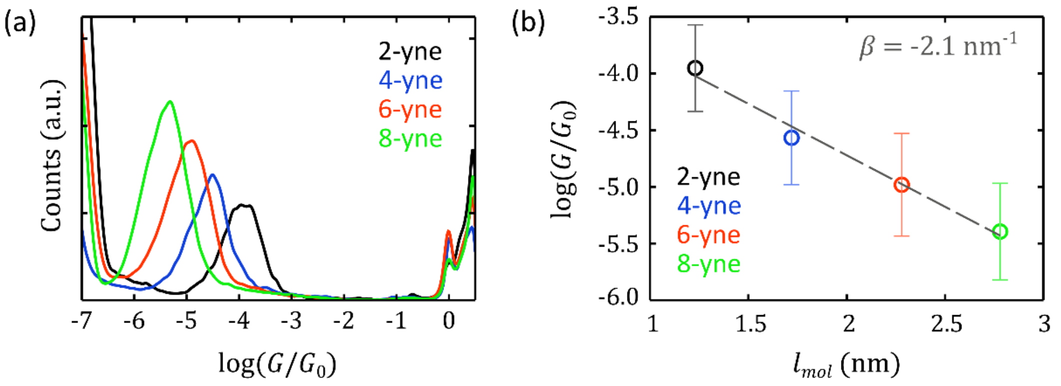

Figure 4.12: Conductance G 1D histograms and β value of the oligoyne wires. (a) G 1D histograms built with all the experimental runs performed for each oligoyne wire. Each histogram is normalized with its total number of measured values. (b) Semilogarithmic plot of the most probable conductance value of each compound $\bar{G}$ *vs* the theoretical molecular length l_{mol}. The β value of the family is determined from the slope of the linear fit, according to Eq. (4.1).

Table 4.6: Conductance experimental values. Measured most probable conductance value $\bar{G}$ (according to Gaussian fits applied in Figure 4.12(a)) and conductance histogram widths σ_G (standard deviation from the same Gaussian fits) for all the oligoyne wires investigated.

Molecule	$\bar{G}$ (G_0)	σ_G (G_0)
2-yne	$10^{-3.9}$	$10^{0.3}$
4-yne	$10^{-4.6}$	$10^{0.3}$
6-yne	$10^{-5.0}$	$10^{0.3}$
8-yne	$10^{-5.4}$	$10^{0.3}$

We find for these oligoyne wires that $\beta = 2.1 \pm 0.1\ \text{nm}^{-1}$. Previous works with oligoynes have studied only chains with up to 4 triple bonds and report β values that differ in a factor 5 ($\beta = 0.6 \pm 0.3\ \text{nm}^{-1}$ [Wang2009]; $\beta = 3.1 \pm 0.4\ \text{nm}^{-1}$ [Moreno-García2013]). The discrepancy between our result and the β obtained in Ref. [Moreno-García2013] it is possibly due to the fact that our investigation includes larger molecules, with twice as much triple carbon bonds in the backbone. Additionally, we have observed in this family that the exact value of the conductance peak in the histograms can vary between different experimental runs, even by half an order of magnitude. This is most likely caused by the pyridine anchor units of our compounds since 4,4’-bipyridine single-molecule junctions have been reported to show two most probable conductance values, explained by two different binding conformations of the compound [Quek2009; Kim2014b]. In our oligoyne wires modified pyridines (with lateral phenyl rings) are employed as binding groups and they seem to result in a broadening of the conductance peaks such that we do not discern the two conformations proposed when plotting together all the experimental data acquired. Nevertheless, we find that the influence of the pyridine units in the exact conductance value between different experimental runs makes delicate the determination of β and a large statistics is required. Regarding the β reported in Ref. [Wang2009], only molecules with up to four triple bonds are studied as well and the conductance window used in the measurements is more reduced, factors which may explain the discrepancy with our β value.

In comparison to other families of organic molecular junctions whose β has been investigated [Wold2002; Venkataraman2006b; Malen2009a], the value found for this oligoyne family is quite large. Our result implies that increasing the molecule length by a factor of 2.3 based on alternating single-triple carbon bonds translates into a reduction of $\bar{G}$ of almost two orders of magnitude (1.6 orders). This illustrates one of the major defies in the implementation of long molecules in electronic circuits.

4.2.2 Thermopower S characterization

Thermopower characterization of oligoyne junctions is performed with the STM-BJ technique (Section 2.4.3) with similar conditions as in the case of fluorene derivatives. During the tip motion the bias voltage applied to the sample is set at $V_{bias} = 100 - 200\ \mathrm{mV}$ and we stop it every $25 - 100\ \mathrm{pm}$ during retraction and ramp the voltage twice between $\pm\Delta V_0 = \pm\, 10 - 40\ \mathrm{mV}$. These parameters ranges are needed due to the conductance values of these molecules, which differ in almost two orders of magnitude from the 2-yne to the 8-yne. The low conductance value of 8-yne in particular results a major challenge in the characterization of its thermopower. Current signals in these junctions are close to the noise level and it is thus more difficult to accurately resolve the thermovoltage in the I-V ramps. In fact, several improvements introduced in the STM-BJ technique, already presented in this chapter and in Chapter 2, have been partly motivated to achieve the simultaneous characterization of G and S of these junctions (as well as to characterize the porphyrin-based junctions introduced in Section 4.3). Thermovoltage V_{th} values of the different oligoynes are measured for four different ΔTs, namely $\Delta T = 0\ \mathrm{K}$, $\sim 15 - 20\ \mathrm{K}$, $\sim 30\ \mathrm{K}$ and $\sim 38\ \mathrm{K}$. Each time a new ΔT is established, the STM setup is allowed to stabilize for at least 20 min before running the experiments.

Individual examples of simultaneous G and V_{th} measurements in 4-yne junctions are shown in Figure 4.13. Red solid lines in this figure correspond to conductance values of the complete retraction curves, measured at V_{bias} ($G = I/V_{bias}$) and show the characteristic features of junction formation (marked in the second junction). The conductance obtained from the slope of the I-V small ramps is also plotted in Figure 4.13(a), as red empty circles, in the values of Δz where they are shot to characterize the thermovoltage. These two conductance values are in very good agreement, confirming that I-V ramps are correctly acquired. In Figure 4.13(b) thermovoltage values measured with the ramps are presented. Notice that each of the individual curves shown is formed in the presence of a different ΔT between tip and sample. This is reflected in the thermovoltage signal, which increases in magnitude when increasing the temperature difference. In the case of this molecule (4-yne junctions), we obtain a negative value of the thermovoltage when applying a temperature difference, which indicates negative thermopower. Conductance ant thermovoltage remain typically almost constant during junction formation, exhibiting both signals correlation in small jumps produced by atomic rearrangements in the junction [Agraït1995]. Equivalent curves for the other three oligoyne wires can be found in Appendix 4.B (at the end of this chapter).

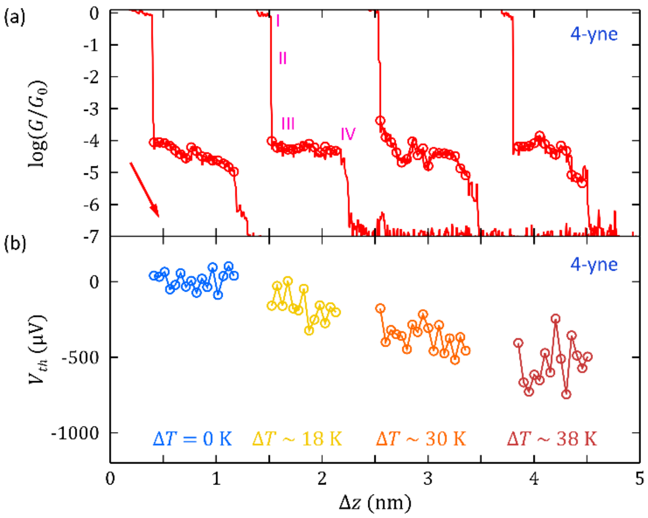

Figure 4.13: Individual conductance G and thermovoltage V_{th} *vs* tip displacement Δz retraction curves. Examples of simultaneous G (a) and V_{th} (b) measurements for single-molecule 4-yne junctions, obtained with different ΔT applied between tip and sample. Main features identifiable in the G trace have been marked in the second junction: one Au atom contact ($G = G_0$) (I); metallic contact breaking (II); conductance plateau signalling molecular junction formation (III), and molecular junction breaking (IV). V_{th} is only acquired in the plateau and G values obtained from the slope of the corresponding I-V ramps are plotted in (a) as red empty circles, showing good agreement with the complete retraction traces where G is measured with $V_{bias} = 100\text{-}200$ mV. Δz of the different traces has been displaced for the sake of clarity. The red arrow indicates the direction of increasing Δz and decreasing G.

Given the variability introduced by different junction conformations and geometries in G and V_{th} values, a statistical analysis is required to account for the particularities of an individual trace *vs* the most probable behavior of each compound. Several experimental runs are carried out for each ΔT and each molecule, collecting hundreds of retraction traces. Conductance G and thermovoltage V_{th} 1D histograms built with all the experimental runs at each ΔT are presented in Figure 4.14. In this figure, measurements performed at each ΔT are plotted separately, in a different color.

The first row of the figure (Figure 4.14(a-d)) contains 1D histograms formed with the G values of the complete retraction curves, from metallic contact breaking (feature I), through the molecular plateau (feature III), down to the noise level (below $G = 10^{-6.5} G_0$). They show correct junction formation in all cases, with junction-characteristic peaks whose most probable conductance value is in general in relative good agreement with the $\bar{G}$ found in the purely G characterization (Section 4.2.1). In particular, conductance of 2-yne junctions seems to be lower in the junctions formed to characterize the thermopower, while in the case of 8-yne a slightly higher conductance is typically observed (see most probable values in Table 4.6). In any case, good agreement is obtained with the conductance measured from the slope of the small I-V ramps shot, which is presented in the second row (Figure 4.14(e-h)). Voltage ramps are only performed in the conductance range corresponding to junction formation and hence just the junction-characteristic peak is formed in the 1D histograms built with this data. Finally, thermovoltage values measured at each ΔT and for each of the molecules are collected in the third row of the figure (Figure 4.14(i-l)), where histogram values have been adequately shifted to place the corresponding 0-ΔT histogram correctly centered at zero. In this figure we also plot the corresponding fit to a Gaussian distribution (plotted in a lighter color on the histograms) to find the most probable value $\overline{V_{th}}$. We obtain that this is in all cases negative and increases as ΔT is increased. Histograms also seem to become broader with increasing ΔT and molecular length.

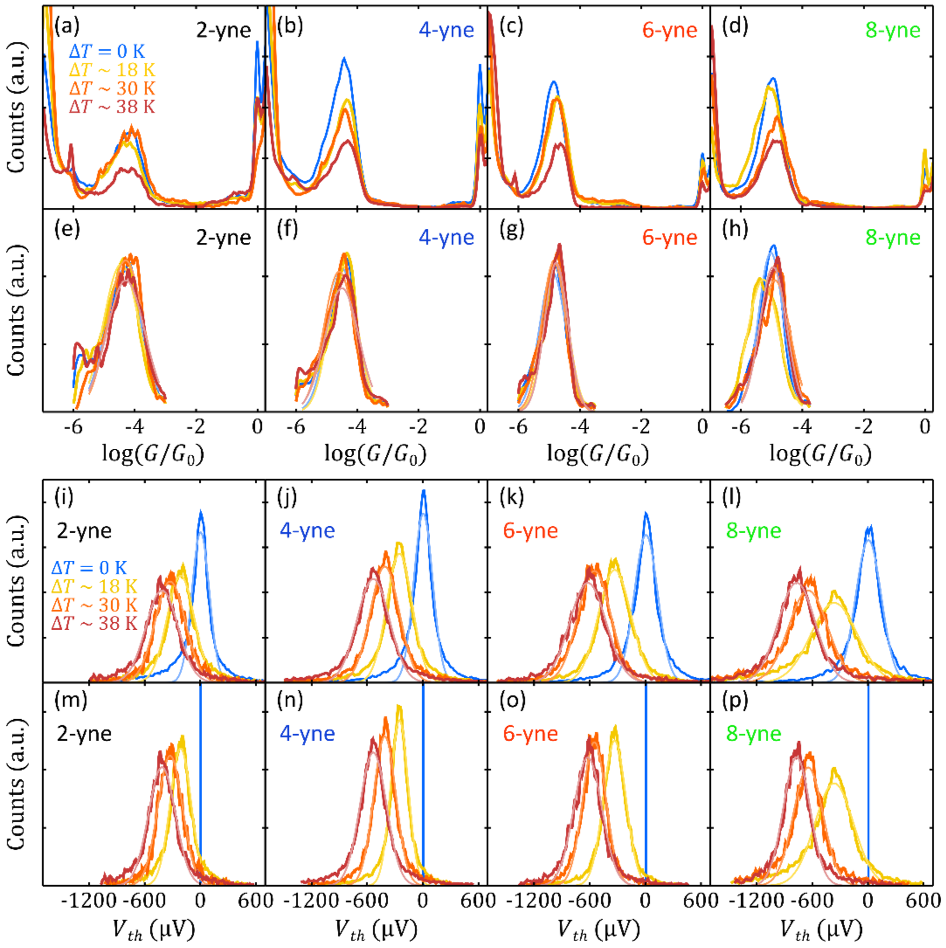

Figure 4.14: Simultaneous conductance G and thermovoltage V_{th} 1D histograms. 1D histograms of each of these magnitudes are built with data from 3058, 5163, 2141 and 2034 curves measured in 2-yne, 4-yne, 6-yne and 8-yne junctions, respectively. Colours correspond to measurements performed with a given temperature difference ΔT applied between tip and sample: blue histograms are built with data acquired with $\Delta T = 0$ K; yellow histograms, with an average $\Delta T \sim 18$ K; orange histograms, with an average $\Delta T \sim 30$ K, and dark red histograms, with an average $\Delta T \sim 38$ K. (a-d) G 1D histograms of the four oligoyne wires where G is measured at $V_{bias} = 100 - 200$ mV. (e-h) G 1D histograms generated with the conductance obtained from the slope of the I-V ramps, plotted separately for each ΔT, and Gaussian fits, plotted superimposed in a lighter color. (i-l) V_{th} 1D histograms for each ΔT employed. Gaussian fits are also plotted in a lighter color superimposed on the histograms. (m-p) V_{th} 1D histograms and Gaussian fits after the dispersion correction is applied.

To further explore the origin of the width of the thermovoltage histograms, we perform a dispersion correction subtracting the contribution introduced in the histograms by the experimental setup and the measurement procedure. This is the dispersion observed in the $\Delta T = 0$ K histograms. No thermoelectric response in the molecular junction is generated when no temperature difference is applied between tip and sample. The width of these histograms (experimental error) is therefore caused by technical limitations: instrumental noise and error in the thermovoltage determination, that is, in the determination of the zero-crossing of the current in the small I-V ramps. This experimental error can be considered to be uncorrelated to the dispersion of the thermovoltage values and hence the dispersion of a measured histogram σ_{meas} can be expressed as:

$$\sigma_{meas}{}^{2} = \sigma_{int}{}^{2} + \sigma_{exp}{}^{2}, \qquad \text{Eq. (4.2)}$$

where σ_{exp} is the dispersion caused by the experimental error and σ_{int} is the intrinsic dispersion of thermovoltage values due to different junction conformations when $\Delta T \neq 0\ \mathrm{K}$. This σ_{exp} can be determined from the thermovoltage measurements at $\Delta T = 0\ \mathrm{K}$. Since $\sigma_{int} = 0\ \mathrm{\mu V/K}$ at $\Delta T = 0\ \mathrm{K}$, then $\sigma_{exp} = \sigma_{0\mathrm{K}}$, i.e. the measured standard deviation of the 0-ΔT histogram. Once we know this value, we correct the experimental error of the thermovoltage measurements for each molecule by subtracting this 0-ΔT dispersion to the dispersion of all the histograms applying the following equation:

$$\sigma_{int} = \sqrt{\sigma_{meas}{}^{2} - \sigma_{exp}{}^{2}}, \qquad \text{Eq. (4.3)}$$

or, written differently,

$$\sigma_{V_{th},corrected} = \sqrt{\sigma_{meas}{}^{2} - \sigma_{0\mathrm{K}}{}^{2}}, \qquad \text{Eq. (4.4)}$$

It is clear from this equation that the corrected dispersion of 0-ΔT histograms would cancel when applying the correction. To accurately maintain the mean value of each thermovoltage measurement $\overline{V_{th}}$, V_{th} data of each histogram is re-scale using the next expression:

$$V_{th} = (V_{th} - \overline{V_{th}})\frac{\sigma_{V_{th},corrected}}{\sigma_{meas}} + \overline{V_{th}}. \qquad \text{Eq. (4.5)}$$

Application of this dispersion correction to the V_{th} 1D histograms of Figure 4.14(i-l) produces the corrected V_{th} 1D histograms shown in Figure 4.14(m-p). Note that the blue vertical lines in these figures are the experimental values of the 0-ΔT histogram collapsed to zero after the application of Eq. (4.5). For the rest of histograms, their dispersion is indeed reduced, while the histograms remain centered at the same $\overline{V_{th}}$ as the original data. This can be better observed in Figure 4.15 where we plot, for both cases, the mean values $\overline{V_{th}}$ and standard deviations $\sigma_{V_{th}}$ of Gaussian distributions used to fit the histograms. These parameters are plotted in Figure 4.15(a-d) for the original data histograms (those of Figure 4.14(i-l)), while we show in the second row, Figure 4.15(e-h), the parameters for the dispersion-corrected histograms (those of Figure 4.14(m-p)). Additionally, linear fits presented in Figure 4.15 are performed considering all the individual thermovoltage values measured. The slope of these fits give us the average thermopower S of each compound, which appears written in the corresponding figure and is also gathered in Table 4.7 for the case of the dispersion-corrected data. The linear fits are also plotted together in Figure 4.16(a) in order to facilitate comparison of the four compounds.

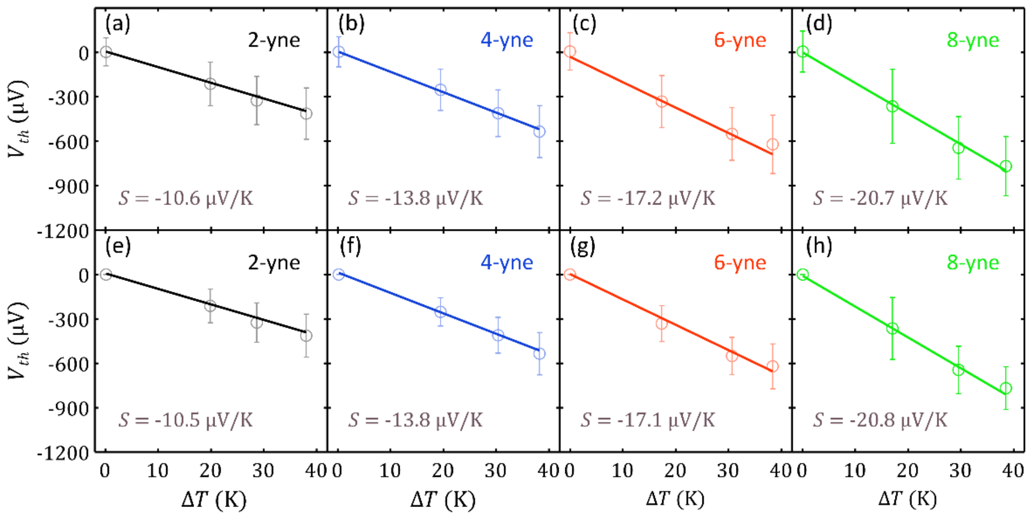

Figure 4.15: Average thermopower S of the four oligoyne wires investigated. (a-d) Least square linear fit to all the original V_{th} values measured for each molecule and average thermopower S given by the slope of the fit. Empty circles correspond to the mean thermovoltage value $\overline{V_{th}}$ obtained from the Gaussian fit of the V_{th} histogram at each ΔT. Error bars are the corresponding standard deviations $\sigma_{V_{th}}$. (e-h) Least square linear fit to all the V_{th} values after the dispersion correction is applied. The slope of the fits determine the average thermopower S of each compound. Empty circles correspond to the mean thermovoltage value $\overline{V_{th}}$ obtained from the Gaussian fit of the V_{th} histogram at each ΔT and the error bars are the corresponding standard deviations $\sigma_{V_{th}}$.

Table 4.7: Average thermopower S of the four oligoyne wires investigated. Thermopower values are obtained from the slope of the linear fits plotted in Figure 4.15(e-h).

Molecule	S (µV/K)
2-yne	-10.5
4-yne	-13.8
6-yne	-17.1
8-yne	-20.8

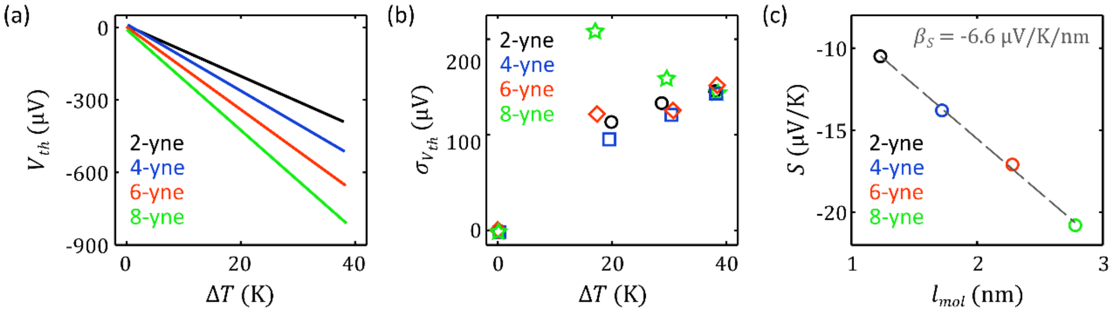

Figure 4.16: Dispersion analysis and length dependence of thermopower. (a) Least square linear fits for the oligoyne wires investigated. These fits are done considering the individual V_{th} values after the dispersion correction is applied. The negative slopes of V_{th} *vs* ΔT suggest transport through the LUMO. (b) Standard deviation $\sigma_{V_{th}}$ *vs* ΔT for each compound. $\sigma_{V_{th}}$ is obtained from the Gaussian fits shown in Figure 4.14(m-p). (c) Length dependence of S for the oligoyne family. A least square linear fit is performed and the value of the slope, the β_S value, is given as an inset.

The experimental results obtained show that all the oligoyne wires investigated present negative values of the average thermopower. In particular, $S_{2-\mathrm{yne}} = -10.7\ \mu\mathrm{V/K}$, $S_{4-\mathrm{yne}} = -13.8\ \mu\mathrm{V/K}$, $S_{6-\mathrm{yne}} = -17.3\ \mu\mathrm{V/K}$ and $S_{8-\mathrm{yne}} = -20.3\ \mu\mathrm{V/K}$. Considering the whole family, a factor 1.9 of enhancement is obtained in the series. The negative S suggests that charge transport through these molecular junctions takes place mainly through the LUMO. This is in good agreement with previously reported Seebeck coefficients of single-molecule junctions formed with pyridyl anchor groups, which typically present negative S. Although our molecules are ended in modified pyridines with two lateral phenyl rings, measurements support electrode connection to the molecules through the pyridine units. To the best of our knowledge, these are the first measurements of the Seebeck coefficient of oligoyne wires junctions.

Returning to the dispersion analysis of the corrected V_{th} histograms, $\sigma_{V_{th}}$ are plotted in Figure 4.16(b) as a function of ΔT for each molecule. We observe that $\sigma_{V_{th}}$ tends to increase with increasing ΔT, which is to be expected because the current through the junction is proportional to the temperature of the tip. With respect to the four molecules, no particular difference is observed between them except in the case of the 8-yne values, which are typically larger and even seem to decrease with increasing ΔT. This is possibly due to the low conductance of the 8-yne junctions (the lowest of the four molecules), which introduces a larger experimental error in the determination of V_{th} in the I-V ramps. Since V_{th} values are smaller for smaller ΔT, the dispersion in V_{th} histograms of 8-yne junctions results larger at $\Delta T \sim 20\ \mathrm{K}$ than at $\Delta T \sim 38\ \mathrm{K}$.

Length dependence of the Seebeck coefficient of oligoyne wires can be also analyzed from the results obtained. S *vs* molecular length l_{mol} is plotted in Figure 4.16(c), showing a linear increase of the thermopower as the molecules become longer. In analogy to G, the degree at which the thermopower changes with respect to length can be defined as the β_S value. Applying a least square linear fit in Figure 4.16(c), we find $\beta_S = -6.6\ \mu\mathrm{V/K/nm}$. Previously reported values of β_S for other compounds are generally very similar to our result. For instance, three groups of molecules are explored in Ref. [Malen2009a] and the values found are $\beta_S = -6 \pm 1\ \mu\mathrm{V/K/nm}$ for alkanedithiols, $\beta_S = 5 \pm 1\ \mu\mathrm{V/K/nm}$, for phenylenediamines and $\beta_S = 7 \pm 2\ \mu\mathrm{V/K/nm}$ for phenylenedithiols (this last value is taken from measurements reported in [Reddy2007]).

To complement this length-dependence analysis with the conductance G and thermopower S combined evolution with length and electrode separation, G and S *vs* tip displacement Δz 2D histograms are built and presented in Figure 4.17. We generate these histograms considering all the individual traces measured with average $\Delta T \sim 18, 30$ and $38\ \mathrm{K}$ and thermopower plots are performed dividing each V_{th} value by the corresponding ΔT, i.e. collecting all the individual thermopower values shown by the molecular junctions as they evolve. Regarding the conductance plotted, Figure 4.17(a-d) histograms contain G values measured at $V_{bias} = 100 - 200\ \mathrm{mV}$, while histograms in Figure 4.17(e-h) are formed with the data acquired from the small I-V ramps. G 2D histograms show typical junction formation features and the plateaus generally present a negative slope, which is usual in BJ experiments. This may suggests that, in average, molecular binding to the electrodes varies in a continuous way as the tip retracts from the surface, probably caused by an initial overlap between the molecules and electrodes and final “sliding” of the molecules. Thermopower histograms, on the contrary, show very straight clouds of values with a very similar profile in all the cases, becoming “sharper” as the junctions become longer. This shape, however, is not a junction characteristic property, but it is mainly caused by the smaller amount of traces maintained for the largest Δz.

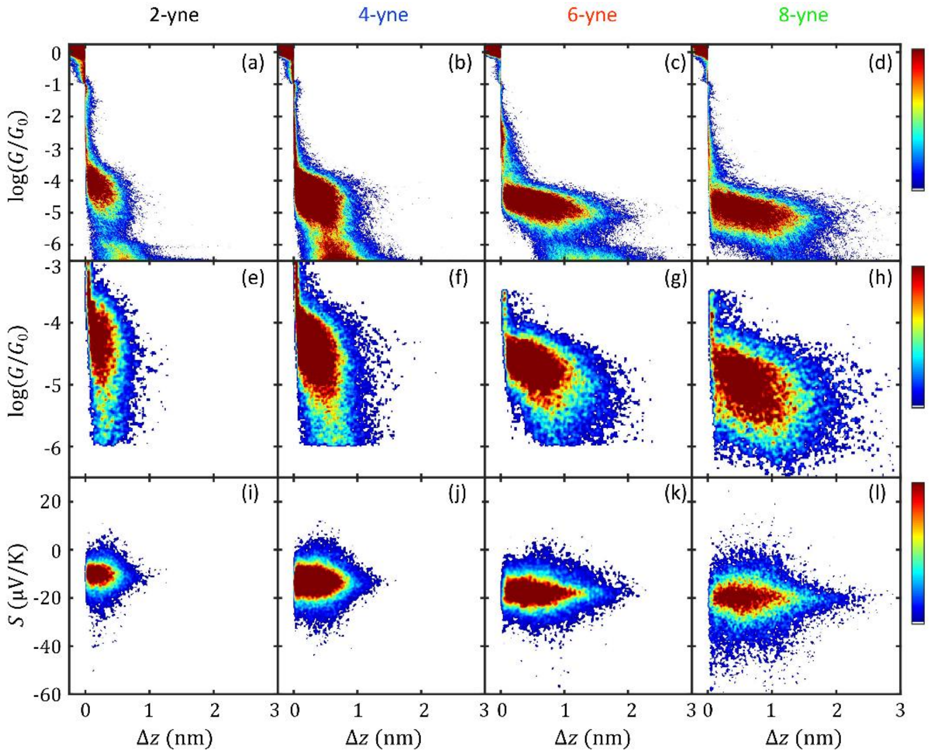

Figure 4.17: Conductance G and thermopower S *vs* tip displacement Δz 2D histograms. (a-d) G *vs* Δz 2D histograms for the four oligoynes investigated. Conductance is obtained from the current I measured at $V_{bias} = 100 - 200$ mV ($G = I/V_{bias}$). (e-h) G *vs* Δz 2D histograms where the conductance is obtained from the slope of the I-V ramps shot every few picometers of tip displacement. (i-l) S *vs* Δz 2D histograms for the oligoyne junctions. Thermopower is obtained from the thermovoltage measured with the small I-V ramps divided by the corresponding ΔT. Data in these histograms for all the molecules is acquired with average $\Delta T \sim 18$ K, ~ 30 K and ~ 38 K and the zero displacement ($\Delta z = 0$ nm) is chosen to be the position where $G = 0.1\,G_0$. Histograms are generated with 1604, 3729, 1502 and 1376 curves for 2-yne, 4-yne, 6-yne and 8-yne junctions, respectively. The colour scale accounts for the number of points in each histogram.

With respect to the broadening of the different histograms, it is notably larger in the case of the conductance plots, where even two orders of variability are obtained for 8-yne junctions. Thermopower histograms present a smaller dispersion, confirming larger sensitivity of G to atomic-scale fluctuations and junction configuration details [Baheti2008]. Considering the variability from molecule to molecule, thermopower broadening follows a similar behavior as characterized for the thermovoltage (see Figure 4.16(b)), which is to be expected since they are linearly related. Comparison between molecules can be better established by plotting the corresponding 1D histograms, which are presented in Figure 4.18(a-b). In these histograms, G and S data are obtained from the small I-V ramps and the mean values and standard deviations of the Gaussian fits, plotted in a lighter colour, are gathered in Table 4.8. Mean values obtained from the Gaussian fit of the thermopower 1D histograms correspond in this case to the most probable Seebeck coefficient $\bar{S}$ of molecular junctions formed with each compound. In the conductance 1D histograms, the tendency of 2-yne junctions to show a relatively small G, in comparison to the pure conductance characterization (see Section 4.2.1), produces a considerable broadening of the G histogram, even encompassing the 4-yne histogram, as can be observed in this plot.

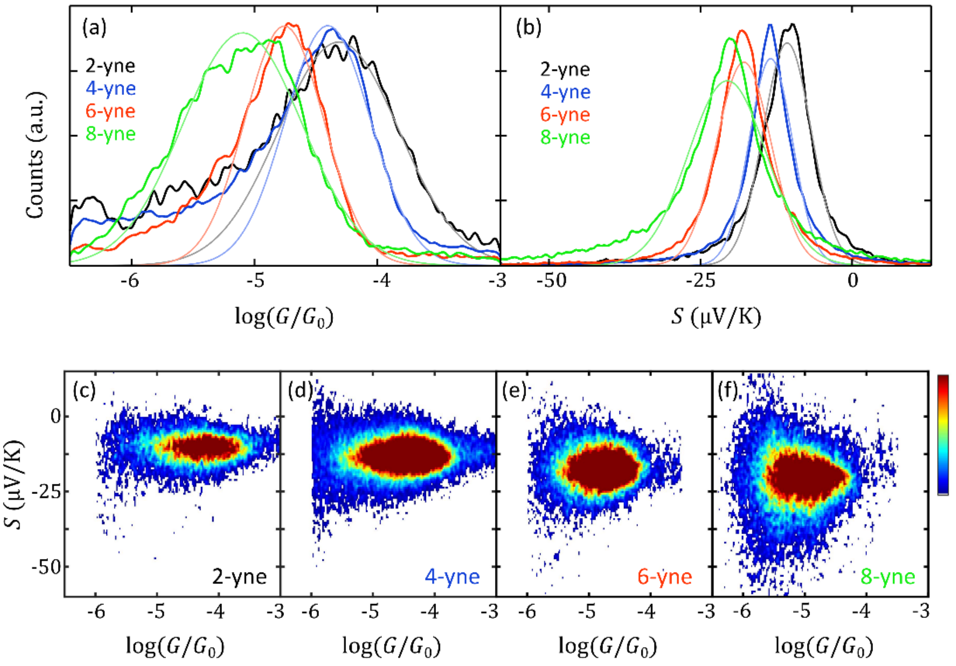

Figure 4.18: Conductance G and thermopower S of oligoynes. (a-b) G and S 1D histograms for the oligoyne wires, formed with the data obtained from the I-V ramps and Gaussian fits plotted superimposed in a lighter colour. (c-f) S *vs* G 2D histograms for the four compounds investigated. The colour scale accounts for the density of points in the histograms.

Table 4.8: Most probable conductance $\bar{G}$ and thermopower $\bar{S}$ of oligoyne wires. $\bar{G}$ and $\bar{S}$ values are acquired from the small I-V ramps shot while single-molecule junctions are formed. Together with the standard deviation reported here, they correspond to the parameters of the Gaussian fits presented in Figure 4.18(a-b).

Molecule	$\bar{G}$ (G_0)	σ_G (G_0)	$\bar{S}$ (μV/K)	σ_S (μV/K)
2-yne	$10^{-4.3}$	$10^{0.5}$	-10.7	4.0
4-yne	$10^{-4.4}$	$10^{0.3}$	-13.5	3.7
6-yne	$10^{-4.8}$	$10^{0.3}$	-17.9	4.5
8-yne	$10^{-5.1}$	$10^{0.5}$	-20.6	6.4

Finally, S *vs* G 2D histograms for the four oligoyne wires investigated are plotted in Figure 4.18(c-f). No particular correlation between these two magnitudes is observed, except in the case of the 8-yne junctions. As can be seen in Figure 4.18(f), this molecule seems to exhibit a larger dispersion of thermopower as the conductance decreases. This may be produced by the fact that these measurements are already very close to the instrumental noise level of the experimental setup and thus, thermovoltage determination (i.e. the zero-crossing of the current) becomes more challenging, especially for smaller ΔT as discussed for Figure 4.16(b). An increase in the dispersion of the thermopower values as the conductance is decreased is to be expected.

4.2.3 Conclusions on oligoyne wires characterization

The characterization of conductance G and thermopower S of oligoyne wires has been performed to explore the length dependence of these properties. To the best of our knowledge, this is the first time that transport properties of oligoyne wires this long, up to eight triple carbon-carbon bonds, are addressed. The compounds, with an even number of triple C-C bonds in the backbone from two to eight, have been synthesized by the group of Prof. Rik R. Tykwinski and present modified pyridine anchor groups to facilitate Au|single-molecule|Au junction formation.

Conductance measurements show an exponential decrease of the most probable G value with increasing molecular length, which is a typical signature of coherent tunnelling of charges through the nanoscale systems. We obtain for this family a decay factor of the conductance with length $\beta = 2.1\ \mathrm{nm}^{-1}$. Discrepancy of this value with respect to previously reported β, for oligoynes up to four triple bonds, is suggested to be due to the fact that our investigation includes longer oligoyne wires and to the influence of pyridine binding groups in the conductance values. We find that the details of the anchor group and possible changes in behaviour when the compound becomes longer are important considerations to be taken into account in the β determination.

Thermoelectricity of oligoyne wires has been measured for the first time, to the best of our knowledge. It has been found to increase with molecular length with a total enhancement close to a factor 2, from $\bar{S} = -10.7 \pm 4.0\ \mu\mathrm{V/K}$ in the case of 2-yne junctions to $\bar{S} = -20.6 \pm 6.4\ \mu\mathrm{V/K}$ for the 8-yne systems. The variation of S with length is linear and a rate of change $\beta_S = -6.6\ \mu\mathrm{V/K/nm}$ is obtained for this family, a value which is similar to others previously reported for organic compounds. The Seebeck coefficient is in all cases negative, indicating transport predominantly through the LUMO.

4.3 Zn-based oligo-porphyrins

STM-BJ experiments have been also performed to investigate the thermoelectric properties of a third group of molecules, namely, a series of five Zn-porphyrin oligomers.

Porphyrins are planar organic molecules and one of their major characteristic features is that these aromatic macrocycles are able to host a metal atom in the centre of their structure. In the series of molecules investigated, the central atom is in all cases a Zn atom. The compounds have been synthesized by the group of Prof. Harry Anderson at the University of Oxford (United Kingdom) and are formed by 1, 2 and 3 porphyrin units connected in series with two different strategies for inter-porphyrin coupling. The first sub-group of porphyrins are linearly connected by butadiyne (C4) linkers, which favour electronic conjugation along the compounds [Sedghi2011] with a moderate coupling between the individual porphyrin units. In the second sub-group, porphyrins are directly fused and connected through three C-C bonds, being the coupling between them considerably stronger [Tanaka2015]. Figure 4.19 shows the chemical structures of the five oligo-porphyrins explored, which are named after the value of N as monomer ($N = 1$); dimer and fused dimer ($N = 2$), and trimer and fused trimer ($N = 3$). Note that the monomer is the same for both series. Additionally, C4-linked molecules (monomer included) and fused porphyrins are functionalized with OC_8H_{17} and $Si(C_6H_{13})_3$ pendent side chains, respectively, to favour solubility and are terminated with thioacetate groups, attached to phenylacetylene groups, in order to promote binding with the Au atoms of the electrodes. Thioacetate groups are known to cleave on the Au surface and produce Au-S bonds [Valkenier2011] and have been previously employed as anchor groups for porphyrin wires [Li2014; Leary2018a]. This way it is possible to prepare solutions of the compounds, deposit them onto a gold substrate by drop casting technique and, once let to dry, effectively connect the molecules with our STM setup.

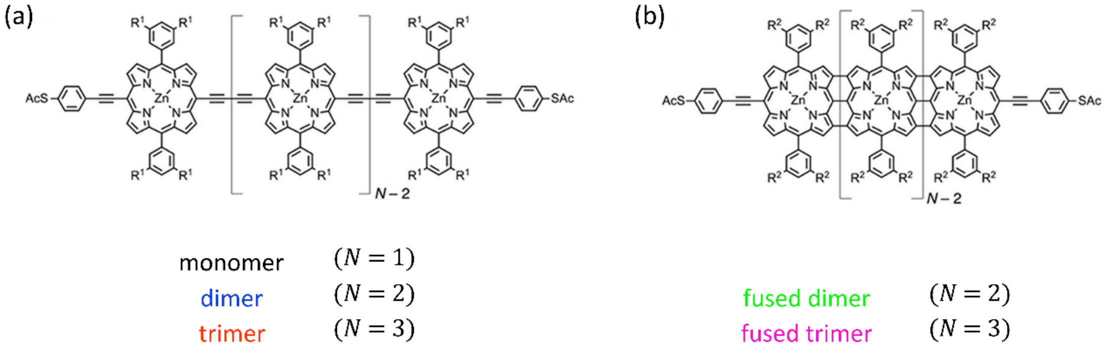

Figure 4.19: Chemical structure of the Zn-based porphyrin oligomers investigated. (a) Structure of the butadiyne-linked oligo-porphyrins (R^1 = OC_8H_{17}). (b) Structure of the fused oligo-porphyrins ($R^2 = Si(C_6H_{13})_3$). N is the number of porphyrin units conforming the molecule: $N = 1$ for the monomer; $N = 2$ in the case of the dimer and the fused dimer, and $N = 3$ for the trimer and the fused trimer. Note that the monomer is the same in both series. All the porphyrin units in these molecules have a Zn atom at the center and are terminated with thioacetate groups.

4.3.1 Background and conductance G characterization

Transport properties of porphyrins and oligo-porphyrins have been intensively studied in the last years [Holten2002; Winters2007; Sedghi2008; Kiguchi2009; Luo2011; Sedghi2011; Sedghi2012; Li2012; Li2013; Perrin2013; Tanaka2015; Kuang2018; Leary2018b]. They result a very appealing system since, for instance, they play an essential role in the photosynthetic process [Scholes2011]. The possibility to conveniently tune their transport properties by changing the nature of the central atom is also of great interest.

Our group has recently explored the bias dependence of the conductance G of these oligo-porphyrins in particular [Leary2018b], finding that their low-bias conductance, measured at $V_{bias} = 0.2$ V, is quite reproducible for all of them and that the β value of this oligomer series is voltage-dependent. In the case of the butadiyne-linked molecules, it decreases from $2.0\ \mathrm{nm}^{-1}$ at $V_{bias} = 0$ V down to $0.9\ \mathrm{nm}^{-1}$ at $V_{bias} = 0.9$ V, while for the fused porphyrins a particularly interesting result is obtained, that is the decrease of β from almost zero at $V_{bias} = 0$ V to a negative value at $V_{bias} = 0.7$ V ($-1.5\ \mathrm{nm}^{-1}$). This means that conductance at moderate bias voltage increases with length in the fused porphyrin tapes and measurements reported in Ref. [Leary2018b] are the first observation of this behaviour in molecular wires. It is explained to originate by a large decrease in the HOMO–LUMO gap of the fused tapes which compensates for the increasing tunnelling distance as they become longer. The dominant transport mechanism through the five molecules is found to be coherent tunnelling.

From the point of view of the thermoelectric response, these compounds result especially appealing due to the presence of the Zn atoms accommodated in the organic macrocycles.

Equivalently to the endohedral metallofullerenes, these metal-organic compounds present, from our point of view, the potential to enhance the thermoelectric response. Furthermore, the two different inter-porphyrin couplings offer the possibility to test its influence in the thermoelectric performance. On the one side, it may be favored in the butadiyne-linked porphyrins by the weak coupling between the porphyrin units, which may translate into each porphyrin acting as a 1D potential well. As discussed in Chapter 1, when having potential barriers connected in series, the total thermopower of the system (the oligomers) would in principle be the addition of the thermopower of each individual unit. On the other side, the strong electronic communication between the porphyrin units in the fused tapes and the peculiar behaviour of their conductance result very promising. Finally, thermoelectricity of porphyrin-based molecules has not been previously explored to the best of our knowledge and it is therefore of great interest to experimentally measure the Seebeck coefficient of these compounds.

Before introducing the results obtained for the thermopower characterization, we present the conductance G characterization-of-control performed, equivalent to that reported in Ref. [Leary2018b]. It is particularly important for the butadiyne-linked porphyrins, given the considerable decrease in G observed for these three molecules. Samples are prepared following the same procedure already introduced for the fluorene series and the oligoyne family: after cooling down to room temperature, freshly flame-annealed commercial gold substrates (Arrandee$^{\mathrm{TM}}$) are dipped for around an hour into low-concentration ($\sim 10^{-3}$ M) DCM solutions of the corresponding compound (see more details in Sections 3.3.2 or 4.1). Finally, samples are carefully removed from the solution container, are blown off with streaming nitrogen and are then mounted in the STM setup, which is allowed to stabilize for at least 15 minutes. Freshly cut $250\ \mu\mathrm{m}$ Au wire (99.99% purity, Goodfellow) is used as tips. Conductance G and thermopower S measurements are then performed in ambient conditions and at room temperature.

For these experiments, we apply a bias voltage $V_{bias} = 200 - 230\ \mathrm{mV}$ to the substrate and use a $12\ \mathrm{M\Omega}$ resistor connected in series to the sample in order to extend the total range of conductance monitored. As in the other STM-BJ experiments (see Section 2.4.3), a linear two-stages current-to-voltage amplifier is employed with a total gain of $2.6 \times 10^{10}\ \mathrm{V/A}$, that allows to measure with an experimental total range of conductance ($G = I/V_{bias}$) from $10^{-7} G_0$ up to $10^{0.5} G_0$ (more than seven orders of magnitude at the best conditions). $G_0 = 2e^2/h$ is the quantum of conductance, e is the electron's charge and h is Planck's constant.

In the BJ experiments, the tip is vertically moved (in the z-direction) in and out of contact with the Au substrate, while the tip displacement and the current signals are monitored. In the presence of molecules on the surface, they may bind to the tip and sample after breaking the metallic contact and thus form molecular junctions. Thanks to the terminal thioacetate groups, all the oligo-porphyrins are found to connect to the gold electrodes, as it was expected. The results are presented in Figure 4.20 and 4.21 for the butadiyne-linked and the fused oligo-porphyrins, respectively. Figure 4.20(a) and 4.21(a) show examples of individual conductance G *vs* tip displacement Δz retraction curves, one for each system investigated, where all the features of junction formation can be observed. Conductance plateaus (i.e. stabilization of the current signal instead of decreasing exponentially with increasing Δz) are easily identifiable in these Au|molecule|Au junctions due to the considerable length of these compounds which helps to maintain the molecular junction during tip retraction (see Table 4.9). Additionally, molecular integrity and sample cleanliness are confirmed by the reproducibility of very stable G *vs* Δz traces.

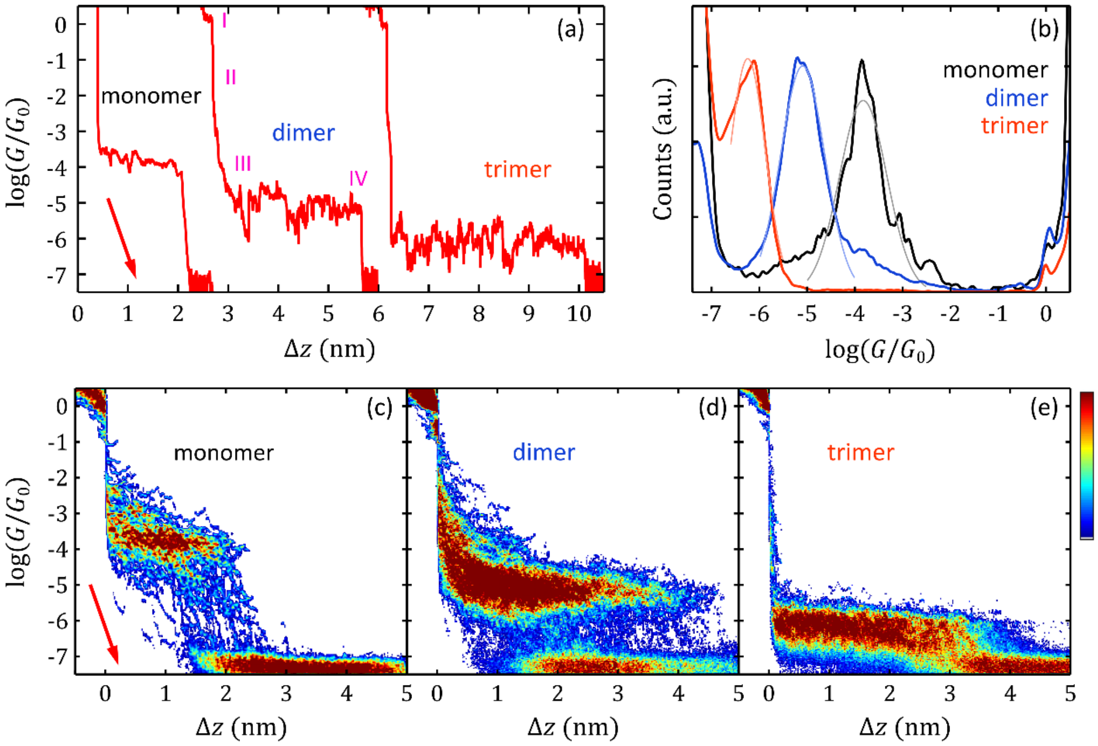

Figure 4.20: Conductance G characterization of butadiyne-linked oligo-porphyrins. (a) Individual examples of conductance G *vs* tip displacement Δz retraction traces for the three compounds. The different features identifiable during tip retraction have been marked in the dimer trace: one Au atom contact ($G = G_0$) (I); metallic contact breaking (II); conductance plateau signalling molecular junction formation (III), and molecular junction breaking (IV). (b) Conductance G 1D histograms for the three oligo-porphyrins investigated. Histograms are formed with 66 monomer junctions (black), 213 dimer junctions (blue) and 134 trimer junctions (orange). Gaussian fits to the molecular characteristic peaks are plotted in a lighter colour. (c-e) Corresponding G *vs* Δz 2D histograms built with the same curves as histograms in (b). For all the panels in this figure, the zero displacement ($\Delta z = 0$ nm) is chosen to be the position where $G = 0.1\, G_0$. Red arrows indicate the direction of increasing Δz and consequent conductance decrease. $G_0 = 2e^2/h$ is the conductance quantum (e is the electron's charge and h is Planck's constant).

This is further established by the conductance G 1D histograms (in Figure 4.20(b) and 4.21(b)) and the conductance G *vs* tip displacement Δz 2D histograms (Figure 4.20(c-e) and 4.21(c-e)). These histograms are built with individual retraction curves exhibiting a plateau after breaking the Au-Au metallic contact. Gaussian fits to the molecule characteristic peaks observed in the 1D histograms are plotted in a lighter color in Figure 4.20(b) and 4.21(b) and are used to determine the most probable conductance value $\bar{G}$ of each oligo-porphyrin, gathered in Table 4.9. For the sake of convenience, this table also contains the low-bias $\bar{G}$ previously reported in Ref. [Leary2018b] for these oligo-porphyrins. Good agreement of our measured values with the results in Ref. [Leary2018b] is achieved, except for the case of the trimer. As it can be observed in Figure 4.20(b,e), trimer characterization is particularly challenging to perform in our setup since the most probable conductance value of these junctions reported in Ref. [Leary2018b] ($\bar{G} = 10^{-6.9}\, G_0$) lies already in the noise level of our measurements. In fact, trimer junctions were initially impossible to detect in our current signal, whose original noise level value was at $G \sim 10^{-6}\, G_0$. A major instrumental effort was made to reduce this noise and increase the total conductance window for the experiments. This involved circuits isolation and grounds careful revision, as well as a thorough reconsideration of the different parameters of the measurement procedure in order to optimize the data acquisition process. Thanks to all this, trimer junctions with conductance values between $G = 10^{-5.5}\, G_0$ and $G = 10^{-6.8}\, G_0$ can be finally clearly identified and, although not complete, this conductance range allows us to gain an insight into the thermoelectric behavior of this three-member sub-series.

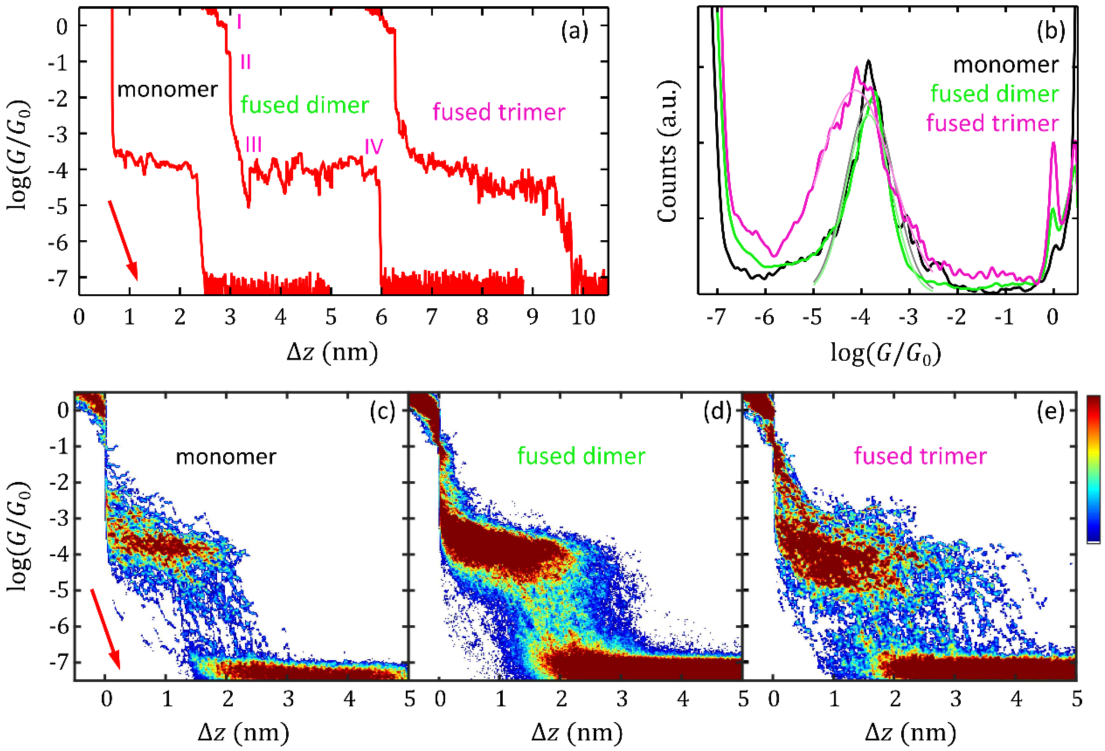

Figure 4.21: Conductance G characterization of fused oligo-porphyrins. (a) Individual examples of conductance G *vs* tip displacement Δz retraction traces for the monomer and the two fused compounds. The different features identifiable during tip retraction have been marked in the fused dimer trace: one Au atom contact ($G = G_0$) (I); metallic contact breaking (II); conductance plateau signalling molecular junction formation (III), and molecular junction breaking (IV). (b) Conductance G 1D histograms for the monomer and the fused oligo-porphyrins investigated. Histograms are formed with 66 monomer junctions (black), 434 fused dimer junctions (green) and 92 fused trimer junctions (pink). Gaussian fits to the molecular characteristic peaks are plotted in a lighter colour. (c-e) Corresponding G *vs* Δz 2D histograms built with the same curves as histograms in (b). For all the panels in this figure, the zero displacement ($\Delta z = 0$ nm) is chosen to be the position where $G = 0.1\, G_0$. Red arrows indicate the direction of increasing Δz and consequent conductance decrease. $G_0 = 2e^2/h$ is the conductance quantum (e is the electron's charge and h is Planck's constant).

In fact, in the case of the trimer we observe junctions with higher conductance values than those reported in Ref. [Leary2018b] and, therefore, we should also consider the possibility that more than one trimer molecule are connected simultaneously in our experiments. As far as the molecules do not interact laterally between them, several (n) molecules connected in parallel between the electrodes would indeed show n-times the conductance of the single-molecule junction. However, this would have in principle a minor effect in the thermoelectric characterization since molecules in parallel would present the same thermopower as the single one, as already discussed in Section 1.4. Notice that the length of the plateaus would be equivalent in both situations (n-molecules *vs* single-molecule junctions). To this respect we find ourselves constrained by the main disadvantage of this technique which is the uncertainty on the exact number of molecules participating in the junction.

Table 4.9: Junction length and most probable conductance $\overline{G}$ value. Column 2: Au-Au distance calculated in Ref. [Leary2018b] for each molecular junction, i.e. the separation between two Au atoms attached to the two terminal S atoms. Columns 3-6: comparison between the expected conductance value $\bar{G}$ measured in our setup previously to the thermopower characterization (column 3) and the low-bias (0.2 V) expected conductance values reported in Ref. [Leary2018b] (column 5). Our values are obtained from Gaussian fits applied to the 1D histograms in Figure 4.20(b) and 4.21(b). FWHM values are also gathered here for comparison (columns 4 and 6).

Molecule	Junction length (nm)	Measured $\bar{G}$ (G_0)	Measured FWHM (G_0)	Reported $\bar{G}$ (G_0)	Reported FWHM (G_0)
monomer	2.6	$10^{-3.8}$	$10^{1.2}$	$10^{-3.7}$	$10^{0.8}$
dimer	3.9	$10^{-5.1}$	$10^{1.1}$	$10^{-5.3}$	$10^{0.8}$
trimer	5.2	$10^{-6.2}$	$10^{0.9}$	$10^{-6.9}$	$10^{0.7}$
fused dimer	3.4	$10^{-3.9}$	$10^{1.1}$	$10^{-3.9}$	$10^{0.8}$
fused trimer	4.2	$10^{-4.1}$	$10^{1.8}$	$10^{-4.1}$	$10^{0.7}$

4.3.2 Thermopower S characterization

Thermoelectricity of the five oligo-porphyrins series is investigated in ambient conditions and at room temperature using the STM-BJ technique introduced in Section 2.4.3. Motivated by the wide range of conductance values of this series of molecules and the poorly conducting trimer junctions in particular, different measurement conditions are explored. The bias voltage applied between tip and sample and the size of the I-V ramps shot for thermovoltage characterization are the main parameters that we vary in order to adequate them to the conductance of each compound. Additionally, some of the experiments with the monomer are performed using just one amplification stage and no series resistor connected to the sample. Voltage and amplification conditions employed in the thermopower characterization of each oligo-porphyrin are summarized in Table 4.10. Regarding the temperature difference applied between both electrodes, we measure the thermovoltage V_{th} of each molecule for three different ΔTs. For the butadiyne-linked compounds, included the monomer, we use $\Delta T = 0$ K, ~ 20 K and ~ 40 K, while for the fused porphyrins $\Delta T = 0$ K, ~ 17 K and ~ 34 K are employed. The STM setup is always allowed to stabilize for around 20-30 min each time the ΔT is varied.

Table 4.10: Voltage and amplification conditions used in the experiments. Column 2: Number of amplification stages. Column 3: total gain for current amplification. Column 4: value of the resistor connected in series to the sample to increase the accessible conductance window. Column 5: bias voltage used for the control of the tip movement. Column 6: voltage values used in the small I-V ramps shot to characterize the thermopower.

Molecule	Number of amplification stages	Total amplification gain $(\mathrm{V/A})$	Series resistor $(\mathrm{M\Omega})$	V_{bias} (mV)	$\pm\Delta V_0(\mathrm{mV})$
monomer	1	10^8	-	50	± 10
	2	2.6×10^{10}	12	200	
dimer	2	2.6×10^{10}	12	120	± 15
trimer	2	2.6×10^{10}	12	200-230	$\pm$ 15-25
fused dimer	2	2.6×10^{10}	12	200	± 10
fused trimer	2	2.6×10^{10}	12	200	± 10

Characteristic examples of simultaneous G and V_{th} measurements for dimer junctions are presented in Figure 4.22, while equivalent curves for the other four compounds can be found in Appendix 4.C (at the end of this chapter). The three individual retraction traces shown in Figure 4.22 are performed with a different ΔT applied between tip and sample and it can be observed that thermovoltage values increase with ΔT and are positive (except for the data with $\Delta T = 0$ K, measured to calibrate the offsets). This indicates that this molecular junction has a positive Seebeck coefficient, $S = V_{th}/\Delta T$. In the case of the conductance (Figure 4.22(a)), solid red lines correspond to the complete conductance traces obtained at $V_{bias} = 120\ \mathrm{mV}$ while the red empty circles are the conductance values measured from the slope of the I-V ramps shot to characterize the thermovoltage. Correct I-V ramps acquisition is confirmed by the good agreement between these two values of G. In addition, correlation between small jumps observed in the conductance and the thermovoltage signals as the junction evolves is a signature of the high sensitivity of both magnitudes to atomic-scale rearrangements. Measurements shown in Figure 4.22 reflect one of the most powerful aspects of the experimental technique [Evangeli2014], which is the simultaneous acquisition of all this data for any molecular junction formed.

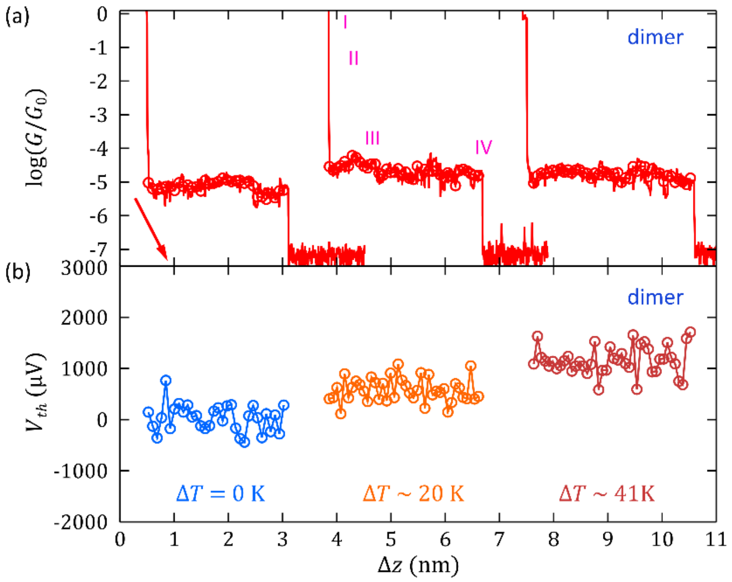

Figure 4.22: Individual conductance G and thermovoltage V_{th} vs tip displacement Δz retraction curves. Examples of simultaneous G (a) and V_{th} (b) measurements for single-molecule dimer junctions. Each junction is formed in the presence of a given temperature difference ΔT between tip and sample. The different features identifiable in the G signal have been marked in the second junction: one Au atom contact ($G = G_0$) (I); metallic contact breaking (II); conductance plateau signalling molecular junction formation (III), and molecular junction breaking (IV). Thermovoltage is only acquired in the plateau and the G values obtained from the slope of the corresponding I-V ramps is plotted in (a) as red empty circles, showing good agreement with the complete retraction curve where G is measured with $V_{bias} = 120$ mV. Δz of the different traces has been displaced for the sake of clarity. The red arrow indicates the direction of increasing Δz and decreasing G.

To find the average thermovoltage of the compounds at each ΔT applied, hundreds of these individual curves are acquired and the data is collected in 1D histograms. To facilitate comparison between molecules, we plot separately the histograms of each sub-series of porphyrin oligomers. Figure 4.23 shows the experimental values obtained for the butadiyne-linked series, while Figure 4.24 presents the data for the monomer and the fused porphyrins. Note that the monomer histograms are the same in both figures.

Before explaining the thermovoltage histograms in detail, let us introduce first the simultaneously acquired conductance 1D histograms, plotted in Figure 4.23(a-f) and 4.24(a-f) for completeness and to confirm junction formation. Conductance data in Figure 4.23(a-c) and 4.24(a-c) correspond to the G values measured at V_{bias} (see Table 4.10) and vary from the Au-Au atomic contact ($G = G_0$) down to the setup noise level, at $G < 10^{-7}G_0$. In between, junction characteristic peaks are observed. In the case of the monomer (Figure 4.23(a) or 4.24(a)), measurements performed with just one amplification stage place the noise level at $G < 10^{-5}G_0$ and produce also a very sharp (artificial) peak at $G \sim 10^{-1.7}G_0$. Between these features, the monomer junction peak at $G \sim 10^{-4}G_0$ is easily identifiable. Complementary, the G obtained from the I-V ramps is presented for the five compounds in Figure 4.23(d-f) and 4.24(d-f) and hence only the junction characteristic peaks are visible in these 1D histograms. In these six panels of each figure described, conductance peaks obtained for all the molecules at the different ΔT are in very good agreement with the G characterization discussed in the previous section and indicate that molecular junctions are correctly formed.

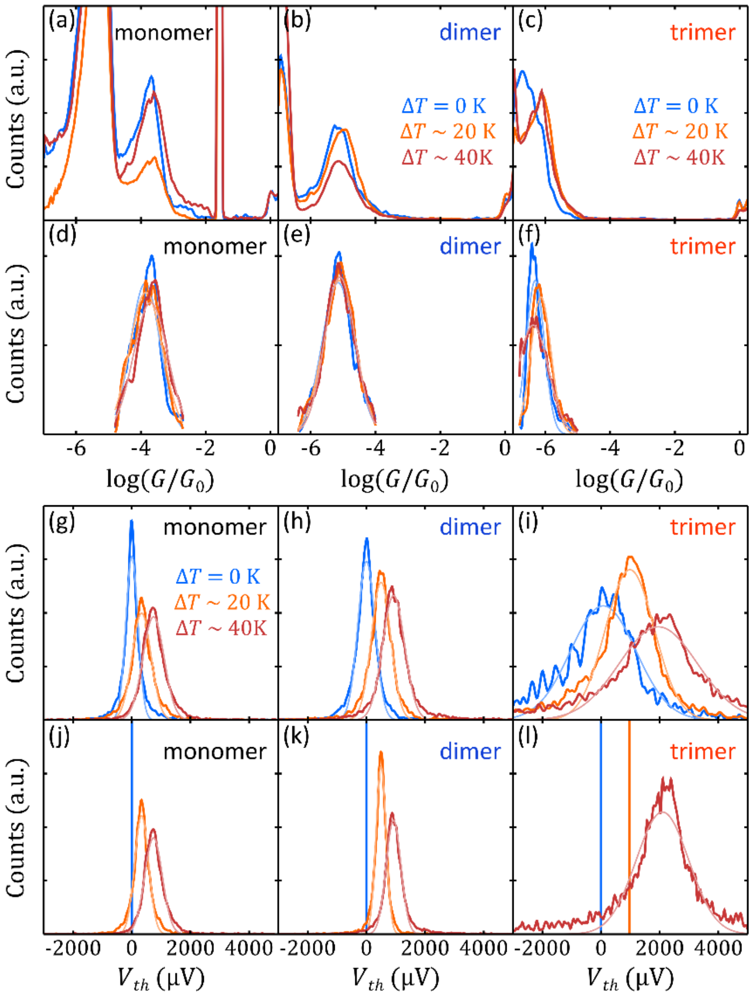

Figure 4.23: Simultaneous conductance G and thermovoltage V_{th} 1D histograms for butadiyne-linked oligo-porphyrins. Data from 357 monomer junctions, 423 dimer junctions and 315 trimer junctions is collected in these histograms. Colours correspond to measurements performed with a given temperature difference ΔT applied between tip and sample: blue histograms correspond to data measured with $\Delta T = 0$ K; orange histograms, with an average $\Delta T \sim 20$ K, and dark red histograms, with an average $\Delta T \sim 40$ K. (a-c) G 1D histograms of the three oligo-porphyrins for the three temperature difference ΔT applied between tip and sample. The conductance is measured at V_{bias} (see Table 4.10). (d-f) G 1D histograms generated with the data obtained from the slope of the I-V ramps, plotted separately for each ΔT, and Gaussian fits, plotted superimposed in a lighter color. (g-i) V_{th} 1D histograms of the porphyrin oligomers for each ΔT employed. Gaussian fits are also plotted in a lighter color superimposed on the histograms. (j-l) V_{th} 1D histograms and Gaussian fits after the dispersion correction is applied. Trimer $\sigma_{V_{th}}$ value at $\Delta T \sim 20$ K is originally smaller than $\sigma_{V_{th}}$ of the 0-K histogram and hence the values collapse to the mean V_{th} value when the dispersion correction is applied, originating the vertical orange line, as it occurs with the 0-K histograms (blue vertical lines).

Returning our attention to the thermovoltage 1D histograms (Figure 4.23(g-i) and 4.24(g-i)), the five oligo-porphyrins investigated show positive V_{th} that increases with the value of the temperature difference applied between the electrodes. Note that all these histograms values are adequately shifted to place the corresponding 0-ΔT histogram centered at zero. Thermovoltage histograms for trimer and fused trimer junctions show particularly large dispersions. In the case of trimer junctions, the fact that this peculiar increase in the dispersion affects also the $\Delta T = 0$ K histogram (in blue in Figure 4.23(i)) suggests that it is mainly produced by an experimental error. Indeed, this molecule shows the lowest conductance of the family and its value is almost in the noise level of the setup, which may certainly introduce a higher experimental error in the determination of the zero-crossing of the I-V ramps. In the case of the fused trimer measurements (Figure 4.24(i)), increased dispersion when compared to the other molecules does not appear in the 0-ΔT histogram and it seems to be proportional to ΔT, thus suggesting a different origin. The variability of thermovoltage values shown by this system may be an effect of the reduce statistics, although it is possibly caused by temperature-induced instabilities in the junction conformation.

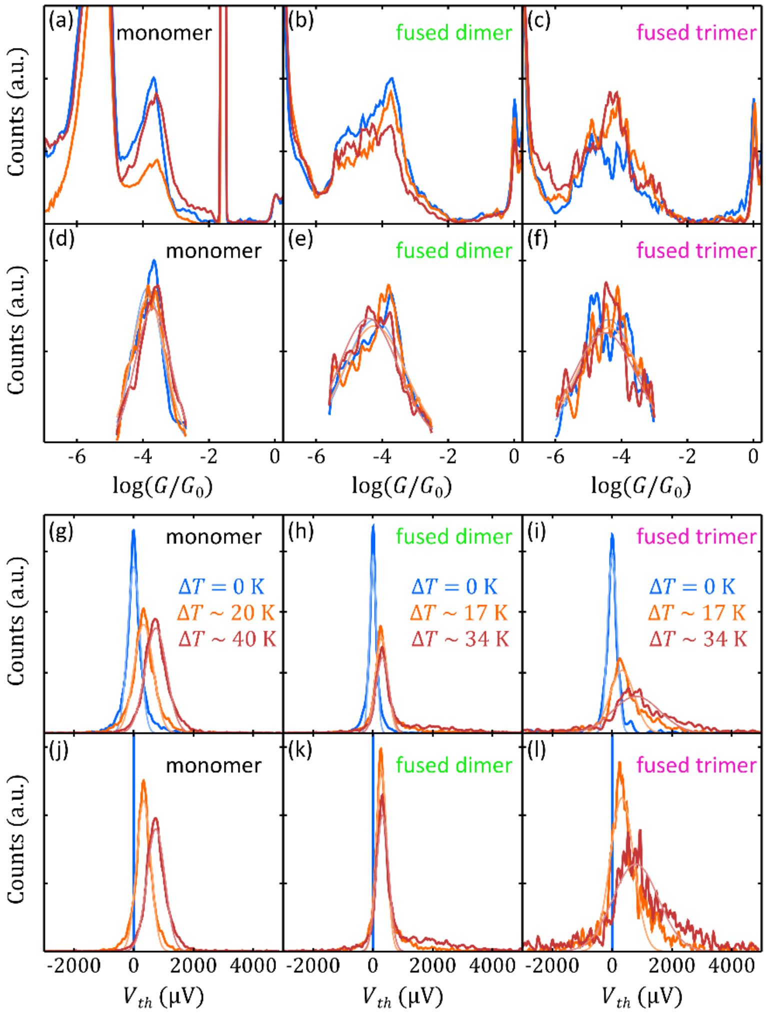

Figure 4.24: Simultaneous conductance G and thermovoltage V_{th} 1D histograms for fused oligo-porphyrins. Data from 357 monomer junctions, 472 fused dimer junctions and 108 fused trimer junctions is collected in these histograms. Colours correspond to measurements performed with a given temperature difference ΔT applied between tip and sample: blue histograms correspond to data measured with $\Delta T = 0$ K; orange histograms, with an average $\Delta T \sim 17$ K ($\Delta T \sim 20$ K for the monomer), and dark red histograms, with an average $\Delta T \sim 34$ K ($\Delta T \sim 40$ K for the monomer). (a-c) G 1D histograms of the three oligo-porphyrins for the three temperature difference ΔT applied between tip and sample. The conductance is measured at V_{bias} (see Table 4.10). (d-f) G 1D histograms generated with the conductance obtained from the slope of the I-V ramps, plotted separately for each ΔT, and Gaussian fits, plotted superimposed in a lighter color. (g-i) V_{th} 1D histograms of the porphyrin oligomers for each ΔT employed. Gaussian fits are also plotted in a lighter color superimposed on the histograms. (j-l) V_{th} 1D histograms and Gaussian fits after the dispersion correction is applied.

In order to account for the experimental error in the trimer measurements and to discern, for all the molecules, between this contribution and intrinsic dispersion of V_{th} values produced by different junction conformations when $\Delta T \neq 0 \text{ K}$ [Malen2009b], we apply the same dispersion correction introduced in Section 4.2.2 for the oligoyne wires. The dispersion of the $\Delta T = 0 \text{ K}$ histogram $\sigma_{0\text{K}}$ (the standard deviation of the Gaussian fit) is taken as a reference and we apply Eq. (4.4) and (4.5) to re-scale the dispersion of the histograms at each ΔT. Figure 4.23(j-l) and 4.24(j-l) show the thermovoltage histograms after this correction is applied. V_{th} values measured at $\Delta T = 0 \text{ K}$ are collapsed to zero, which gives rise to the sharp (blue) lines in the figures, and the other histograms show a reduced dispersion with respect to the original data. Trimer $\sigma_{V_{th}}$ value at $\Delta T \sim 20 \text{ K}$ is originally smaller than $\sigma_{V_{th}}$ of the 0-K histogram and hence the values are collapsed to the mean V_{th} value when the dispersion correction is applied, originating the vertical orange line in Figure 4.23(l).

The effect of the dispersion correction and any influence of ΔT or molecular length on the thermovoltage and its dispersion are better quantified using Gaussian distributions to fit the thermovoltage histograms in Figure 4.23(g-l) and 4.24(g-l). Mean values $\overline{V_{th}}$ and standard deviations $\sigma_{V_{th}}$ of these fits are plotted as open circles and error bars, respectively, in Figure 4.25 and 4.26 for the C4-linked and the fused oligo-porphyrins, respectively. Figure 4.25(a-c) and 4.26(a-c) presents the results obtained with the original data and Figure 4.25(d-f) and 4.26(d-f), the parameters of the fits after applying the dispersion correction. The least square linear fits shown are obtained by fitting all the individual V_{th} values independently, thus giving to all of them the same weight. The slope of this fit corresponds to the average thermopower S of the corresponding molecule and the values are shown in each plot. Except for the fused trimer data, the relative error of S obtained with this linear fit is smaller than 2% in all cases, which means that there are sufficient measurements to give a reliable value of the average S of each oligo-porphyrin. In the case of the fused trimer, the relative error in the slope of the linear fit is of 4.8%. It is a quite small value as well, but in comparison to the other fits it reflects the fact that we obtain a considerable dispersion of thermovoltage values. Given the nature of the dispersion correction applied, which reduces the width of the histograms but not its mean value, S is basically the same when fitting the data before or after the application of dispersion correction. Certain deviation is found in the case of the trimer but this is due to the large dispersion of the thermovoltage and the not-completely Gaussian shape of the thermovoltage histograms.

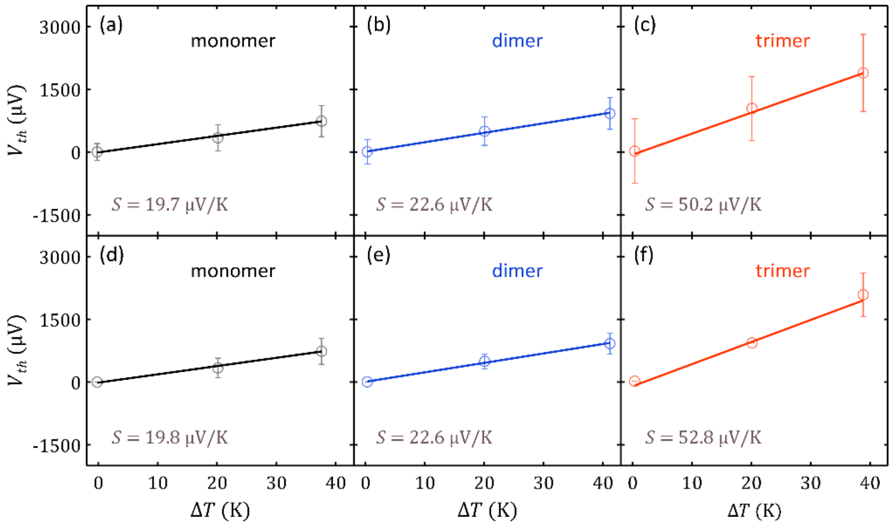

Figure 4.25: Average thermopower S for butadiyne-linked oligo-porphyrin junctions. (a-c) Least square linear fit to all the original V_{th} values of each oligo-porphyrin and average thermopower S given by the slope of the fit. Empty circles correspond to the mean thermovoltage value $\overline{V_{th}}$ obtained from the Gaussian fit of the V_{th} histogram at each ΔT. Error bars are the corresponding standard deviations $\sigma_{V_{th}}$. (d-f) Least square linear fit to all the V_{th} values after the dispersion correction is applied. The average thermopower S of each oligo-porphyrin is given by the slope of the fit. Empty circles correspond to the mean thermovoltage value $\overline{V_{th}}$ obtained from the Gaussian fit of the V_{th} histogram at each ΔT. Error bars are the corresponding standard deviations $\sigma_{V_{th}}$. Trimer $\sigma_{V_{th}}$ value at $\Delta T \sim 20$ K is originally smaller than $\sigma_{V_{th}}$ of the 0-K histogram (see (c)) and it is thus zero after the correction.

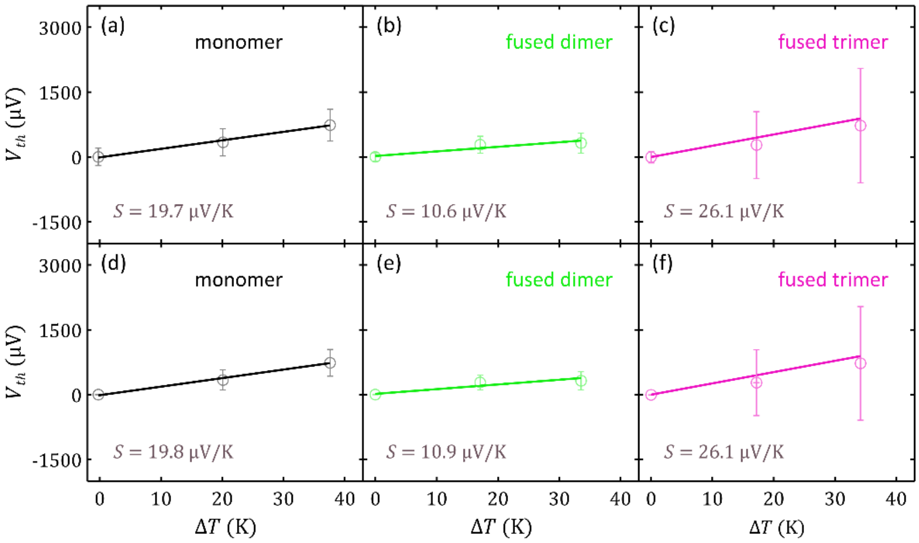

Figure 4.26: Average thermopower S for fused oligo-porphyrin junctions. (a-c) Least square linear fit to all the original V_{th} values of each oligo-porphyrin and average thermopower S given by the slope of the fit. Empty circles correspond to the mean thermovoltage value $\overline{V_{th}}$ obtained from the Gaussian fit of the V_{th} histogram at each ΔT. Error bars are the corresponding standard deviations $\sigma_{V_{th}}$. (d-f) Least square linear fit to all the V_{th} values after the dispersion correction is applied. The average thermopower S of each oligo-porphyrin is given by the slope of the fit. Empty circles correspond to the mean thermovoltage value $\overline{V_{th}}$ obtained from the Gaussian fit of the V_{th} histogram at each ΔT. Error bars are the corresponding standard deviations $\sigma_{V_{th}}$.

In the following, we focus our attention on the dispersion corrected data. To facilitate comparison, least square linear fits for the three C4-linked molecules are plotted together in Figure 4.27(a), while those of the fused tapes are plotted in Figure 4.27(d). All the average thermopower values are collected in Table 4.11. The Seebeck coefficients shown by these molecular junctions are in all cases positive and remarkably large. In fact, all of them are among the highest positive values reported in literature for organic compounds, to the best of our knowledge. The positive thermopower suggests transport mainly through the HOMO of the molecules, i.e. the Fermi level of the junction is closer to this molecular orbital [Malen2010; Rincón-García2016b]. This is in good agreement with theoretical calculations reported for this series of molecules [Leary2018b] (see Section 4.3.3) and with previously reported measurements with thiol-based anchor groups [Reddy2007].

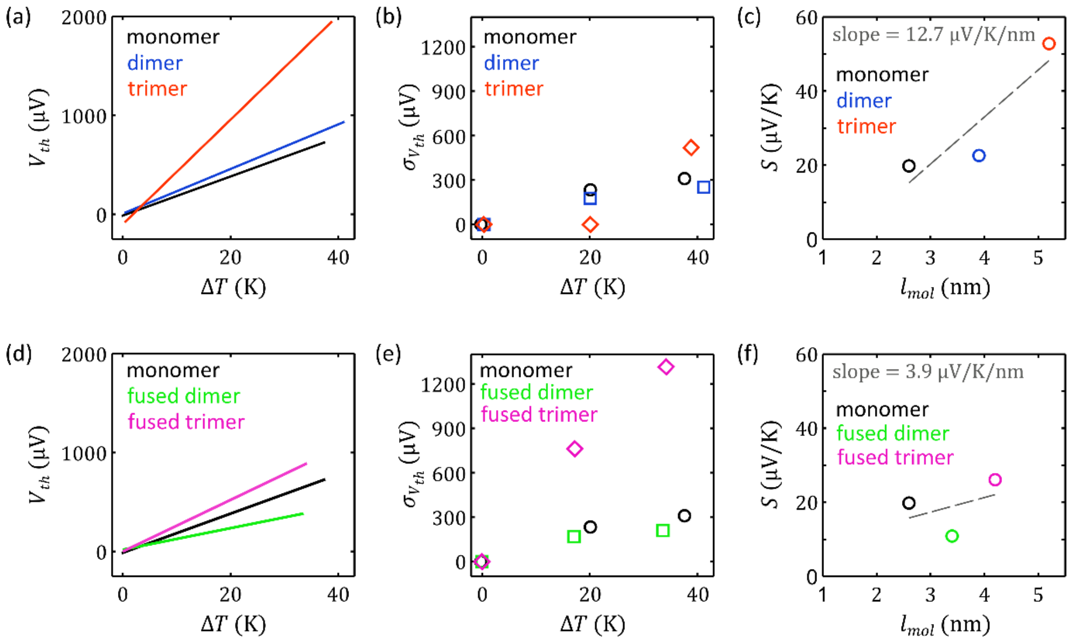

Figure 4.27: Dispersion analysis and length dependence of thermopower. (a,d) Least square linear fits for the three butadiyne-linked oligo-porphyrins investigated (a) and the fused oligo-porphyrins series (d). These fits are done considering the individual V_{th} values after the dispersion correction is applied. The positive slopes of V_{th} *vs* ΔT suggest transport through the HOMO. (b,e) Standard deviation $\sigma_{V_{th}}$ *vs* ΔT for each molecule of the C4-linked compounds (b) and the fused tapes (e). $\sigma_{V_{th}}$ is obtained from the Gaussian fits shown in Figure 4.23(j-l) and 4.24(j-l). Trimer $\sigma_{V_{th}}$ value at $\Delta T \sim 20$ K, originally smaller than $\sigma_{V_{th}}$ of the 0-K histogram (Figure 4.25(c)), becomes zero after the dispersion correction. (c,f) Length dependence of S for the two oligo-porphyrin series, butadiyne-linked molecules in (c) and fused porphyrins in (f). A least square linear fit is performed in each plot as a reference and the value of the slope is given as an inset.

With respect to the dispersion of the thermovoltage histograms, we show in Figure 4.27(b,e) the standard deviation $\sigma_{V_{th}}$ of the corresponding Gaussian fit as a function of ΔT, for the five compounds. $\sigma_{V_{th}}$ of trimer junctions at $\Delta T \sim 20$ K is originally smaller than $\sigma_{V_{th}}$ of the $\Delta T = 0$ K histogram (see Figure 4.25(c)), and it is thus zero after the correction is applied. Without considering this data point, dispersion seems to increase with increasing ΔT but it does not follow a clear trend with molecular length. Dimer and fused dimer histograms show smaller $\sigma_{V_{th}}$ than those generated for the monomer, but the trimer $\sigma_{V_{th}}$ for $\Delta T \sim 40$ K is larger (almost double) than the standard deviation of the same ΔT of monomer and dimer, even when the dispersion correction is applied (see Figure (4.27(b)). Finally, fused trimer standard deviations are by far the largest values for the two ΔT explored and a clear temperature dependence is observed. This larger dispersion in three-porphyrin molecules might be due to several reasons. On the one side, it is well known that different geometrical configurations or junction conformations affect the value of the Seebeck coefficient. Since more configurations are accessible in the case of the trimer and the fused trimer junctions, it is not surprising that these molecules present the largest dispersion of values. However, this should be then also reflected in the dimer and fused dimer dispersion values with respect to the monomer, but this is not what we observe. On the other side, despite the correction applied, trimer dispersion might still be influenced by the fact that this molecule shows the lowest conductance of the family and that its value is almost in the noise level of the setup. Fused trimer dispersion values are possibly due to large temperature-induced instabilities of junction conformation, although this is not a completely satisfactory explanation.

Table 4.11: Average thermopower S of the five oligo-porphyrins investigated. Thermopower values are obtained from the slope of the linear fits plotted in Figure 4.25(d-f) and 4.26(d-f).

Molecule	S (μV/K)
monomer	19.8
dimer	22.6
trimer	52.8
fused dimer	10.9
fused trimer	26.1

Dependence of the Seebeck coefficient with the molecular junction length is explored in Figure 4.27(c,f). Although data of both series can be linearly fit (see value of the slope as an inset in the figure), it is clear from the figure that the thermopower of these oligo-porphyrins do not follow a simple linear trend with length. It does increase as the molecules become longer, as expected, for the butadiyne-linked porphyrins, but S is enhanced by a factor 1.1 from the monomer to the dimer junctions while the enhancement reaches a factor 2.3 from the dimer to the trimer. Considering the whole C4-linked series, S is in total enhanced by a factor 2.7 from the monomer to the trimer junctions. More interestingly, thermopower does not follow a well-defined trend in the fused porphyrin series. It is reduced in fused dimer junctions with respect to the monomer value, but as the molecule length keeps increasing so does the thermopower, and the Seebeck coefficient of the fused trimer is larger than that of the monomer. Charge transport in the oligo-porphyrin junctions investigated has been reported to be through phase-coherent tunnelling [Sedghi2011; Leary2018b], although combination with incoherent hopping mechanisms have been also considered [Sedghi2008]. Coherent tunnelling transport through single-molecule junctions typically results in a linear dependence of thermopower with length [Reddy2007; Malen2009a]. This is also the case for the oligoyne wires presented in the previous section. In contrast to this situation, non-linear dependence of thermopower with length has been also observed in systems such as oligophenyls [Widawsky2013] and oligo-thiophene-1,1-dioxides [Dell2015], although in these cases a “saturation” of thermopower with increasing length was observed. Our results show a reduction of the thermopower in the two-porphyrin oligomers with respect to the value expected from the trend between the monomer and the corresponding three-porphyrin oligomer, which makes us consider that the origin of these non-linearity of thermopower with molecular length lies in an odd-even effect.

Conductance G and thermopower S *vs* tip displacement Δz 2D histograms are built in order to evaluate their (combined) evolution with the electrode separation. These histograms are presented in Figure 4.28 for the C4-linked porphyrins and are generated with the traces acquired at $\Delta T \sim 20\,\mathrm{K}$ and $\Delta T \sim 40\,\mathrm{K}$. Fused tapes results are plotted in Figure 4.29 and collect measurements perform with $\Delta T \sim 17\,\mathrm{K}$ and $\Delta T \sim 34\,\mathrm{K}$. Thermopower in these figures is obtained dividing each measured thermovoltage value by the corresponding ΔT, thus reflecting the individual thermopower values measured as the molecular junctions evolve. While Figure 4.28(a-c) and 4.29(a-c) show G values measured at V_{bias} (see Table 4.10), histograms in Figure 4.28(d-g) and 4.29(d-g) are formed with the data acquired from the small I-V ramps. Note that the area with high density of data below the monomer plateau in Figure 4.28(a), and that extends for more than $4\,\mathrm{nm}$, proceeds from the measurements performed with just one amplification stage and corresponds to the noise level of these experiments. The noise level of traces obtained with the two-stages amplification is below, at $G \sim 10^{-7} G_0$. Measurements are plotted this way for the sake of consistency.

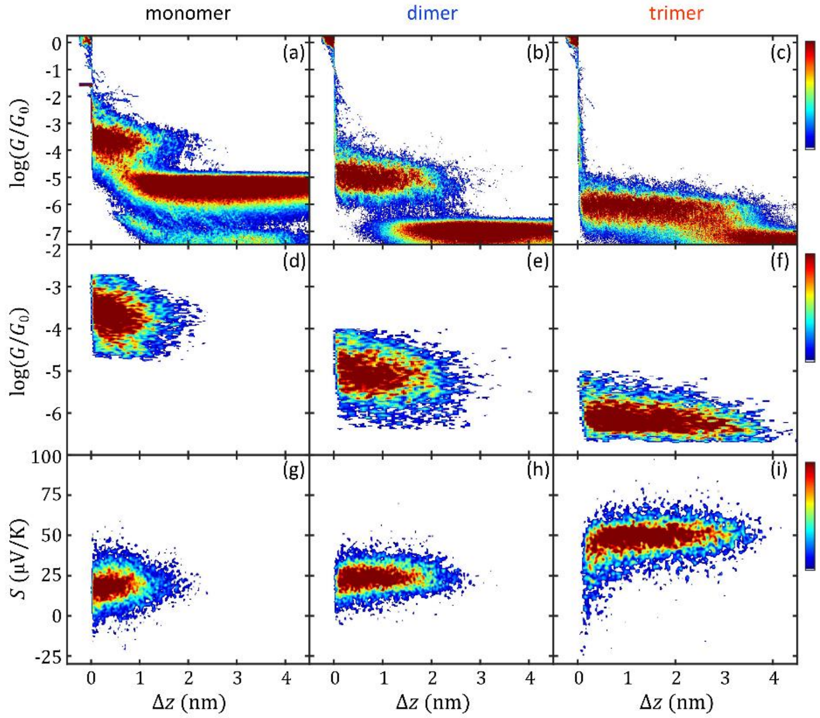

Figure 4.28: Conductance G and thermopower S *vs* tip displacement Δz 2D histograms for butadiyne-linked oligo-poprhyrins. (a-c) G *vs* Δz 2D histograms for the three compounds of this sub-series. Conductance is obtained from the current signal measured at V_{bias} (see Table 4.10): $G = I/V_{bias}$. (d-f) G *vs* Δz 2D histograms for the three molecules investigated. Conductance is obtained from the slope of the I-V ramps shot every few picometers of tip displacement (see values of $\pm\Delta V_0$ in Table 4.10). (g-i) S *vs* Δz 2D histograms for the three oligo-porphyrins. Thermopower is obtained from the thermovoltage measured with the small I-V ramps and divided by the corresponding ΔT. Data in these histograms is acquired with $\Delta T \sim 20\,\mathrm{K}$ and $\Delta T \sim 40\,\mathrm{K}$ for all the molecules and the zero displacement ($\Delta z = 0\,\mathrm{nm}$) is chosen to be the position where $G = 0.1\,G_0$. Histograms are generated with 225, 293 and 271 curves for monomer, dimer and trimer junctions, respectively. The colour scale accounts for the number of points in each histogram.

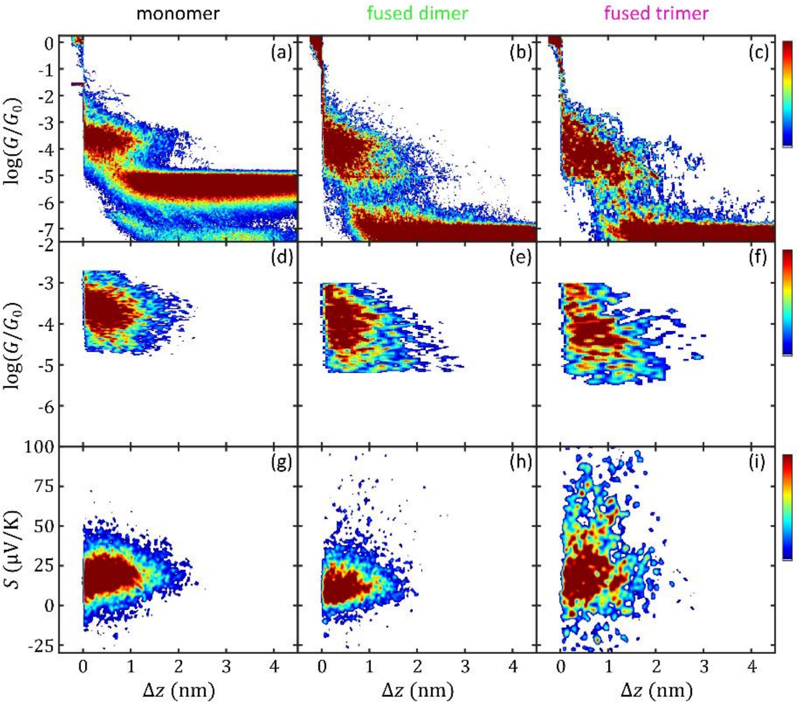

Figure 4.29: Conductance G and thermopower S *vs* tip displacement Δz 2D histograms for fused oligo-poprhyrins. (a-c) G *vs* Δz 2D histograms for the three compounds of this sub-series. Conductance is obtained from the current signal measured at V_{bias} (see Table 4.10): $G = I/V_{bias}$. (d-f) G *vs* Δz 2D histograms for the three molecules investigated. Conductance is obtained from the slope of the I-V ramps shot every few picometers of tip displacement (see values of $\pm\Delta V_0$ in Table 4.10). (g-i) S *vs* Δz 2D histograms for the three fused oligo-porphyrins. Thermopower is obtained from the thermovoltage measured with the small I-V ramps and divided by the corresponding ΔT. Data in these histograms is acquired with $\Delta T \sim 17$ K and $\Delta T \sim 34$ K for all the molecules and the zero displacement ($\Delta z = 0$ nm) is chosen to be the position where $G = 0.1\,G_0$. Histograms are generated with 225, 271 and 61 curves for monomer, fused dimer and fused trimer junctions, respectively. The colour scale accounts for the number of points in each histogram.

We do not observe any clear dependence of the thermopower with the tip displacement. In Figure 4.28 it might seem that for $\Delta z < 0.5$ nm Seebeck coefficients are smaller in value but this is just an artifact of the 2D histogram. Careful examination of the individual curves shows that these “small” thermopower values correspond to I-V ramps shot before the properly-called conductance plateau and suggests that they are a consequence of the molecular junction being formed right after the Au-Au contact is broken, whose thermopower is well-known to be approximately -1 μV/K [Evangeli2015; Ludoph1999; Tsutsui2013].

Regarding the broadening of the histograms, junction to junction variability produces a considerable dispersion in all the histograms, larger than an order of magnitude in the case of the conductance (even of two orders of magnitude for dimer and trimer junctions). The dispersion of the thermopower is much smaller than that of the conductance, confirming that G is more sensitive than S to atomic-scale fluctuations and junction configuration details [Baheti2008]. Comparing the different oligo-porphyrins, thermopower dispersion reflects the same behaviour as described for the thermovoltage (see Figure 2.27(b,e)), being the dimer the molecule with the smallest dispersion. Fused trimer 2D plot in Figure 2.29(i) shows a cloud of experimental data with an unusual general shape and it is atypically extended towards larger positive thermopower. These behaviours can be also observed in the 1D histograms shown in Figure 4.30(a-b) and 4.31(a-b), plotted with the data acquired from the I-V ramps, and in Table 4.12, where the parameters of the Gaussian fits applied to the 1D histograms of the five molecules are gathered. Mean values of these fits correspond to the most probable conductance $\bar{G}$ and thermopower $\bar{S}$ values found for molecular junctions formed with each compound. The thermopower 1D histogram for fused trimer junctions presents a not-completely Gaussian shape, with a clear tail towards large positive S values (see Figure 4.31(b)).

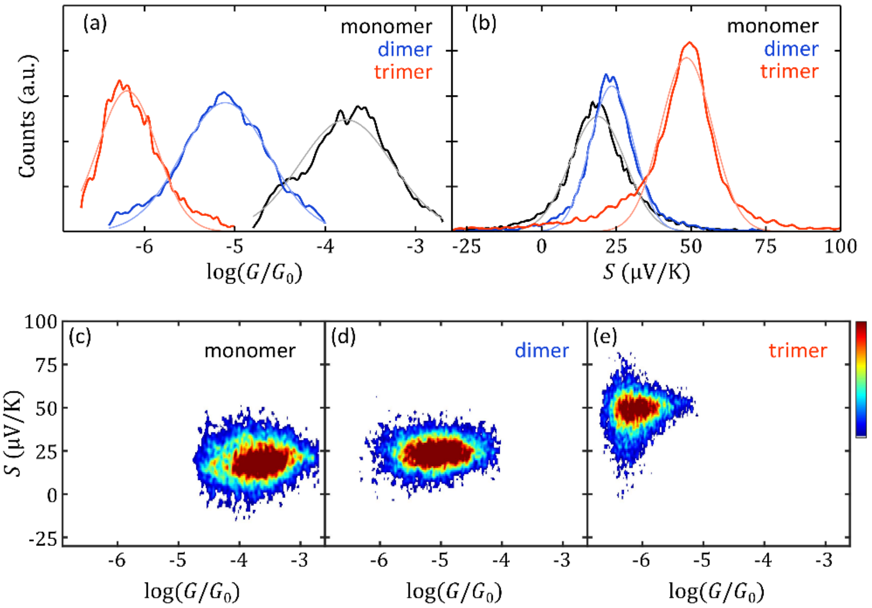

Figure 4.30: Conductance G and thermopower S of butadiyne-linked oligo-porphyrins. (a-b) G and S 1D histograms built with the data acquired from the I-V ramps and Gaussian fits plotted superimposed in a lighter colour. (c-e) S *vs* G 2D histograms for the three molecules investigated. The colour scale accounts for the number of points in each histogram.

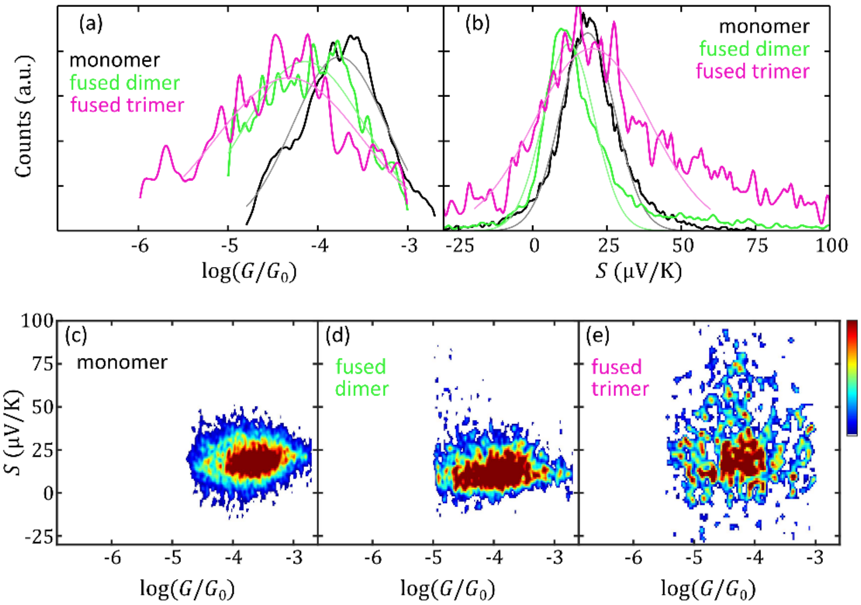

Figure 4.31: Conductance G and thermopower S of fused oligo-porphyrins. (a-b) G and S 1D histograms built with the data acquired from the I-V ramps and Gaussian fits plotted superimposed in a lighter colour. (c-e) S *vs* G 2D histograms for the three molecules investigated. The colour scale accounts for the number of points in each histogram.

Table 4.12: Most probable conductance $\bar{G}$ and thermopower $\bar{S}$ of oligo-porphyrins. $\bar{G}$ and $\bar{S}$ values in this table are acquired from the small I-V ramps shot while molecular junctions are formed. Together with the standard deviation reported here, they correspond to the parameters of the Gaussian fits presented in Figure 4.30(a-b) and 4.31(a-b).

Molecule	$\bar{G}$ (G_0)	σ_G (G_0)	$\bar{S}$ (μV/K)	σ_S (μV/K)
monomer	$10^{-3.8}$	$10^{0.5}$	18.8	9.3
dimer	$10^{-5.1}$	$10^{0.5}$	23.5	7.3
trimer	$10^{-6.2}$	$10^{0.4}$	48.5	8.6
fused dimer	$10^{-4.1}$	$10^{0.7}$	12.1	8.6
fused trimer	$10^{-4.3}$	$10^{0.8}$	19.9	19.3

Finally, S *vs* G 2D histograms for the five oligo-porphyrins investigated are presented in Figure 4.30(c-e) and 4.31(c-e). They do not show any particular correlation between these two magnitudes, except in the case of the trimer. According to Figure 4.30(e), this molecule exhibits a larger dispersion of thermopower as the conductance decreases. However, it should be kept in mind that measurements of these junctions are already very close to the noise level of the experimental setup and that noise has a more remarkable impact in the I-V ramps as the conductance becomes smaller. Thermovoltage determination (i.e. the zero-crossing of the current) becomes more challenging and an increase in the dispersion at this extremely low conductance is thus to be expected. Fused trimer 2D histogram in Figure 4.31(e) also shows the aforementioned extension of the cloud of points towards larger positive thermopower values, but no correlation with conductance values is observed.

4.3.3 Theoretical calculations and qualitative comparison with experimental results

DFT theoretical calculations for the three butadiyne-linked and the two fused oligo-porphyrins investigated are reported in Ref. [Leary2018b] and the transmission function for Au|single-molecule|Au junctions is presented. Applying the so-called scissor correction they obtain the transmission functions shown in Figure 4.32.

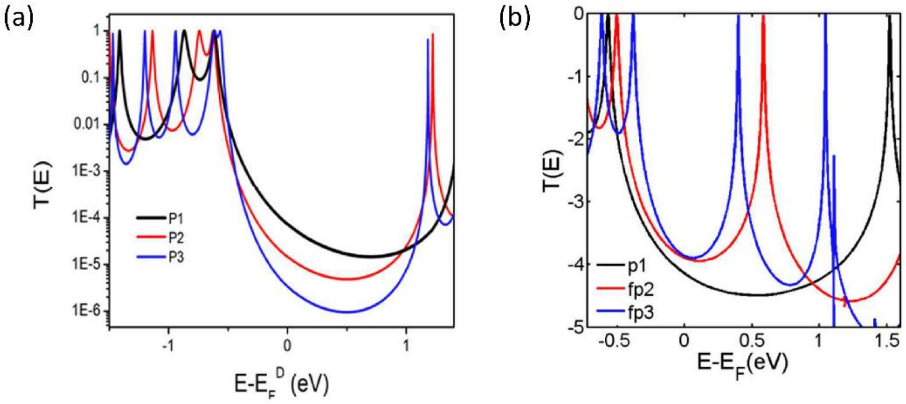

Figure 4.32: Theoretical transmission functions of the five oligo-porphyrin junctions. P1, P2 and P3 are the monomer, dimer and trimer molecules, respectively, while fp2 and fp3 correspond to the fused dimer and fused trimer compounds, respectively. Figures from Ref. [Leary2018b].

We consider that our experimental results are qualitatively in good agreement with the reported theoretical calculations. Limitations of DFT calculations in determining precisely the relative alignment of molecular levels with respect to the Fermi level E_F of the electrodes have been already discussed (see Section 1.4), but, having this in mind, we observe the thermoelectric response qualitatively expected from the transmission functions of Figure 4.32(a) for the butadiyne-linked molecules. The positive Seebeck coefficient measured for the three molecules and the increasing value as porphyrin units are added are in good agreement with the E_F of these systems lying closer to the HOMO of the molecules and the fact that the slope of the transmission around E_F increases with molecular length.

With respect to the fused porphyrins, it seems that peculiar behaviour of the thermopower within this series can be also explained in terms of the transmission curves of Figure 4.32(b). The slope of the fused dimer transmission function for theoretical values $E - E_F \sim 0\ \mathrm{eV}$ is smaller than the slope of the transmission curve of the monomer, while fused trimer transmission curve shows a more pronounced slope similar to that of the monomer, which is also in good agreement with the experimental results.

Additionally, the small HOMO-LUMO gap of fused trimer junctions in particular may explain the large dispersion in thermopower values obtained for this compound. The Fermi level is relatively close to the HOMO resonance of this molecule and hence, variations in junction conformation may result in larger variability of the slope of the transmission and the Seebeck coefficient.

4.3.4 Conclusions on oligo-porphyrins characterization

We have performed a thermoelectric characterization of Zn-based oligo-porphyrins where both molecular length and inter-porphyrin coupling are varied. The molecules have been synthesized by the group of Prof. Harry Anderson and consist of 1, 2 or 3 individual porphyrin units linearly connected in two different modes: using butadiyne linkers or directly “fusing” the porphyrins between them by three single C-C bonds. The monomer, i.e. the compound formed by just one porphyrin unit, is the same for both groups of molecules, thus serving as a common reference.

Conductance of the five oligo-porphyrins has been previously studied in our group and were found to present a voltage-dependent β value. Additionally, fused porphyrins were reported to be the first molecules showing a negative β for moderate bias voltages. At low bias voltage the β value of these porphyrins is rather small, almost zero, while the β of the butadiyne-linked porphyrins is considerably larger, around $2\ \mathrm{nm}^{-1}$.

Measurements of the thermoelectric response of these five compounds have been performed, finding in all cases a positive value of the Seebeck coefficient. This indicates charge transport mainly through the HOMO, in good agreement with previously reported theoretical calculations. Monomer junctions have a most probable thermopower value $\bar{S} = -18.8 \pm 9.3\ \mu\mathrm{V/K}$ and our measurements demonstrate a 2.7-fold enhancement in the thermopower with increasing length in the case of butadyine-linked porphyrin oligomers, from the monomer to the trimer. Indeed, trimer junctions Seebeck coefficient ($\bar{S} = 48.5 \pm 8.6\ \mu\mathrm{V/K}$) is one of the largest values reported so far, to the best our knowledge.

Thermopower of fused porphyrin tapes exhibits a different behaviour with increasing molecular length. In particular, the fused dimer Seebeck coefficient is almost half the S of the monomer while the fused trimer S is similar to that of the single-porphyrin unit or even larger, depending on the consideration we make about the large dispersion of thermovoltage values of junctions formed with this molecule. In fused trimer junctions with respect to the monomer values, a molecular length increase by a factor 1.6 occurs without dramatically reducing the conductance nor the thermopower, which is a very promising result for molecular wiring.

More interestingly, our results suggest the influence of an odd-effect effect in the thermopower of these whole series and we have found that, independently of the coupling in the backbone, oligo-porphyrins formed by two porphyrin units present a reduced thermopower value in comparison to the value expected from the observed trend between the monomer and the corresponding three-porphyrin compound.

In summary, the thermoelectric characterization performed for this series of compounds suggests that thermopower enhancement based on porphyrin oligomers is a very appealing strategy, especially in systems where a relatively high conductance value is maintained when increasing the molecular length, such as the fused trimer. Furthermore, the study performed opens the door to future investigations on the dependence of the thermoelectric behaviour of porphyrins with different metallic atoms in their structure.

4.4 Conclusions

We have addressed in this chapter different strategies to enhance the thermopower of single-molecule junctions. In particular, we have investigated the addition of side-groups into a fluorene backbone and the effect of increasing length in a series of oligoyne wires and Zn-based oligo-porphyrins. Using the STM-Break Junction (STM-BJ) technique, Au|single-molecule|Au junctions of these compounds have been formed and their conductance and thermopower simultaneously characterized in ambient conditions and at room temperature.

Our experimental measurements with the fluorene derivatives show that the C(9) substituent has little effect on the conductance, although there is a more significant influence on the thermopower, with the Seebeck coefficient varying by a factor of 1.65 within the series. The combined experimental and computational study, with density functional theory (DFT) calculations performed by the group of Prof. Colin J. Lambert, provides insights into the interplay of conductance and thermopower in single-molecule junctions.

With respect to the second strategy, based on length tunability of the thermopower, we have investigated its effect in two families with different linking-nature between the conforming units: oligoyne wires (where the number of alternating single and triple is varied from molecule to molecule) and oligo-porphyrins (where porphyrin units are softly linked by alkynes). Our results show that the oligoyne family presents a negative Seebeck coefficient which increases linearly with increasing length, while the porphyrin-based compounds exhibit positive values of thermopower and the trend with increasing length seems to present an odd-even effect, with partial suppression of the thermopower in molecules formed by two porphyrin units connected in series.

In summary, our experiments provide insights into the interplay of conductance and thermopower in single-molecule junctions and are expected to serve as a guide for new strategies for thermopower modulation.

Appendix 4.A: Individual traces of simultaneous conductance G and thermovoltage V_{th} measurements *vs* tip displacement Δz for fluorene derivative junctions

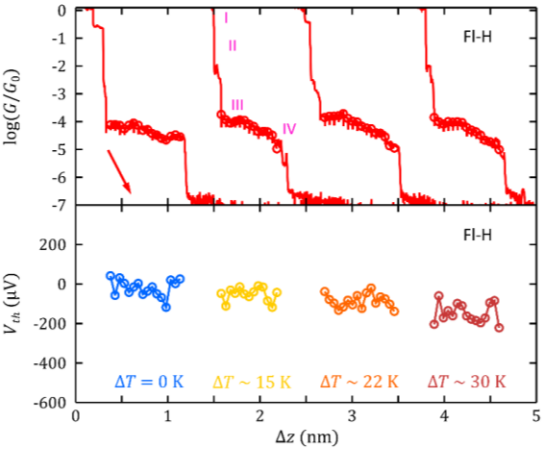

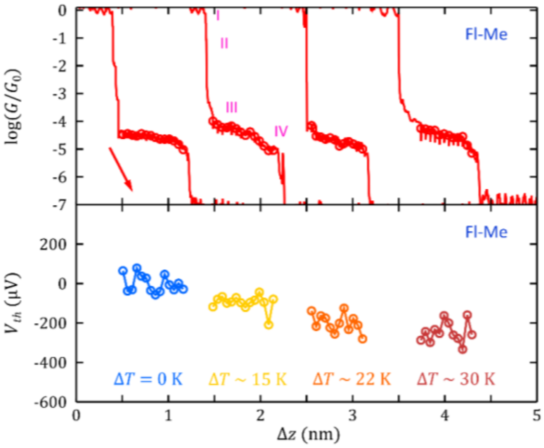

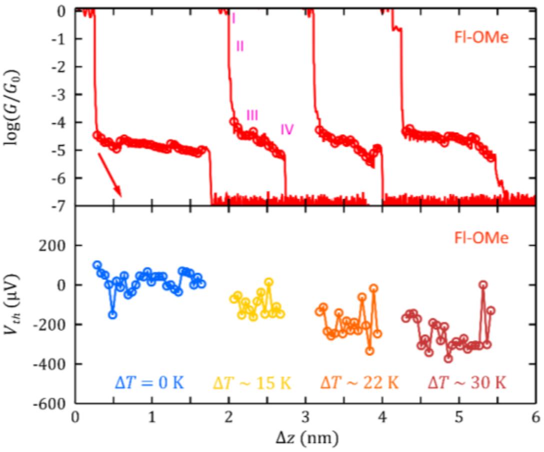

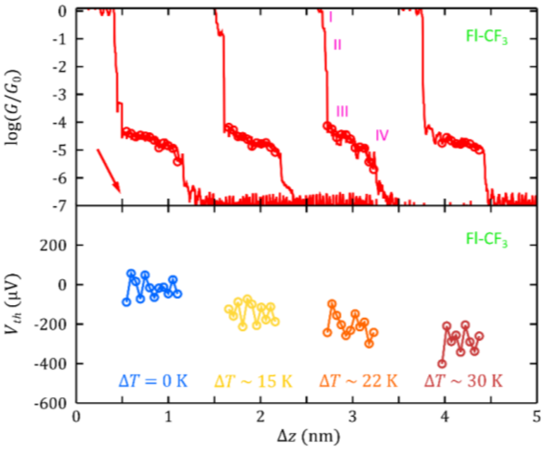

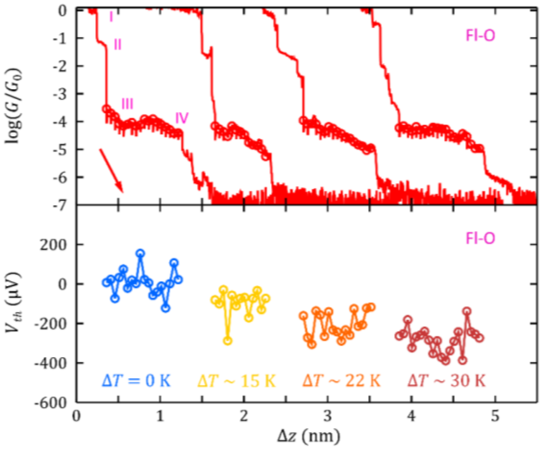

Appendix 4.B: Individual traces of simultaneous conductance G and thermovoltage V_{th} measurements *vs* tip displacement Δz for oligoyne wire junctions

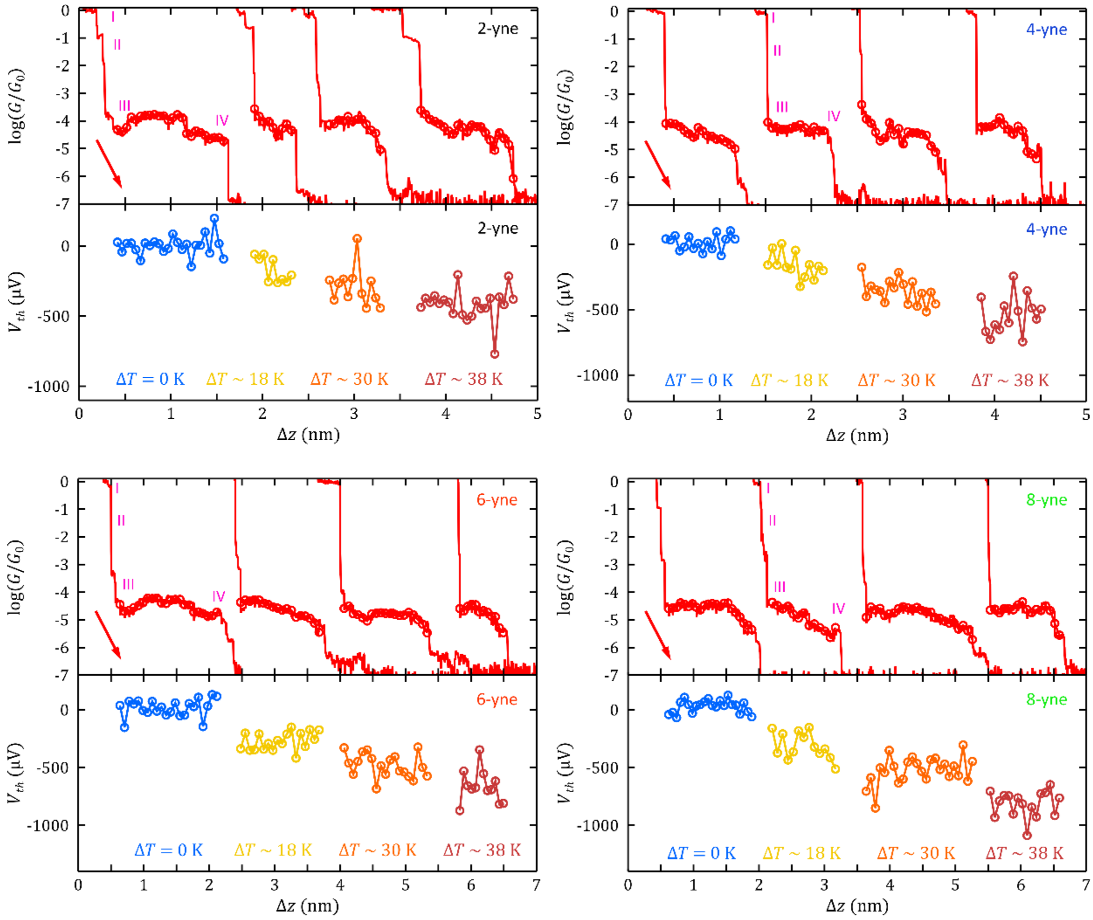

Appendix 4.C: Individual traces of simultaneous conductance G and thermovoltage V_{th} measurements *vs* tip displacement Δz for Zn-based oligo-porphyrin junctions

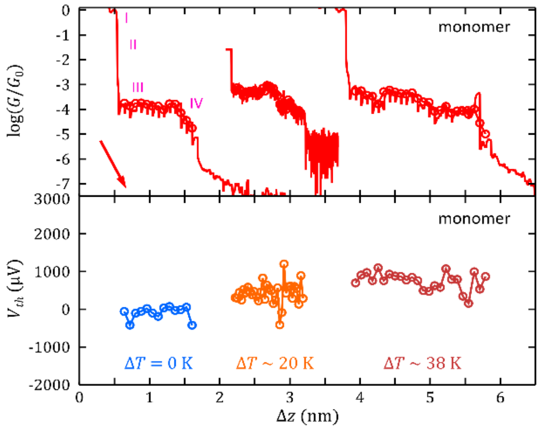

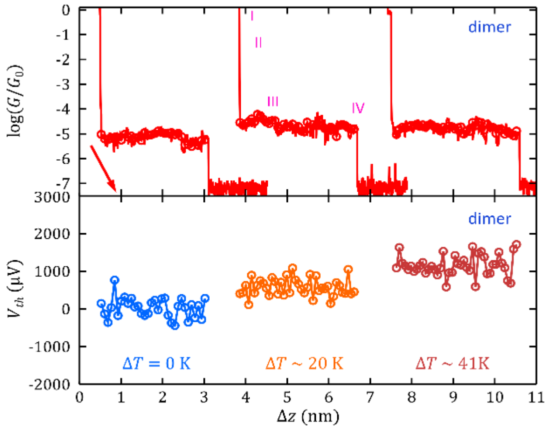

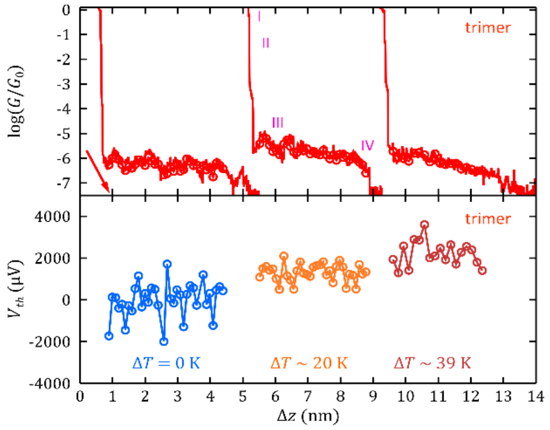

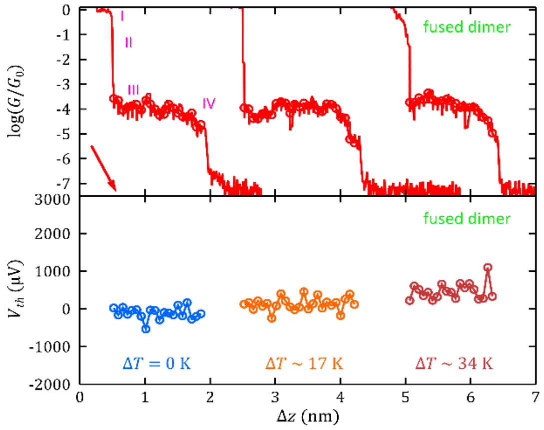

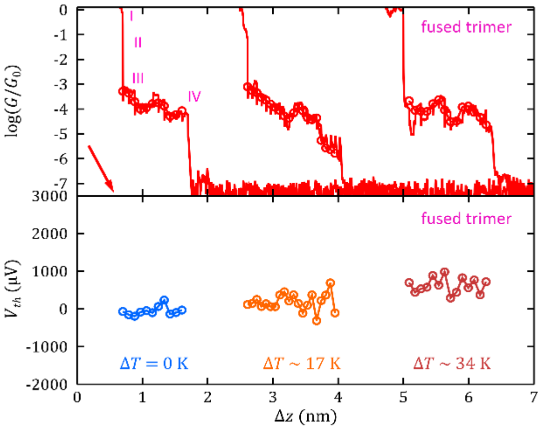

References

[Agraït1995] N. Agraït, G. Rubio and S. Vieira. "Plastic Deformation of Nanometer-Scale Gold Connective Necks". *Physical Review Letters* **74**(20), 3995-3998 (1995).

[Atienza-Castellanos2007] C. Atienza-Castellanos, M. Wielopolski, D. M. Guldi, C. van der Pol, M. R. Bryce, S. Filippone and N. Martín. "Determination of the attenuation factor in fluorene-based molecular wires". *Chemical Communications* **48**, 5164-5166 (2007).

[Baheti2008] K. Baheti, J. A. Malen, P. Doak, P. Reddy, S.-Y. Jang, T. D. Tilley, A. Majumdar and R. A. Segalman. "Probing the Chemistry of Molecular Heterojunctions Using Thermoelectricity". *Nano Letters* **8**(2), 715-719 (2008).

[Balachandran2012] J. Balachandran, P. Reddy, B. D. Dunietz and V. Gavini, "End-group-induced charge transfer in molecular junctions: Effect on electronic-structure and thermopower". *The Journal of Physical Chemistry Letters* **3**(15), 1962-1967 (2012).

[Chalifoux2010] W. A. Chalifoux and R. R. Tykwinski. "Synthesis of polyynes to model the sp-carbon allotrope carbine", *Nature Chemistry* **2**, 967-971 (2010).

[Chang2014] W. B. Chang, C.-K. Mai, M. Kotiuga, J. B. Neaton, G. C. Bazan and R. A. Segalman. "Controlling the Thermoelectric Properties of Thiophene-Derived Single-Molecule Junctions". *Chemistry of Materials* **26**(24), 7229-7235 (2014).

[Claughton1995] N. R. Claughton, M. Leadbeater and C. J. Lambert. "Theory of Andreev Resonances in Quantum Dots". *Journal of Physics: Condensed Matter* **7**(46), 8757 (1995).

[Dell2015] E. J. Dell, B. Capozzi, J. Xia, L. Venkataraman and L. M. Campos. "Molecular length dictates the nature of charge carriers in single-molecule junctions of oxidized oligothiophenes". *Nature Chemistry* **7**, 209-2014 (2015).

[Evangeli2013] C. Evangeli, K. Gillemot, E. Leary, M. T. González, G. Rubio-Bollinger, C. J. Lambert and N. Agraït. "Engineering the Thermopower of C_{60} Molecular Junctions". *Nano Letters* **13**(5), 2141-2145 (2013).

[Evangeli2014] C. Evangeli. "Thermopower and Conductance of single-Molecule Junctions and Atomic Contacts". PhD Thesis (2014).

[Evangeli2015] C. Evangeli, M. Matt, L. Rincón-García, F. Pauly, P. Nielaba, G. Rubio-Bollinger, J. C. Cuevas and N. Agraït. "Quantum Thermopower of Metallic Atomic-Size Contacts at Room Temperature". *Nano Letters* **15**(2), 1006-1011 (2015).

[Ferrer2014] J. Ferrer, C. J. Lambert, V. M. Garcia-Suarez, D. Z. Manrique, D. Visontai, L. Oroszlany, R. Rodriguez-Ferradas, I. Grace, S. W. D. Bailey, K. Gillemot, H. Sadeghi and L. A. Algharagholy. "GOLLUM: a Next-Generation Simulation Tool for Electron, Thermal and Spin Transport". *New Journal of Physics* **16**, 093029 (2014).

[Gantenbein2017] M. Gantenbein, L. Wang, A. A. Al-Jobory, A. K. Ismael, C. J. Lambert, W. J. Hong and M. R. Bryce. "Quantum Interference and Heteroaromaticity of *Para*- and *Meta*-Linked Bridged Biphenyl Units in Single Molecular Conductance Measurements". *Scientific Reports* **7**, 1794 (2017).

[García-Suárez2014] V. M. García-Suárez, C. J. Lambert, D. Z. Manrique and T. Wandlowski. "Redox control of thermopower and figure of merit in phase-coherent molecular wires". *Nanotechnology* **25**, 205402 (2014).

[González2006] M. T. González, S. Wu, R. Huber, S. J. van der Molen, C. Schönenberger and M. Calame. "Electrical Conductance of Molecular Junctions by a Robust Statistical Analysis". *Nano Letters* **6**(10), 2238-2242 (2006).

[Guo2013] S. Guo, G. Zhou, N. Tao. "Single Molecule Conductance, Thermopower, and Transition Voltage". *Nano Letters* **13**(9), 4326–4332 (2013).

[Haiss2008] W. Haiss, C. Wang, R. Jitchati, I. Grace, S. Martin, A. S. Batsanov, S. J. Higgins, M. R. Bryce, C. J. Lambert, P. S. Jensen and R. J. Nichols. "Variable Contact Gap Single-Molecule Conductance Determination for a Series of Conjugated Molecular Bridges". *Journal of Physics: Condensed Matter* 20(37), 4119 (2008).

[Hines2010] T. Hines, I. Diez-Perez, J. Hihath, H. Liu, Z.-S. Wang, J. Zhao, G. Zhou, K. Müllen and N. Tao. "Transition from Tunneling to Hopping in Single Molecular Junctions by Measuring Length and Temperature Dependence". *Journal of the American Chemical Society* **132**(33), 11658-11664 (2010).

[Holten2002] D. Holten, D. F. Bocian and J. S. Lindsey. "Probing Electronic Communication in Covalently Linked Multiporphyrin Arrays. A Guide to the Rational Design of Molecular Photonic Devices". *Accounts of Chemical Research* **35**(1), 57-69 (2002).

[Hung2009] Y.-C. Hung, J.-C. Jiang, C.-Y. Chao, W.-F. Su and S.-T. Lin. "Theoretical Study on the Correlation Between Band Gap, Bandwidth, and Oscillator Strength in Fluorene-Based Donor-Acceptor Conjugated Copolymers". *The Journal of Physical Chemistry B* **113**(24), 8268-8277 (2009).

[Hüser2015] F. Hüser and G. C. Solomon. "From Chemistry to Functionality: Trends for the Length Dependence of the Thermopower in Molecular Junctions". *The Journal of Physical Chemistry C* **119**(25), 14056–14062 (2015).

[James2006] P. V. James, P. K. Sudeep, C. H. Suresh and K. George Thomas. "Photophysical and Theoretical Investigations of Oligo(p-phenyleneethynylene)s: Effect of Alkoxy Substitution and Alkyne–Aryl Bond Rotations". *The Journal of Physical Chemistry A* **110**(13), 4329-4337 (2006).

[Kiguchi2009] M. Kiguchi, T. Takahashi, M. Kanehara, T. Teranishi and K. Murakoshi. "Effect of End Group Position on the Formation of a Single Porphyrin Molecular Junction". *The Journal of Physical Chemistry C* **113**(21), 9014-9017 (2009).

[Kim2014a] S. Kim, W. Jeong, K. Kim, W. Lee and P. Reddy. "Electrostatic control of thermoelectricity in molecular junctions". *Nature Nanotechnology* **9**(), 881-885 (2014).

[Kim2014b] T. Kim, P. Darancet, J. R. Widawsky, M. Kotiuga, S. Y. Quek, J. B. Neaton and L. Venkataraman. "Determination of Energy Level Alignment and Coupling Strength in 4,4′-Bipyridine Single-Molecule Junctions". *Nano Letters* **14**(2), 794-798 (2014).

[Klausen2014] R. S. Klausen, J. R. Widawsky, T. A. Su, H. Li, Q. Chen, M. L. Steigerwald, L. Venkataraman and C. Nuckolls. "Evaluating Atomic Components in Fluorene Wires". *Chemical Science* **5**(4), 1561-1564 (2014).

[Krempe2016] M. Krempe, R. Lippert, F. Hampel, I. Ivanović-Burmazović, N. Jux and R. R. Tykwinski. "Pyridyl-Endcapped Polyynes: Stabilized Wire-like Molecules". *Angewandte Chemie International Edition* **55**(47), 14802-14806 (2016).

[Kuang2018] G. Kuang, S. Z. Chen, L. Yan, K. Q. Chen, X. Shang, P. N. Liu and N. J. Lin. "Negative Differential Conductance in Polyporphyrin Oligomers with Nonlinear Backbones". *Journal of the American Chemical Society* **140**(2), 570-573 (2018).

[Leary2018a] E. Leary, C. Roche, H.-W. Jiang, I. Grace, M. T. González, G. Rubio-Bollinger, C. Romero-Muñiz, Y. Xiong, Q. Al-Galiby, M. Noori, M. A. Lebedeva, K. Porfyrakis, N. Agraït, A. Hodgson, S. J. Higgins, C. J. Lambert, H. L. Anderson and R. J. Nichols. "Detecting Mechanochemical Atropisomerization within an STM Break Junction". *Journal of the American Chemical Society* **140**(2), 710-718 (2018).

[Leary2018b] E. Leary, B. Limburg, A. Alanazy, S. Sangtarash, I. Grace, K. Swada, L. J. Esdaile, M. Noori, M. T. González, G. Rubio-Bollinger, H. Sadeghi, A. Hodgson, N. Agraït, S. J. Higgins, C. J. Lambert, H. L. Anderson and R. J. Nichols. "Bias-Driven Conductance Increase with Length in Porphyrin Tapes". *Journal of the American Chemical Society* **140**(40), 12877-12883 (2018).

[Lee2014] S. K. Lee, T. Ohto, R. Yamada and H. Tada. "Thermopower of benzenedithiol and C_{60} molecular junctions with Ni and Au electrodes". *Nano Letters* **14**(9), 5276-5280 (2014).

[Li2012] Z. Li, T.-H. Park, J. Rawson, M. J. Therien and E. Borguet. “Quasi-Ohmic Single Molecule Charge Transport through Highly Conjugated *meso*-to-*meso* Ethyne-Bridged Porphyrin Wires”. *Nano Letters* **12**(6), 2722-2727 (2012).

[Li2013] Z. Li, M. Smeu, M. A. Ratner and E. Borguet. “Effect of Anchoring Groups on Single Molecule Charge Transport through Porphyrins”. *The Journal of Physical Chemistry C* **117**(29), 14890−14898 (2013).

[Li2014] Z. Li, M. Smeu, T.-H. Park, J. Rawson, Y. Xing, M. J. Therien, M. A. Ratner and E. Borguet. “Hapticity-Dependent Charge Transport through Carbodithioate-Terminated [5,15-Bis(phenylethynyl)porphinato]zinc(II) Complexes in Metal–Molecule–Metal Junctions”. *Nano Letters* **14**(10), 5493-5499 (2014).

[Lof1992] R. W. Lof, M. A. van Veenendaal, B. Koopmans, H. T. Jonkman and G. A. Sawatzky. “Band Gap, Excitons, and Coulomb Interaction in Solid C_{60}”. *Physical Review Letters* **68**, 3924-3927 (1992).

[Ludoph1999] B. Ludoph and J. M. van Ruitenbeek. “Thermopower of atomic-size metallic contacts”. *Physical Review B* **59**(19), 12290-12293 (1999).

[Luo2011] L. Luo, S. H. Choi and C. D. Frisbie. “Probing Hopping Conduction in Conjugated Molecular Wires Connected to Metal Electrodes”. *Chemistry of Materials*, **23**(3), 631-645 (2011).

[Malen2009a] J. A. Malen, P. Doak, K. Baheti, T. D. Tilley, R. A. Segalman and A. Majumdar. “Identifying the Length Dependence of Orbital Alignment and Contact Coupling in Molecular Heterojunctions”. *Nano Letters* **9**(3), 1164–1169 (2009).

[Malen2009b] J. A. Malen, P. Doak, K. Baheti, T. D. Tilley, A. Majumdar and Rachel A. Segalman. “The Nature of Transport Variations in Molecular Heterojunction Electronics”. *Nano Letters* **9**(10), 3406-3412 (2009).

[Malen2010] J. A. Malen, S. K. Yee, A. Majumdar and R. A. Segalman. “Fundamentals of Energy Transport, Energy Conversion and Thermal Properties in Organic-Inorganic Heterojunctions”. *Chemical Physics Letters* **491**(4-6), 109-122 (2010).

[Miao2018] R. Miao, H. Xu, M. Skripnik, L. Cui, K. Wang, K. G. L. Pedersen, M. Leijnse, F. Pauly, K. Wärnmark, E. Meyhofer, P. Reddy and H. Linke, “Influence of Quantum Interference on the Thermoelectric Properties of Molecular Junctions”. *Nano Letters* **18**(9), 5666-5672 (2018).

[Moreno-García2013] P. Moreno-García, M. Gulcur, D. Z. Manrique, T. Pope, W. Hong, V. Kaliginedi, C. Huang, A. S. Batsanov, M. R. Bryce, C. J. Lambert and T. Wandlowski. “Single-Molecule Conductance of Functionalized Oligoynes: Length Dependence and Junction Evolution”. *Journal of the American Chemical Society* **135**(33), 12228-12240 (2013).

[Perrin2013] M. L. Perrin, C. J. O. Verzijl, C. A. Martin, A. J. Shaikh, R. Eelkema, J. H. van Esch, J. M. van Ruitenbeek, J. M. Thijssen, H. S. J. van Der Zant and D. Dulić. “Large tunable image-charge effects in single-molecule junctions”. *Nature Nanotechnology* **8**, 282-287 (2013).

[Quek2009] S. Y. Quek, M. Kamenetska, M. L. Steigerwald, H. J. Choi, S. G. Louie, M. S. Hybertsen, J. B. Neaton, and L. Venkataraman. “Mechanically controlled binary conductance switching of a single-molecule junction”. *Nature Nanotechnology* **4**, 230-234 (2009).

[Reddy2007] P. Reddy, S.-Y. Jang, R. A. Segalman and A. Majumdar. “Thermoelectricity in Molecular Junctions”. *Science* **315**, 1568-1571 (2007).

[Rincón-García2016a] L. Rincón-García, A. K. Ismael, C. Evangeli, I. Grace, G. Rubio-Bollinger, K. Porfyrakis, N. Agraït and C. J. Lambert. “Molecular Design and Control of Fullerene-Based Bi-Thermoelectric Materials”. *Nature Materials* **15**, 289–293 (2016).

[Rincón-García2016b] L. Rincón-García, C. Evangeli, G. Rubio-Bollinger and N. Agraït. “Thermopower Measurements in Molecular Junctions”. *Chemical Society Reviews* **45**, 4285-4306 (2016).

[Sadeghi2015] H. Sadeghi, S. Sangtarash and C. J. Lambert. "Oligoyne Molecular Junctions for Efficient Room Temperature Thermoelectric Power Generation". *Nano Letters* **15**(11), 7467−7472 (2015).

[Scholes2011] G. D. Scholes, G. R. Fleming, A. Olaya-Castro, R. Van Grondelle. "Lessons from nature about solar light harvesting". *Nature Chemistry* **3**, 763-774 (2011).

[Sedghi2008] G. Sedghi, K. Sawada, L. J. Esdaile, M. Hoffmann, H. L. Anderson, D. Bethell, W. Haiss, S. J. Higgins, R. J. Nichols. "Single Molecule Conductance of Porphyrin Wires with Ultralow Attenuation". *Journal of the American Chemical Society* **130**(27), 8582-8583 (2008).

[Sedghi2011] G. Sedghi, V. M. García-Suárez, L. J. Esdaile, H. L. Anderson, C. J. Lambert, S. Martín, D. Bethell, S. J. Higgins, M. Elliott, N. Bennett, J. E. Macdonald and R. J. Nichols. "Long-range electron tunnelling in oligo-porphyrin molecular wires". *Nature Nanotechnology* **6**, 517-523 (2011).

[Sedghi2012] G. Sedghi, L. J. Esdaile, H. L. Anderson, S. Martin, D. Bethell, S. J. Higgins and R. J. Nichols. "Comparison of the Conductance of Three Types of Porphyrin-Based Molecular Wires: β,*meso*,β-Fused Tapes, *meso*-Butadiyne-Linked and Twisted *meso-meso* Linked Oligomers". *Advanced Materials* **24**(5), 653-657 (2012).

[Soler2002] J. M. Soler, E. Artacho, J. D. Gale, A. Garcia, J. Junquera, P. Ordejon, D. Sanchez-Portal. "The SIESTA Method for *ab initio* Order-*N* Materials Simulation". *Journal of Physics: Condensed Matter* **14**(11), 2745-2779 (2002).

[Szafert2003] S. Szafert and J. A. Gladysz. "Carbon in One Dimension: Structural Analysis of the Higher Conjugated Polyynes". *Chemical Reviews* **103**(11), 4175-4206 (2003).

[Szafert2006] S. Szafert and J. A. Gladysz. "Update 1 of: Carbon in One Dimension: Structural Analysis of the Higher Conjugated Polyynes". *Chemical Reviews* **106**(11), PR1-PR33 (2006).

[Tan2011] A. Tan, J. Balachandran, S. Sadat, V. Gavini, B. D. Dunietz, S.-Y. Jang and P. Reddy. "Effect of length and contact chemistry on the electronic structure and thermoelectric properties of molecular junctions". *Journal of the American Chemical Society* **133**(23), 8838-8841 (2011).

[Tanaka2015] T. Tanaka and A. Osuka. "Conjugated porphyrin arrays: synthesis, properties and applications for functional materials". *Chemical Society Reviews* **44**(4), 943-969 (2015).

[Taylor2003] J. Taylor, M. Brandbyge and K. Stokbro. "Conductance switching in a molecular device: The role of side groups and intermolecular interactions". *Physical Review B* **68**, 121101(R) (2003).

[Tsutsui2013] M. Tsutsui, T. Morikawa, A. Arima and M. Taniguchi. "Thermoelectricity in atom-sized junctions at room temperatures". *Scientific Reports* **3**, 3326 (2013).

[Valkenier2011] H. Valkenier, E. H. Huisman, P. A. van Hal, D. M. de Leeuw, R. C. Chiechi and J. C. Hummelen. "Formation of High-Quality Self-Assembled Monolayers of Conjugated Dithiols on Gold: Base Matters". *Journal of the American Chemical Society* **133**(13), 4930-4939 (2011).

[Venkataraman2006a] L. Venkataraman, J. E. Klare, I. W. Tam, C. Nuckolls, M. S. Hybertsen and M. L. Steigerwald. "Single-Molecule Circuits with Well-Defined Molecular Conductance". *Nano Letters* **6**(3), 458-462 (2006).

[Venkataraman2006b] L. Venkataraman, J. E. Klare, C. Nuckolls, M. S. Hybertsen, M. L. Steigerwald. "Dependence of single-molecule junction conductance on molecular conformation". *Nature* **442**(7105), 904-907 (2006).

[Vonlanthen2009] D. Vonlanthen, A. Mishchenko, M. Elbing, M. Neuburger, T. Wandlowski and M. Mayor. "Chemically Controlled Conductivity: Torsion-Angle Dependence in a Single-Molecule Biphenyldithiol Junction". *Angewandte Chemie International Edition* **48**(47), 8886–8890 (2009).

[Wang2009] C. Wang, A. S. Batsanov, M. R. Bryce, S. Martín, R. J. Nichols, S. J. Higgins, Víctor M. García-Suárez and C. J. Lambert. "Oligoyne Single Molecule Wires". *Journal of the American Chemical Society* **131**(43), 15647-15654 (2009).

[Widawsky2012] J. R. Widawsky, P. Darancet, J. B. Neaton and L. Venkataraman. “Simultaneous Determination of Conductance and Thermopower of Single Molecule Junctions”. *Nano Letters* **12**(1), 354-358 (2012).

[Widawsky2013] J. R. Widawsky, W. Chen, H. Vázquez, T. Kim, R. Breslow, M. S. Hybertsen and L. Venkataraman. “Length-dependent thermopower of highly conducting Au-C bonded single molecule junctions”. *Nano Letters* **13**(6), 2889-2894 (2013).

[Winters2007] M. U. Winters, E. Dahlstedt, H. E. Blades, C. J. Wilson, M. J. Frampton, H. L. Anderson and B. J. Albinsson. “Probing the Efficiency of Electron Transfer through Porphyrin-Based Molecular Wires”. *Journal of the American Chemical Society* **129**(14), 4291–4297 (2007).

[Wold2002] D. J. Wold, R. Haag, M. A. Rampi, C. D. Frisbie. “Distance Dependence of Electron Tunneling through Self-Assembled Monolayers Measured by Conducting Probe Atomic Force Microscopy: Unsaturated versus Saturated Molecular Junctions”. *The Journal of Physical Chemistry B* **106**(11), 2813-2816 (2002).

[Xu2003] B. Q. Xu and N. J. Tao. “Measurement of Single-Molecule Resistance by Repeated Formation of Molecular Junctions”. *Science* **301**, 1221-1223 (2003).

[Yee2011] S. K. Yee, J. A. Malen, A. Majumdar and R. Segalman. “Thermoelectricity in fullerene-metal heterojunctions”. *Nano Letters* **11**(10), 4089-4094 (2011).

[Yzambart2018] G. Yzambart, L. Rincón-García, A. A. Al-Jobory, A. K. Ismael, G. Rubio-Bollinger, C. J. Lambert, N. Agraït and M. R. Bryce. “Thermoelectric Properties of 2,7-Dipyridylfluorene Derivatives in Single-Molecule Junctions”. *The Journal of Physical Chemistry C* **122**(48), 27198−27204 (2018).

PART 2:

DEVELOPMENT OF A HOT-WIRE-BASED STM TECHNIQUE FOR THERMAL CONDUCTANCE MEASUREMENTS IN ATOMIC CONTACTS

5. Thermal conductance measurements in atomic contacts using a hot-wire-based STM technique

Thermal conductance measurements at the nanoscale have become of fundamental interest both for scientific and technological reasons. Heat transfer between two bodies is typically a macroscopically defined and comprehended process, with their temperatures generally given by the average kinetic energy of stochastic (random) motions of the constituent microscopic particles (such as atoms or molecules). So the fundamentals of heat transfer when reducing the size of the involved systems down to a few of these constituent particles need undoubtedly some reconsideration and even revisiting some concepts or suppositions. Technologically, the race towards the miniaturization of electronic devices introduced in Chapter 1 has made it mandatory to be able to answer questions regarding heat evacuation at the nanoscale.

We present a new experimental technique based on a hot wire STM-probe for thermal conductance *ac* measurements in nanoscale systems such as atomic contacts and, potentially, molecular junctions. In this chapter we first briefly introduce in Section 5.1 the approaches taken by other groups for the study of heat transfer at the nanoscale. In Section 5.2 we present the main aspects of the developed experimental technique, including a motivation to the use of a hot wire, the theoretical formalism and a description of the employed hot wires and the experimental technique, including an analysis of its sensitivity. After this, the main experimental results obtained for thermal conductance measurements on Au-Au atomic contacts are shown and discussed in Section 5.3. Then we comment on different strategies for further development of the technique in Section 5.4 and make some conclusions in Section 5.5.

5.1 Background

Experimental measurements of thermal conductance G_{th} at the atomic scale are challenging due to several reasons [Dames2007; Mosso2017]. On the one side, the small values of this magnitude in the sampled systems require the use of highly thermally isolating probes in order to minimize heat leakage. On the other side, the difficulty to obtain stable, reproducible thermal contacts and hence, to obtain reproducible measurements, typically poses serious analysis issues. Investigation of heat conduction properties in nanoscale systems involves therefore demanding experimental requirements to overcome the challenges in thermal sensitivity and mechanical stability.

Two groups have recently managed to measure the thermal conductance of atomic contacts [Cui2017; Mosso2017] and molecular junctions [Cui2019; Mosso2019]. Most of the solutions proposed so far rely on microfabrication of some specific device and all of them require measurements in high vacuum conditions (see Figure 5.1).

Results show, for instance, that Wiedemann-Franz law is satisfied in atomic contacts, revealing proportional and quantized electrical and thermal conductances [Cui2017; Mosso2017]. In the case of molecular junctions, a series of alkanedithiol with increasing length have been explored [Cui2019] and thermal conductance was found to be independent of molecular length, in strong contrast with the electrical conductance, which decays exponentially. Comparison between the thermal conductance of dithiol-oligo(phenylene ethynylene) and octane dithiol junctions have been also reported and the results obtained indicate that heat transport across these systems is mainly governed by the phonon at the organic-inorganic interfaces [Mosso2019].

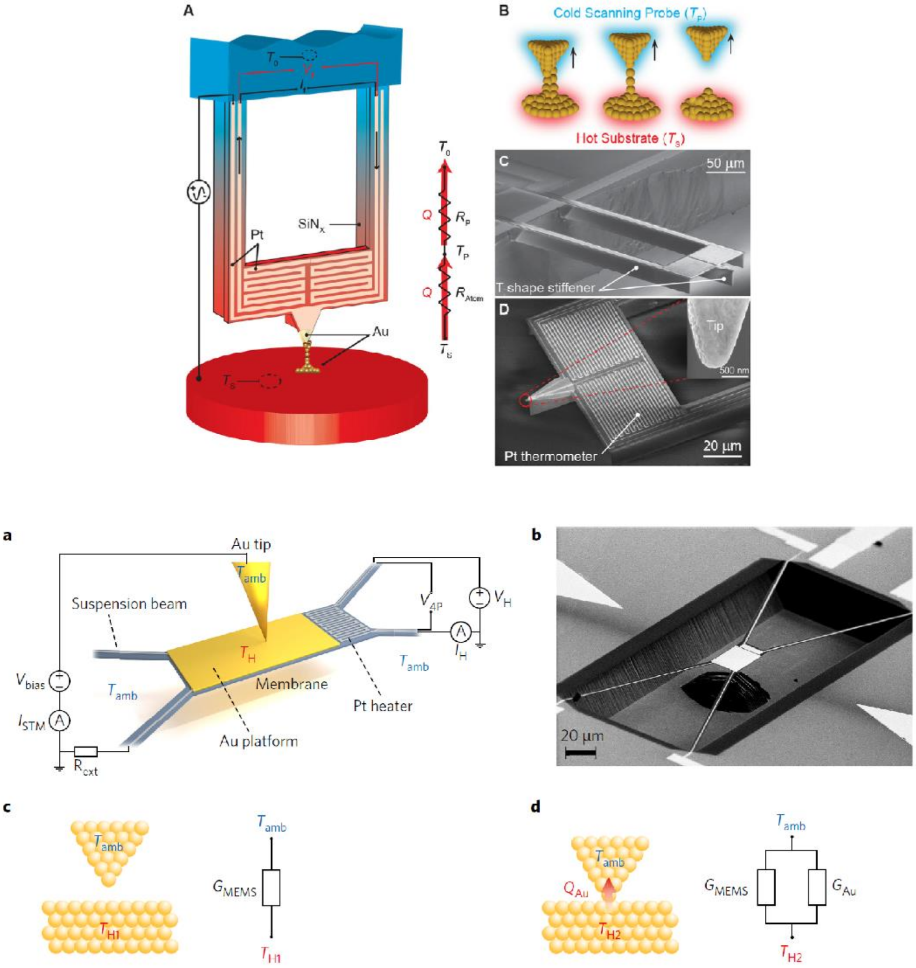

Figure 5.1: First reported experimental techniques for thermal conductance characterization of atomic contacts. Figures with uppercase letters (A-D) are from Ref. [Cui2017], while those with lowercase letters (a-d) are from Ref. [Mosso2017]. “(A) Schematic of a calorimetric scanning thermal microscopy (C-SThM) probe used to make atomic contacts with a heated metallic substrate (Au or Pt). The electrical conductance of the tip-substrate junction is monitored by applying a small sinusoidal voltage bias and measuring the resultant current. The resistance of the Pt resistance thermometer is monitored by applying a sinusoidal current and recording the voltage output. Thermal resistance network describes the resistances of the atomic chain and the scanning probe, as well as the heat current flow (red arrow). (B) Schematics of the atomic chains forming, narrowing and breaking during the withdrawal of the probe from the heated substrate. (C) SEM image (side view) of a scanning probe with two long and stiff “T” shaped $\mathrm{SiN_X}$ beams. (D) SEM image (top view) of the scanning probe, featuring a Au coated tip (inset) and a serpentine Pt thermometer”. After Ref. [Cui2017]. “(a) Schematic diagram of the experiment. To monitor the temperature of the gold electrode, the four-probe voltage and the heater current are measured. Simultaneous measurement of the tunnelling current allows us to extract the electrical resistance. An external resistor limits the current. (b) Scanning electron micrograph of the MEMS used in this work. The MEMS consists of a silicon nitride membrane $150\ \mathrm{nm}$ thick with four $3.5\ \mu\mathrm{m}$ wide and $255\ \mu\mathrm{m}$ long suspension beams. (c) Prior to contact formation, the membrane is heated. The total thermal conductance of the system is given only by the contribution of the suspension beams of the MEMS. (d) After contact formation, the temperature of the membrane decreases. The total thermal conductance is now given by the sum of the thermal conductance of the MEMS and that of the quantum point contact”. After Ref. [Mosso2017].

5.2 Our approach: Hot-wire-based STM technique

5.2.1 Motivation

Our approach for the measurement of thermal conductance G_{th} in nanoscale systems is based on the use of a hot wire probe implemented in a home-made scanning tunnelling microscopy (STM) setup. With this strategy we aim to combine simultaneous thermal and electrical characterization of conductive nanoscale systems such as metallic atomic contacts or model molecules as fullerenes.

A hot wire probe consists of a fine metal wire connected between two macroscopic electrodes (see scheme in Figure 5.2(a)). The temperature of these electrodes is usually well-known and stable and they behave as heat sinks. Besides an appropriate material selection, reduced diameter and high aspect ratio are typically fundamental characteristics of any hot wire with two main consequences: heating of the wire by an electrical current and quite large thermal resistance values.

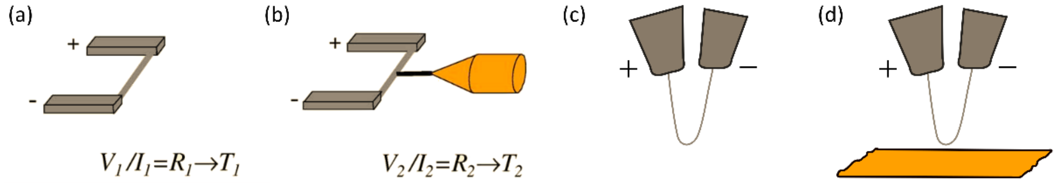

Figure 5.2: Hot wire probe approach. (a-b) A hot wire is typically used both as a local heater and as a thermometer (figures from Ref. [Dames2007]). In (a), the wire is heated to a temperature T_1 above ambient temperature by Joule heating. A current $I_1 = I_{el,HW}$ passes between the macroscopic electrodes through the thin metallic wire and, measuring the voltage drop V_1, the wire electrical resistance $R_{el,HW}$ is obtained. As a temperature-dependent magnitude, it allows to find the wire temperature T_1. In (b), the middle point of the hot wire is contacted with the nanosystem whose thermal conductance is studied. In this example (from Ref. [Dames2007]), the hot wire is contacted with a nanotube connected to a STM tip. This contact reduces the hot wire temperature to $T_2 < T_1$ and hence modifies the wire electrical resistance to R_2, measured with the voltage drop V_2 divided by the flowing current I_2. (c-d) Schematics of our approach based on the use of the hot wire as a STM probe. The wire is bended to adopt a double-leg tip-like shape (c) and is implemented in a STM piezo scanner setup to approach metallic surfaces in a controlled way (d) and form atomic contacts or molecular junctions.

Regarding the first aspect, a hot wire can be easily heated by Joule effect making an electrical current $I_{el,HW}$ pass between the electrodes, which also serves to monitor the electrical resistance of the wire $R_{el,HW}$ and hence its temperature. Resistance thermometry with hot wires is typically performed thanks to the sensitivity of $R_{el,HW}$ to the wire temperature T_w. For most materials and considering a not very large temperature increase, this dependence can be given by the following linear approximation:

$$R_{el,HW}(T_w) = R_{el,HW,0}[1+\alpha(T_w - T_0)], \qquad \text{Eq. (5.1)}$$

where $R_{el,HW,0}$ is the “cold-wire” electrical resistance, i.e. $R_{el,HW}(T_0)$. It is the resistance of the wire measured at a temperature of reference T_0, typically ambient temperature. α is the temperature coefficient of resistivity, in units of $1/\mathrm{K}$, and is characteristic of the hot wire material. One of the main strengths of a hot wire sensor is therefore the possibility to use it both as a heat source and as a thermometer. Temperature changes in the wire produced by thermal leakage when contacting the nanoscale system under study would vary its resistance and can thus be detected, as schematized in Figure 5.2(b). Additionally, it favors local heating that avoids long-time thermal stabilization of the whole setup, offers information about *in situ* temperature and favors fast response times of the sensor.

Also because of its high aspect ratio, hot wires thermal resistance $R_{th,HW}$ is typically relatively large. It depends on the dimensions of the wire and its constituent material and it is given by:

$$R_{th,HW} = \frac{L}{k_{th,HW} S}, \qquad \text{Eq. (5.2)}$$

where L and S are the hot wire length and cross-sectional area, respectively, and $k_{th,HW}$ is its thermal conductivity (in units of $\mathrm{Wm^{-1}K^{-1}}$). As will be detailed later, the relatively large thermal resistance of hot wires make of their use especially advantageous when studying very resistive thermal processes, such as those taking place in nanoscale systems. Heat transfer processes at the nanoscale involve thermal resistances typically larger than $10^7 – 10^8$ K/W, so a probe with a comparable R_{th} is required to minimize the uncertainty in the thermal measurement. Further discussion of this point is made in Section 5.2.4 where we comment on the sensitivity of a hot wire.

Our approach is based on the use of a hot wire as a STM probe. This would allow us to acquire STM images of metallic surfaces and the localization of individual adsorbed molecules, as well as facilitate active formation of atomic contacts or molecular junctions using the piezotube capability of a standard STM setup and the well-established STM-Break Junction technique. To reach this objective, we decide on giving the hot wire a more appropriate geometry by simply bending the wire to acquire a double-leg tip-like shape, as the one schematized in Figure 5.2(c). This tip-shaped hot wire probe can be easily implemented in a STM piezo scanner and confronted to a metallic sample acting as a third electrode (see Figure 5.2(d)). A voltage difference applied between the hot wire sensor and the metallic surface enables to measure the tunnelling current passing between them and to actively control the wire-substrate distance. During junction formation, both the tunnelling current and the minute temperature variations of the hot wire tip can be simultaneously followed in this approach, thereby extracting the electrical and thermal conductances of the junction. We must note that these STM-BJ experiments typically require a response time less than tenths of seconds in order to adequately follow the junction formation. To this respect, the use of a hot wire with a high aspect ratio results also very convenient, especially in ambient conditions where convection helps to reduce the relaxation time.

5.2.2 Theoretical formalism

When resistance thermometry is performed using a hot wire, based on Eq. (5.1), the electrical resistance measured $R_{el,HW}$ offers only information about the average temperature T_{av} of the hot wire (i.e. $T_{av} = T_w$ in Eq. (5.1)). In order to extract the thermal conductance of a contact formed between the hot wire and a nanoscale system, we need to model in detail the temperature profile of the wire or its position-dependent temperature, especially when measuring in ambient conditions.

The temperature profile of a hot wire probe can be described starting with classical heat transfer equations.[3] For the stationary case where the temperature depends only on the position on the wire $T(x)$ (see Figure 5.3(a)), and neglecting heat loses to the environment for the moment, we begin with the steady, one-dimensional heat equation:

$$k_{th,HW} \frac{d^2T(x)}{dx^2} = -\frac{Q}{LS}, \qquad \text{Eq. (5.3)}$$

where $k_{th,HW}$, L and S are the hot wire characteristics already introduced (see Figure 5.3(b)), $T(x)$ is the local temperature at a position x with respect to the center of the hot wire (which corresponds to $x = 0$) and Q is the Joule heat dissipated in the conducting wire heated by an electrical current, $Q = I_{el,HW}^2 \cdot R_{el,HW,0}$. Equivalently to the thermal resistance given by Eq. (5.2), $R_{el,HW,0}$ is determined by the wire dimensions and material properties and can be expressed as:

$$R_{el,HW,0} = \frac{L}{k_{el,HW}S}, \qquad \text{Eq. (5.4)}$$

where $k_{el,HW}$ is the electrical conductivity of the hot wire material at the temperature of reference T_0 (ambient temperature in our case) and has units of $\mathrm{m}^{-1}\Omega^{-1}$.

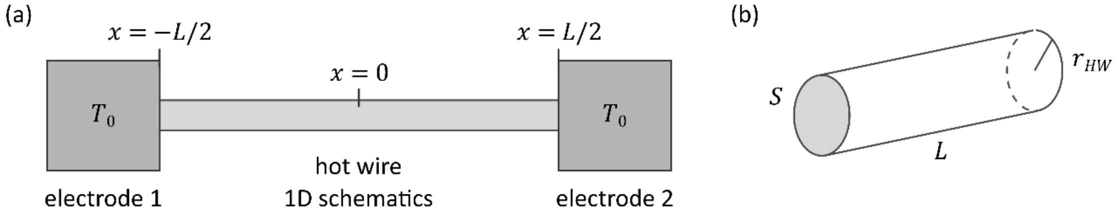

Figure 5.3: Hot wire probe schematics. (a) The hot wire (in the center, with a total length L) is connected between two electrodes (1 and 2) acting as heat sinks at ambient temperature T_0. The middle point of the hot wire is considered to be at position $x = 0$, being the electrodes at $x = L/2$ and $x = -L/2$. (b) Schematics of a homogeneous, cylindrical hot wire, with a cross-sectional area $S = \pi r_{HW}^2$, radius r_{HW} and length L.

Both extremes of the hot wire are assumed to be in excellent thermal contact with the electrodes, which act as macroscopic reservoirs. The wire ends are thus kept at ambient temperature and from this we derive a first boundary condition: $T(L/2) = T(-L/2) = T_0$ (see Figure 5.3(a)). The second boundary condition is fixed by the contact formation with the nanoscale system studied. When this contact is formed, a thermal current passes through it due to the temperature difference between the wire central temperature ($T(x = 0) = T_C$) and the other extreme of the nanoscale system, which is at ambient temperature in our case. This translates into the following expression:

$$\frac{T(x=0) - T_0}{R_{th,NS}} = k_{th,HW}S\left(\frac{\partial T(x)}{\partial x}\bigg|_{x=0^+} - \frac{\partial T(x)}{\partial x}\bigg|_{x=0^-}\right), \qquad \text{Eq. (5.5)}$$

where $T(x = 0^+) = T(x = 0^-)$ is also a requirement. $R_{th,NS}$ is the thermal resistance of the nanoscale system studied, the magnitude we want to obtain from the measurement.

Considering a homogeneous cylindrical hot wire as the one depicted in Figure 5.3(b), the solution for the previous equations is as follows:

---

[3] Theoretical formalism for the steady, one-dimensional situation follows Ref. [Dames2007].

$$T(x) - T_0 = \frac{1}{8} Q R_{th,HW} \left[1 - \left(\frac{x}{L/2} \right)^2 + \left(\frac{\gamma}{1+\gamma} \right) \left(-1 + \left| \frac{x}{L/2} \right| \right) \right], \qquad \text{Eq. (5.6)}$$

where $\gamma \equiv R_{th,HW}/(4 \cdot R_{th,NS})$ is just a ratio of thermal resistances used to simplify the expression. This definition will be of assistance for the analysis of the hot wire sensitivity as well. This analytical solution, plotted in Figure 5.4 for several values of γ, shows that the temperature profile of a hot wire heated by an electrical current is parabolic, in the case in which there are no heat exchanges between the wire and the environment.

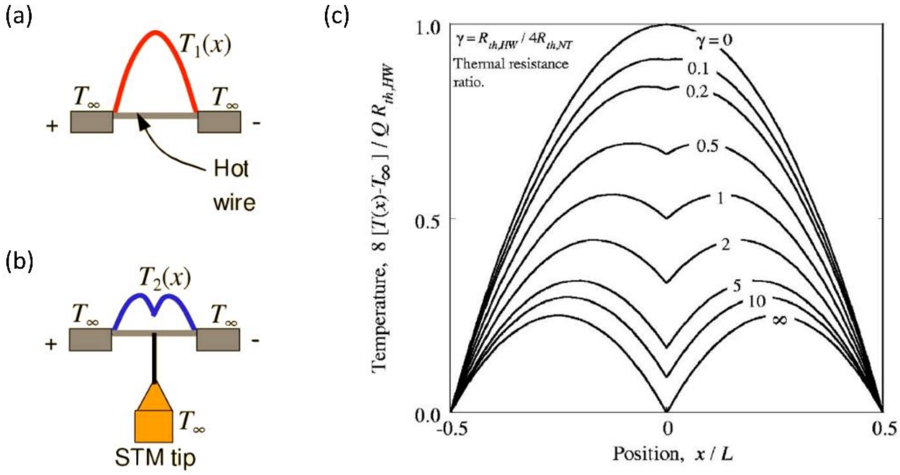

Figure 5.4: Solutions of the steady, one dimensional heat equation for a hot wire heated with an electrical current by Joule effect. (a) Schematic of the temperature profile of the hot wire connected between two electrodes (heat sinks at T_0). (b) Schematic of the temperature profile when the hot wire central part makes contact with a nanoscale system whose thermal resistance is to be measured. The nanoscale system, in our case a metallic surface or a molecule deposited on it, acts as a heat leakage for the wire, reducing its temperature. (c) Temperature profiles $T(x)$ for various ratios of thermal resistances γ, according to Eq. (5.6). Figures (a-c) from Ref. [Dames2007].

Under these conditions, the electrical resistance of the hot wire $R_{el,HW}$ is then:

$$R_{el,HW} = R_{el,HW,0} \left[1 + \frac{\alpha}{L} \int_{-L/2}^{L/2} (T(x) - T_0)\, dx \right] = R_{el,HW,0}(1 + \alpha T_{av}), \qquad \text{Eq. (5.7)}$$

where the temperature coefficient of resistivity α (characteristic of the hot wire material) is considered to be constant and T_{av} is the average temperature rise of the hot wire above ambient temperature T_0. Combining Eqs. (5.6) and (5.7), it is possible to derive an expression for the hot wire average temperature rise T_{av} as a function of the thermal resistances ratio γ:

$$T_{av} = \frac{1}{12} Q R_{th,HW} \left[1 - \frac{3}{4} (1 + \gamma^{-1})^{-1} \right]. \qquad \text{Eq. (5.8)}$$

This relation is plotted in Figure 5.5 and it suggests that, by measuring the average temperature rise of the hot wire T_{av} at a given power Q, and knowing $R_{th,HW}$, we can determine γ and hence the thermal resistance $R_{th,NS}$ of the contacted nanoscale system. Furthermore, we can also derive an expression to relate T_{av} (directly obtained from resistance thermometry measurements) and the temperature at the center of the hot wire T_C:

$$T_C - T_0 = \frac{6 T_{av}}{4 + \gamma}. \qquad \text{Eq. (5.9)}$$

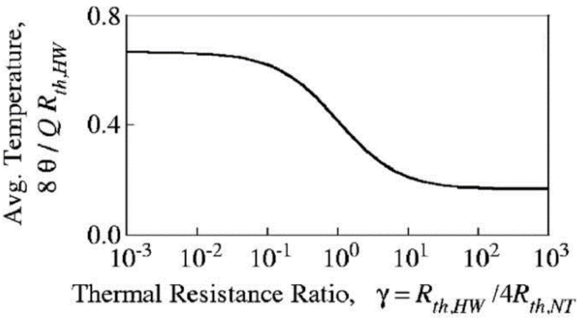

Figure 5.5: Average temperature rise as a function of γ. $\theta = T_{av}$ in the text. From Ref. [Dames2007].

Beyond the stationary situation considered for the moment, a more complete description of the hot wire temperature profile can be derived considering the one-dimensional time-dependent heat equation:

$$\rho c \frac{\partial T(x,t)}{\partial t} = k_{th,HW} \frac{\partial^2 T(x,t)}{\partial x^2} + \frac{Q}{LS}. \qquad \text{Eq. (5.10)}$$

In this equation, ρ and c are the density and the specific heat of the conducting wire material, respectively. In the case of a homogeneous, uniform wire as considered until now, these are constants, as well as L, S and $k_{th,HW}$. Reorganizing the terms:

$$\frac{\partial T(x,t)}{\partial t} = \kappa \frac{\partial^2 T(x,t)}{\partial x^2} + \frac{Q}{LS\rho c}, \qquad \text{Eq. (5.11)}$$

where $\kappa = k_{th,HW}/(\rho c)$ is called the thermal diffusivity, has units of m^2/s and corresponds to the time constant for the heat transfer in a situation without heat exchange with the environment.

However, in a real hot wire operating in air, as in our experiments, heat loses to the environment due to convection and radiation are important and need to be considered. In this case we consider more convenient to use a numerical approach. In particular, we model the hot wire as a sequence of discrete nodes and use a finite differences scheme to address the problem.

In this model, the temperature of each node is $T_i = T(x = i)$, where $i = 1, \dots, N$ (see Figure 5.6(a)) and the ends of the wire are additional nodes fixed at ambient temperature T_0. Separation between nodes is then $\Delta L = L/(N+1)$, where L is the wire total length, and each T_i is thermally connected to the adjacent nodes through the thermal conductance K.

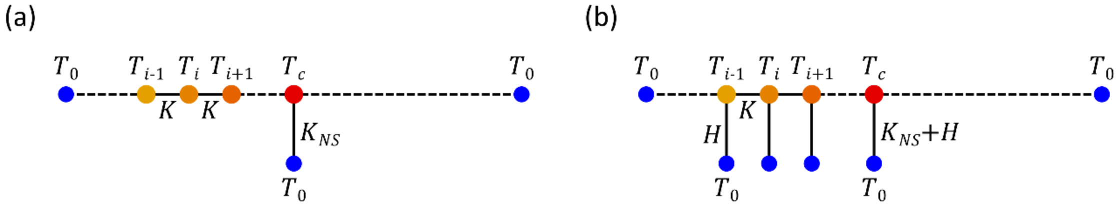

Figure 5.6: Discretization of the hot wire. (a) One-dimensional hot wire model in which it is divided into a sequence of N nodes of temperature T_i, where $i = 1, \dots, N$. The ends of the wire are additional nodes kept at ambient temperature T_0. Heat exchanges to the environment are not considered in this schematics, only the heat lose produced by contact formation with a nanoscale system whose thermal conductance is K_{NS}. (b) Discretization of the hot wire considering heat loses to the environment. Each node experiences heat loses mainly through convection processes, quantified by the thermal conductance H.

To find the temperature of each node T_i when a current $I_{el,HW}$ flows through the wire, we consider Eq. (5.11) and apply a finite difference method, getting the following heat equation:

$$\frac{\partial T_i(t)}{\partial t} = \kappa \frac{T_{i-1} - 2T_i + T_{i+1}}{\Delta L^2} + \frac{Q}{LS\rho c}. \qquad \text{Eq. (5.12)}$$

In the stationary situation, when a balance between Joule dissipation and thermal conductance in the wire is achieved, $\partial T_i(t)/\partial t = 0$ and Eq. (5.12) is equal to zero. We can then solve it numerically to find the steady state solution, i.e. the equilibrium temperature of each node:

$$\begin{aligned} K(T_{i-1} - 2T_i + T_{i+1}) + I_{el,HW}^2 R_{el,i} = 0 \qquad (\text{for } i \neq c), \\ K(T_{i-1} - 2T_i + T_{i+1}) + I_{el,HW}^2 R_{el,i} - K_{NS}(T_i - T_0) = 0 \qquad (\text{for } i = c), \end{aligned} \qquad \text{Eq. (5.13)}$$

where $K = k_{th,HW}S/\Delta L$ is the thermal conductance between two consecutive nodes and $R_{el,i} = R_{el,HW,0}[1 + \alpha(T_i - T_0)](\Delta L/L) = \rho_{el,HW}[1 + \alpha(T_i - T_0)](\Delta L/S)$ is the electrical resistance between two consecutive nodes and depends on their temperature ($\rho_{el,HW} = 1/k_{el,HW}$ is the wire material electrical resistivity and Eq. (5.4) has been used). In this solution we have taken into account the thermal current trough the contact established between the hot wire and the nanoscale system under study whose thermal conductance K_{NS} is the magnitude we want to measure. This heat lose needs to be considered in the central node, i.e. for $i = c$ (see Figure 5.6(a)), and prior to contact formation, this term simply vanishes.

In ambient conditions, heat exchange with the environment needs also to be considered. As it is well-known, these exchanges can follow three different mechanisms: (i) conduction; (ii) convection, which involves the motion of liquids or gases, and (iii) radiation, which takes place with no material carrier (i.e. even in vacuum conditions). In all the cases, heat transfer to the environment depends on the hot wire temperature rise at a given position ($T_i - T_0$) and is proportional to the surface of the wire. It is also proportional to the corresponding heat transfer coefficient:

- the convection coefficient h_{conv} depends on the dimensions of the hot wire and the physical properties of the environment, and consequently h_{conv} is constant in our model.
- the radiation coefficient h_{rad} is temperature dependent and is generally calculated as $h_{rad} = \varepsilon\sigma(T_1^2 + T_2^2)(T_1 + T_2)$, where ε is the surface emissivity and σ is the Stefan-Boltzmann constant ($\sigma = 5.67 \times 10^{-8}\ \mathrm{W/m^2/K^4}$).
- the conduction coefficient h_{cond} depends mainly on the materials involved in the heat exchange and it is typically very small in the case of air.

Conduction and radiation coefficients in our experiments are negligible in comparison with natural convection happening when the heat from the hot wire initiates the surrounding fluid movement, so we only consider for the moment an additional term for convection in the heat equation:

$$\frac{\partial T_i(t)}{\partial t} = \kappa \frac{(T_{i-1} - 2T_i + T_{i+1})}{(\Delta L)^2} + \frac{Q}{LS\rho c} - \frac{h_{conv}P}{S\rho c}(T_i - T_0). \qquad \text{Eq. (5.14)}$$

Here we are considering that convection loses in the hot wire take place in each of the nodes due to thermal disequilibrium with the ambient, at ambient temperature, and are quantified by the convection heat transfer coefficient h_{conv}. The numerical solution is then the following:

$$\begin{aligned} &K(T_{i-1} - 2T_i + T_{i+1}) + I_{el,HW}^2 R_{el,i} - H(T_i - T_0) = 0 \qquad (\text{for } i \neq c), \\ &K(T_{i-1} - 2T_i + T_{i+1}) + I_{el,HW}^2 R_{el,i} - H(T_i - T_0) - K_{NS}(T_i - T_0) = 0 \quad (\text{for } i = c), \end{aligned} \qquad \text{Eq. (5.15)}$$

where $H = h_{conv} P \Delta L$ is the thermal conductance between each node and the environment, in units of $\mathrm{W/K}$ (see Figure 5.6(b)). h_{conv} is determined in our experiments from a fit of the observed change in resistance from the “cold-wire” value to the hot wire resistance when the heating current is established.

The time-dependent heat equation can equivalently be solved using a Crank-Nicholson scheme in our finite differences method, allowing us to compute the time evolution of the wire temperature and to find its relaxation time. This is an important feature of the hot wires employed in our experiments since STM-BJ measurements take advantage of response times of the sensor less than tenths of seconds. We must note that the relaxation time is conveniently reduced by convection.

5.2.3 Hot wires used: Wollaston wires

During this Thesis we have investigated two different options for the hot wires: gold-plated tungsten 5-μm-diameter wires (99.95% purity) and platinum Wollaston wires, formed by a Pt core of diverse diameters encased in silver coating (99.9% purity). Both options are commercially-available (Goodfellow Cambridge Ltd., UK) and would facilitate thermal characterization of nanoscale junctions without nanofabrication of any specific device to perform the measurements. This approach has been followed by other groups (see Section 5.1) but requires further time and money investments and we originally decided to challenge it with alternatives. Regarding the two main options explored, Au-plated W wires were finally disesteemed for the challenging manipulation and the uncertainty in the actual wire length and we focused our attention on Wollaston wires.

A Wollaston wire (WW) consists of a central thin metal wire covered by a larger silver sheath of 50- to 100-μm-diameter (see Figure 5.7). Typical core diameters are 0.5 - 20 μm and the metal material is usually platinum or alloys such as platinum/rhodium [Dames2007]. The Ag sheath can be easily dissolved with a nitric acid etch (HNO_3, 50% or higher concentration), exposing the inner fine metallic core of a selected small region with the desired dimensions. Due to their large aspect ratio and characteristic materials, WW typically present relatively large thermal resistance, heating up easily with flowing current. WW-based probes are commonly used for hot-wire anemometry [Perry1982] and they have been also adapted as local thermal probes for scanning thermal microscopy (see Figure 5.7) [Pylkki1994; Lefèvre2003; Lefèvre2006].

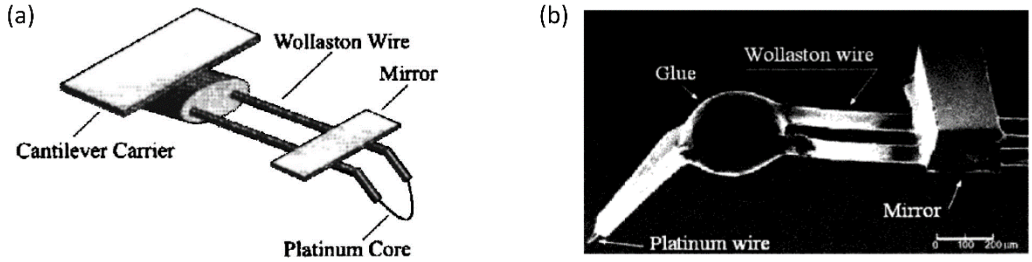

Figure 5.7: Examples of Wollaston wires employed for scanning thermal microscopy. (a) Scheme of the experimental setup from Ref. [Lefèvre2003]. (b) Image of the setup used in Ref. [Lefèvre2006]. Both tips are made with a WW platinum/rhodium central core (5-μm-diameter).

Figure 5.8 show optical images of a Pt WW used in our experiments, before and after the nitric acid etch. Different Pt diameters ranging from $10\ \mu\mathrm{m}$ down to $2\ \mu\mathrm{m}$ have been investigated, all of them with a 100-$\mu\mathrm{m}$-diameter Ag sheath, and we obtain the best results with a wire diameter of $5\ \mu\mathrm{m}$. This diameter allows us to find a good compromise between thermal resolution and mechanical stability of the hot wire used as a local STM probe. Thinner WW show larger thermal resolutions since the thermal sensitivity scales with r_{HW}^2, being r_{HW} the wire radius, but the tip becomes then too compliant to form stable atomic contacts or to aim at taking STM images. Further discussion on this point is developed in Section 5.4.

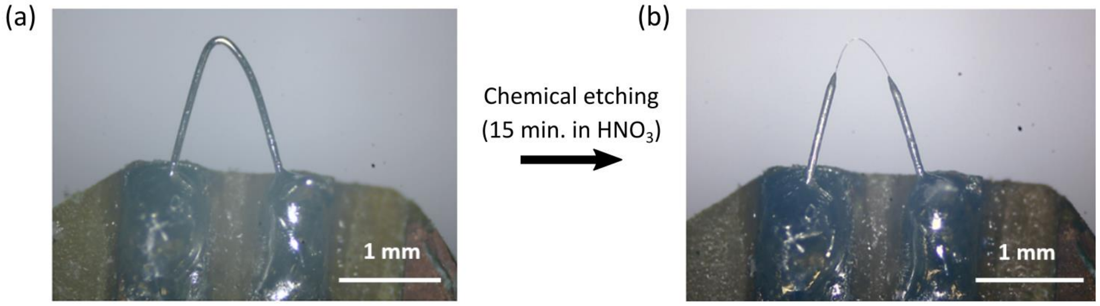

Figure 5.8: Wollaston wire used as a hot wire and STM probe. Optical images of the WW used, which consists of a 5-$\mu\mathrm{m}$-diameter Pt core surrounded by a 100-$\mu\mathrm{m}$-diameter Ag coating. (a) WW modeled with a double-leg tip-like shape soldered on the circuit board used as tip support. Only the external Ag sheath is visible. (b) WW after 15 minutes in nitric acid etch (HNO_3). The portion of the Pt core exposed, with the desired length, is the Pt hot wire used as heater and thermometer for the measurements. The Ag coating extremes are the effective macroscopic electrodes acting as heat sinks.

The experimental procedure to prepare a WW-based STM tip as the one shown in Figure 5.8(b) consists of several steps. Initially, a piece of WW with a length of around $1\ \mathrm{cm}$ is carefully cut from the original wire supplied and, without touching the central part of the cut fragment, it is gently manipulated with tweezers on a glass slide. To bend the wire, one extreme is fixed to the glass using soft Scotch tape and, placing a sharp tweezer tip next to a central point of wire, its free extreme is pulled back towards the fixed side and partially rotated, as making a lace, around the tweezer tip, which acts as a pivot. It is important to keep this movement vertically as close as possible to the glass slide so that both extremes of the wire are maintained in the same plane without unwanted torsion angles between both legs. After this, a kink in the wire is already formed and both legs of the wire are approximately parallel to each other. The external side of this kink will be the hot wire tip extreme.

In parallel, the circuit board where the wire will be mounted is prepared (see Figure 5.9) and some tin is prepared to solder the wire with the smallest possible damage. Once this is ready, the wire is removed from the glass slide, using the Scotch tape that holds it on one extreme, and is placed on top of the circuit board where it will be soldered. The wire is oriented over the ciruit board in such a way that approximately $1\ \mathrm{mm}$ of the WW excels from the front of the piece and one of the legs of the wire lies over the small amount of prepared tin. The relative aligmemnt of the wire with respect to the circuit board is then fixed with the Scotch tape and the wire is sold, first the leg already in position and then the second one. Figure 5.8(a) shows an image of a Wollaston wire right after soldering it to both tin contacts. Both legs of the wire would ideally remain parallel after contacting the wire, in order to be mechanically more stable, but the dimensions of the circuit board and the soldering tip make it difficult to maintain them parallel and the legs form typically an angle of around $30°$. During all these steps the front of the wire is never touched in order to avoid deterioration or accidental damage. In addition, the circuit board is already mounted on a screw which will allow its implementation in the STM setup.

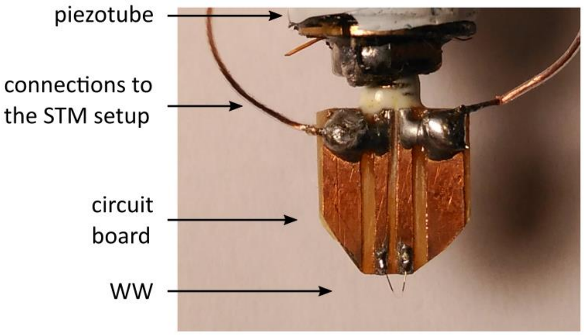

Figure 5.9: Final Wollaston wire sensor mounted on a STM head. The Wollaston wire (WW) is soldered on a circuit board and then chemically etched, becoming the Pt hot wire used for the measurements. Connections to the STM setup are added afterwards and the circuit is finally screwed into a nut glued at the end of the STM piezotube.

Once the WW is electrically connected to the circuit board, there is one last step remaining which is the chemical etching of the Ag sheath. We use 69% concentration nitric acid (HNO_3) (Sigma Aldrich, > 99.9 purity) and, to protect the circuit board from the acid vapours, we cover it with Nito tape, which leaves no residues after removal. Once protected, the cicruit board is placed with the WW facing down over a watch glass with the nitric acid and, using a micromanipulator, we controllably immerse the extreme of the wire (less than $0.5\ \mathrm{mm}$) in the acid for 15 minutes. After this time optical microscopy characterization shows that the Pt core immsersed is free of Ag coating (visual examination with x50 augmentation) (see Figure 5.8(b)). The Nito tape is softly removed, the circuit board is screwed into the piezotube support and the final connections from the STM setup to the circuit board are soldered, being the WW finally ready to be used, as can be seen in Figure 5.9. STM-BJ measurements in our experiments are performed after mounting the WW probe in a STM scanner setup and confronting it to a metallic substrate. In this configuration, metallic atomic contacts or molecular junctions with molecules deposited on the Au surface can be formed.

Optical images allow us also to find the length of the hot wire, which in the case of the wire shown in Figure 5.8(b) is $L_{HW} = 860\ \pm 40\ \mathrm{\mu m}$. Its diameter, according to manufacturer specifications, is $d_{HW} = 2r_{HW} = 5.0 \pm 0.5\ \mathrm{\mu m}$ and the thermal conductivity of platinum is $k_{th,Pt}\ = 71.6\ \mathrm{Wm^{-1}K^{-1}}$ [efunda.]. Using Eq. (5.2) we can calculate the thermal resistance of the hot wire probe $R_{th,HW}$:

$$R_{th,HW} = \frac{L}{k_{th,HW}S} = \frac{L_{HW}}{k_{th,Pt}\pi r_{HW}^2} = (6.1 \pm 1.5) \times 10^5\ \mathrm{K/W}. \qquad \text{Eq. (5.16)}$$

This value is important to estimate the sensitivity of the hot wire for thermal measurements, as it is discussed in more detail in Section 5.2.5. Compared to previously reported thermal resistance values used to investigate nanoscale systems [Dames2007; Cui2017; Mosso2017] (introduced in Section 5.1), our $R_{th,HW}$ results slightly smaller than desirable, but on an appropriate range (Ref. [Cui2017] reports $R_{th,probe} =\ 1.3\ \times\ 10^6\ \mathrm{K/W}$, just a factor 2 larger). We must note that longer or thinner wires would show larger thermal resistance values, especially if decreasing their diameter, but this would greatly affect their mechanical stability, challenging junction formation, and we find a good compromise between thermal resolution and mechanical response for wires of 5-μm diameter and length of around 700-900 μm.

For completeness, the electrical resistance of the Pt hot wire shown in Figure 5.8(b) can be calculated considering Eq. (5.4):

$$R_{el,HW,0} = \frac{L}{k_{el,HW}S} = \frac{L_{HW}}{k_{el,Pt}\pi r_{HW}^2} = 4.6 \pm 1.1\ \Omega, \qquad \text{Eq. (5.17)}$$

where we have used that $k_{el,Pt} = 9.45 \times 10^6\ \mathrm{m^{-1}\Omega^{-1}}$.

5.2.4 Experimental setup and technique

Resistance thermometry with the aforementioned WW probes is performed using an *ac* resistance bridge and a high frequency digital lock-in amplifier (Zurich Instruments HF2LI). Figure 5.10 shows the schematics of the measurement electrical circuit which consists basically of a Wheatstone bridge adapted to satisfy as well the STM-BJ measurement requirements.

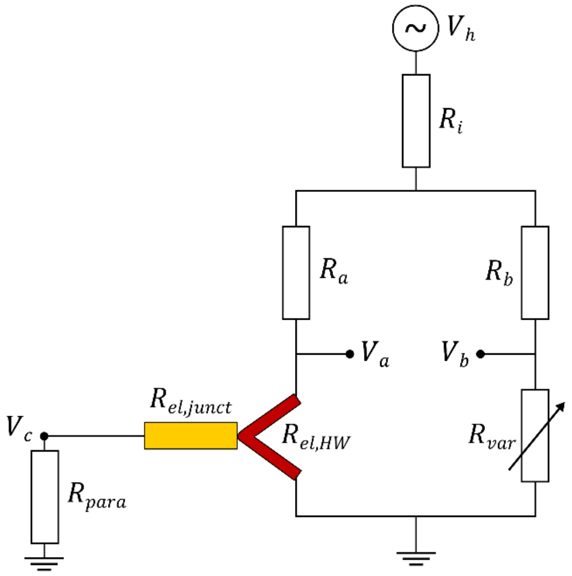

Figure 5.10: Schematics of the electrical circuit based on a Wheatstone resistance bridge. V_h is the *ac* voltage applied to establish the heating current through the Wollaston wire, highlighted in dark red in the diagram. Its electrical resistance $R_{el,HW}$ is the unknown parameter of the bridge, formed also by $R_a = R_b = 100\ \Omega$ and R_{var}, a variable resistor used to balance the bridge by initially matching its value to the “cold-wire” electrical resistance $R_{el,HW,0}$, typically $4-6\ \Omega$. $R_i = 50\ \Omega$ is the internal resistance of the voltage source. $R_{el,junct}$ is the electrical resistance of the junction formed between the hot wire and the system of interest (a metallic substrate, for instance) and typically varies from a virtual infinite value when the junction is open to even just few ohms, for example, when a large metallic contact is formed. $R_{para} = 9.94\ \mathrm{k\Omega}$ is a resistor connected in parallel to the junction to avoid saturation of the lock-in amplifier input before reaching a few atoms contact. Finally, $V_{ab} = V_a - V_b$ and V_c are the measured voltage signals and correspond to the hot-wire temperature signal and the junction current signal, respectively.

A Wheatstone bridge is an electrical circuit typically used to accurately measure small changes in an unknown electrical resistance, which in this case is the electrical resistance of the hot wire $R_{el,HW}$ (plotted in dark red in the circuit diagram). The two legs of our bridge contain in total four resistances: the first leg is formed by R_a and the unknown $R_{el,HW}$ connected in series, while the other leg is formed by R_b and R_{var}, a variable resistor. To favor symmetry in the legs, R_a and R_b are chosen to be equal and with a value of $100\ \Omega$ to obtain adequate values of heating current through the hot wire. This current is generated by applying an *ac* voltage V_h of frequency f_h, named this way because it is the voltage that controls the heating. The actual voltage at the entry of the bridge is actually reduced by the presence of $R_i = 50\ \Omega$, the internal resistance of the voltage source of the lock-in. Since its value is of the same order of R_a and R_b it is necessary to include it in our model of the electrical circuit to calculate the heating current.

Being the Wheatstone bridge grounded at the opposite extreme of V_h, the sum of resistances in each leg determines the value of the current flowing through them and hence, through the wire. The variable resistor of the bridge R_{var} is then one of the key elements of these circuits because it allows to initially balance the total resistance in the two legs of the Wheatstone bridge by matching the wire resistance $R_{el,HW}$. There is hence the same total resistance in both legs and the response of the bridge $V_{ab} = V_a - V_b$ is cancelled. From this moment, any change in the resistance of the hot wire, i.e. on its temperature, will decompensate the balance in the bridge and will be reflected in a deviation of V_{ab} from the initial zero value. Considering that there is not current leakage to the input of the lock-in (i.e. its input impedance is high enough), the response of the bridge can be written as:

$$V_{ab} = \left[\frac{R_{el,HW}}{R_a + R_{el,HW}} - \frac{R_{var}}{R_b + R_{var}}\right][V_h - I_{tot}R_i], \qquad \text{Eq. (5.18)}$$

where I_{tot} is the total current flowing into the circuit and it is given by:

$$I_{tot} = \frac{V_h}{R_{tot}} = \frac{V_h}{R_i + \left[\frac{1}{R_a + R_{el,HW}} + \frac{1}{R_b + R_{var}}\right]^{-1}}. \qquad \text{Eq. (5.19)}$$

With this working principle, small changes in $R_{el,HW}$ can be detected. Considering a heated hot wire and the bridge balanced in such a way that $R_{var} = R_{el,HW,hot}$, the signal measured in the bridge is then the following:

$$V_{ab} = \frac{R_a \Delta R_{el,HW}}{\left(R_a + R_{el,HW,hot}\right)^2}[V_h - I_{tot}R_i], \qquad \text{Eq. (5.20)}$$

where $\Delta R_{el,HW}$ is the change in the electrical resistance of the hot wire that we want to measure and that can be converted into average temperature changes using Eq. (5.1).

During the STM-BJ experiments, simultaneously to V_{ab} and to control junction formation, the voltage at the sample V_c is also measured. This voltage is given, essentially, by the tunnelling current flowing through the junction and its electrical resistance $R_{el,junct}$. The tunnelling current through the junction is established due to the voltage difference between the hot wire tip (the part that forms the junction) and the substrate. In fact, since the hot wire is metallic, this current is part of the heating electric current flowing through the wire $I_{el,HW}$. When a contact is formed with the substrate, this current can also flow towards the sample because both elements are at a different voltage. This allows us to measure the tunnelling current of the junction, essential for the STM-BJ experiments, but it also causes a major problem since part of the current is leaking to the sample and would affect the accuracy in the resistance measurement. Additionally, the junction resistance $R_{el,junct}$ varies from a virtual infinite value when the hot wire is far away from the sample surface to a value of just some ohms when the metallic contact is formed. This huge range of $R_{el,junct}$ largely influence the amount of heating electrical current lost from the wire towards the sample, thus making it difficult to compensate it.

This problematics has been recently solved using two symmetric resistance bridges that allow to cancel the voltage created by the heating current signal at the contact point of the wire, thus avoiding loses to the substrate. In this configuration, a second voltage at a different frequency is used to establish the tunnelling current. This improvement, further introduced in Section 5.5, has been only very recently implemented and during this Thesis only preliminary proof-of-concept tests were performed. For the experiments presented in this manuscript, the solution found relies on the thorough theoretical model developed, which is thereby essential to discern between purely thermal and electrical contributions. Modelling the electrical circuit and the position-dependent temperature of the hot wire (Section 5.2.2) we can calculate the response of the bridge V_{ab} that would be produced by the electrical currents flowing through the contact between the tip and the substrate and use it to subtract the purely electric contribution from the experimental signals.

To verify the validity of this approach and fit the different experimental parameters, baseline measurements without heating the wire are acquired before increasing the heating electrical current through the probe and perform the thermal conductance measurements. In the case of the baseline measurements, the heating current loses to the substrate are not significant because the voltage at the contact point of the wire is small and we are not heating the wire; all the signals are electrical. It is also important to notice that, since measurements are performed with *ac* signals, impedance rather resistance of the different elements of the circuit is considered in the model.

Some further considerations regarding the validity of the model can be made at this point. For example, one of the major assumptions we are making in these experiments is that the convection coefficient is position-independent. Given the double-leg tip geometry of our probes, though, it is to be expected that this coefficient is not exactly identical in the wire middle point (close to the surface of the substrate during experiments) or at the ends of the wire near the macroscopic electrodes (further away to the substrate). The validity of other assumptions, such as the surface temperature of the substrate being equal to ambient temperature or ignoring independent contributions from conduction or radiation to heat loses in the wire, needs also to be confirmed by the experiments. Radiation might be especially non-negligible when the wire approaches the surface and is placed just some nanometers above it. An extreme enhancement of radiative heat transfer between Au surfaces in the extreme near field has been recently reported [Kim2015] and an additional term for radiation loses might need to be included in the heat equation, with a position-dependent radiation coefficient.

Taking all this into account, any effect of neglecting radiation and conduction through air in the model might be largely compensated by the consideration of the convection coefficient. The three type of heat loses to the environment depend on the hot wire temperature rise at a given position and are proportional to the surface of the wire and to the corresponding coefficient. By fitting the experimental data with the model, h_{conv} is actually a phenomenological coefficient for heat loses to the environment that may comprise several contributions. With respect to the necessity to consider a position-dependent coefficient, current work in the group is being done to this respect to ascertain the impact of this assumption.

Finally, another experimental limitation to consider is the fact that the contact with the nanoscale system is highly probably not perfectly centered in the middle point of the hot wire (i.e. $x = 0$ in the model), but at a certain distance of the center l. Then the temperature change caused by the contact at this point would be smaller than in the ideal case, at $x = 0$. Ref. [Dames2007] estimates the stationary 1D heat transfer analysis to be still valid as long as $l < 0.112 \cdot L_{HW}$, that is, within a deviation from the center of $\sim 11\%$ the length of the wire. For the wire shown in Figure 5.8(b), whose $L_{HW} = 860 \pm 40$ μm, translates into $l \sim 96$ μm. From the optical images of the wire, the point of the wire where the contact is formed in our experiments is within this range.

5.2.5 Sensitivity of the hot wire

The sensitivity of the Wollaston wires employed to perform thermal conductance measurements can be estimated calculating the variation on the average temperature T_{av} of the wire that would result from the formation of one gold atom contact. This change ΔT_{av} would be proportional to the thermal conductance of the Au atom which, according to Wiedemann-Franz law, is related to the electrical conductance and it is given by:

$$G_{th,0} = LT_0 G_0 = 0.567 \text{ nW/K}, \qquad \text{Eq. (5.21)}$$

where $L = 2.44 \times 10^{-8}\ \text{W}\Omega/\text{K}^2$ is the Lorenz number, T_0 is ambient temperature and G_0 is the quantum of conductance ($G_0 = 2e^2/h$, where e is the electron's charge and h is Planck's constant) and the electrical conductance of one Au atom contact. This thermal conductance corresponds to a thermal resistance of the Au atom $R_{th,0} = 1/G_{th,0} = 1.76 \times 10^9$ K/W.

Considering the first situation introduced in the theoretical formalism, that is, the stationary case with no heat loses to the environment, Eq. (5.8) gives us an expression to relate the measured average temperature rise of the hot wire T_{av} and the thermal resistance of the junction formed $R_{th,NS} = R_{th,junct}$, through the variable $\gamma \equiv R_{th,HW}/(4 \cdot R_{th,junct})$ [Dames2007]. According to Figure 5.5, the best resolution or minimized uncertainty would be achieved for $0.1 < \gamma < 10$, approximately. For the hot wire shown in Figure 5.8(b), the thermal resistance has been already calculated in Section 5.2.3 to be $R_{th,HW} = (6.1 \pm 1.5) \times 10^5$ K/W, which means that we would better resolved thermal resistance values in the range $1.5 \times 10^4\ \text{K/W} < R_{th,junct} < 1.5 \times 10^6$ K/W. With this estimation, our hot wires sensors seem to be hopeless to measure the thermal conductance of a single atom contact.

However, our experiments are performed in ambient conditions and using a Wheatstone bridge to detect small changes of resistance, combined with a lock-in detection method, which altogether allows us to obtain accurate $\Delta R_{el,HW}$ measurements with an improved signal-to-noise ratio. Considering the hot wire shown in Figure 5.8(b) as an example and the value of heating current $I_{el,HW}$ used in our experiments (see further details in next section), formation of a one Au atom contact should cause the average temperature of the hot wire T_{av} to decrease by $\Delta T_{av} = 0.4$ mK. Using Eq. (5.1) this temperature drop translates into a change of the electrical resistance $\Delta R_{el,HW} = 7.5$ μΩ, which in the bridge response would be a change in V_{ab} by 142 nV, according to the model of the electrical circuit. In this estimation, the convection coefficient is taken to be $h_{conv} = 1320\ \text{W/m}^2/\text{K}$ after a phenomenological fit performed when heating up the wire (see next section). Note that the minimum output noise of the lock-in amplifier output channel, for the conditions we are considering and a bandwidth of 600 Hz, is of around $150\ \mathrm{nV}$ and therefore, this hot wire probe has in principle a sensitivity close to the limit to measure the thermal conductance of a Au atom contact. Since we are going to measure differences in the bridge signal, it is also useful to express this sensitivity as a ratio. For the hot wire shown in Figure 5.8(b) and the experimental parameters of the electrical circuit, introduced together with the measurements in the next section, we obtain a sensitivity of $355\ \mu\mathrm{V/K}$.

5.3 Thermal conductance G_{th} measurements in Au-Au atomic contacts

Thermal conductance measurements with the novel experimental technique presented in Section 5.2 are tested with metallic atomic contacts, as a proof-of-concept. For this purpose we use Au samples with a freshly flame annealed polycrystalline (111) surface, the same commercial 250-nm-thick Au films on glass substrates ($11 \times 11\ \mathrm{mm}^2$, Arrandee, Germany) previously introduced for conductance and thermopower characterization (see Section 3.2.2 or 4.1).

Hot-wire probes are also tested as pure STM probes, applying a V_{bias} and controlling with the tunnelling current measured (amplification gain $1 \times 10^8\ \mathrm{V/A}$, home-made current-to-voltage amplifier, SEGAINVEX). STM images where Au atomic steps seem to be resolved by the Pt hot wire tip are shown in Figure 5.11. The Au surface is in this case scanned in the y-direction with a $V_{bias} = 0.5\ \mathrm{V}$. Forward and backward scanning of the same area show a large hysteresis between them, strongly suggesting that the wire tip apex is not very sharp.

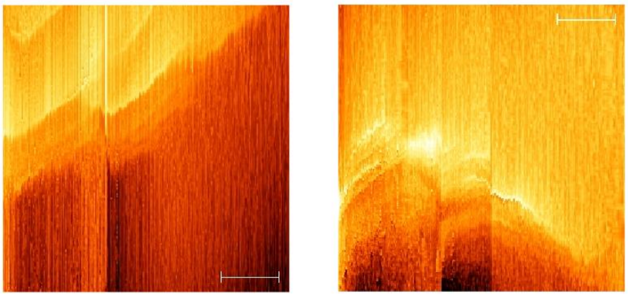

Figure 5.11: Hot wire sensor operated in standard STM mode. STM images of the Au surface scanned with the Pt hot wire, with a $V_{bias} = 0.5\ \mathrm{V}$ and scanning in the y-direction (forward and backward signals for the same scanned area). Images show a large hysteresis between them, suggesting a not very sharp tip. Image size is $98 \times 98\ \mathrm{nm}^2$ and scale bars are equal to $20\ \mathrm{nm}$.

To measure the thermal conductance of Au-Au atomic contacts we proceed in two steps, as already introduced. Initial baseline measurements with a small electrical current through the wire, and the bridge balanced with $R_{var} = R_{el,HW,0}$, allow us to experimentally determine the different parameters of the electrical circuit.

Once this is done, the electrical current through the wire is increased and it heats up. This is monitored using the Wheatstone bridge in order to find the average temperature rise of the wire and comparison with the model serves at this point to phenomenologically fit the convection coefficient h_{conv}. The resistance bridge is then balanced again, this time by matching $R_{var} = R_{el,HW,hot}$. After this, voltage differences measured in the bridge V_{ab} are proportional to changes in the hot wire resistance $\Delta R_{el,HW}$ and the relation is given by Eq. (5.28). In both situations, for baseline and thermal conductance measurements, atomic contacts with the substrate are formed using the STM-BJ approach, controlling the piezo movement with the input voltage V_c. Its real component is amplified by a factor 100 in the lock-in and send to the piezocontroller using one of the auxiliary outputs of the lock-in.

For the baseline measurements, without heating the wire, we apply $V_h = 1\ \mathrm{V}$ at a frequency $f_h = 10.123 \times 10^3\ \mathrm{Hz}$. This frequency is higher than the inverse of the time response of the hot wire (which is of the order of ms) and high enough to avoid the $1/f$ output noise of the lock-in amplifier ($> 10\ \mathrm{kHz}$). The bridge is balanced matching the variable resistor to the “cold-wire” electrical resistance $R_{el,HW,0}$, which is typically $\sim 4-6\ \Omega$. Applying the model for the electrical circuit, we obtain that $I_{el,HW} \sim 3.45\ \mathrm{mA}$ in this situation. Contact formation with these conditions results in measurements as the one presented in Figure 5.12, where V_{ab} and V_c simultaneously acquired for a contact formation are shown as a function of time in Figure 5.12(a,b), respectively.

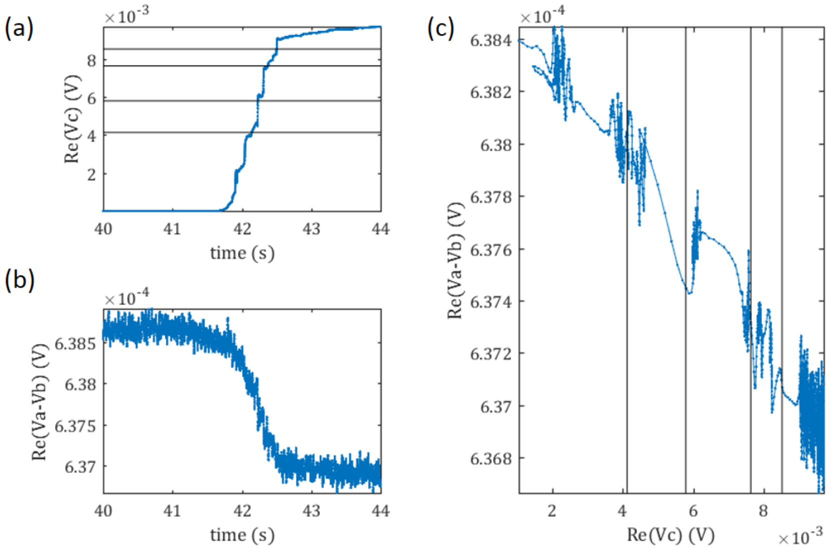

Figure 5.12: Individual approach curve for the baseline characterization. (a) V_c measured while the hot wire approaches to form a metallic contact. Black horizontal lines indicate the expected values for 1-, 2-, 5- and 10- atom contacts. (b) V_{ab} simultaneously acquired to V_c in (a). The changes in the bridge response are due to the electrical leaking current though the contact. (c) V_{ab} *vs* V_c plot showing a linear dependence between them. As the contact (V_c) increases, the bridge response V_{ab} decreases (artificially “cooling down”).

In Figure 5.12(a), the wire approaches the substrate from the tunnelling regime and the current through the junction V_c rapidly increases when reaching the contact. According to the model, this occurs for $V_c \sim 4.2\ \mathrm{mV}$ and, for the sake of commodity, we have marked it with a black horizontal line in the figure. Larger contacts corresponding to 2, 5 and 10 atoms contributing to the current have been also indicated with black horizontal lines. Above $\sim 9\ \mathrm{mV}$ the signal saturates, due to the reduced input voltage range of the amplifier (2.1 V), while the wire is still moving towards the substrate, as it happens in standard BJ experiments. A resistor $R_{para} = 9.94\ \mathrm{k\Omega}$ connected in parallel to the entry of the input channel is used in the experiments to enlarge this input range and be able to identify one and few atom contacts. The total displacement of the wire is in this measurement around $300\text{-}400\ \mathrm{nm}$, which is quite large compared to tip displacements in standard STM-BJ experiments and it is possibly due to the compliant wire encountering difficulties to form the electrical contact with the substrate. V_{ab} signal shows an equivalent behaviour to V_c, decreasing rapidly upon contact formation, but with less resolution in the features of the signal since the measured values are smaller. This V_{ab}

signal are the changes experienced by the electrical resistance of the hot wire due to the leaking electrical current, which is very small but not negligible. Figure 5.12(c) shows the changes in the bridge response V_{ab} as a function of the electrical signal through the junction V_c. This representation evidences the relation between these two magnitudes since the variation of V_{ab} as V_c increases (and the contact is formed) is caused by the electrical current loses that determine the value of V_c, once considered the electrical resistance of the junction. The black vertical lines presented in this plot correspond to the V_c value for 1-, 2-, 5- and 10-atom contacts.

When the wire is mechanically stable enough, reproducible approach-retraction cycles forming and braking the contact can be acquired, as shown in Figure 5.13(a,b). In these plots, each approach and retraction curve is shown in a different colour. Reproducibility of the measurements can be better ascertained from Figure 5.13(c), where two plots are presented, one generated from the direct data acquired and a second one is a density plot. In Figure 5.13(c) the width in the V_{ab} signal (its dispersion) is partially due to the resolution of the measurements combined with the thermal drift with time observed in Figure 5.13(b). The black thick lines superimposed to the data corresponds to V_{ab} *vs* V_c values calculated with the model of the electric circuit, fitted to be in good agreement with the experiments and include all the electrical contributions to the signal. We observe in these plots that there is a linear relation between V_{ab} and V_c, as expected, and in the 2D histograms conductance quantization is also identifiable.

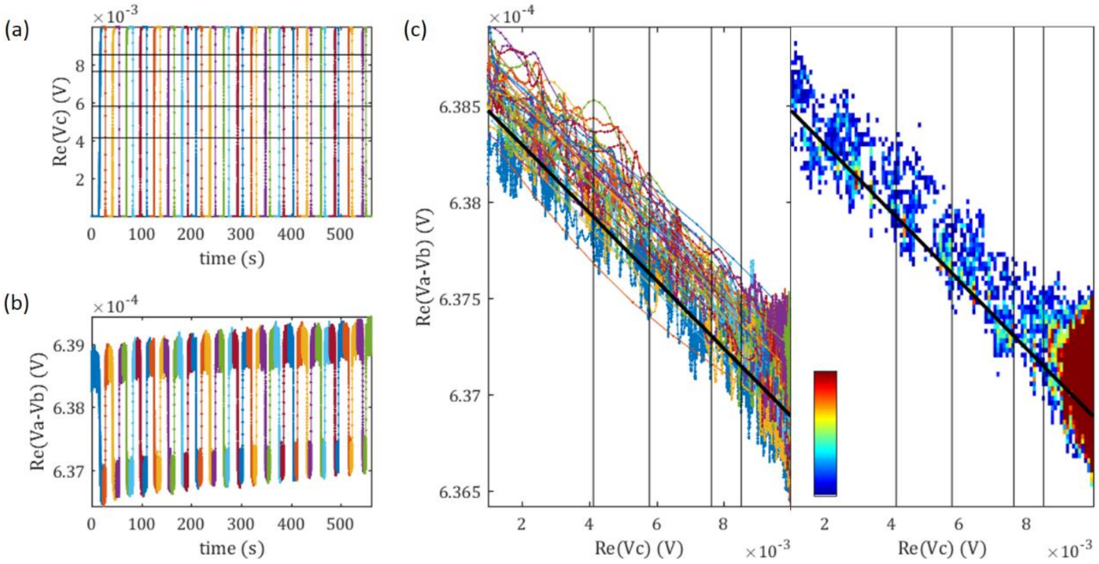

Figure 5.13: Reproducibility of baseline measurements and fit with the model. (a,b) V_c and V_{ab} simultaneously measured for 20 consecutive approach-retraction cycles forming a metallic contact in all cases. Each half-cycle is plotted in a different color. Black horizontal lines indicate the expected values for 1-, 2-, 5- and 10- atom contacts. The changes in the bridge response are due to the electrical leaking current through the contact. (c) V_{ab} *vs* V_c plot (left panel) and corresponding 2D histogram (right panel). These representations show a linear dependence of V_{ab} *vs* V_c as expected with the model (black thick line) for this situation in which we are not heating the wire. Conductance quantitation in V_c is observed in the 2D histogram.

Heating of the wire is then performed to address the targeted thermal conductance measurements of atomic contacts. The heating voltage is set to provide $V_h = 4\ \mathrm{V}$ which translates into a heating current $I_{el,HW} \sim 13.8\ \mathrm{mA}$ through the wire. Its electrical resistance is observed to increase until $R_{el,HW,hot} = 4.818\ \Omega$ and from the change in the resistance with respect to the "cold-wire" value, applying Eq. (5.1) ($\Delta R_{el,HW} = R_{el,HW,0}\alpha_{Pt}\Delta T_{av}$, where $\alpha_{Pt} =$

$3.927 \times 10^{-3}\ 1/\mathrm{K}$), the average temperature rise can be extracted, giving $\Delta T_{av} = 12.07\ \mathrm{K}$. The convection coefficient coefficient h_{conv} is adjusted after heating the wire, based on the expected average temperature rise of the wire when it is close to the surface without touching it. The bridge is then balanced again using the variable resistance R_{var}. This way we start the experimental measurements with V_{ab} cancelled and registering resistance changes with respect to $R_{el,HW,hot}$. Figure 5.14(a,b) shows an example of V_{ab} an V_c measurement, respectively, simultaneously acquired during an retraction of the wire. V_c signal is initially saturated since we have a large contact between the wire and the substrate and it then starts decreasing as the wire retracts from the surface. A rapid decrease in V_c is observed when the metallic contact is finally broken, at $t \sim 277.2$ s in the Figure. Note the plateau in the signal at V_c value corresponding to one atom contact. V_c keeps decreasing in the tunnelling regime, although is not visible in this linear representation. The simultaneous bridge response V_{ab} starts increasing as the wire retracts from the substrate, meaning that the wire is heating up since the contact is progressively smaller and the heat and electrical current lost through it are smaller. Note that in this signal is never saturated and it is possible to trace large contact variations not identifiable with the electrical signal V_c. When the metallic contact is finally broken, we observe a jump up in V_{ab} followed by a small plateau at $V_{ab} \sim 3.685\ \mathrm{mV}$, a second slightly larger jump up followed by a larger plateau with a certain slope at $V_{ab} \sim 3.690\ \mathrm{mV}$ and further rapid increase of V_{ab} with a final change in the slope for $t > 278.5$ s, aproximately. The correlation of the small plateau at $V_{ab} \sim 3.685\ \mathrm{mV}$ with the simultaneous plateau observed in the V_c signal indicates that corresponds to one atom contact. The second (longer) plateau, observed in our measurements also when forming the contacts, is possibly due to the ambient water layer present on the surface and it reflects thermal current contributions flowing through the water meniscus formed between the wire and the surface when they are in close proximity, as it is the case. Figure 5.14(c) shows a V_{ab} *vs* V_c plot of this individual retraction curve. The main feature distinct to the baseline measurements is the curvature shown by V_{ab} as V_c increases. Note that in these measurements the resolution is improved with respect to the baseline characterization thanks to the larger electrical current employed to heat the wire.

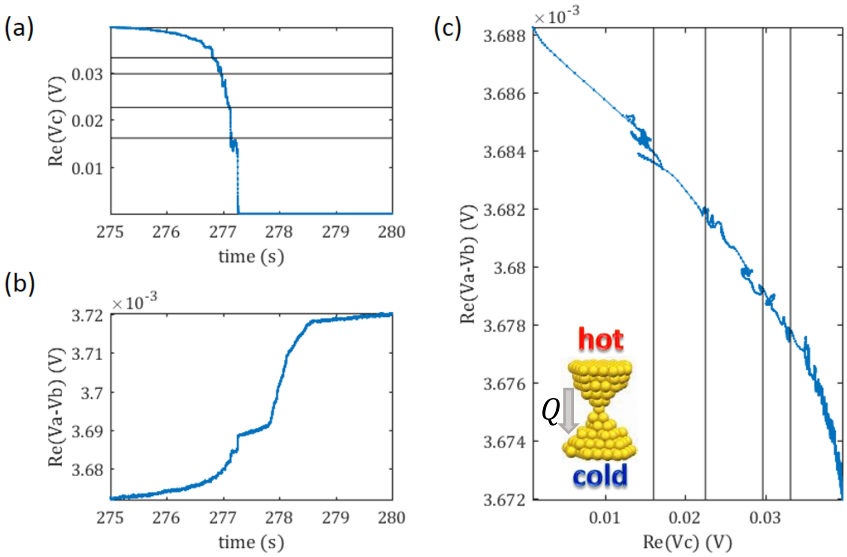

Figure 5.14: Individual retraction traces for thermal conductance characterization. (a,b) Simultaneous V_c and V_{ab} measurements with the hot wire for a metallic Au-Au contact breaking. Black horizontal lines indicate the expected values for 1-, 2-, 5- and 10- atom contacts. (c) V_{ab} *vs* V_c plot showing a curvature of the bridge response as the contact (V_c) increases. This is the signature of a thermal current through the junction.

Reproducible contact formation is achievable when the wire presents enough mechanical stability and measurements as those shown in Figure 5.15 are acquired. As it can be observed, the curvature of V_{ab} when the contact becomes larger is a general behaviour present in all the individual curves. This is indeed the signature of a thermal current flowing through the atomic contact, as confirmed by comparison with the model (thick black line). Here we are not considering thermal current loses in the model, we are only introducing electrical contributions and thus obtain a linear relation between V_{ab} and V_c in the model. The deviation of the experimental curves with respect to these purely electrical modelled values is directly the contribution of the thermal currents through the atomic contacts. We therefore subtract the modelled values to the experimental data, both for the baseline measurements and the thermal conductance measurements, and obtain the “cooling” signal, without electrical contributions. 2D histograms of this cooling signal are shown in Figure 5.16. In these plots, the average value of V_{ab} for the tunnelling regime has been also subtracted in order to facilitate comparison (offset correction). As can be observed, subtraction of the modelled electrical values results in a zero cooling signal in the baseline measurement. The dispersion of these values is caused by the smaller resolution in these measurements. In the hot wire measurements, however, the cooling signal increases as V_c increases, linearly at the beginning and much faster at the end. Note also the change in scale between the baseline measurements and the measurements with the wire heated.

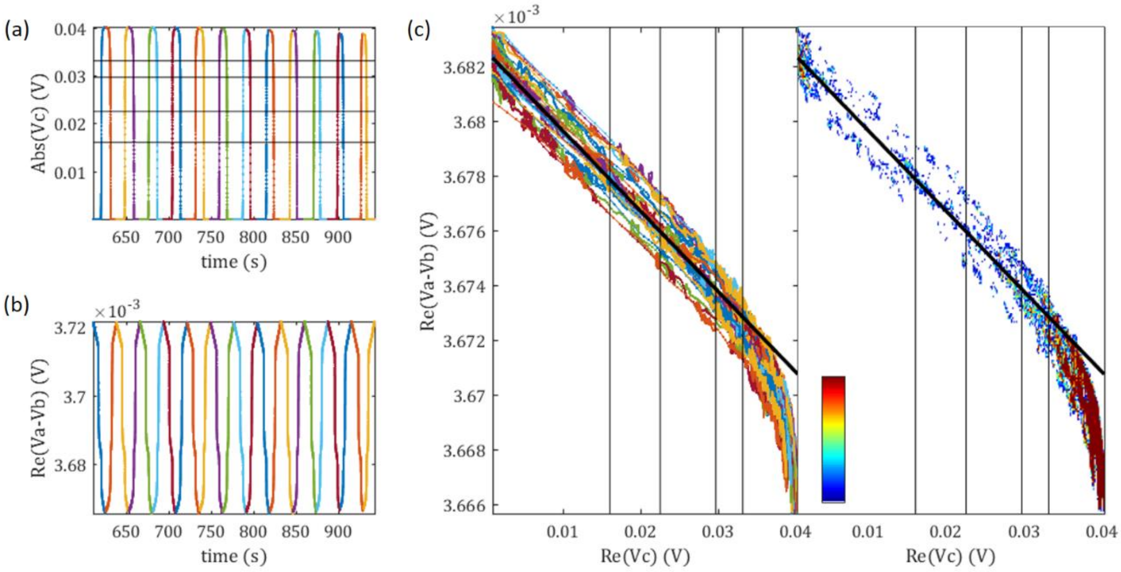

Figure 5.15: Reproducibility of thermal conductance measurements and fit with the model. (a,b) V_c and V_{ab} simultaneously measured for 12 consecutive approach-retraction cycles forming a metallic contact in all cases. Each half-cycle is plotted in a different color. Black horizontal lines indicate the expected values for 1-, 2-, 5- and 10- atom contacts. (c) V_{ab} *vs* V_c plot (left panel) and corresponding 2D histogram (right panel). V_{ab} curves down as the metallic contact becomes larger and deviates from the expected values calculated with the model for purely electrical contributions (black thick lines on both plots). The difference between the experimental data and the model corresponds to the resistance changes in the wire due to thermal current through the atomic contact.

Finally, Figure 5.17 shows the offset corrected cooling signal, i.e. the measured V_{ab} after subtracting the modelled and the tunnelling offset, as a function of the number of atoms in the atomic contact, up to 10. In the baseline measurements, mainly small atomic contacts up to 4 atoms are registered in this range, which translates into a reduced density in the 2D plot for contacts between 4 and 10 atoms. Nevertheless, it can be observed that there is no dependence of the cooling signal with the number of atoms, being essentially zero. In the case of the thermal conductance measurements, a linear increase of the cooling signal can be observed at least up to 5-atom contacts, where the slope of the cooling signal seems to vary. This slope is in good agreement with the ratio of V_{ab} changes per atom thermal conductance that we estimated when discussing the sensitivity of the wires (Section 5.2.5), around $140\ \mathrm{nV}/G_0$, thus confirming the validity of the Wiedemann-Franz law and the resolution of our hot wire probes to measure the thermal conductance of Au single-atom contacts.

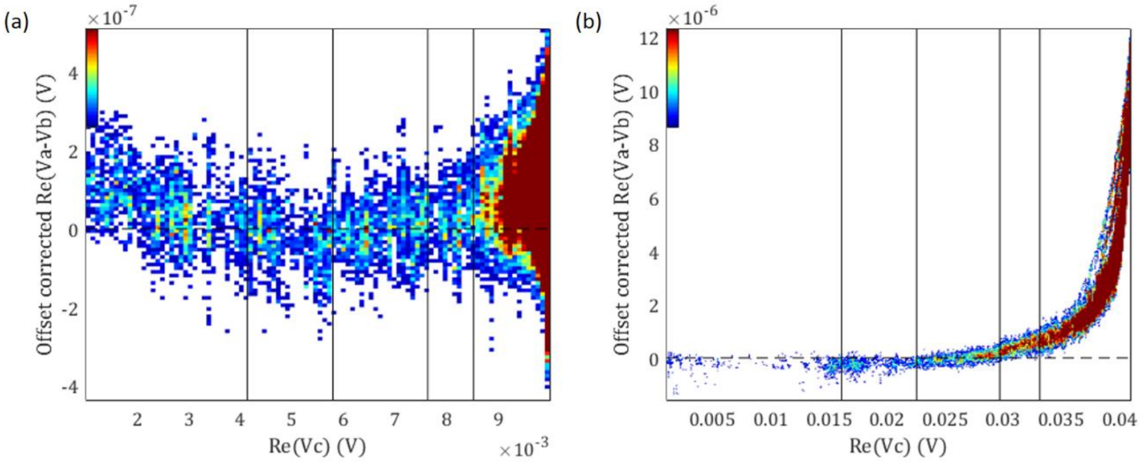

Figure 5.16: Cooling signals for the baseline (a) and the thermal conductance measurements (b). 2D histograms formed with 20 consecutive approach-retraction curves for (a) and 38 retraction traces for (b). Baseline measurements show no dependence with the contact size (we are not heating the wire) while the bridge response clearly increases with the contact size, given by V_c. Black vertical lines indicate the expected values of V_c for 1-, 2-, 5- and 10- atom contacts. Note the different scale of the offset corrected V_{ab} values in both plots.

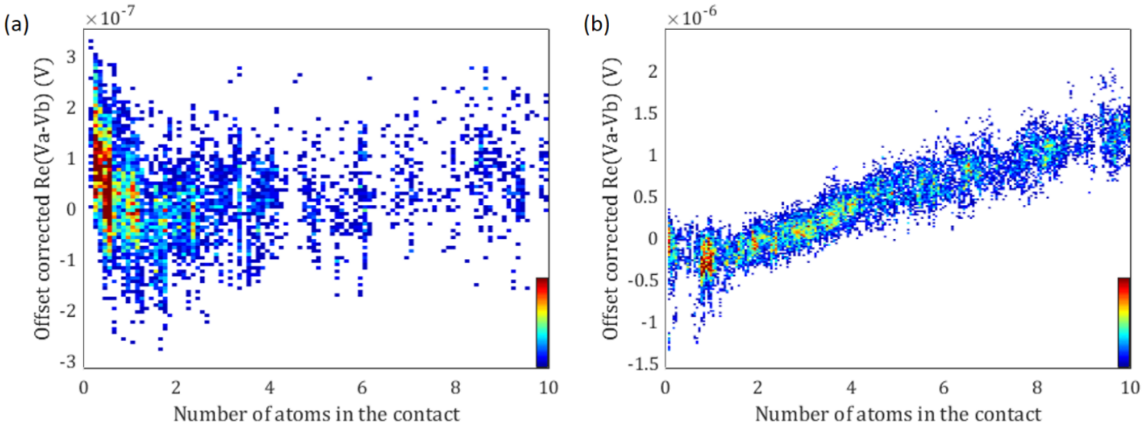

Figure 5.17: Cooling signals for the baseline (a) and the thermal conductance measurements (b) as a function of the number of Au atoms in the atomic contact. 2D histograms formed with the same curves as Figure 5.16 for the offset corrected V_{ab} values as a function of the number of Au atoms in the contact. Despite the reduced number of points in the range between 5 and atoms, baseline measurements show no dependence with the contact size (we are not heating the wire). The bridge response (b) increases linearly with the number of atoms in the contact and the slope is in good agreement with Wiedemann-Franz law for few-atom contacts. Note the different scale of the offset corrected V_{ab} values in both plots.

5.4 Further development of the technique

Several developments and improvements to the technique have been very recently think of or implemented.

The major improvement is the modification of the measurement electrical circuit to a double Wheatstone bridge to control the bias voltage at the center of the hot wire and reduce the heating electrical current loses. The two symmetric resistance bridges allow to use two independent voltage sources (at both ends) which provide signals at two different frequencies to separately control the heating current and the voltage difference between the hot wire and the sample. An adequate compensation of the voltage in the wire at the frequency of the heating current cancels the current leakages to the substrate while a second frequency and a small voltage difference are used to measure the tunnelling current through the junction. Thermal and electrical signals are thereby decoupled.

Another improvement recently implemented is a controlled coarse approach of the hot wire towards the substrate using three piezomotors to regulate and maintain the inclination and incident angle of the hot wire middle point. This implementation would also to explore the change in the hot wire resistance (and temperature) as the tip approaches the surface from very far away (microns).

Finally, further development of the model is also required. It has to account for this observed strong dependence of the wire temperature with its distance to the sample surface and for the possibility of having a substrate temperature T_S different from ambient temperature or a local ambient temperature T_0' at the surface of the wire different to T_0.

5.5 Conclusions

We have built a new setup based on a hot wire sensor to measure simultaneously the thermal conductance and the electrical conductance of metallic atomic contacts and, potentially, molecular junctions in ambient conditions.

A novel, versatile technique has been developed based on the use of a Wollaston wire, a resistance bridge and lock-in detection, with a considerable cost reduction in time and money with respect to the state-of-the-art techniques. The thorough thermal and electrical model considered, crucial to determine the thermal conductance of the junctions, has been also introduced, as well as the baseline measurements that confirm its validity.

Our measurements have demonstrated enough thermal resolution to measure one gold atom thermal conductance with a Wollaston wire and confirmed the validity of Wiedemann-Franz law.

Additionally, experiments in ambient conditions show a large effect of convection on the thermal signal undoubtedly of interest for future characterization.

References

[Cuevas2010] J. C. Cuevas and E. Scheer. “Molecular Electronics: An Introduction to Theory and Experiment”. World Scientific Publishers, Singapore (2010).

[Cui2017] L. Cui, W. Jeong, S. Hur, M. Matt, J.C. Klöckner, F. Pauly, P. Nielaba, J.C. Cuevas, E. Meyhofer and P. Reddy. “Quantized thermal transport in single-atom junctions”. *Science* **355**(6330), 1192-119 (2017).

[Cui2019] L. Cui, S. Hur, Z. Alaia Akbar, J. C. Klöckner, W. Jeong, F. Pauly, S.-Y. Jang, P. Reddy and E. Meyhofer. “Thermal conductance of single-molecule junctions”. *Nature* **572**, 628-633 (2019).

[Dames2007] C. Dames, S. Chen, C. T. Harris, J. Y. Huang, Z. F. Ren, M. S. Dresselhaus and G. Chen. “A hot-wire probe for thermal measurements of nanowires and nanotubes inside a transmission electron microscope”. *Review of Scientific Instruments* **78**, 104903 (2007).

[efunda] https://www.efunda.com/materials/elements/TC_Table.cfm?Element_ID=Pt

[Kim2015] K. Kim, B. Song, V. Fernández-Hurtado, W. Lee, W. Jeong, L. Cui, D. Thompson, J. Feist, M. T. H. Reid, F. J. García-Vidal, J. C. Cuevas, E. Meyhofer and P. Reddy. “Radiative heat transfer in the extreme near field”. *Nature* **28**, 387-391 (2015).

[Lefèvre2003] S. Lefèvre, S. Volz, J.-B. Saulnier, C. Fuentes and N. Trannoy. “Thermal conductivity calibration for hot wire based dc scanning thermal microscopy”. *Review of Scientific Instruments* **74**(4), 2418-2423 (2003).

[Lefèvre2006] S. Lefèvre, S. Volz, P.-O. Chapuis. “Nanoscale heat transfer at contact between a hot tip and a substrate”. *International Journal of Heat and Mass Transfer* **49**(1-2), 251-258 (2006).

[Mosso2017] N. Mosso, U. Drechsler, F. Menges, P. Nirmalraj, S. Karg, H. Riel and B. Gotsmann. “Heat transport through atomic contacts”. *Nature Nanotechnology* **12**, 430-433 (2017).

[Mosso2019] N. Mosso, H. Sadeghi, A. Gemma, S. Sangtarash, U. Drechsler, C. J. Lambert and Bernd Gotsmann. “Thermal Transport through Single-Molecule Junctions”. *Nano Letters*, doi: 10.1021/acs.nanolett.9b02089 (2019).

[Perry1982] A. E. Perry. “Hot Wire Anemometry”. Oxford University Press, New York (1982).

[Pylkki1994] R. J. Pylkki, P. J. Moyer and P. E. West. “Scanning Near-Field Optical Microscopy and Scanning Thermal Microscopy”. *Japanese Journal of Applied Physics* **33**, Part 1, 3785-3790 (1994).

General Conclusions

The aim of this PhD Thesis is the experimental investigation of charge and heat transport in molecular junctions and atomic contacts. The ultimate goal of this research is paving the way for the development of molecular electronic and thermoelectric devices, for which the measurement, control and understanding of these transport properties at the single-molecule level are essential. More importantly, detailed examination of these versatile systems is of great fundamental interest since they are an exceptional platform to test quantum transport theories at the nanoscale.

Thermoelectricity of single-molecule junctions, complemented with electrical conductance characterization, has been explored using a home-built scanning tunnelling microscope (STM) operating in ambient conditions and at room temperature. The experimental technique, previously initiated in our group during Dr. Charalambos Evangeli PhD Thesis, has allowed us to perform simultaneous measurements of conductance G and thermopower S of Au|single-molecule|Au junctions with two different approaches: the STM-Imaging technique and the STM-Break Junction (STM-BJ) technique.

The STM-Imaging technique has been exploited to investigate the transport properties of three endohedral metallofullerenes (EMFs), namely, $Sc_3N@C_{80}$, $Sc_3C_2@C_{80}$ and $Er_3N@C_{80}$ junctions. This is the first reported characterization of thermoelectricity of endohedral metallofullerenes with inner clusters this large, to the best of our knowledge, and it has enabled the discovery of their bi-thermoelectric nature when connected between gold electrodes. Imaging of the surface prior to junction formation allows us to know precisely the number of molecules participating in the junction and systems with one and two EMFs connected in series between the electrodes have been studied. Our experiments with single-EMF junctions have shown that their thermopower at first contact can be positive or negative, depending on the selected molecule without doping and without changing the chemical composition, an effect that we have named bi-thermoelectricity. Furthermore, tunnelling spectroscopy on different isolated molecules has confirmed a change in the asymmetry of the curves correlated with the sign of the thermopower obtained when contacting the molecule. DFT theoretical calculations performed by the group of Prof. Colin J. Lambert for $Sc_3N@C_{80}$ junctions have contributed to elucidate the origin of this peculiar performance. Their calculations strongly suggest that the bi-thermoelectric behaviour is due to the presence of the metallic cluster inside the fullerene cage, which creates an additional transmission resonance very close to the Fermi level and whose exact energy and shape depend on the orientation of the molecule. Our combined results have also demonstrated the possibility to tune the sign of the thermopower by mechanical compression of the junctions, caused by the high sensitivity of the resonance energy and shape to compression. Additionally, dimer EMF junctions experimentally investigated have shown similar bi-thermoelectricity with even larger spread of thermopower values, especially for $Er_3N@C_{80}$ junctions, due to the combined effect of the individual molecules.

Complementary, different strategies for thermoelectric response enhancement have been also explored using the STM-BJ technique. This technique, based on repeated formation of reproducible molecular junctions, has been fully implemented in our experimental setup and has been adapted to gain access to a wide range of molecular systems. Collaboration with research groups specialized in organic chemical synthesis has been also essential to achieve this goal. To the best of our knowledge, we have performed thermoelectricity characterization of three different groups of molecules for the first time: fluorene derivatives, oligoyne wires and porphyrin-based oligomers.

Transport properties tunability by chemical substitution of the side-group in a given backbone has been demonstrated for a series of five 2,7-dipyridylfluorene derivatives, synthesized by the group of Prof. Martin Bryce with different substituents at the C(9) position of the fluorene. Au|single-molecule|Au junctions show in all cases very similar most probable conductance values, strongly suggesting similar transport pathways through all the compounds, predominantly through the π-conjugated backbone. With respect to the thermoelectric response, they exhibit negative Seebeck coefficients varying from $S = -5.5\ \mu\mathrm{V/K}$ for molecule Fl-H to $S = -9.0\ \mu\mathrm{V/K}$ for molecule Fl-O. The sign of these coefficients indicates transport through the LUMO, as it is typically the case in pyridine-anchored compounds. Our results demonstrate a 1.6-fold enhancement in the thermopower of the fluorene derivatives by substituent modification without affecting the conductance of the molecular junctions, which remains essentially unchanged across the series of molecules. DFT calculations performed by the group of Prof. Colin J. Lambert show that excellent agreement with the experimental results can be obtained under the consideration of variations from molecule to molecule of the Fermi level position relative to the frontier molecular orbital energies. Thus, this combined experimental and theoretical study sheds light on the influence of non-conjugated pendant substituents on the thermopower of a molecular system.

The characterization of conductance and thermopower of oligoyne wires has been performed to explore the length dependence of these properties. The molecules, synthesized by the group of Prof. Rik R. Tykwinski, present an even number of triple carbon-carbon bonds in the backbone (from 2 to 8) and modified pyridine anchor groups. Our results demonstrate an exponential decrease of the most probable conductance value as the oligoyne wires become longer, indicating charge tunnelling transport through the molecular junctions. For this series, which includes longer oligoynes than previously reported, $\beta = 2.1\ \mathrm{nm}^{-1}$ has been obtained. Thermopower measurements in these junctions show in all cases negative values of the Seebeck coefficient and transport mainly through the LUMO is thereby indicated. The absolute value of thermopower has been demonstrated to linearly increase with the molecular length from $S = -10.7\ \mu\mathrm{V/K}$ for 2-yne junctions to $S = -20.6\ \mu\mathrm{V/K}$ in the case of 8-yne systems, giving a rate of change $\beta_S = -6.6\ \mu\mathrm{V/K/nm}$ and a total 2-fold enhancement in the thermopower of these oligoyne wires. The linear dependence of the thermopower with increasing length further confirms the coherent tunnelling mechanism.

Length dependence of thermopower has been also explored in a series of five Zn-based oligo-porphyrins, in which the influence of different inter-porphyrin coupling has been addressed as well. The family investigated, synthesized by the group of Prof. Harry Anderson, consists of three butadiyne-linked oligo-porphyrins (named monomer, dimer and trimer and formed by one, two and three Zn-porphyrin units, respectively) and of two fused oligo-porphyrins, where two and three porphyrin units are strongly connected directly between them (fused dimer and fused trimer). These two molecules in particular result especially appealing since their conductance at low bias voltage has been previously reported decrease only slightly with increasing length. With respect to the thermoelectricity, the five compounds are found to exhibit positive Seebeck coefficients, signature of predominant transport through the HOMO. Interestingly, our results indicate a possible odd-even effect in the thermopower of these series and we have found that, independently of the inter-porphyrin coupling in the backbone, oligomers formed by two porphyrin units present a reduced thermopower value compared to the trend with increasing length shown by the monomer and the corresponding three-porphyrin molecule. Regarding these trends, butadiyne-linked oligomers thermopower is enhanced by a factor 2.7 from monomer to trimer junctions, being the Seebeck coefficient shown by trimer junctions ($S = 52.8\ \mu\mathrm{V/K}$) among the highest values reported so far, to the best our knowledge. In the case of fused systems, the Seebeck coefficient enhancement of fused trimer junctions with respect to the monomer is considerably smaller, around a factor 1.3. Therefore, an increase of the molecular length by a factor 1.6 translates into minor, and unconventional, conductance reduction and thermopower enhancement.

Finally, a new experimental technique to perform thermal conductance measurements in model nanoscale junctions, such as atomic contacts or molecular junctions, has been presented. The novel setup mounted consists of a Wollaston hot wire acting simultaneously as a local heater and thermometer as well as a STM probe. This approach allows us to perform combined electrical and thermal conductance measurements in nanoscale junctions formed in a controlled way with the well-known STM-BJ technique. A resistance bridge and *ac* signals detection with a lock-in are used to obtain an improved signal-to-noise ratio and accurately find the hot wire resistance and hence its temperature. Minute temperature and electrical conductance variations can be followed during junction formation thanks to the fast response time of the wires used. Complementary, the tip-shaped hot wire mounted on the STM piezo scanner facilitates scanning of the sample surface. The experimental technique has been tested in Au atomic contacts and the results obtained have demonstrated enough thermal resolution of the hot wire sensors as well as good agreement with previously reported values of the thermal conductance of few atoms contacts. Furthermore, the theoretical formalism used to obtain these results has confirmed that it is crucial to consider convection loses to the environment, observed to greatly affect the hot wire thermal equilibrium, and that thermal currents through atomic contacts dominate over any other contribution when the contact is formed. Thermal transport measurements performed with this versatile technique in ambient conditions go beyond the state-of-the-art and the strategies suggested for mechanical stability and thermal resolution improvement open the door to the single-molecule thermal conductance characterization.

Conclusiones Generales

El propósito de esta Tesis Doctoral es la investigación experimental del transporte de carga y calor en uniones moleculares y contactos atómicos. El objetivo final de esta investigación es allanar el camino para el desarrollo de electrónica molecular y dispositivos termoeléctricos, para lo cual la medida, control y comprensión de estas propiedades de transporte a nivel de una única molécula son esenciales. Aún más importante, el examen detallado de estos versátiles sistemas es de gran interés fundamental dado que son plataformas excepcionales para poner a prueba teorías de transporte cuántico en la escala nanométrica.

La termoelectricidad de uniones moleculares individuales, complementada con la caracterización de la conductancia eléctrica, ha sido explorada utilizando un microscopio de efecto túnel (STM, por sus siglas en inglés) de fabricación propia y operado en condiciones y a temperatura ambiente. La técnica experimental, iniciada previamente en nuestro grupo durante la Tesis Doctoral del Dr. Charalambos Evangeli, nos ha permitido realizar medidas simultáneas de conductancia G y coeficiente Seebeck S de uniones Au|molécula|Au con dos enfoques diferentes: la técnica de STM-Imaging y la técnica de STM-Break Junction (STM-BJ).

La técnica de STM-Imaging se ha explotado para investigar las propiedades de transporte tres fullerenos endohédricos metálicos (EMFs, por sus siglas en inglés), en concreto, uniones formadas por $Sc_3N@C_{80}$, $Sc_3C_2@C_{80}$ y $Er_3N@C_{80}$. Esta es la primera caracterización de termoelectricidad reportada de fullerenos endohédricos metálicos con grupos internos de átomos tan grandes, que conozcamos, y ha permitido el descubrimiento de su naturaleza bi-termoeléctrica cuando se conectan con electrodos de oro. Imágenes de la superficie antes de formar la unión nos permite conocer con precisión el número de moléculas que participan en las uniones y se han estudiado sistemas con uno y dos EMFs conectados en serie entre los electrodos. Nuestros experimentos con uniones de EMF individuales han mostrado que su coeficiente Seebeck puede ser positivo o negativo, dependiendo de la molécula seleccionada, sin dopaje y sin cambiar su composición química, un efecto que hemos denominado bi-termoelectricidad. Además, espectroscopía túnel en diferentes moléculas aisladas ha confirmado un cambio en la asimetría de las curvas correlacionada con el signo del coeficiente Seebeck obtenido cuando se contacta la molécula. Cálculos teóricos de DFT realizados por el grupo del Prof. Colin J. Lambert para las uniones de $Sc_3N@C_{80}$ han contribuido a elucidar el origen de este desempeño peculiar. Sus cálculos sugieren fuertemente que el comportamiento bi-termoeléctrico es debido a la presencia del grupo de átomos metálicos dentro del fullereno, lo que crea una resonancia de transmisión adicional muy cerca del nivel de Fermi y cuya energía y forma exacta depende de la orientación de la molécula. Nuestros resultados combinados han demostrado también la posibilidad de modificar el signo del coeficiente Seebeck mediante compresión mecánica de las uniones, causada por la alta sensibilidad de la energía y la forma de la resonancia a la compresión. Adicionalmente, uniones de dímeros de EMF investigados experimentalmente han mostrado una bi-termoelectricidad similar con una mayor dispersión de los valores de coeficiente Seebeck, especialmente para las uniones de $Er_3N@C_{80}$, debido al efecto combinado de las moléculas individuales.

Complementariamente, se han explorado diferentes estrategias para mejorar la respuesta termoeléctrica utilizando la técnica de STM-BJ. Esta técnica, basada en la repetida formación de uniones moleculares reproducibles, ha sido implementada por completo en nuestro equipo experimental y se ha adaptado para ganar acceso a un amplio rango de sistemas moleculares. La colaboración con grupos de investigación especializados en síntesis química ha sido también esencial para alcanzar este objetivo. Por lo que sabemos, hemos realizado la caracterización termoeléctrica de tres grupos diferentes de moléculas por primera vez: derivados de fluorenos, cables moleculares de oligoinos y oligómeros de porfirinas.

La modificación de las propiedades de transporte mediante sustitución química del grupo lateral en una misma estructura molecular se ha demostrado para una serie de cinco derivados de 2,7-dipyridylfluoreno, sintetizados por el grupo del Prof. Martin Bryce con diferentes sustituyentes en la posición C(9) del fluoreno. Uniones Au|molécula|Au muestran en todos los casos valores más probables de conductancia similares, fuertemente sugiriendo caminos de transporte similares a través de todos los compuestos, predominantemente a través de la estructura central con conjugación π. Con respecto a la respuesta termoeléctrica, exhiben coeficientes Seebeck negativos que varían entre $S = -5.5\ \mu\mathrm{V/K}$ para la molécula Fl-H y $S = -9.0\ \mu\mathrm{V/K}$ para la molécula Fl-O. El signo de estos coeficientes indica transporte a través del LUMO, como es típicamente el caso en compuestos con piridina como grupo de anclaje. Nuestros resultados demuestran un aumento de 1.6 veces en el coeficiente Seebeck de derivados de fluorenos mediante modificación de los sustituyentes sin afectar la conductancia de las uniones moleculares. Cálculos de DFT realizados por el grupo del Prof. Colin J. Lambert muestran que es posible alcanzar un acuerdo excelente con los resultados experimentales bajo la consideración de variaciones entre moléculas de la posición del nivel de Fermi relativa a las energías de los orbitales moleculares de frontera. Así, este estudio experimental y teórico combinado aporta luz sobre la influencia de sustituyentes laterales no conjugados sobre el coeficiente Seebeck un sistema molecular.

La caracterización de la conductancia y el coeficiente Seebeck de cables moleculares de oligoinos ha sido realizada para explorar la dependencia con la longitud de estas propiedades. Las moléculas, sintetizadas por el grupo del Prof. Rik R. Tykwinski, presentan un número par de enlaces triples carbono-carbono en la estructura central (de 2 a 8) y grupos de anclaje piridina modificados. Nuestros resultados demuestran una disminución exponencial del valor más probable de conductancia a medida que el oligoino se hace más largo, indicando transporte túnel de las cargas a través de las uniones moleculares. Para esta serie, que incluye oligoinos más largos de los reportados hasta ahora, se ha obtenido $\beta = 2.1\ \mathrm{nm}^{-1}$. Las medidas de coeficiente Seebeck en estas uniones muestran en todos los casos valores negativos del mismo y transporte principalmente a través del LUMO es por lo tanto indicado. Se ha demostrado que el valor absoluto de coeficiente Seebeck aumenta linealmente con la longitud molecular desde $S = -10.7\ \mu\mathrm{V/K}$ para uniones de 2-yne a $S = -20.6\ \mu\mathrm{V/K}$ en el caso de sistemas de 8-yne, dando un ratio de cambio $\beta_S = -6.6\ \mu\mathrm{V/K/nm}$ y una incremento total de un factor 2 en el coeficiente Seebeck de estos cables moleculares de oligoinos. La dependencia lineal del coeficiente Seebeck refuerza el mecanismo de túnel coherente.

La dependencia con la longitud del coeficiente Seebeck también se ha explorado en una serie de cinco oligo-porfirinas con átomos de Zn, en la cual también se ha abordado la influencia de diferentes acoples entre las porfirinas. La familia investigada, sintetizada por el grupo del Prof. Haary Anderson, consiste en tres oligómeros de porfirinas conectadas por un buta-1,3-diino o diacetileno (denominados monómero, dímero y trímero y formados por una, dos y tres unidades de porfirinas con átomo de Zn, respectivamente) y por dos oligómeros de porfirinas fusionadas, donde dos y tres unidades de porfirinas están fuertemente conectadas directamente entre ellas (dímero fusionado y trímero fusionado). Estas dos moléculas en particular resultan especialmente atractivas dado que fue previamente publicado que su conductancia a valores bajos de voltaje bias sólo disminuye ligeramente al aumentar la longitud. Respecto a la termoelectricidad, se ha encontrado que los cinco compuestos exhiben coeficientes Seebeck positivos, indicativo de transporte predominante a través del HOMO. De forma muy interesante, nuestros resultados indican un posible efecto impar-par en el coeficiente Seebeck de esta serie y hemos encontrado que, independientemente del acople entre porfirinas en la estructura molecular, oligómeros formados por dos unidades de porfirina presentan un coeficiente Seebeck reducido comparado con la tendencia para longitud en aumento mostrada por el monómero y el trímero correspondiente. Sobre estas tendencias, el coeficiente Seebeck de oligómeros unidos con butadiino aumenta en un factor 2.7 de uniones de monómero a uniones formadas con el trímero, estando el coeficiente Seebeck de las uniones de trímero ($S = 52.8\ \mu\mathrm{V/K}$) entre los valores más alto reportados hasta la fecha, por lo que sabemos. En el caso de los sistemas fusionados, el aumento del coeficiente Seebeck de las uniones del trímero fusionado con respecto al monómero es considerablemente menor, estando en torno a un factor 1.3. Por lo tanto, un aumento de la longitud de las moléculas en un factor 1.6 se traduce en una reducción mínima, e inconvencional, de la conductancia y un ligero aumento del coeficiente Seebeck.

Finalmente, una nueva técnica experimental para realizar medidas de conductancia térmica en uniones nanométricas modelo, como contactos atómicos o uniones moleculares, ha sido presentada. El novedoso equipo montado consiste de un hilo caliente Wollaston actuando simultáneamente como calentador local y termómetro, así como punta de STM. Este enfoque nos permite realizar medidas combinadas de conductancia eléctrica y térmica en uniones nanométricas formadas de una manera controlada con la conocida técnica de STM-BJ. Un puente de resistencias y detección de señales *ac* con un lock-in se utilizan para obtener un ratio de señal-ruido mejorado y encontrar con precisión la resistencia del hilo caliente y, por lo tanto, su temperatura. Los pequeños cambios de temperatura y conductancia se pueden seguir durante la formación de la unión gracias al rápido tiempo de respuesta de los hilos utilizados. De manera complementaria, el hilo caliente con forma de punta montado en el sistema de piezos del STM facilita escanear la superficie de la muestra. La técnica experimental ha sido puesta a prueba en contactos atómicos de Au y los resultados obtenidos han demostrado suficiente resolución térmica de los sensores basados en hilo caliente, así como buen acuerdo con valores previamente reportados de conductancia térmica de contactos de unos pocos átomos. Además, el formalismo teórico utilizado para obtener estos resultados ha confirmado que es crucial considerar las pérdidas al ambiente por convección, las cuales se ha observado que afectan enormemente al equilibrio térmico del hilo caliente, y que las corrientes térmicas a través de contactos atómicos dominan sobre cualquier otra contribución cuando se forma en contacto. Las medidas de transporte térmico realizadas con esta versátil técnica en condiciones ambiente van más allá de los últimos avances en el campo y las estrategias sugeridas para mejorar la estabilidad mecánica y la resolución térmica abren la puerta para la caracterización de la conductancia térmica de moléculas individuales.

Publication List

[1] "Molecular design and control of fullerene-based bi-thermoelectric materials"
Laura Rincón-García, Ali K. Ismael, Charalambos Evangeli, Iain Grace, Gabino Rubio-Bollinger, Kyriakos Porfyrakis, Nicolás Agraït and Colin J. Lambert.
Nature Materials **15**, 289-293 (2016). doi: 10.1038/nmat4487.

[2] "Thermopower measurements in molecular junctions"
Laura Rincón-García, Charalambos Evangeli, Gabino Rubio-Bollinger and Nicolás Agraït.
Chemical Society Reviews **45**, 4285-4306 (2016). doi: 10.1039/C6CS00141F.

[3] "Conductancia y termoelectricidad de uniones unimoleculares"
Laura Rincón-García, Gabino Rubio-Bollinger and Nicolás Agraït.
Revista de Física de la Real Sociedad Española de Física **30**(3), 17-20 (2016). ISSN: 0213-862X

[4] "Thermoelectric Properties of 2,7-Dipyridylfluorene Derivatives in Single-Molecule Junctions"
Gilles Yzambart, Laura Rincón-García, Alaa A. Al-Jobory, Ali K. Ismael, Gabino Rubio-Bollinger, Colin J. Lambert, Nicolás Agraït and Martin R. Bryce.
Journal of Physical Chemistry C **122**(48), 27198-27204 (2018). doi: 10.1021/acs.jpcc.8b08488.

[5] "Endohedral metallofullerenes as bi-thermoelectric nanomaterials"
Ali K. Ismael, Laura Rincón-García, Charalambos Evangeli, Panagiotis Dallas, Alaa A. Al-Jobory, Iain Grace, Kyriakos Porfyrakis, Colin J. Lambert and Nicolás Agraït.
In preparation.

[6] "Thermoelectricity of single-molecule junctions formed with porphyrin oligomers and tapes"
In preparation.

[7] "Direct probing of Landauer formula in oligoyne single-molecule junctions"
In preparation.

Additionally to this Thesis

[8] "Quantum Thermopower of Metallic Atomic-Size Contacts at Room Temperature"
Charalambos Evangeli, Manuel Matt, Laura Rincón-García, Fabian Pauly, Peter Nielaba, Gabino Rubio-Bollinger, Juan Carlos Cuevas and Nicolás Agraït.
Nano Letters **15**(2), 1006-1011 (2015). doi: 10.1021/nl503853v (previous to this Thesis).

[9] "Quantum thermopower enhancement in multilayer MoS_2"
Simon A. Svatek, Alexandros El Sachat, Hatef Sadeghi, Sara Sangtarash, Laura Rincón-García, Riccardo Frisenda, Patricia Gant, David Pérez de Lara, Gabino Rubio-Bollinger, Andrés Castellanos-Gómez, Colin J. Lambert and Nicolás Agraït.
Submitted to *Nanoscale Horizons* (August 2019).

UAM

UNIVERSIDAD AUTONOMA

DE MADRID